Adam Mickiewicz University in Poznan
Faculty of Physics and Astronomy
Institute of Spintronics and Quantum Information

Mirali Jafari

Electronic, magnetic and transport properties of selected van der Waals heterostructures

PhD thesis

Supervisor: **Prof. UAM Dr. hab. Anna Dyrdał**
Co-supervisor: **Dr. Martin Gmitra**

Poznań, October 2025

Streszczenie

Badania nad dwuwymiarowymi (2D) kryształami oraz heterostrukturami van der Waalsa (vdW), dzięki swoim niezwykłym właściwościom, w ostatnich latach cieszą się ogromnym zainteresowaniem z uwagi na ich potencjalne zastosowania w elektronice, spintronice oraz optoelektronice. Pierwszym eksperymentalnie otrzymanym i zarazem jednym z najbardziej obiecujących kryształów dwuwymiarowych jest grafen, który mimo swoich wyjątkowych cech (takich jak niezwykle wysoka ruchliwość elektronów, wytrzymałość mechaniczna, doskonała przewodność elektryczna i cieplna oraz wiele innych) to jednak, ze względu na brak przerwy energetycznej, wydaje się mieć dość ograniczone zastosowanie w kontekście technologii półprzewodnikowych i elementów elektronicznych (np. tranzystory). To ograniczenie skłoniło badaczy do poszukiwania kolejnych dwuwymiarowych materiałów i doprowadziło do odkrycia nowych struktur 2D, takich jak silicen (dwuwymiarowy kryształ krzemu), heksagonalny azotek boru (h-BN), dichalkogenki metali przejściowych (TMDC) oraz inne materiały warstwowe. Każdy z tych materiałów wykazuje odmienne zachowania, od metalicznych po nieprzewodzące, a także od niemagnetycznych po magnetyczne. Ponieważ magnetyzm odgrywa istotną rolę we współczesnych technologiach, materiały 2D o właściwościach magnetycznych wzbudzają szczególne zainteresowanie. Wśród nich na uwagę zasługują dwuwymiarowe dichalkogenki wanadu (VX_2) oraz trójjodki chromu (CrI_3), charakteryzujące się wewnętrznym magnetyzmem i będące podstawą do dalszych badań nad rozwojem wydajnych urządzeń dla elektroniki spinowej (np. zawory spinowe).

Niniejsza rozprawa doktorska, składająca się ze zbioru powiązanych tematycznie artykułów naukowych, przedstawia wyniki badań teoretycznych dotyczących własności elektronowych, magnetycznych i transportowych wybranych kryształów dwuwymiarowych oraz ich heterostruktur van der Waalsa. W badaniach zastosowano zaawansowane techniki obliczeniowe oparte na teorii funkcjonału gęstości (DFT), uzupełnione metodami teoretycznymi takimi jak nierównowagowe funkcje Greena, oraz modele efektywne oparte o metodę k·p.

Rozprawa rozpoczyna się od części wprowadzającej, obejmującej cele i motywacje pracy, a następnie omawia najważniejsze materiały 2D wykorzystane w badaniach. W dalszej

części przedstawiono wstęp do teorii obliczeń z pierwszych zasad, w tym do teorii funkcjonału gęstości (DFT) oraz krótki opis pozostałych zagadnień teoretycznych stosowanych w publikacjach składających się na rozprawę doktorską. Następnie zaprezentowano cztery artykuły oraz preprint wchodzące w skład cyklu prac stanowiących rozprawę.

Badania obejmują analizę wpływu dwuosiowych naprężeń mechanicznych oraz różnych metod domieszkowania atomami magnetycznymi na silicen, co pozwala znacząco zmienić jego znakomite właściwości w postaci bez domieszek. W drugim etapie pracy szczegółowo zbadano monowarstwy oraz dwuwarstwy dichalkogenków wanadu w różnych fazach krystalograficznych, wskazując na ich wewnętrzne uporządkowanie magnetyczne i potencjalne zastosowania w urządzeniach typu zawór spinowy. W niniejszej pracy przedstawiono także wyniki badań nad nowymi skręconymi heterostrukturami zawierającymi grafen, w szczególności nad heterostrukturą grafen/CrI_3, w celu analizy zjawisk magnetyzmu indukowanego efektami bliskościowymi oraz dolinowo-zależnego transportu, z myślą o potencjalnych zastosowaniach takich struktur w urządzeniach elektronicznych.

Słowa kluczowe: heterostruktury van der Waalsa (vdW) – materiały magnetyczne – spintronika – zawory spinowe – teoria funkcjonału gęstości (DFT)

Abstract

Research on the two-dimensional (2D) van der Waals materials has significantly accelerated progress in electronics, spintronics, and optoelectronics due to their extraordinary properties. The pioneer of these materials is graphene. However, despite of its exotic properties like extraordinary electron mobility, strength, high electrical and thermal conductivity, and numerous other properties, its lack of an intrinsic energy bandgap restricted its applicability in semiconductor technologies. This limitation led researchers to find alternative materials and resulted in the discovery of novel 2D materials such as Silicene, hexagonal Boron Nitride (h-BN), transition metal dichalcogenides (TMDCs), and other 2D materials. Each 2D material showed distinct behaviors ranging from metallic to insulating and from non-magnetic to magnetic materials. As magnetism plays an important role in the current technology, magnetic 2D materials have attracted much interest, and among them, vanadium-based dichalcogenides (VX_2) and chromium trihalides (CrI_3) are much more prominent owing to their intrinsic magnetic behavior. The former shows the fascinating spin-dependent electronic transition and applicability for the spin-valve systems, and the latter has the intrinsic magnetism essential for robust spintronic or magnetic devices.

This thesis, consisting of a collection of thematically connected scientific articles, presents the results of theoretical research on the electronic, magnetic, and transport properties of selected two-dimensional (2D) materials and their van der Waals (vdW) heterostructures. Advanced computational techniques based on first-principles Density Functional Theory (DFT), combined with complementary theoretical methods such as the non-equilibrium Green Function, and k.p model, are employed to investigate the materials.

The thesis begins with an introductory part, including the aims and motivations of the work, and then briefly discusses the 2D crystals investigated in the thesis. Then, a short introduction to the Density Functional Theory (DFT) methods is given alongside some of the other complementary methods used in the thesis. Next, four articles and one preprint constituting the thesis are presented and discussed.

The research includes an analysis of the impact of bi-axial mechanical strain and different magnetic doping schemes on Silicene to further modify and improve its outstanding

properties. In the next part of this thesis, the mono- and bilayers of Vanadium-based TMDCs, in different crystallographic phases, have been comprehensively studied, highlighting the intrinsic magnetic ordering and potential applications in spintronics (e.g., for spin-valves). Furthermore, in this thesis, the twisted heterostructures are considered, particularly graphene deposited on CrI_3 monolayer is studied to explore the effect of the twist angle on proximity-induced magnetism and valley-dependent transport.

Keywords: vdW heterostructures – magnetic materials – spintronics – spin valves – Density Functional Theory (DFT)

Notations

m	meter	
Kg	kilogram	
K	kelvin	
s	second	
A	ampere	
J	joule	1 J = 1 m kg s^{-2}
C	coulomb	1 C = 1 A s
V	volt	1 V = 1 m^2 kg s^{-3} A^{-1}
F	farad	1 F = 1 C V^{-1}
Pa	pascal	1 Pa = 1 m^{-1} kg s^{-2}
Hz	hertz	1 Hz = 1 s^{-1}
T	tesla	1 T = 1 kg s^{-2} A^{-1}
eV	electronvolt	1 eV = 1.60218.10^{-19} J
Ha	hartree	1 Ha = 27.2114 eV
A	angstrom	1 A = 10^{-10} m
bohr	1 bohr = 0.529177 A	
e	electron charge	e = 1.60218.10^{-19} C
me	electron mass	me = 9.10938.10^{-31} kg
mp	proton mass	mp = 1.67262.10^{-27} kg = 1836.15 m_e
c	speed of light	c = 2.99792.10^8 m s{\textasciicircum{}-1}
$\hbar$	reduced Planck constant	$\hbar$ = 1.05457.10^{-34} J s
ϵ_0	dielectric permittivity of vacuum	ϵ_0 = 8.85419.10^{-12} F m^{-1}
a_0	Bohr magneton	a_0 = $4\pi\epsilon_0\hbar^2$ / m_e e^2 = 0.529177 A
μ_B	Bohr magneton	μ_B = e $\hbar$ / 2 m_e = 5.78838.10^{-5} eV T^{-1}
k_B	Boltzmann constant	k_B = 1.38065.10^{-23} m^2 kg s^{-2} K^{-1}
		k_B T = 25.8 meV for T = 300 K
$\hbar$ c		$\hbar$ c = 197.327 MeV fm
m_e c^2		m_e c^2 = 0.510999 MeV
G	giga	10^9
M	mega	10^6
k	kilo	10^3
m	mili	10^{-3}
mu	micro	10^{-6}
n	nano	10^{-9}
p	pico	10^{-12}
f	femto	10^{-15}

List of Figures

List of publications constituting the thesis

[P1] M. A. Jafari, A. A. Kordbacheh, and A. Dyrdał, *"Electronic and magnetic properties of silicene monolayer under bi-axial mechanical strain: a first-principles study,"*Journal of Magnetism and Magnetic Materials 554, 169260 (2022). DOI: 10.1016/j.jmmm.2022.169260

[P2] M. A. Jafari, W. Rudzinski, J. Barnaś, and A. Dyrdał, *"Electronic and magnetic properties of 2D vanadium-based transition metal dichalcogenides"*, Scientific Reports 13, 20947 (2023). DOI: 10.1038/s41598-023-48141-1

[P3] M. A. Jafari and A. Dyrdał, *"Effect of strain on the electronic and magnetic properties of bilayer T-phase VS_2: A first-principles study"*, Journal of Magnetism and Magnetic Materials 589, 171618 (2024). DOI: 10.1016/j.jmmm.2023.171618

[P4] M. A. Jafari, M. Wawrzyniak-Adamczewska, S. Stagraczyński, A. Dyrdał, and J. Barnaś, *"Spin valve effect in two-dimensional VSe_2 system"*, Journal of Magnetism and Magnetic Materials 548 168921 (2022). DOI: 10.1016/j.jmmm.2021.168921

[P5] M. A. Jafari, M. Gmitra, and A. Dyrdał, *"Exchange and spin-orbit proximity driven topological and transport phenomena in twisted graphene/CrI_3 heterostructures"*, *arXiv:2509.11670* (2025). DOI: 10.48550/arXiv.2509.11670

Acknowledgments

Completing this thesis is one of the most important milestones in my life, but it is not a way I have done alone. During the almost five years of my PhD, I have been supported, guided, and encouraged by many wonderful people, without whom this work would not have been possible. I am extremely thankful for their help, and I would like to take this opportunity to express my heartfelt thanks.

First and foremost, I consider myself extremely lucky to have been a student of Prof. Anna Dyrdał. Her guidance, patience, and encouragement have been invaluable throughout my PhD journey. When I compare myself before and after PhD, I confidently say that she has not only helped me grow as an independent researcher but also inspired me with her knowledge, professionalism, and kindness. I am extremely grateful for her constant support in creating a comfortable and motivating work environment, and also for always believing in my work, and for allowing me to examine my ideas while guiding me in the right direction. Her careful review and valuable feedback have been essential in preparing the results of this thesis to be reliable and accurate. I truly appreciate the time and effort she has invested in me, and I could not have asked for a better supervisor.

I would also like to thank my co-supervisor, Dr. Martin Gmitra, for his great support, especially in helping me solve challenges in DFT. His advice and valuable discussions have been a great help in my research. More than that, I am truly grateful for his warm hospitality during my four-month internship stay in Košice. He made me feel welcome and was always generous to share his knowledge and time. Our discussions not only helped me in my work but also made the experience even more enjoyable. I deeply appreciate his kindness, support, and collaboration.

I am also deeply grateful to Prof. Józef Barnaś for his kindness and invaluable discussions and support. I was fortunate to work closely with him on several projects and have many discussions that greatly enriched my research. More than a mentor of our 2Dtronic group, he has been a true role model for me, and I feel incredibly lucky to have had the opportunity to work with such a distinguished scientist.

I would also like to thank Poland, its people, and the beautiful city of Poznań with a special thanks to Adam Mickiewicz University and all the members of the Mesoscopic Physics Division for many fruitful discussions and a great atmosphere. I am also grateful for my collaborations with my master's supervisor, Dr. Amirhossien Kordbacheh, as well as Prof. Wojciech Rudziński, Dr. Stefan Stagraczyński, Dr. Małgorzata Wawrzyniak, Dr. Pavel Baláž, and Izabella Wojciechowska.

While this may not be the final acknowledgement, it is certainly one of the most important. I am extremely thankful to my family, and especially my parents, for their endless love, patience, and encouragement. I know that being far from them has been difficult not only for me but even more so for them. Yet, they have always supported me in pursuing my dreams, and for that, I am truly thankful. Their unwavering support has been my greatest source of strength throughout my life.

Finally, I would like to thank all those who have supported me during my PhD, even if I have not mentioned their names. To my friends and colleagues, whose encouragement and presence kept me motivated and strong during this journey—I am truly grateful.

The financial support received for the following project is also acknowledged:

- The Norwegian Financial Mechanism 2014–2021 under the Polish-Norwegian Research Project NCN GRIEG "2Dtronics" no. 2019/34/H/ST3/00515.

Contents

Chapter 1

Introduction

Since the first decade of the 20th century, the existence of two-dimensional (2D) crystals has been a hot but debated topic among scientists. Two-dimensional crystals, according to classical physics, are thermodynamically unstable at finite temperatures, which is due to the thermal lattice fluctuations [1]. This behavior was in agreement with the fact that the melting temperature point decreases with decreasing thickness of the thin films. However, recent spectroscopic studies, such as Raman spectroscopy and angle-resolved photoemission spectroscopy (ARPES), have shown that certain three-dimensional materials, including graphite, exhibit layered structures suitable for exfoliation into two-dimensional forms [2, 3]. Up to that point, the exfoliation of these 3D materials to 2D and 1D materials was almost impossible thoughts, [4]. This idea was strong as Mermin had proved that by describing the crystals with harmonic approximation, 1D and 2D materials can only exist hypothetically [5]. Eventually, this impossible became possible when Novoselov and Geim [6] (Figure (1.1)) in 2004 discovered the two-dimensional graphene, which revolutionized the field of material science. This remarkable success was much more apparent when, six years later, they achieved the Nobel prize in 2010 [7]. Graphene represents a single atomic sheet extracted from

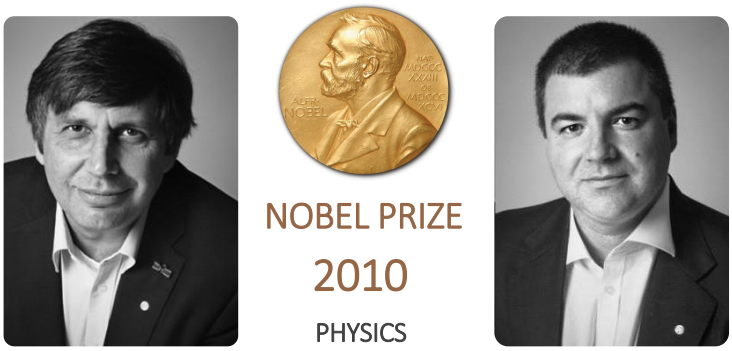

Figure 1.1. In 2010, two Nobel Prize laureates were awarded for discovering the monolayer of Graphene: Andre Geim (left) and Konstantin Novoselov (right). Credit for photos of scientists is the Nobel Prize website. Copy-Right permission is in 7.1.3

graphite, composed of carbon atoms arranged in a two-dimensional honeycomb lattice, as depicted in Figure (1.2). This material displays an exceptional mixture of physical characteristics, such as extremely high charge-carrier mobility (reaching values close to 2×10^5 $cm^2/V{\cdot}s$), superior tensile strength (around 130 GPa), remarkable elasticity, and outstanding thermal conductivity approaching

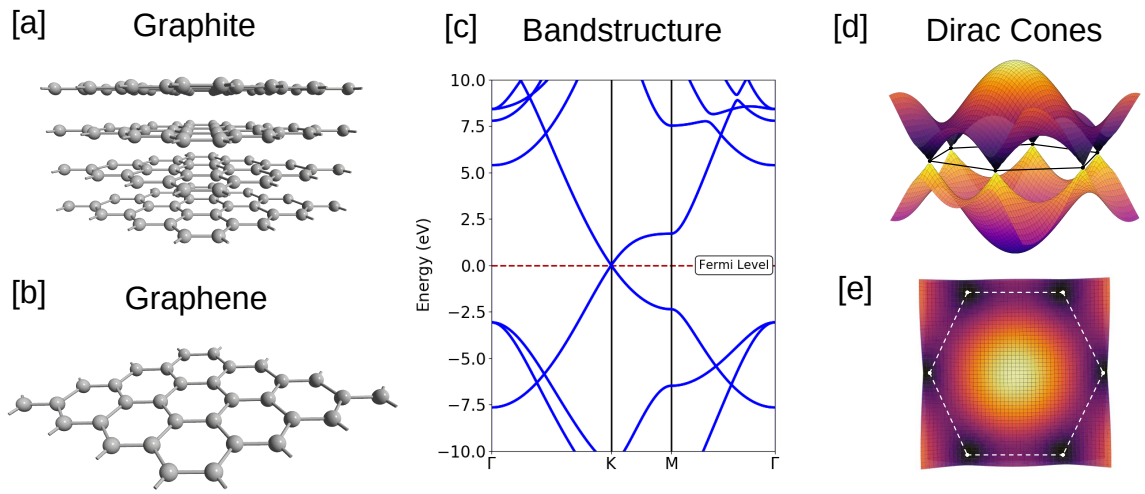

Figure 1.2. Schematic structure of (a) Graphite, (b) Graphene, (c) Band structure of a monolayer of Graphene obtained using the DFT method by Quantum ATK code, and (d), (e) 3D plot of the Graphene band structure calculated using simplified Tight-Binding model computed by Python 3.6.0, showing the Dirac cones from the side and top perspective, respectively.

5000 W/m·K. Its distinctive bonding topology ensures remarkable structural robustness. In contrast to diamond, where every carbon atom forms four sp^3 bonds, each atom in graphene is linked to only three neighbors through strong sp^2 bonds. This planar configuration not only grants graphene an exceptional in-plane rigidity but also makes it roughly 25% stronger than diamond in terms of ultimate strength [8]. Owing to this bonding framework, graphene is considered one of the most stable materials known. Besides its mechanical superiority, graphene also possesses fascinating electronic characteristics that make it a central material in contemporary condensed matter physics. Graphene is classified as a semi-metal where there is no energy band gap, but the density of states (DOS) close to the Fermi level is also zero. In the reciprocal space, the band structure of graphene has six distinct points where the energy of the charge carriers follows the linear dispersion relation [9]. As shown in Figure (1.2), at these points, which are well known as Dirac points, the electrons and holes act as massless particles, which create an extremely high electrical conductivity. Additionally, graphene, due to its exceptional electron mobility (even at non-zero temperatures) and its minimal spin-orbit coupling, is a strongly suitable material for transporting spin information [10]. All of these properties, plus a considerable number of other properties, make graphene a groundbreaking material for various applications from spintronic and advanced electronic technologies to medical science.

Even though graphene has extraordinary properties, the vanishingly small intrinsic energy band gap is a challenging point in its practical applications in semiconductor technologies, especially applications such as field-effect transistors (FETs) where the switching on/off of electron current is essential. Therefore, graphene is not a suitable material for high-performance digital logic circuits. This issue with graphene, forced the scientists to find an alternative way to identify other $2D$ materials that inherently have a large bandgap. The new materials act like a bridge between graphene's extraordinary properties and the essential requirement of semiconductor devices (i.e., having the inherent tunable energy band gap), and they open a new way of designing the new generation of electronic and optoelectronic devices. After Graphene, many other two-dimensional

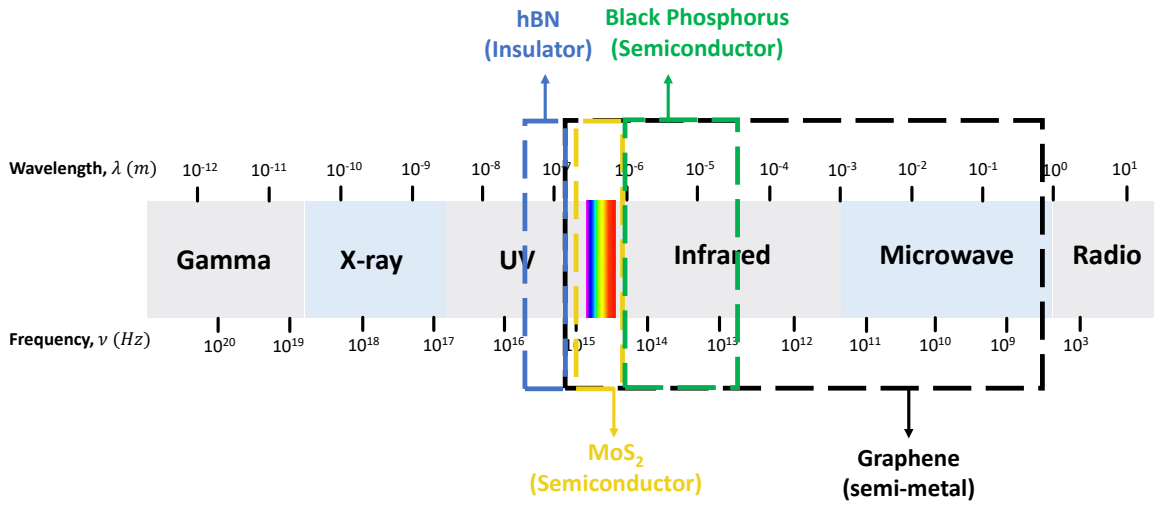

Figure 1.3. The examples of different types of 2D materials according to the electromagnetic spectrum.

(2D) crystals were discovered, which broadened the research in the layered materials area. These materials indicate different behaviors, such as metallic, semi-metallic, insulating, and semiconductor, where their energy band gap includes the various ranges of the electromagnetic spectrum from ultraviolet to infrared in the visible region (Figure (1.3)). The recent advancements in developing new technologies in experimental methods have made the exfoliation of a monolayer from almost any layered bulk material possible. This opens a way to study and probe 2D crystals deeply to understand their intrinsic properties. One can classify the 2D crystals into distinct categories based on their chemical compositions [11]: mono-elemental materials (e.g., graphene, silicene, germanene, and antimonide); transition metal dichalcogenides (TMDCs) of the form MX_2 (e.g., MoS_2, WS_2, and WSe_2); transition metal carbides (TMCs) of the form MX ($III-VI$ group, and $IV-VI$ group compounds) [12]; topological insulators (TIs) of the $V-VI$ group (e.g., Bi_2Te_3 and Sb_2Se_3) [13, 14]; transition metal oxides/hydroxides; and unique materials like layered insulators (e.g., $h-BN$) [15] and other 2D materials like metal-organic framework[16]. Each of these materials showed outstanding properties and sometimes covered the drawbacks of graphene. For instance, graphene has linear dispersion at Dirac points, leading to the room-temperature quantum Hall effect (QHE) [17], which is one of the essential factors in quantum technologies. However, other 2D materials like Transition Metal Dichalcogenides (TMDCs) and Topological Insulators (TIs) exhibit distinctive and sometimes more unique features that extend the potential applications. Topological Insulators, with their metallic surface states and spin-momentum locking, provide a remarkable way for new devices in spintronics where charge currents can control spin polarization [18, 19]. TMDCs also show layer-dependent electronic properties [20, 21]; somehow, their bulk structure has an indirect bandgap of energy, but the exfoliated monolayer of these materials indicates the energy band gap in the range of 1-2 eV, which is highly attractive for optoelectronic and photonic devices. Furthermore, the presence of strong SOC leads the TMDCs to be applicable in spintronic and valleytronics [22, 23]. Another part of the materials that were fabricated to cover the limitation of the graphene was the design of the van der Waals heterostructure. These are the materials

formed by stacking different 2D materials vertically on top of each other, creating interfaces that enable new phenomena, such as proximity-induced magnetism and superconductivity. These new and various interfaces of the 2D materials lead to the design of multifunctional devices with possible flexibility in both quantum computing and spintronics technologies. Graphene, with the other 2D materials, fabricated heterostructures of such materials, have raised the possibility of engineering the properties of materials. This allows researchers to tune the properties according to the requirements of the desired devices. Currently, many other 2D materials and heterostructures have the potential to be identified and studied, and one of the aims of this thesis is to provide comprehensive studies into this area.

Overall, this thesis aims to investigate the electronic, magnetic, and transport properties of selected van der Waals structures through comprehensive investigations based on first-principle studies and model analysis. Specifically, this work is looking to answer questions like how the intrinsic and proximity-induced magnetic behaviors, as well as charge and spin transport phenomena, can be precisely tuned in two-dimensional systems such as graphene, silicene, transition metal dichalcogenides (TMDCs), and twisted graphene-based vdW heterostructures. To achieve this, the thesis develops and applies state-of-the-art computational approaches —including Density Functional Theory (DFT) with advanced exchange-correlation approximations, many-body Schrödinger equation techniques, and corrections for van der Waals interactions— to predict and analyze the fundamental electronic, magnetic, and transport characteristics of such systems. Moreover, by linking the first-principles calculations with the low-energy effective models, like the k·p models, the research aims to identify the efficient ways of control the electronic, magnetic and transport properties of van der Waals heterostructures by doping and external fields or forces.

The thesis is organized as follows: Chapter 1 introduces the evolution of two-dimensional materials and discusses the aims and motivation of the work; Chapter 2 provides a detailed review of the materials, their experimental aspects like synthesis techniques, and experimental setups used to probe their properties; Chapter 3 lays out the theoretical framework and computational methodologies essential for modeling these systems at the atomic scale; Chapter 4 discusses the electronic, and magnetic properties of Silicene nanosheets under strain and Cr-doping; Chapters 5, and 6 gives a comprehensive study concerning the V-based TMDCs; Eventually, chapter 7 discusses the proximity effects on twisted-Graphene/CrI_3 vdW heterostructures.

Chapter 2

Materials

After discovering graphene as the first two-dimensional crystal, which constituted a single layer of carbon atoms arranged in a honeycomb structure, condensed matter physics and materials science started to have significant advancements. This discovery was a starting point for searching other 2D materials that we know nowadays. The successful isolation of graphene and its subsequent relevant research showed that the atomically thin layer is not only obtainable but also remarkably stable. These studies made graphene an excellent material because of its novel and extraordinary properties, and they opened the way to discovering new 2D materials. These found materials attained significant interest due to their substantial properties and potential for a wide range of applications, from electronics and energy storage to quantum technologies. This progress did not stop at this stage and advanced beyond the 2D materials with identical atomic structures, where the new structures fabricated by stacking different 2D materials laterally or vertically established entirely novel results. These stacked materials, so-called van der Waals heterostructures, added new freedom for the spintronic devices and enabled researchers to design new structures with the desirable properties. For instance, the ability to combine the different 2D layers and fabricate such heterostructures has opened new avenues for studying exotic physical phenomena such as emergent quantum phases. In conclusion, the field of 2D materials is rapidly growing, and the transition from research to technology is swift. In this chapter of the thesis, I will discuss a brief background of the selected 2D materials used in the thesis, from Graphene to TMDCs, and then examine the challenges and applications of each material.

2.1 Graphene and other monolayer 2D materials

2.1.1 Graphene

Carbon is a chemically versatile element capable of forming sp, sp^2, and sp^3 hybridized bonds, which enables it to form a wide range of structures with different physical and chemical properties. Graphene, a two-dimensional allotrope of carbon, stands out due to its exceptional electronic properties [9].As illustrated schematically in Figure (1.2), the carbon atoms in graphene form a two-dimensional honeycomb lattice. Although graphene is inherently a 2D crystal, several other carbon-based nanostructures can be regarded as its dimensional relatives: one-dimensional (1D) graphene nanoribbons and zero-dimensional (0D) fullerenes represent geometrical reductions of the same lattice network [24]. In a similar manner, carbon nanotubes (CNTs) can be described as tubular structures conceptually produced by rolling a graphene sheet into a cylinder [25]. Another allotrope of carbon, graphite, consists of multiple graphene layers stacked through weak van der Waals interactions [26]. This layered nature is familiar from daily experience—when a pencil leaves a trace on paper, it deposits thin graphite flakes made up of several graphene sheets [27]. The fundamental understanding that graphite is composed of graphene layers was known for decades, but it was not until 2004 that Andre Geim and Konstantin Novoselov successfully isolated a single monolayer of graphene [6]. Their achievement was remarkable for two main reasons: first, the existence of a stable, freestanding atomic monolayer was previously considered thermodynamically impossible [28]; second, no experimental methods were thought capable of extracting such ultrathin layers from bulk crystals. Surprisingly, the two researchers achieved this using a simple mechanical exfoliation technique involving adhesive tape, and the resulting monolayers were identified under an optical microscope [29, 30, 31]. This straightforward yet groundbreaking approach launched an entirely new field of two-dimensional materials research encompassing condensed matter physics, nanotechnology, and materials science. The discovery of graphene—recognized by the 2010 Nobel Prize in Physics awarded to Geim and Novoselov [32] (see Figure (1.1))—profoundly reshaped our understanding of the stability of atomically thin crystals [33] and initiated extensive studies of quantum phenomena in single-layer systems [27], paving the way for diverse applications in electronics, mechanics, and thermal technologies [34, 35, 36].

Theoretical Background and Historical Insights

The theoretical understanding of graphene dates back to 1947, when Wallace first predicted its electronic band structure using a tight-binding model [28]. Wallace demonstrated that graphene's conduction and valence bands meet at six points, known as Dirac points, about which the energy dispersion relation becomes linear. The low-energy dispersion resembles that of relativistic quasi particles, despite the fact that the electrons in graphene are not relativistic [28]. This theoretical discovery provided a way to investigate the relativistic behavior of electrons in a solid-state material. As shown in Figure (1.2), the electronic structure of graphene close to these points is described by a Dirac cone, a characteristic of graphene that leads to excellent electronic properties. Before the seminal work of Giem and Novoselov, the stability of the 2D crystals was thought to be impossible thermodynamically due to the thermal fluctuations, as explained by the Mermin-Wagner theorem [1]. However, 2D materials could be stable at room temperature because of the slight out-of-plane

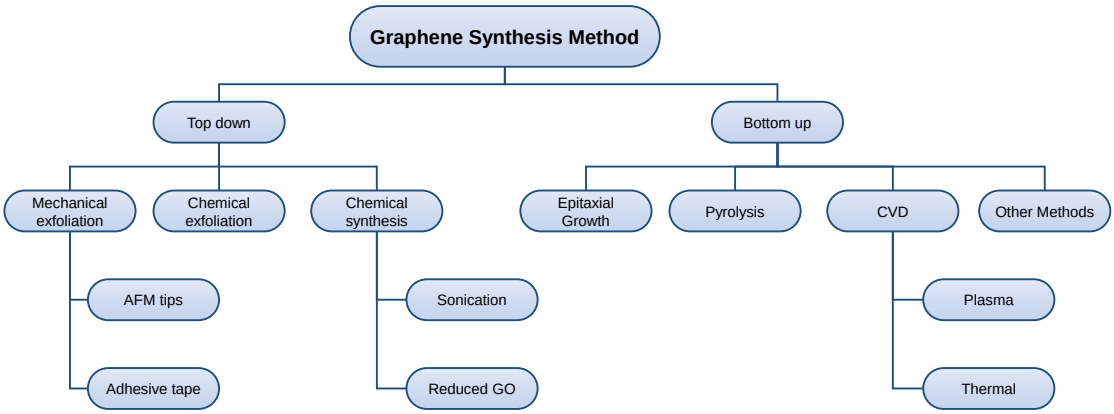

Figure 2.1. Schematic representation of different methods of graphene synthesis. The figure's concept is from the reference [41].

deformation or "ripples" that prevent thermal instabilities. In spite of that, these ripples are not perfectly flat; however, they help stabilize the structure using the long-wavelength thermal fluctuations reduction [37, 38]. The following Hamiltonian could describe the electronic properties of the graphene close to the Dirac point [39]:

$$H = -t \sum_{\langle i,j\rangle,\sigma} \left(a^{\dagger}_{\sigma,i} b_{\sigma,j} + \text{H.c.} \right) - t' \sum_{\langle\langle i,j\rangle\rangle,\sigma} \left(a^{\dagger}_{\sigma,i} a_{\sigma,j} + b^{\dagger}_{\sigma,i} b_{\sigma,j} + \text{H.c.} \right), \tag{2.1}$$

where t, t' are the hopping integrals for the nearest and next-nearest nighbours respectively, $a_{i,\sigma}$ and $a^{\dagger}_{i,\sigma}$ are the annihillation and creationoperators for electrons at site i with spin σ ($\sigma = (\uparrow, \downarrow)$), and $\langle i, j\rangle$ is the summation of all nearest neighbors, and $\langle\langle i, j\rangle\rangle$ is the summation of all next-nearest neighbors. The Fermi velocity in graphene is some at $v_F = 10^6$ m/s [28], which is 300 times slower than the speed of light but still fast compared to traditional electron velocities in materials [39]. The electrons near the Dirac points (at K and K') can be calculated by expanding the full band structure of Equation (2.1), as $k = K + q$ with $|q| \ll |K|$ [28, 39]:

$$E_{\pm}(\mathbf{q}) \approx \pm v_F |\mathbf{q}| + O[(q/K)^2], \tag{2.2}$$

where q is the momentum measured relative to the Dirac points. This linearity leads to many properties, such as the Klein paradox [40], where electrons in graphene can tunnel through potential barriers without backscattering, even if the energy barrier is classically forbidden. Moreover, the lack of a band gap in graphene is both a blessing and a curse. On the one hand, it allows for high electronic conductivity; on the other hand, it makes graphene inappropriate for use in traditional transistors unless the band gap is tuned. This has led to the investigation of different methods for the generation of a band gap in graphene band structure, like applying strain, changing the sheets of graphene to the nanoribbons, and forming graphene-based heterostructures with materials like boron nitride, which we discuss in the following sections with all details [9].

After the isolation of graphene, several methods were used to synthesize it at different scales, and each of them had its advantages and limitations, as illustrated in Figure (2.1). The first

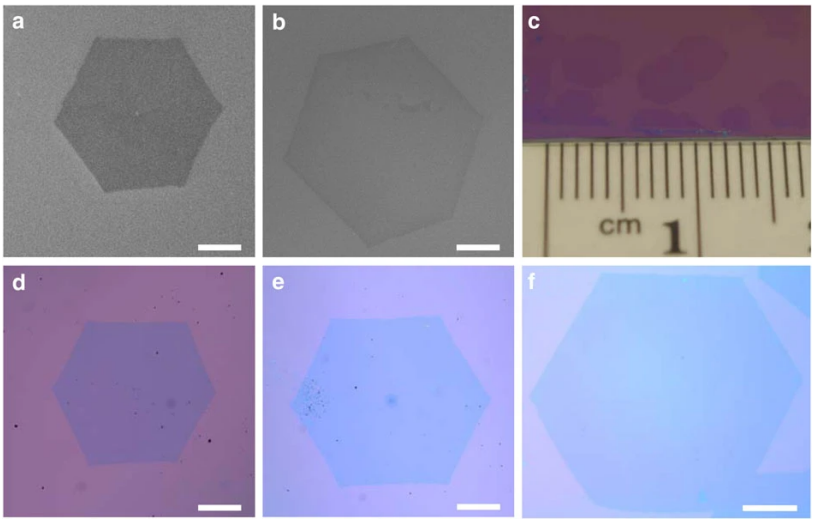

Figure 2.2. CVD growth of graphene domains at different times: (a) SEM image and (d) optical microscopy image after 6 h, (b) SEM image and (e) optical microscopy image after 24 h, and (c) photograph and (f) optical microscopy image after 48 h. Scale bars: 0.2 mm (a,d), 0.4 mm (b,e), and 1 mm (f). Image reproduced from [44], © Springer Nature. License Number: 5990150903280.

successful technique for obtaining single-layer graphene was mechanical exfoliation, often referred to as the "Scotch tape" method, originally demonstrated by Geim and Novoselov [6]. This simple yet ingenious approach involved repeatedly peeling thin layers from a graphite crystal using adhesive tape and transferring them onto a silicon substrate coated with a thin layer of silicon dioxide. The method yields graphene of exceptional structural quality, suitable for fundamental studies, though it is not practical for large-scale production [35]. An alternative route for fabricating high-quality graphene is chemical vapor deposition (CVD) on metallic substrates, most commonly copper. In this process, hydrocarbons such as methane are decomposed at elevated temperatures, and carbon atoms self-assemble into a graphene film on the metal surface [42]. The main advantage of the CVD method lies in its scalability—it allows continuous growth of large-area graphene sheets with excellent uniformity, as illustrated in Figure (2.2)—making it highly attractive for electronic applications [43].

Another effective synthesis route involves epitaxial growth of graphene on silicon carbide (SiC). During this process, high-temperature annealing causes partial sublimation of silicon atoms, leaving a carbon-enriched surface on which graphene layers spontaneously form [45]. A key advantage of this method is that graphene develops directly on an insulating or semiconducting substrate, offering strong potential for integration into electronic devices [46]. For low-cost, large-scale production, a chemical approach is typically employed involving the reduction of graphene oxide (GO) [47]. In this process, graphite is first oxidized to obtain GO, which is subsequently reduced to form reduced graphene oxide (rGO). Although scalable, the resulting films often contain structural imperfections and reduced conductivity relative to pristine graphene, limiting their use in high-performance electronic systems [48].

Beyond its fabrication methods, graphene is celebrated for its extraordinary mechanical, thermal, and optical properties. It remains the strongest material known, with a tensile strength near 130 GPa and an intrinsic elastic modulus around 1 TPa [49]. Such exceptional rigidity originates from strong

in-plane σ bonds between carbon atoms, making graphene ideal for composites, flexible devices, and other applications demanding both strength and elasticity [49]. Graphene also demonstrates outstanding thermal performance, with a conductivity approaching 5000 W/m·K–far exceeding that of copper (410 W/m·K) [36]. The efficient phonon transport within the two-dimensional lattice accounts for this high thermal conductivity, establishing graphene as a promising material for thermal management and heat dissipation [36]. In terms of optical characteristics, monolayer graphene exhibits a universal light absorption of approximately 2.3% in the visible range [50]. This combination of optical transparency and high electrical conductivity makes it an excellent candidate for transparent electrodes in displays and solar cells. Moreover, its unique optical response continues to inspire advances in photonics and optoelectronic technologies [35].

Graphene has a range of applications in various fields due to its extraordinary electronic, mechanical, thermal, and optical properties. Concerning the applications of graphene in electronics, one can directly mention the high carrier mobility and ambipolar conduction, which have made graphene a promising candidate for future electronic devices, particularly for transistors that operate at gigahertz frequencies. New graphene-based field-effect transistors (GFETs) have much higher speeds in their performance compared to traditional silicon-based transistors. These fascinating applications opened new possibilities of faster and more efficient electronic devices [34]. High-performance supercapacitors and batteries require materials with high surface area and conductivity, and graphene is an ideal candidate. Graphene is used to enhance the performance of energy storage devices, improve the charging time, and achieve higher energy densities [51]. Additionally, graphene is also being investigated in hybrid devices, combining the properties of capacitors and batteries [52]. Another application of graphene is related to its potential in spintronics, which is investigated by its long spin diffusion length and the possibility of engineering spin-orbit coupling in graphene-based heterostructures [53]. These features open the door to new spin-based computing devices like spin transistors and quantum spin logic gates [54].

Eventually, despite the wide range of properties of graphene, several challenges affect its applications. While there are some experimental techniques to produce high-quality graphene, large-scale production of graphene is still challenging due to the presence of defects [6]. Furthermore, pristine graphene has no natural energy band gap, which restricts its usability in traditional semiconductor applications, particularly for digital electronics [9]. However, by overcoming these challenges, graphene will be unrivaled in the new generation of electronic devices and be applicable to revolutionary applications like quantum computing and advanced photonics. In the following sections, we will discuss the vdW heterostructure, which is a combination of graphene with other 2D materials where the new stacked materials introduce new functionalities and modify the graphene properties, making it more attractive for spintronic devices.

2.1.2 Hexagonal Boron Nitride [h-BN]

Boron nitride from the geometrical point is an analogy of graphene with this difference that instead of carbon atoms, there exist an equal number of boron and nitrogen atoms in a honeycomb arrangement of sp^2 hybridization 2D layer (see Figure (2.3)). The pristine layers of the h-BN are intrinsic insulators and have a wide band gap, about 4.62 eV [55] (see Figure (2.3)). Hence, it is strong insulator and is used as a sound barrier in devices. Additionally, it shows ultraviolet light emission, which is due to its wide direct band gap. In the last decade, the h-BN has become not only popular because of its similarity to graphene but also because of its remarkable stability and

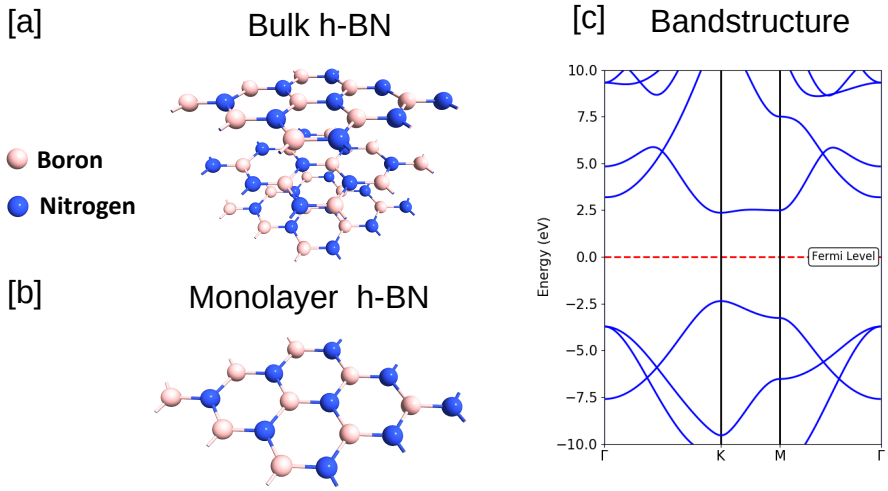

Figure 2.3. Schematic structure of the h-BN, (a) Bulk, (b) Monolayer, (c) Band structure of a monolayer of h-BN obtained using the DFT method by Quantum ATK code.

intrinsic insulator behavior. The individual and even multilayer of h-BN is used on top of the other 2D materials (especially graphene) as a flat substrate for designing the improved graphene transistors [56]. For instance, the researchers reported that one graphene monolayer sandwiched between two h-BN layers as a substrate and covered by another graphene layer has been found as an insulator. Since graphene and h-BN have similar lattice structures, h-BN is an excellent material to support the stability of graphene, making it a good choice for graphene-based electronics [57, 58, 59].

Besides the intrinsic insulator behavior, h-BN shows a range of physical properties which has gained remarkable attention in both fundamental research and technological applications [60, 61, 62]. From a theoretical side, one can describe the h-BN within the framework of layered materials that exist in a honeycomb shape similar to graphene. However, the electronic structure is significantly different as it has a different ionic bonding character between boron and nitrogen atoms. This difference in bonding is the main reason for the wide band gap observed in both bulk and thin layer forms, and it places this material in the category of wide-band-gap semiconductors. Due to this behavior, the unique electronic and optical properties are expected for both bulk and few layers of the h-BN [61, 63]. The electronic bandstructure of h-BN has been studied using various computational methods, from the advanced Density Functional Theory (DFT) approaches to the many-body perturbation theory (GW) calculations. The efforts of these methods were focused on estimating the band gap of h-BN in the layered and bulk form, which often is in the range of approximately 5.5 – 6.0 eV under certain circumstances. These certain levels of sensitivity show the dependency of the energy band gap estimation on the computation parameters [60]. From the experimental side, the photoluminescence measurements and cathodoluminescence experiments confirmed the direct energy band gap of h-BN, which is in the range of ultraviolet (UV) region as shown in Figure (1.3). Such strong UV emission has led to the remarkable potential of using h-BN for deep-UV light-emitting diodes and laser applications [61, 64]. Similar to graphene, a single layer of h-BN can also be grown by different experimental methods such as chemical vapor deposition

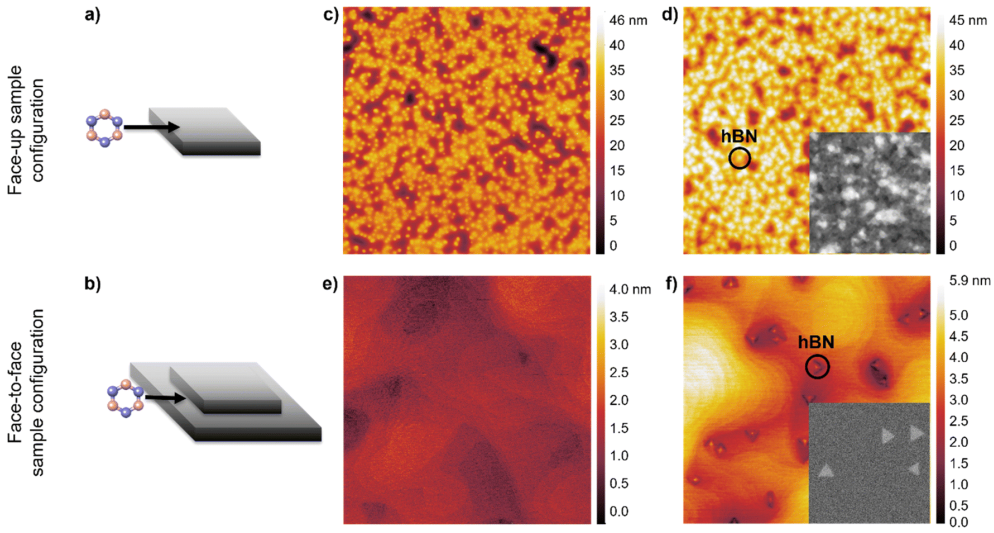

Figure 2.4. Schematics illustrating the (a) face-up and (b) face-to-face sample configurations. (c,e) AFM height maps of the Ge(001) surface after high-vacuum annealing for 30min at 920°C, and (d,f) AFM maps after hBN growth under a borazine partial pressure of 1×10^{-10} torr for 30min at 920°C. All AFM images are $5\mu m \times 5\mu m$. The insets in (d,f) show enlarged SEM images of hBN islands from the same samples. Caption reproduced (with minor edits for brevity) from reference [66]. Licensed under CC BY-NC 3.0.

(CVD), high-temperature and high-pressure techniques, and epitaxial growth on appropriate substrate [60, 62]. Take the CVD method as an example, and one can see that this method has provided a route to producing relatively large-scale and high-quality layers, which are essential for use in advanced electronic devices. From the structural side, also the same as the graphene, even though h-BN flakes can be exfoliated down to a single atomic layer, specific exfoliation processes are required to be optimized to preserve crystallinity and decrease the number of defects as much as possible. These defects or impurities should be minimized unless the electronic properties of the materials could be affected. Furthermore, experimentally, the layered nature of h-BN is also entirely beneficial when used as an ultra-flat dielectric or encapsulating substrate of other 2D materials from graphene itself to the transition metal dichalcogenides (TMDs) like MoS_2, WS_2, and WSe_2. This atomically flat surface is like a shelter for such 2D materials, and it preserves their intrinsic electronic properties by reducing inhomogeneities and scattering events that decline the device performance [65].

Due to the wide band gap and dielectric nature, h-BN has a significant role in device applications and is well-known as an outstanding insulating material. Applicability of h-BN is not limited to playing the role of a substrate material, and it also works as a dielectric gate or a protective capping layer in field-effect transistors based on graphene or other 2D semiconductors [60, 62]. Another prominent feature of h-BN concerns its chemical and thermal stability even at higher temperatures, which makes it often applicable to high-power electronics and other extreme-operating-environment applications. This material is considered an excellent one to use in heat dissipation in micro and nanoelectronic devices due to its high in-plane thermal conductivity. Recently, researchers have performed several works concerning the doping strategies for h-BN or the fabrication of defect-engineered h-BN to introduce functionalities like single-photon emission centers. These defect-induced photonic centers are extremely interesting for quantum optics and

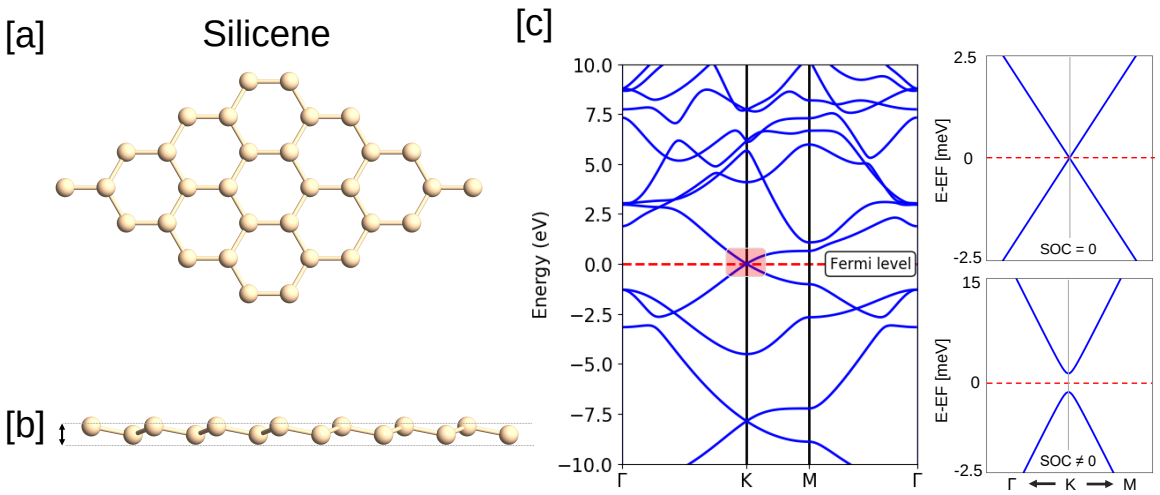

Figure 2.5. Schematic structure of the silicene, (a) top-view, (b) side-view showing the buckling of atoms, (c) Band structure of a monolayer of silicene with and without SOC obtained using the DFT method by Quantum ATK code.

quantum communication technologies, where stable emission lines are desired [67]. By performing the phonon calculations of h-BN, one can find an insight into its thermal properties and see the potential coupling with electronic states. Raman spectroscopy, infrared spectroscopy, and inelastic X-ray scattering provide detailed information concerning the phonon modes and lattice vibrations, which is in the relationship between the material's thermal conductivity and mechanical properties [61, 63]. From the Mechanical side, h-BN shows strength and stability under different stress conditions, with an in-plane Young's module comparable to graphene, even though its interlayer interaction has a different mechanical response along the stacking direction. This combination of the mechanical, electronic, and optical properties of the h-BN made it one of the cornerstones of the field of 2D materials and heterostructures [60, 61, 62, 64, 67, 68].

2.1.3 Silicene

Another material that is a counterpart of graphene is silicene. Silicene is a 2D material made of silicon atoms arranged in a hexagonal honeycomb lattice (see Fig. (2.5)). The first theoretical foundation of silicene comes back to 1994 when Takeda and Shiraishi proposed this material [69]. However, the experimental synthesis of silicene stopped until 2010, when the researcher achieved the growth of silicene on a silver (Ag) substrate under Ultra-High vacuum (UHV) conditions [70]. Subsequent to the discovery of silicene, it attracted significant attention due to its highest similarity to graphene and its excellent compatibility with current semiconductor technologies. Despite the similarity of silicene to graphene, the structure of graphene is planar, and silicene has slight buckling due to the silicon's sp3 hybridization, leading to a mix of sp2 and sp3 configurations [71]. Silicene also shows high carrier mobility and quantum spin Hall effect under certain conditions [72]. The band structure of a monolayer of silicene, similar to graphene, supports the Dirac-like fermions and makes this material an excellent candidate for electronic applications [73].

Additionally, silicene, due to its high flexibility, strong covalent bonds, and ability to maintain its structure under deformation without losing its electrical properties, is one of the important

materials in current technologies [74]. As already mentioned, buckling in silicene makes it distinct compared to graphene in chemical reactive properties and enables surface modification with hydrogen, halogens, or other functional groups [75]. Despite many properties of silicene, it is highly susceptible to air exposure, and it tends to oxidize rapidly and form silicon dioxide (SiO_2) under ambient conditions. Silicene, because of the semiconductor behavior in certain conditions, combined with its compatibility with the silicon-based electronic industry, allows it to integrate with the current technologies. Therefore, there exists a potential application of silicene in field-effect transistors (FETs), optoelectronic devices, and quantum computing platforms. Unlike graphene, with a lack of energy band gap, silicene can be used directly in transistor technologies, which work with the on/off ratio mechanism [76]. Silicene also has an excellent attraction from both theoretical and experimental researchers in designing two-dimensional materials with tunable electronic properties [77, 78, 79]. As shown in Figure (2.5), the silicene's buckled crystal structure is directly related to the larger covalent radius of silicon atoms compared to the carbon atoms in graphene. This buckling not only affects the electronic band dispersion close to the Dirac points but also provides an additional degree of freedom for chemical functionalization and external field modulation. From the theoretical side, the finite buckling height leads to an intrinsic spin-orbit coupling, which opens the band gap and enables the quantum spin Hall effect in silicene [80, 81]. Furthermore, due to the mixed sp^2 and sp^3 hybridization of silicon atoms, the electronic band structure of silicene exhibits Dirac-like cones at the K points of the Brillouin zone, but with a reduced Fermi velocity compared to graphene. The energy band gap can also be tuned by applying an external electric field perpendicular to the silicene sheet originating from the sublattice symmetry breaking, which has been performed using the first-principle Density Functional Theory (DFT) method [82, 83]. This property is entirely essential for electronic applications since moderating the energy band gap is necessary for digital logic devices.

For synthesizing the silicene, usually, the epitaxial growth on metal surfaces such as Ag(111), Ir(111), and ZrB_2 is used under UHV conditions [70, 84, 85]. In this method, using these substrates, the monolayer and multilayer of silicene form. In addition, the long-range ordering and uniform large-scale growth also remain with some challenges as the buckled nature of silicene is more sensitive to the lattice mismatch compared to the planar graphene [86]. Silicene is prone to forming SiO_2 under ambient conditions, and it requires some acts like encapsulation methods or protective capping layers, such as Al_2O_3, which reduce the oxidation and maintain its intrinsic properties after transfer steps [87]. The schematic structure of the procedure of Silicene growth and also the STM image of the 2D Si layer on Ag(111) have been illustrated in Figure (2.6).

Another important aspect concerns the possibility of doping and functionalization. Hydrogenation, halogenation, or decoration with metal adatoms can modify the electronic and magnetic properties of silicene without destroying the Dirac cone structure under appropriate conditions like sublattice symmetry preserving [88, 89]. This approach is well-known among researchers for designing silicene-based spintronic devices and sensors because these properties rely strongly on the spin-orbit coupling strength and chemical environment. Regarding the applications, one can emphasize the silicene field-effect transistors (FETs), which have intrinsic semiconductor behavior at specific strain or gating conditions [76]. Even though large-scale production of silicene in real devices is still in development, there are some developing works in substrate engineering, protecting layering, and post-growth processing in continuing the practical electronics [90, 91, 92, 93]. The possibility of integration of silicene with well-established silicon-based technology is still a compelling

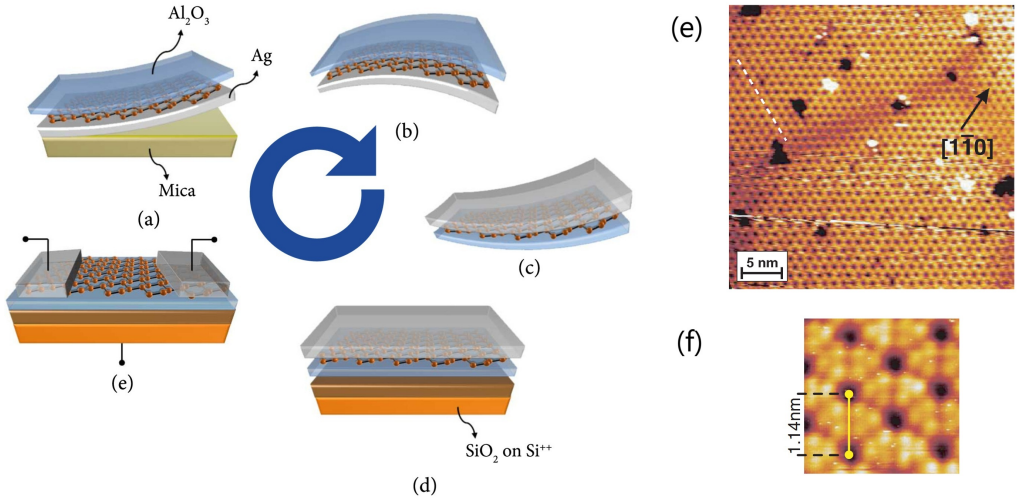

Figure 2.6. (a)–(d) Schematic of silicene grown on Ag(111)/mica and transferred to a new substrate (from [87]): (a) Al_2O_3 encapsulation, (b) mica removal, (c) flipping onto SiO_2/Si^{++}, and (d) electrode patterning plus residual Ag etching. (e)–(f) Filled-states STM images of the 2D Si layer on Ag(111) (from [70]), showing the honeycomb-like (1×1) structure (acquired at $U_{\text{bias}} = -1.3\,\text{V}$ and $I = 0.35\,\text{nA}$). (e) Wider-area image; (f) high-resolution (3×3 nm) topograph with ∼1.14 nm lattice spacing. Caption reproduced (with minor edits for brevity) from [70, 87]. © With permission from the American Physical Society (APS), License Number: RNP/25/MAR/089112

motivation, particularly for flexible and wearable electronics, which is highly desirable for ultrathin and lightweight materials. Moreover, the high carrier mobility and spin-orbit-driven phenomena also opened the way for silicene-based quantum devices as well as including topological transistors and spin-qubit architectures [77].

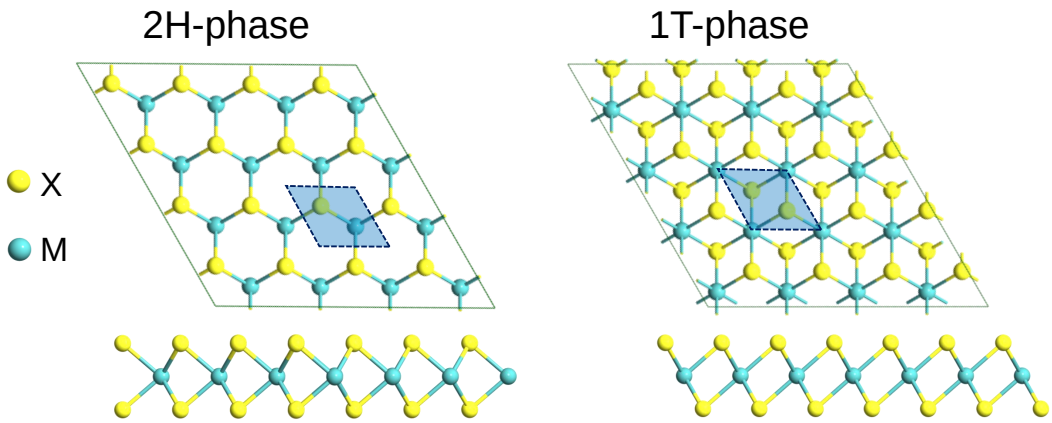

Figure 2.7. Schematic structure of the TMDCs for both 2H/1T phases. The unit cell of each phase is depicted with dashed lines.

2.2 Magnetic van der Waals 2D materials

2.2.1 General Overview of 2D magnetic materials

After discovering graphene, a lot of 2D materials were found; among them, Transition Metal Dichalcogenides (TMDCs) have gained excellent attention in recent decades due to their remarkable structural, electronic, magnetic, and optical properties [27]. As illustrated in Figure (2.7), transition metal dichalcogenides (TMDCs) crystallize in a hexagonal lattice structure. As suggested by their name and depicted in Figure (2.8), these compounds are generally represented by the chemical formula MX_2, where M denotes a transition metal atom and X corresponds to a chalcogen element such as sulfur, selenium, or tellurium. The inherently layered arrangement of TMDCs, held together by weak van der Waals forces, enables their exfoliation from bulk crystals down to few-layer or even single-layer forms [27]. It allows researchers to aim for new properties and applications in these materials and, subsequently, in novel 2D materials [94]. The first study of the TMDCs refers to their lubrication properties, which originated from their weak interlayer van der Waals forces [12]. TMDCs have a wide range of properties and behaviors, from metallic behavior to semiconductor behavior, depending on the combination of M and X atoms [95]. Moreover, due to the tunable band structure and the existence of spin-orbit coupling in some of them, the TMDCs have been made versatile candidates for fundamental studies as well as technological applications [26].

More than sixty essential combinations of transition metal atoms with chalcogen atoms have been synthesized [26]. In addition to these combinations, TMDCs have different behavior and properties according to the coordination of the metal and chalcogen atoms. The most common structures are trigonal prismatic coordinates (2H-phase) and octahedral coordinates (1T-phase), which significantly alter the electronic properties of these materials. For instance, the multilayer of MoS_2 has a phase transition from semiconducting 2H to metallic 1T, which has been proved using the chemical methods [96]. Another example is changing the direct bandgap semiconductor of the 2H-phase of MoS_2 in its monolayer form to the indirect bandgap in its bulk counterpart [20]. The

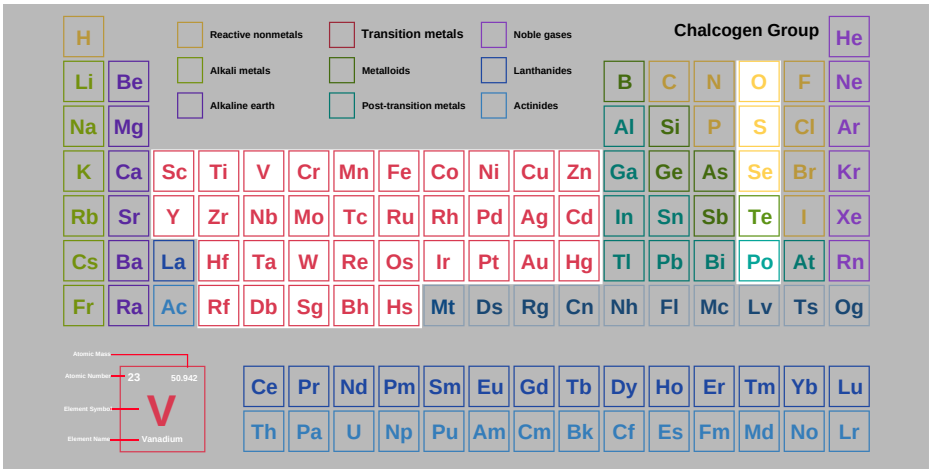

Figure 2.8. Periodic table and highlighting the Transition metal [TM] atoms and chalcogenide group of atoms. TMDCs are the combination of the TM atoms with the chalcogenide atoms having the general formula of MX_2, where M = [Mo, V, W, etc] and X =[S, Se, Te, etc].

variety of combinations of TMDCs and their different phases makes TMDCs excellent candidates for electronic and optoelectronic devices. Among TMDC materials, non-magnetic materials like MoS_2, WS_2, and WSe_2 have been studied widely due to their semiconductor properties [97]. These materials are suitable for field-effect transistors (FETs), photodetectors, and valleytronics [23].

TMDCs initially gained remarkable attention for their semiconducting properties, particularly for transistor applications and photodetectors [20]. However, they typically do not have intrinsic magnetism due to their filled or empty d-orbitals, which do not carry the spontaneous spin ordering [98, 99]. Several early methods were suggested and performed to induce magnetism in these materials, from magnetic defect engineering, chemical doping, to the coupling with other magnetic layers as heterostructures. Therefore, through the extrinsic factors, one can observe spin properties even in nonmagnetic 2D hosts [100, 101]. Most of the works on the 2D magnetism research occurred in 2017 when experiments showed the intrinsic long-range magnetic order in monolayer CrI_3 and bilayer $Cr_2Ge_2Te_6$ [102, 103]. These studies confirmed that magnetic order can persist even when the thickness is reduced from the multilayer regime down to the monolayer limit, provided that sufficient magnetic anisotropy is present. This anisotropy, with the help of spin-orbit coupling and crystal-field effects, plays a crucial role in stabilizing magnetic behavior in 2D structures. Other studies on materials such as Fe_3GeTe_2 and VSe_2 expanded the concept of 2D magnetism and showed a remarkable diversity of itinerant ferromagnetic and other spin-ordered ground states [104, 105]. Recently, there have been many studies concerning how the different factors like crystal structure, layer thickness, doping, strain, and external fields can modify the magnetic ground state, aiming to find ways to control and tune the magnetism in the ultra thin limit [98, 106]. Before these fascinating experimental researches, several theoretical models were established to understand the concept of magnetism in the low dimensions. Some simplified models like Ising, Heisenberg, and XY models were essential tools for describing spin systems in one and two dimensions [107, 108, 109]. As schematically shown in Figure (2.9), Ising spins point up or down, Heisenberg spins are fully vectorial, and XY spins rotate within a plane even though these models focus on various symmetries in spin space. However, they clearly show how dimensional

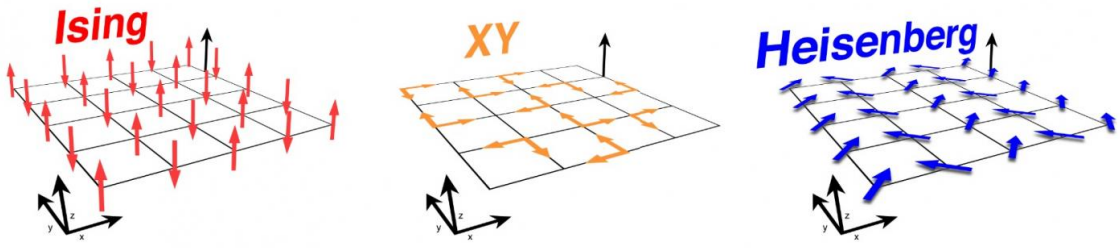

Figure 2.9. Schematic model of spin configuration in different Ising, Heisenberg, and XY models. Credit for this picture is for IBS - Institute for Basic Science.

constraints and thermal fluctuation can drastically affect the magnetic order of the materials. One of the important theoretical points was concerning the Mermin-Wagner theorem, which states that continuous spin symmetry can not be spontaneously broken at finite temperature in 1D or 2D isotropic systems [110]. This theory shows that purely isotropic Heisenberg or XY magnets can not keep their long-range order in two dimensions; however, once magnetic anisotropy has appeared, full rotational symmetry is broken, and an energy gap in the spin-wave spectrum can emerge. Subsequently, the spins can align in a preferred direction, and stabilizing magnetic order despite the strong thermal fluctuations [111, 112, 113]. Modern computational methods are developing to improve our understanding of 2D materials. For instance, Density Functional Theory (DFT), many-body perturbation theory (MBPT), and tight-binding models introduced by the first-principles calculations give the prediction of magnetic ground states, Curie temperature, and spin texture with sufficient accuracy compared to the experimental results [114]. Furthermore, these theoretical results help the experiments to identify promising materials or uncover the microscopic origins of magnetism. On the other hand, machine learning and high-level computational approaches help to provide an extensive database of layered crystals for appropriate orbital occupations, lattice geometries, and spin-orbit coupling strength, and therefore, one can discover a new 2D magnetic materials (see the well-known 2D magnets in Figure (2.10)) [98].

From an experimental aspect, many advanced techniques have confirmed and explored the magnetic behavior in 2D systems. Take the Magneto-optical Kerr effect (MOKE) measurements as an example, which were the important measurements in verifying ferromagnetism in exfoliated or grown flakes by detecting polarization changes in reflected light [98, 102]. To provide atomic-scale insights into the local density of states, spin-polarized states, and the interplay between doping, moire patterns, and lattice reconstruction, one can use scanning tunnelling microscopy (STM) and spectroscopy (STS) techniques [106, 115]. Even though Raman spectroscopy is usually employed to study the vibrational modes, it is also sensitive to spin-phonon coupling and makes it an attractive non-destructive method in detecting spin reordering in 2D magnets [116, 117]. In Figure (2.11), one can see an example of Raman spectra as well as an experimental setup for circularly polarized Raman spectra. The 2D materials with metallic or semimetallic behavior often show the anomalous Hall effect (AHE), in which a transverse voltage appears in response to a longitudinal current even without an external magnetic field, as illustrated in Figure (2.12) b. Using these measurements, one can investigate rich information concerning spin-orbit coupling, Berry curvature, and topological spin texture [98, 105]. Furthermore, element-specific alongside momentum-resolved

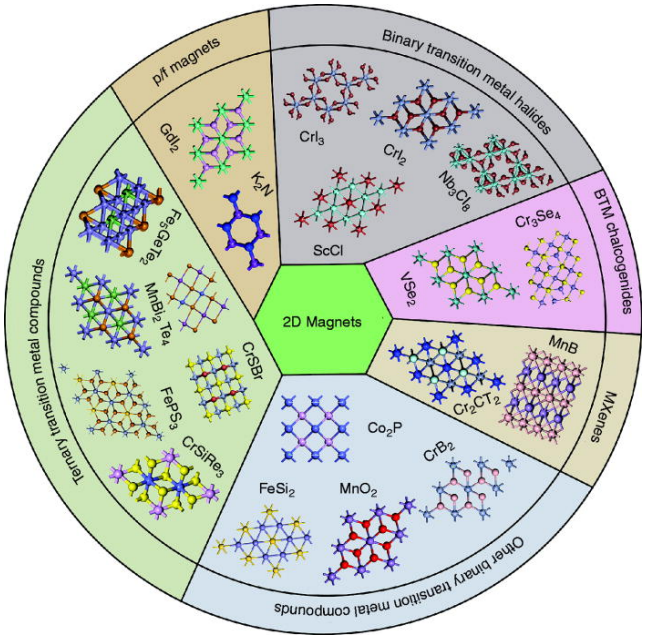

Figure 2.10. The most well-known 2D inorganic magnetic materials. Figure is from reference [106] under the Creative Commons Attribution 4.0 International (CC BY 4.0) license.

techniques like X-ray magnetic circular dichroism (XMCD) and neutron scattering have suggested essential details on the contribution of individual atomic species to magnetism and on the spin-wave dispersion and other collective excitations [119]. In 2D magnets, the collection of different spin orders, ferromagnetic, antiferromagnetic, and more complex noncollinear states, has been explored. The original findings with a monolayer of CrI_3 and bilayer $Cr_2Ge_2Te_6$ showed the presence of ferromagnetism at low temperature [102, 103], but the subsequent work exhibited antiferromagnetism in related compounds such as $MnPS_3$ and $MnPSe_3$ [121]. In recent years, researchers have been looking for higher ordering temperatures, both for academic interest and for applications. Strain, also with its mechanical deformation of a crystal, plays a significant role as a powerful strategy to help enhance the exchange interaction or spin-orbit coupling, thus stabilizing magnetic order. Chemical functionalization or doping can also alter the electronic filling of the bands that participate in spin ordering and then increase the Curie temperature. Meanwhile, heterostructure design also using the proximity effects can be another strategy to tune the existing magnetism [122]. Real-life applications of these materials not only rely on achieving room-temperature magnetism but also on developing scalable production techniques. Current methods like mechanical exfoliation, chemical vapor deposition (CVD), molecular beam epitaxy (MBE), and electrochemical growth are good techniques but are struggling with several challenges such as uniform thickness control, reproducibility over large areas, and environmental stability [98, 106]. Concerning the devices, the integration of the 2D magnets into the multilayered designed devices requires precise interface engineering to control many factors like chemical reactivity, lattice mismatch, and spin transport across layers [113]. There are still many questions that remain about the magnetism in ultra-thin materials. Researchers are working on methods to control interlayer magnetic interaction, understand the spin-orbit coupling effects, and find the electron correlations

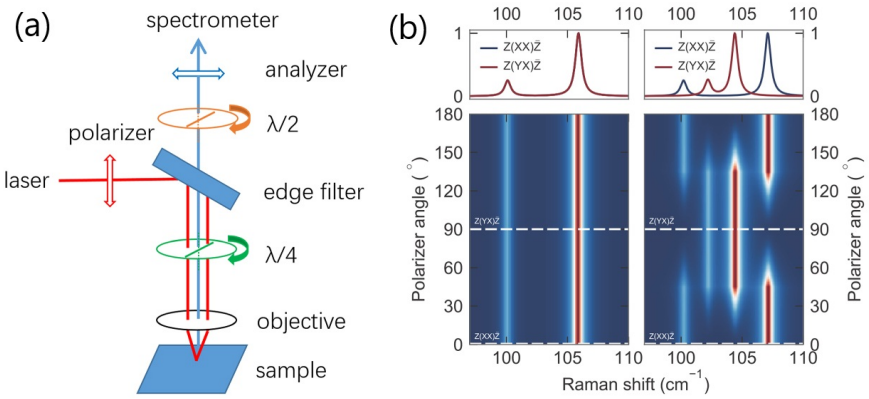

Figure 2.11. (a) Experimental setup of circularly polarized Raman spectra. (b) The intensity maps of the polarized-dependent Raman spectra in rhombohedral (left) and monoclinic (right) phases of bulk CrI3. Figure reprinted and Caption reproduced from references [117], and [118] for the Figures (a) and (b), respectively. under the Creative Commons Attribution 3.0 (CC BY 3.0) license.

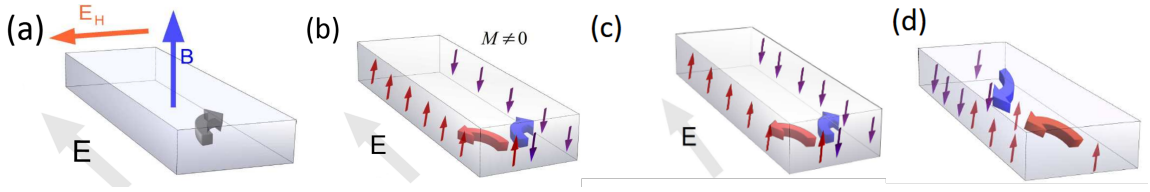

Figure 2.12. Schematic representation of the different Hall effects, (a) Classical Hall effect, (b) anomalous Hall effect, (c) spin Hall effect, and (D) inverse spin Hall effect. Figure reprinted and Caption reproduced from references [120].

in moiré-patterned bands [106, 111, 112]. In spintronics, energy efficiency gate-tunable spin control can be seen in the van der Waals heterostructure, which combines magnetic and semiconducting layers. 2D magnets may support exotic quasiparticles like Majorana fermions, particularly when they are paired with superconductors or topological insulators [98, 113, 123, 124]. Their strong spin signals also make them ideal for magnetic sensors, wearable devices, and nanoscale applications such as drug delivery and soft robotics. Altogether, recent advances in fabrication, study, and design of 2D magnets have made them a promising group of materials. By controlling magnetic properties at the atomic level, these materials will be used in new technologies in fields like spintronics, quantum computing, and sensing [125, 126].

2.2.2 V-based Transition Metal Dichalcogenides (TMDCs)

Transition metal dichalcogenides (TMDCs) have been extensively studied for decades, with early research focusing on fundamental properties such as charge density waves (CDW) and superconductivity [127, 128, 129, 130]. Among them, vanadium-based TMDCs have emerged as a distinct subgroup with rich structural, electronic, and magnetic behavior. In particular, V-based ditellurides crystallize in a monoclinic structure with a $1T^{'}$ phase below 300 K [131, 132, 133, 134, 135, 136]. In contrast, the diselenides and disulfides often favor trigonal crystal structures in the $1T$ or $2H$ phase [137, 138, 139, 140]. Although these compounds can be isostructural, they display a wide range of intrinsic electronic and magnetic properties. For example, VTe_2 undergoes a transition

to a commensurate CDW phase at 474 K [133, 141, 142], while VSe_2 exhibits an incommensurate CDW state around 110 K, followed by a transition to a commensurate phase at 70 K [143, 144]. These CDW transitions are closely tied to Fermi surface nesting and semimetallic band structures, as shown in ARPES studies [145, 146]. DFT calculations predict that VTe_2 is most stable in the $1T$ phase under ambient conditions, though strain or pressure can induce transitions to $1T^{'}$ or $2H$ phases [147, 148, 149, 150]. These theoretical findings have been supported by experimental techniques such as X-ray diffraction (XRD) and Raman spectroscopy, which confirm structural transitions in VSe_2 and VTe_2 across different temperatures [151, 152].

One of the defining intrinsic features of monolayer VSe_2 is its predicted ferromagnetic order, driven by Stoner-type instability. This has been experimentally confirmed using the magneto-optical Kerr effect (MOKE) and SQUID magnetometry [145]. Although bulk VTe_2 does not exhibit superconductivity under ambient conditions, superconducting phases can be induced via alkali metal intercalation, electrostatic doping, or pressure [145]. Vanadium-based TMDCs have great potential applications in nanoelectronics, spintronics, and quantum materials research. They can be tuned for their electronic and magnetic properties, which makes them promising for next-generation devices such as field-effect transistors (FETs) [153, 154] Moreover, recent studies show that under suitable conditions (such as strain, doping, etc.) these materials can have topological insulating phases [155, 156, 157, 158]. For instance, recent wok has shown that in materials like VTe_2, a charge density wave (CDW) can couple to a band inversion between V-3d and Te-5p orbitals and modulate the topological surface states, effectively switching between topological non-trivial and trivial phases [159]. This suggests that in addition to the intrinsic magnetic behavior, the V-based TMDCs can have a controllable topological phases. Future research aims to synthesize high-quality monolayers, strain engineering to stabilize novel phases, and investigate topological quantum states [147, 160].

2.2.3 Chromium Trihalides [CrI_3; X= Cl, Br, and I]

During the last few years, the chromium trihalides with the general formula of CrX_3, where X can be I, Cl, and Br, have gained significant attention. CrX_3 materials have a layered structure nature where the nanosheets of the chromium atoms are sandwiched between halogen atoms, which form weak van der Waals interlayer interactions between layers (see Figure (2.13)). The first study and experimental synthesizing are traced back to the middle of the 20th century for the bulk magnetic properties [161], and later, the CrX_3 became one of the essential materials in 2D magnetism research. The highest interest in research on CrX_3 evolved when the intrinsic ferromagnetism in a monolayer of CrI_3 at low temperature was discovered [103]. Research on CrX_3 materials grows rapidly due to their tunable magnetic properties and their compatibility with van der Waals heterostructures, making them highly relevant for spintronic applications, quantum information science, and fundamental studies of low-dimensional magnetism [111, 122, 162, 163]. The origin of the magnetic properties of the CrX_3 materials is due to the Cr^{3+} ions, which have unpaired electrons in the 3d-orbital of the electron's configuration. These ions interact via superexchange mediated by the halogen atoms and make the magnetic ordering. The magnetic ordering depends on the strength of the exchange interactions and spin-orbit coupling [164]. Among all CrX_3 compounds, CrI_3 is the most common material and studied member due to the remarkable ferromagnetic behavior in monolayer. The Curie-temperature of the monolayer of CrI_3 is around 45 Kelvin and increases with the increasing number of layers originating from the interlayer exchange coupling [165]. On the

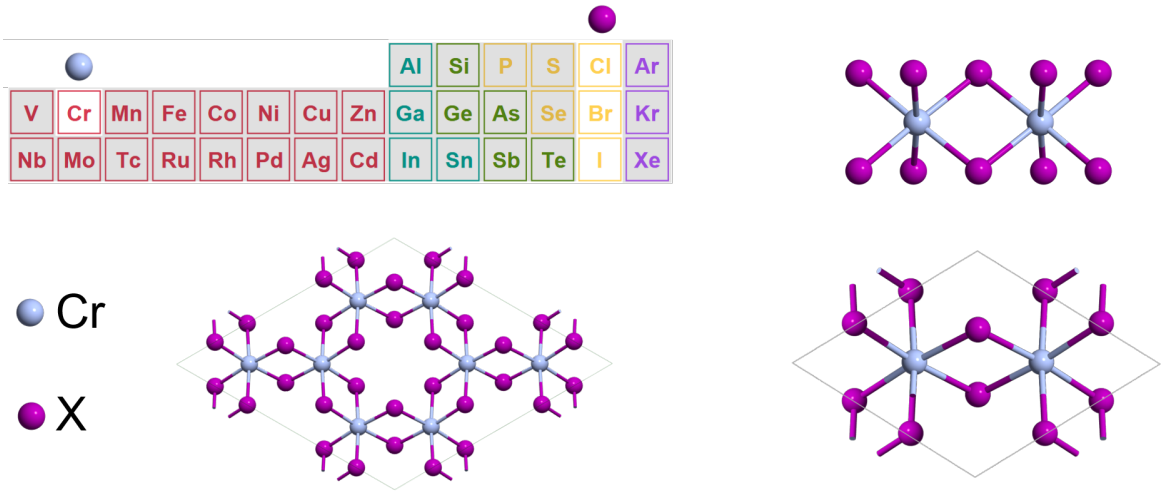

Figure 2.13. Periodic table of CrX_3 [X = Cl, Br, and I] components and elements with a schematic structure on different top and side views.

other hand, the $CrCl_3$ shows the antiferromagnetic order with a Néel temperature of approximately 17 K originated because of the weaker spin-orbit coupling of Cl atoms compared to the iodine [166]. The CrI_3 and $CrCl_3$ are firmly anisotropic, and for the case of a pristine monolayer of CrI_3, the preferred direction of magnetization is out-of-plane, and for $CrCl_3$ it is in-plane. The magnetic properties of these materials are susceptible to external factors such as strain, electric fields, and proximity to other 2D materials [167, 168]. Chromium halides, particularly CrI_3 and $CrCl_3$ in our thesis, are tunable 2D magnetic materials with wide bandgap and prominent layer-dependent properties, offering a wide range of applications in spintronic as well as for magnetoelectric applications. This type of material has been discussed in more detail in chapter (7).

2.2.4 Modelling of Magnetism in van der Waals Heterostructures

The origin of the magnetism in 2D vdW heterostructures is due to the interplay between localized magnetic moments and the exchange interactions that couple them. These interactions can be tuned by changing the interlayer stacking, applying strain, or through external fields, which provide a versatile platform for novel spintronic devices. As the main part of my thesis is based on magnetism, in this section, I will briefly discuss the derivation and theoretical model for the effective spin Hamiltonian and some details concerning the exchange interaction from first-principle methods based on DFT and analyze collective excitations within the spin-wave formalism. In vdW crystals and their heterostructures, magnetic order can arise from localized moments (Hund's rules on partially filled d shells) coupled by superexchange/double exchange [106], or from itinerant bands that spontaneously spin polarize (Stoner mechanism) [169]. Conduction electrons may further mediate long-range, oscillatory couplings (RKKY). Reduced symmetry and spin–orbit coupling (SOC) generate the anisotropies necessary to stabilize 2D order [170, 171].

The first point of describing the magnetism in 2D vdW heterostructures is based on the effective spin Hamiltonian. In these systems, the localized magnetic moment and exchange coupling interact and are often strongly modified due to the reduced dimensionality, weak interlayer bonding, and the influence of spin-orbit interactions. The effective Hamiltonian is commonly expressed as

$$\mathcal{H} = -\sum_{\langle i,j \rangle} J_{ij}\, \mathbf{S}_i \cdot \mathbf{S}_j - K \sum_i (\mathbf{S}_i^z)^2 - \sum_{\langle i,j \rangle} \mathbf{D}_{ij} \cdot \left(\mathbf{S}_i \times \mathbf{S}_j\right), \tag{2.3}$$

where the first term, proportional to J_{ij} is the isotropic exchange interaction between spins at lattice sites i and j. This interaction is central to establishing either ferromagnetic or antiferromagnetic order and has been successfully derived from first-principles calculations using the magnetic force theorem [172, 173]. The second term, involving the anisotropy constant K, arises predominantly from spin-orbit coupling effects and is essential for stabilizing long-range magnetic order in 2D systems by overcoming the restrictions imposed by the Mermin–Wagner theorem [174]. In particular, a positive K tends to favor an easy-axis configuration, whereas a negative K supports an easy-plane alignment [175, 176]. The final term in equation (2.3) represents the Dzyaloshinskii–Moriya (DM) interaction, which becomes nonzero in the presence of broken inversion symmetry at the midpoint between interacting spins. This antisymmetric exchange has been shown to give rise to chiral spin textures, such as spin spirals and skyrmions, and has been extensively discussed in both theoretical and experimental studies [177, 178, 179]. In layered van der Waals materials, the interplay between the DM interaction and conventional exchange is particularly significant, as it can lead to complex magnetic ground states and influence the dynamics of spin excitations [180, 181].

The derivation of equation (2.3) from a microscopic electronic Hamiltonian typically proceeds via Density Functional Theory (DFT) or DFT+U methods, which capture the essential electronic correlations in the d-orbitals of transition metal atoms. By considering small deviations from a collinear magnetic ground state, one can apply the magnetic force theorem to relate the change in total energy to infinitesimal rotations of the local moments [172, 173]. In this way, the isotropic exchange constants J_{ij} are expressed in terms of the spin-resolved Green functions and the on-site exchange splittings. A commonly used expression, known as Liechtenstein-Katsnelson-Antropov-Gubanov (LKAG) formula, in this context is:

$$J_{0i,\mathbf{R}j} = -\frac{1}{4\pi} \int_{-\infty}^{E_F} \mathrm{d}\epsilon\, \mathrm{Im\,Tr}\left[\Delta_i G_{i,j}(\epsilon, \mathbf{R}) \Delta_j G_{i,j}(\epsilon, -\mathbf{R})\right] \tag{2.4}$$

where $\mathbf{R}$ stands for the lattice vector at distance $\mathbf{0}$ (labeled as a central atom), $\Delta_{i,j}$ denotes the local exchange splitting at site i, j, and $\Delta_{i,j} = H_{i,j}^{\uparrow} - H_{i,j}^{\downarrow}$, and $G_{ij}^{\uparrow,\downarrow}(E)$ are the corresponding spin-resolved real-space Green functions [182]:

$$G(\epsilon, \mathbf{R}) = \sum_{\mathbf{k}_i} w_{\mathbf{k}_i} G(\mathbf{k}_i, \epsilon) e^{-i\mathbf{k}_i \cdot \mathbf{R}}, \tag{2.5}$$

where $w_{\mathbf{k}_i}$ is the k-point weight and with the reciprocal space Green's function given by:

$$G(\mathbf{k}, \epsilon) = (\epsilon \mathbf{S}(\mathbf{k}) - \mathbf{H}(\mathbf{k}))^{-1}, \tag{2.6}$$

Here, $\mathbf{H}(\mathbf{k})$ is the spin-dependent Kohn–Sham Hamiltonian matrix, with elements,

$$H^{\sigma}_{\mu\nu}(\mathbf{k}) = \langle \phi^{\sigma}_{\mu}(\mathbf{k}) \,|\, \hat{H}^{\sigma}_{\mathrm{KS}} \,|\, \phi^{\sigma}_{\nu}(\mathbf{k}) \rangle, \tag{2.7}$$

and $\mathbf{S}(\mathbf{k})$ is the overlap matrix,

$$S_{\mu\nu}(\mathbf{k}) = \langle \phi_{\mu}(\mathbf{k}) \,|\, \phi_{\nu}(\mathbf{k}) \rangle, \tag{2.8}$$

where $\phi_{\mu}(\mathbf{k})$ are the localized basis functions. The indices μ and ν label the orbital (basis function) degrees of freedom, while $\sigma = \uparrow, \downarrow$ denotes the spin channel [183, 184]. The energy integral in equation (2.4) is calculated using complex contour integration. Such derivations not only provide a quantitative basis for the parameters in equation (2.3) but also clarify their dependence on the electronic structure, which may exhibit oscillatory (RKKY-like) behavior in metallic systems [185, 186, 187]. Recent review articles have synthesized these theoretical developments, highlighting both the successes and challenges in modeling magnetism in low-dimensional materials. For example, Burch *et al.* [181] and Gibertini *et al.* [180] provide extensive discussions of the effective Hamiltonian approach in the context of vdW materials, while other reviews [176] emphasize the role of anisotropy and DM interactions in stabilizing novel magnetic textures.

The effective Hamiltonian (2.3) allows us to study collective excitations (magnons) using the linear spin-wave theory. Employing, for instance, the Holstein-Primakoff transformation for a ferromagnetic ground state, the Hamiltonian can be diagonalized to yield the spin-wave dispersion:

$$E(\mathbf{q}) = 2S\,[J(0) - J(\mathbf{q})] + \Delta, \tag{2.9}$$

where S is the spin quantum number, $\Delta = 2KS$ is the anisotropy-induced gap (i.e. the magnon energy at $\mathbf{q} = 0$), and $J(\mathbf{q})$ is the Fourier transform of the exchange couplings,

$$J(\mathbf{q}) = \sum_{j} J_{0j}\, e^{i\mathbf{q}\cdot\mathbf{R}_{0j}}. \tag{2.10}$$

In the long-wavelength regime(small $\mathbf{q}$), the dispersion is approximated as

$$E(\mathbf{q}) \approx \Delta + D\,q^2, \tag{2.11}$$

which defines the spin-wave stiffness D. For a Heisenberg ferromagnet on a Bravais lattice, D is given by

$$D = \frac{S}{d} \sum_{j} J_{0j}\, |\mathbf{R}_{0j}|^2. \tag{2.12}$$

where d is the spatial dimension (here $d = 2$ for a 2D lattice). Note that for systems where J_{0j} exhibits oscillatory (RKKY-like) behavior, special care must be taken to regularize the summation in Eq. (2.12). Thermal fluctuations lead to the destruction of long-range magnetic order at a finite temperature. In the mean-field approximation (MFA), the Curie temperature T_C for a ferromagnet is estimated as:

$$k_B T_C^{(\mathrm{MFA})} = \frac{2}{3} S(S+1)\, J(0), \tag{2.13}$$

where $J(0) = \sum_j J_{0j}$. More refined analytical estimates can be obtained using the random-phase approximation (RPA) or Green's function method (Tyablikov's decoupling scheme), and the spin-wave (SW) theory in its interacting form. These methods effectively incorporate the effect of

spin-wave (magnon) excitations that reduce the ordering temperature. For example, in the RPA (also known as the Tyablikov or Callen–Green's function approach), one finds a lower T_C than MFA, often in better agreement with experiments, by solving self-consistently for the divergence of the uniform susceptibility [188, 189]. In the context of 2D magnets, the RPA or a renormalized spin-wave theory predicts that T_C depends sensitively on the anisotropy gap Δ and is significantly reduced when Δ is small.

Beyond the previous approaches, which are mostly post-processing analytical approaches, numerical simulations such as Monte Carlo (MC) calculations based on Metropolis (or other) algorithms are used to study phase transitions and thermodynamic quantities in spin models. In this thesis, we use classical Monte Carlo simulations on the effective Hamiltonian (2.3) to extract parameters such as the temperature dependence of magnetization, magnetic susceptibility, and heat capacity, as well as to estimate T_C from the peak of the susceptibility or specific heat. The MC method is considered one of the most accurate ways to determine the T_C for 2D magnets, since in these simulations one can fully account for thermal spin fluctuations beyond any MFA [166, 167]. Additionally, we use MC simulations to model field-dependent magnetic properties, such as magnetization hysteresis loops. When system is placed under an external magnetic field that is slowly ramed up and down, one can investigate a theoritcal M–H curve (hysteresis loop) and subsequently find the coercive fields and remanence [190].

In vdW heterostructures, the weak interlayer interactions can substantially influence the overall magnetic behavior. Effective interlayer exchange is often introduced as

$$\mathcal{H}_{\text{int}} = -J_{\text{int}} \sum_{\substack{i\in\text{layer 1}\\ j\in\text{layer 2}}} \mathbf{S}_i \cdot \mathbf{S}_j, \tag{2.14}$$

which may lead to either ferromagnetic or antiferromagnetic alignment between layers. Additionally, the breaking of inversion symmetry at the interface can activate interfacial DM interactions, as described by:

$$\mathcal{H}_{\text{DM}} = -\sum_{\langle i,j\rangle} \mathbf{D}_{ij} \cdot \left(\mathbf{S}_i \times \mathbf{S}_j\right). \tag{2.15}$$

These terms are crucial for understanding the stabilization of complex magnetic textures such as skyrmions in 2D systems. ***More details about the methods and also derivations could be found: For the LKAG formalism [191] – For ab-initio aspect combined with LKAG [192] – Concept of magnetism in 2D vdW heterostructures [193].***

2.3 van der Waals heterostructures

2.3.1 General Overview of vdW heterostructures and their devices

The discovery of graphene was a starting point of the investigation of the physics of 2D materials, which nowadays has been shifted towards searching for new hybrid structures made of 2D materials that may serve as a platform for various devices, and in which various new phenomena occur. Despite these trends, the fundamental science of graphene, especially for many-body physics, has not been fully considered and requires more attention and work. Due to the steadily improving

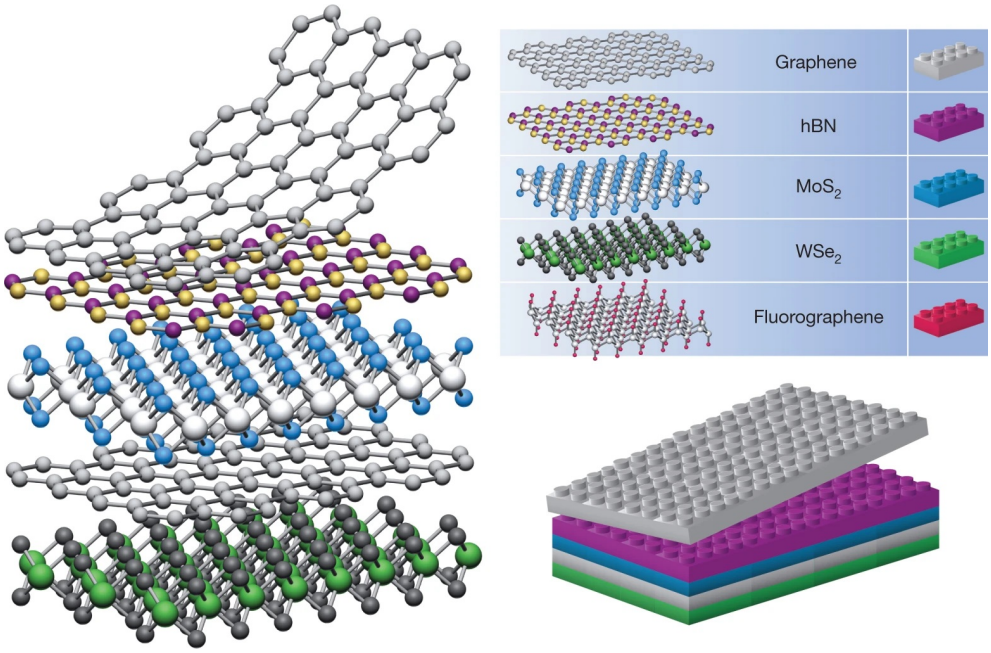

Figure 2.14. Schematic structure of the van der Waals heterostructures of 2D materials. Figure reprinted and Caption reproduced from references [210]. © Springer Nature. License Number: 5990180248156.

quality of graphene-based devices [56, 194, 195, 196], further progress is expected. As most of the fundamental graphene research has already been performed, there are many efforts to focus on the other two-dimensional (2D) atomic crystals [27] like monolayer and few-layer forms of hexagonal boron nitride (h-BN), molybdenum disulfide (MoS_2), various dichalcogenides, and layered oxides. A few years after discovery of graphene, only a few experimental publications worked on 2D materials beyond graphene. However, now there is a tremendous number of works on the 2D materials beyond the graphene [197, 198, 97, 199, 200]. Research on emerging 2D materials suggests that they may become as technologically significant as graphene, particularly as synthesis methods improve for few-layer crystals such as MoS_2 and magnetic 2D compounds like CrI_3 [201, 202, 203]. Alongside the significant studies on graphene and graphene-like 2D materials, a new field of investigation has emerged over the last decade. This field aims to create heterostructures and functional devices that are formed by stacking different 2D crystals on top of each other. The concept of heterostructures is straightforward, and it places one monolayer of 2D material on another monolayer and adds more and more similar stacked 2D layers. The created structure is essentially an artificial material built up in a certain sequence, similar to Lego blocks as shown in Figure (2.14), where each block is defined for one monolayer in a one-atomic-plane precision. When the heterostructure is made by stacking 2D materials vertically, the new crystal shows remarkable covalent bonding in each layer, while weak van der Waals (vdW) forces are sufficient to keep the layered stack together. Even though proving this idea experimentally was performed with delay [204, 205, 206, 207, 208, 209], it has quickly progressed very fastly, where we have lots of work and promising novel stacked crystals.

While there are hundreds of layered compounds that can be cleaved and investigated theoretically from the different methods like the Scotch-tape method [27], the created stable 2D vdW

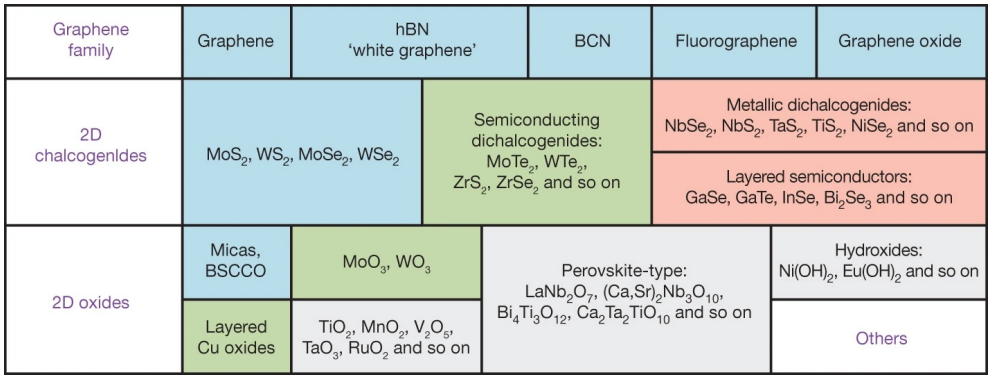

Figure 2.15. Few example of 2D materials in different groups including Graphene family, 2D chachogenides, and 2D oxides. Figure reprinted and Caption reproduced from references [210]. © Springer Nature. License Number: 5990180248156.

heterostructure on the scale of atomically thin layers requires considering several conditions. One of the key limitations is due to the intrinsic properties of ultra-thin films. Firstly, when the thickness of a crystal is decreased [211], its melting temperature generally decreases. On the second point, most materials maintain their stability under an ambient environment only through the natural passivation of their surfaces [212]. At this moment, the mechanically or chemically isolated 2D layers cannot be performed in an integrated manner under high vacuum or low-temperature circumstances, which leads to significant challenges in surface-science experiments. Additionally, it is figured out that the monolayers of graphene indicate higher reactivity compared to the bilayer cases [213, 214]. Therefore, some of the theoretically possible 2D crystals could be impractical to isolate or sustain in ambient conditions due to the possibility of rapid chemical degradation like corrosion, decomposition, or segregation [212]. To have a reliable 2D crystal, its bulk (or three-dimensional) parent materials should show sufficient chemical and thermal stability. Several 2D crystals, as shown in Figure (2.15), can also show a stable structure, but most of them exhibit only marginal stability. For instance, MoS_2 starts to oxidize below 100 °C in moist air [215]. However, the graphene remains intact even if typical room temperatures are raised to 600 K [213]. On the other hand, some layered materials like GaSe, TaS_2, or Bi_2Se_3 are stable in their bulk form but corrode rapidly once their thickness decreases to a few layers. One example of such materials is silicene [70, 216], where even though the 2D form of silicon can be grown epitaxially and be studied in ultra-high vacuum, it can not survive once it is removed from the substrate or when it is exposed to air. In short, one can say that the poor stability of 2D materials compared to their 3D counterpart exhibits that the number of viable 2D materials is still not too high. However, further research and experimental techniques are making an effort to increase the possibility of stable 2D materials [206, 209, 217]. Now, one can look at the methods of synthesis and how to assemble the vdW heterostructures experimentally. Researchers usually use the two principal methodologies, namely top-down and bottom-up, to synthesize the monolayer or few-layer 2D layered materials (2DLMs) for vdW heterostructures. From the historical part, mechanical or micromechanical exfoliations were first used to obtain the graphene with the technique of peeling successive layers from the 3D graphite [6]. This top-down strategy is extended to other 2D materials like molybdenite (MoS_2) [27] and black phosphorus [218, 219] and results in producing outstanding crystallographic and electronic quality. However, the typical production is restricted only to micrometer-scale flakes,

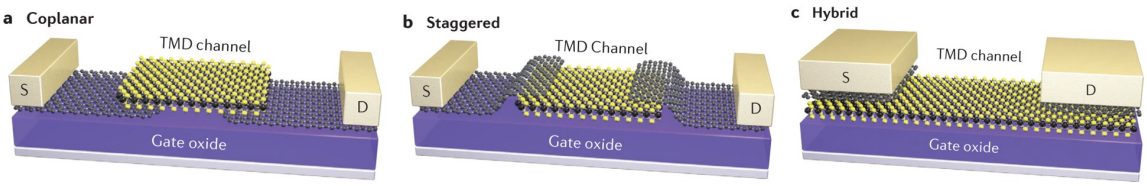

Figure 2.16. Schematics of van der Waals contact architectures for 2D semiconductors: (a) coplanar, (b) staggered, and (c) hybrid types. Source (S) and drain (D) electrodes are indicated. Adapted from [239]. © Springer Nature. License No. 5990180773380.

and its mechanical exfoliations have limitations in both scale and lateral size. To achieve scalability, chemical and solution-based exfoliation methods have been developed [220, 221]. These involve processes like chemical intercalation or mechanical sonication, which give the larger quantities of mono- or few-layer flakes dispersed in solution. As already discussed in section 2.1.1 for graphene, while the mentioned processes produce significant amounts of materials, they usually are along with defects, impurities, and other forms of degradation that alter the precise electronic or photonic devices. Despite these drawbacks, solution-exfoliated 2DLMs could be appropriate for applications in photocatalysis or electrocatalysis [26, 222]. On the other hand, bottom-up techniques, particularly chemical vapor deposition (CVD), have been very successful in growing large-area, high-quality 2DLMS (including graphene, hexagonal boron nitride (BN), and different transition metal dichalcogenides as well as their alloys). Even though CVD can produce relatively uniform thin films over large substrates, fine-tuning growth conditions for multiple 2D materials could not exist, and this may limit the formation of complex heterostructures in a single multi-step process [223, 224, 225, 226, 227, 228, 229, 230, 231, 232, 233].

Two-dimensional semiconductors (2DSCs), especially transition metal dichalcogenides (TMDCs), are promising channels for atomically thin transistors owing to their excellent electrostatic control and potential for high-frequency operation [201]. While few-layer MoS_2 transistors have shown cut-off frequencies up to 42 GHz and power-gain frequencies of 50 GHz [234], their performance is still behind the silicon-based devices. One of the issues is related to the high contact resistance (R_c) at the source-drain interface, where the conventional doping approaches are challenging to implement for atomically thin materials [235]. With the deposition of direct metals on 2DSCs, their covalent bonds can be disrupted and lead to the appearance of defects after Fermi-level pinning and a Schottky barrier that increases the R_c [235, 236]. To overcome these issues, one can use graphene as a contact layer via vdW bonding, which creates an atomically sharp and defect-minimized interface while avoiding Fermi-level pinning [237, 238]. Three typical geometries have been proposed for van der Waals contacts in 2D semiconductor channels, as shown schematically in Figure (2.16)(a–c).

- *Coplanar contacts*: The gate and graphene electrodes lie on the same side of the 2D semiconductor (2DSC). Owing to the tunable work function of graphene, both *p*- and *n*-type contacts can be realized in WSe_2 and MoS_2 devices [237, 240, 241, 242]. Near-ideal band alignment enables barrier-free transport even at low temperatures [237].
- *Staggered contacts*: Graphene electrodes are placed on the opposite side of the 2DSC from the gate, reducing interfacial contamination and enabling large-scale fabrication. Hall mobilities up to ∼34,000 $cm^2V^{-1}s^{-1}$ have been reported [238, 243, 244, 245, 246, 247]. Efficient Schottky barrier modulation is achieved when the layer thickness $t < \lambda$ [248, 249].

- *Hybrid contacts*: A graphene layer is inserted between the metal and 2DSC, preventing damage from metal deposition. In Ti/graphene/MoS_2, the contact resistance R_c decreases by about threefold compared with direct Ti–MoS_2 contacts [250], while Ni/graphene/MoS_2 can reach as low as 0.26 kΩ μm [251], comparable to 1T-MoS_2 contacts [252].

Eventually, graphene-based vdW contacts provide the lowest possible presence of defects, a Fermi-level-pin-free platform for 2D transistors. Hybrid metal-graphene-2DSC schemes show particular promise for achieving low R_c without the need for doping-induced phase transformations, which could lead to stability issues [252, 253, 254, 255, 256]. As technology improves, these contacts can help 2D semiconductors perform as well as silicon chips.

2.3.2 van der Waals heterostructures for spintronic Devices

The integration of two-dimensional materials into the vdW heterostructures has opened a way for designing new spintronic and opto-spintronic devices where their performance is tunable and functionalities are due to the proximity effects rather than direct chemical bonding. The possibility of combining the graphene, TMDCs, topological insulators, and 2D magnets into vertically stacked heterostructures gives the possibility for precise control of spin transport, spin-orbit coupling (SOC), charge-to-spin interconversion (CSI), and magnetic exchange interactions. This provides an excellent platform for ultra-compact, energy-efficient spintronic devices that could be designed for memory, logic, and quantum computing applications. Recent advances in spin dynamics in 2D materials have shown that graphene, due to its exceptionally high carrier mobility and long spin diffusion length, can be an ideal spin channel. Having an efficient spin injection and detection requires tunnel barriers like a hexagonal boron-nitride (hBN), fluorinated graphene, and SrO, which significantly increase spin polarization efficiency ($P_s > 40\%$) [257] as shown in Figure (2.17)a. Beyond the electrical spin injection, opto-spintronics uses the strong spin-photon coupling of TMDCs, which allows optical spin injection into graphene. Experimental results for the MoS_2 and WSe_2 heterostructures have shown that spin-polarized photocarriers can be transferred into graphene, as proved by antisymmetric Hanle spin precession signals [258, 259] as illustrated in Figure (2.17) (c, and d). The spin diffusion length in hBN-encapsulated graphene has reached up to 30 μm, with spin lifetimes (τ_s) exceeding 10 ns at room temperature, which shows its suitability for long-range spin transport [260, 261] as shown in Figure (2.17) (e, and f). One of the most important progresses in vdW heterostructure is the ability to engineer SOC strength in graphene using the proximity effects [266, 267]. When graphene is placed on TMDCs like MoS_2 or WSe_2, it attains a valley-Zeeman SOC and Rashba SOC, which modify the spin texture of its nanostructure [267]. For instance, the effect of graphene on different materials has been shown in Figure (2.18) (more details could be found in the references [268, 269, 270, 271, 272]). Despite the intrinsic graphene with weak SOC, the proximity-induced SOC can reach up to several meVs, significantly modifying the spin relaxation mechanism [266]. Studies for the graphene-TMDC heterostructure showed the high anisotropy spin relaxation, where in-plane spin components relax two orders of magnitude faster than out-of-plane spins [273, 274]. This effect allows for designing spin filters where only specific spin orientations can be scattered [267]. The presence of charge-to-spin interconversion (CSI) in vdW heterostructures has raised the capabilities of spintronic logic and memory devices. CSI, which is driven by SOC effects, leads to the conversion of charge currents into spin currents and vice versa, which is a key mechanism for spin-orbit torque memories [258, 275]. Recent research

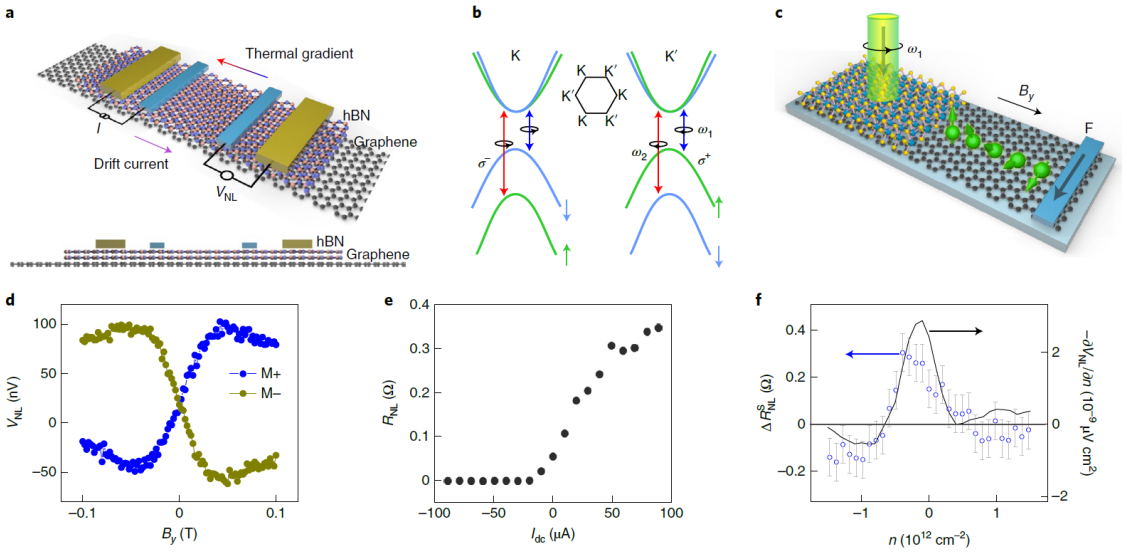

Figure 2.17. Illustration of a graphene-hBN spin device with spin transport controlled by electric and thermal drifts. (a) Device schematic with ferromagnetic (blue) and non-magnetic (yellow) contacts. (b) TMDC band structure and optical spin injection via circularly polarized light. (c) Spin transport in graphene and detection at contact F. (d) Non-local voltage V_{NL} showing spin precession. (e) Spin signal R_{NL} modulation by drift current I_{dc}. (f) Spin signal changes ΔR_{NL} due to a thermal gradient. Figure reprinted and Caption reproduced from references [262, 263, 264, 265]. © Springer Nature. License Number: 5990181398741.

showed that the room temperature CSI in graphene/TMDCs heterostructures where both the spin Hall effect and spin galvanic effect (see Figure (2.12)) coexist. These effects, tuning by electrostatic gating, allow for dynamic control of spin transport and give efficiencies comparable to heavy metal systems [276]. Additionally, unconventional CSI phenomena like multi-directional spin-to-charge conversion in $MoTe_2$ highlight the role of reduced crystal symmetries in defining spin transport properties [258, 275, 276].

Beyond manipulating the spin-orbit coupling, magnetic proximity effects in vdW heterostructures could change the behavior of non-magnetic materials to ferromagnetic or antiferromagnetic ones. When graphene is placed on 2D magnetic materials such as CrSBr and CrSe, the proximity-induced exchange interactions appear in graphene with the exchange fields exceeding 130 meV. This effect can be increased in graphene-CrSBe heterostructure, where exchange fields of 170 T have been observed at cryogenic temperatures. The ability to control magnetic interaction using interfacial engineering has also led to the discovery of topological magnetic textures, such as skyrmions in WTe_2-Fe_3GeTe_2 heterostructures driven by Dzyaloshinskii-Moriya interactions (DMI) [277]. These magnetic textures have the potential to be applied to low-power memory and logic devices [278, 279]. vdW heterostructures have control over valley-dependent spin phenomena, with exciton dynamics in transition metal dichalcogenides (TMDCs) affected by proximity-induced magnetism. In WSe_2-CrI_3 heterostructures, the valley-dependent optical transitions of WSe_2 could be tuned using the CrI_3 magnetization, which highlights a layer-dependent magnetic proximity effect [280]. Twist angle is also a crucial point in modifying the spin-orbit coupling and magnetic exchange interactions, which, with more details, will be discussed in a subsequent section. In principle, future spintronic advances working with stabilized room-temperature 2D magnetism,

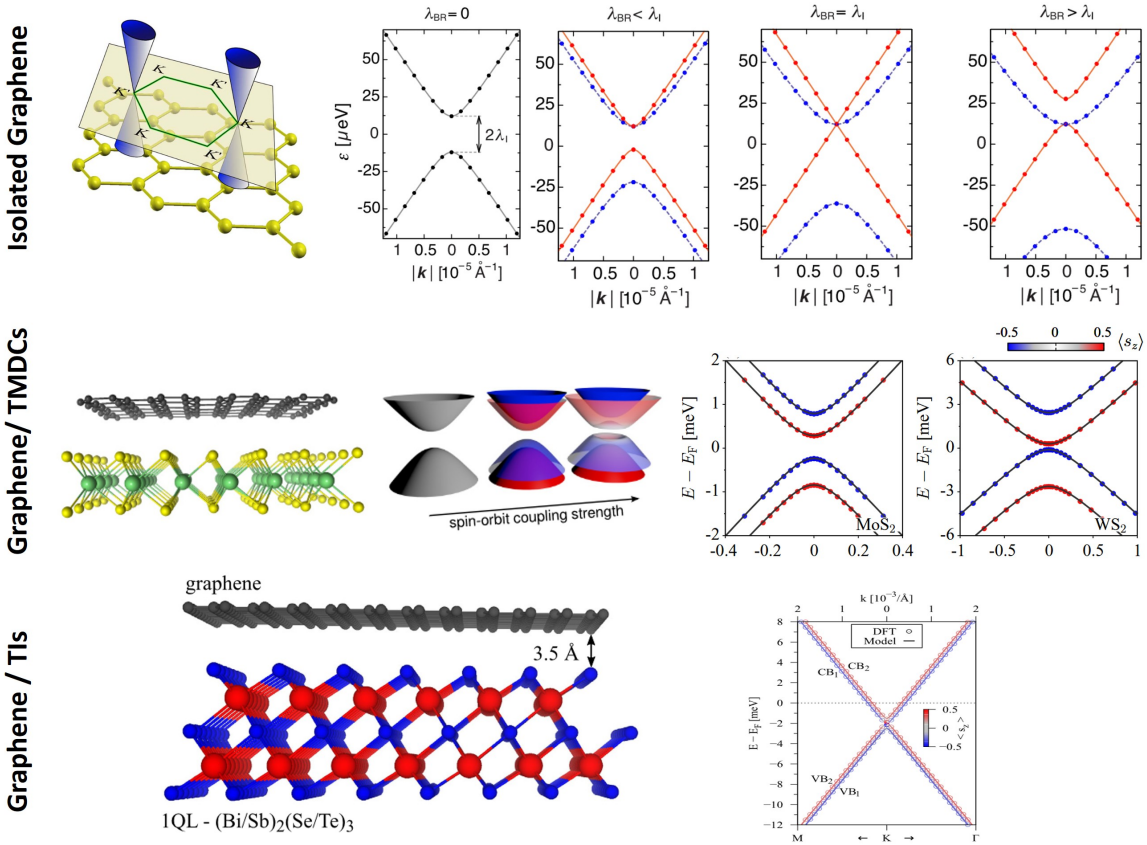

Figure 2.18. Schematic structure of the Graphene and graphene-based structure with their corresponding spectra. Figure reprinted and Caption reproduced from references [268, 269, 270]. © Springer Nature. License Number: 5990181398741.

enhanced Curie temperature using proximity SOC, and optimized spin interactions via precise stacking. Subsequently, these developments could enable topological quantum phases such as the quantum spin Hall effect, quantum anomalous Hall effect, and Majorana fermions. Even though the progress in this area is highly rapid, there are still challenges in large-area fabrication, interface engineering, and theoretical modeling to realize vdW heterostructure for next-generation quantum and spintronic technologies fully [273, 281, 282, 283, 280].

2.4 Twistronics

2.4.1 General overview on twistronics

Twistronics is the field that studies the electronic properties in stacked 2D materials where one of the layers has a twist angle compared to the others, and it creates novel electronic behavior. The central concept refers to the ability of moiré patterns to modify the band structure and electron interactions. After the discovery of unconventional superconductivity and correlated insulating

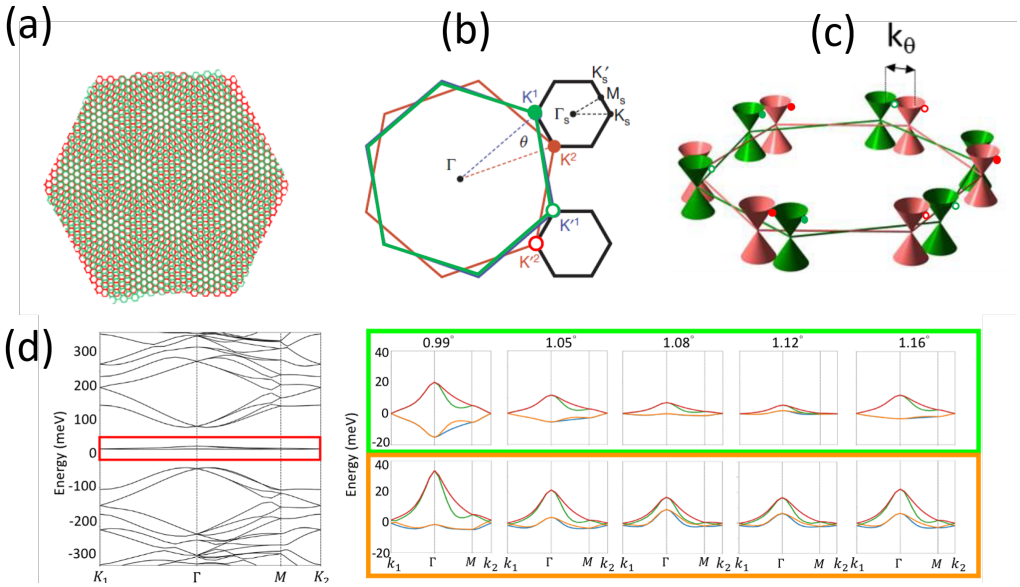

Figure 2.19. Moiré superlattice formed by twisted bilayer graphene, leading to modified electronic structure and flat bands. (a) Moiré pattern, (b) Formation of the moiré Brillouin zone in twisted bilayer graphene due to the rotation angle θ between the top and bottom layers, (c) Dirac cone for valleys for the twisted and untwisted graphene layers, (d) modified bands close to the magic angle showing the flat bands. Figure reprinted and Caption reproduced from references [286, 290]. © Springer Nature. License Number: 5990191463735.

states in the twisted bilayer of graphene (TBG), the interest in twisted structures increased [284, 285]. In the case of TBG, when two monolayers of graphene display a slight rotational misalignment corresponding to each other, they form a periodic moiré pattern, which results in some flat bands and correlated electronic states [284, 285, 286]. The main parameter that plays an essential role in the twistronics is the twist angle between the layers θ, which directly influences interlayer coupling and electronic dispersion. The magic angle is approximately at some 1.1°, which results in flat electronic bands and enables strong electron correlations [287, 288]. The moiré pattern, which is generated by a relative twist between 2D layers, leads to a moiré superlattice, which significantly modifies the band structure. In principle, as shown in Figure (2.19), these moiré superlattices are the reason for creating mini-Brillouin zones, which change the electronic dispersion and lead to the van Hove singularities (unique points in the electronic band structure of a material where the density of states (DOS) becomes very large) and the decreasing of the Fermi velocity [289]. Consequently, these structures support various correlated electronic phases from Mott-like insulators to unconventional superconductors [288].

At small twist angles, the interlayer hybridization is much more significant, and the electronic wavefunctions localize within the moiré unitcell. The substantial modification of the electronic density of states (DOS) is the reason for the appearance of quantum phases, including superconductivity and correlated insulating states [284]. Additionally, to achieve precise control over these phases, the ability to electrostatically tune the carrier density in moiré systems is requested. These two features make the twisted heterostructures a versatile platform for exploring strongly correlated physics [288, 291]. From a historical perspective, as discussed in the previous sections in detail, 2D materials gained remarkable attention after the isolation of the monolayer of graphene in

2004. However, the primary attention to the field of twistronics comes back to the years after the discovery of magic-angle TGB in 2018 [284, 285]. Early experiments showed that moiré patterns could affect the electronic properties of 2D materials, but it was not until the work of Cao et al. [284, 285] that realized the potential for strongly correlated states in TBG. At the magic angle ($\sim 1.1^\circ$), the electronic bands of TBG show the nearly flat bands (Figure (2.19)), which exhibit strong electron-electron interactions [291]. Experimental results of correlated insulating states and superconductivity in magic-angle graphene superlattices provided a new platform to investigate unconventional quantum phases [284, 286]. This was a motivation point for extending the research theoretically and exploring twistronics as a promising way to design novel quantum materials.

In beyond-"magic-angle" twistronics, particularly for the systems with larger twist angles and smaller moiré-superlattices, first-principle calculations based on Density Functional Theory (DFT) using the strongly constrained appropriately normed (SCAN) exchange-correlation functional [292, 293] have shown a remarkable success in modeling monolayer materials, which gives a highly accurate meta-GGA approach despite its cubic scaling with the number of atoms [294]. This success in modeling has motivated the development of advanced, affordable theoretical methods that can efficiently handle systems with massive numbers of atoms on the scale of a million. At the same time, capturing phenomena such as the quantization of Hall conductivity in tBLG and the twist-dependent band gaps in TMDCs remains challenging for first-principles approaches, motivating the development of alternative multiscale or effective models [295]. Furthermore, although atomistic simulations of superlattices are computationally costable due to the long-range interlayer interactions, a non-linear finite element plate model using a discrete-continuum interlayer potential based on the Kolmogorov–Crespi model [296, 297] (with an updated version for TMDs proposed in [298]) has turned out successfull in capturing essential exchange-correlation effects absent in simpler potentials such as the Lennard-Jones potential. Additionally, it has been shown that the real-space misalignment of two repetitive patterns leads to localized states in momentum space, which enable a reformulation of quantum mechanics, and the requirement of referencing to the 2D lattices is omitted, allowing for more efficient calculations [299].

2.4.2 Twist-dependent experimental discoveries

Twistronics research has shown that the interlayer region—typically 0.3–0.4 nm thickness—plays a crucial role in the electronic and structural properties of vertically stacked 2D materials. In graphene-based systems (e.g., tBLG and graphene+hBN) [301, 302, 300, 303, 304, 305], a significant fraction of the total volume is occupied by this region, which enables significant charge redistribution and modifies interlayer hopping parameters [306, 307, 308, 309, 310]. This coupling not only drives the emergence of a purely electronic moiré superlattice [311, 312, 313, 314, 315, 309] (as illustrated in Figures 2.20) but also promotes atomic reconstruction at the van der Waals interface and leads to buckling and domain formation which could be observed by SAED, DF-TEM, and multislice simulations [316, 317, 318, 319, 320, 296, 321] (see Figure (2.21)).

Together, twist-angle–dependent transport phenomena have shown exotic electronic states in these systems. Notably, tBLG exhibits unconventional superconductivity at "magic" angles (1.08°–1.15°) where flat bands occur that lead to the strong electronic correlations, fractal quantum Hall states, and 1D topological channels [284, 285, 322, 289, 321, 323, 324] (Figure (2.19)). These properties are due to the interplay between interlayer hybridization and the relative twist-induced modification of the Dirac cone interactions, which can be finely tuned to manipulate insulat-

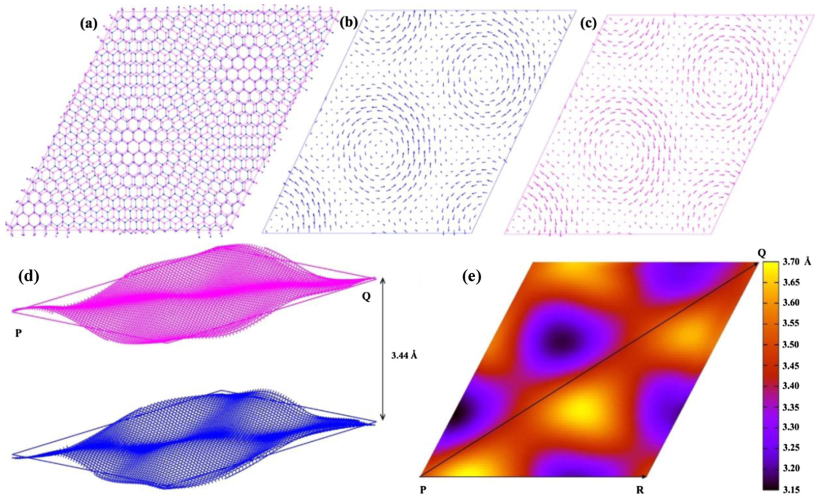

Figure 2.20. Interlayer coupling effects in twisted bilayer graphene (tBLG). (a)–(c) tBLG twisted at 5.09°: (a) before reconstruction, (b) bottom layer (counterclockwise rotation near the vortex), (c) top layer (clockwise rotation). (d) and (e) Buckling in tBLG twisted at 1.61° (15,132 atoms) with an equilibrium interlayer separation of 3.44A; (e) shows the top layer buckling profile (0.51A height). Figure reprinted and Caption reproduced from references [300] with permission from IOP Publishing (License ID: 1588638-1).

ing states and topological effects. The evolution of these correlated states is also supported by conductive-AFM mapping and transport measurements across various twist angles [325, 326]. Further experimental studies extend these phenomena to excitonic and magnetic properties. In bilayer TMD heterostructures, strong interlayer coupling produces moiré exciton quasiparticles with twist-angle–dependent confinement and valley polarization [327, 328, 329, 330, 331], while emergent ferromagnetism has been observed in tBLG/hBN structures, with robust hysteretic behavior and controllable magnetic domain switching at specific carrier densities [332, 325, 333] (Figure (2.22)a). Additionally, twist-sensitive Raman spectroscopy has been instrumental in probing phonon modes, charge interactions, and local atomic symmetry changes induced by interlayer coupling and atomic reconstruction [334, 310, 335, 309]. The potential of moiré superlattice to show unexpected quantum phenomena in twisted 2D heterostructures is enormous.

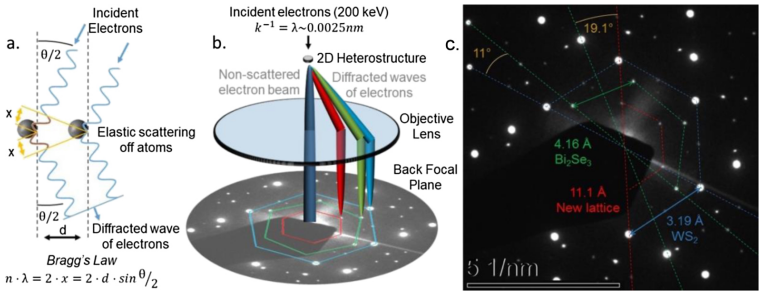

Figure 2.21. Simplified SAED concepts: (a) High-energy electrons scatter at non-zero angles per Bragg's law; (b) TEM schematic in SAED mode shows diffraction from lattices with different spacings; (c) SAED of a Bi_2Se_3/WS_2 heterostructure reveals diffraction spots from each lattice and a moiré pattern induced by interlayer coupling. Figure reprinted and Caption reproduced from references [309] with permission from IOP Publishing (License ID: 1588639-1).

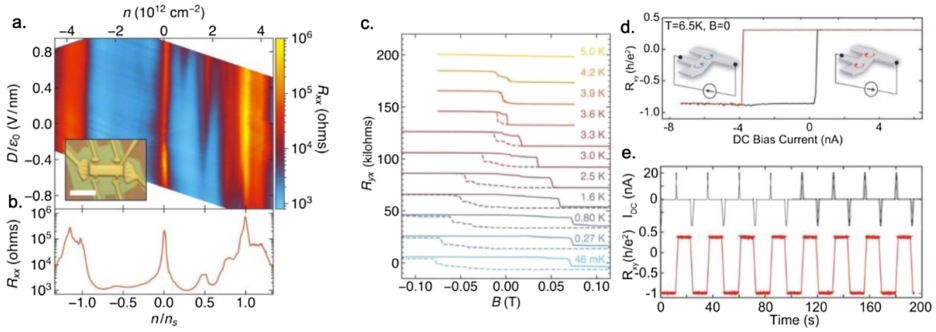

Figure 2.22. Magic-angle tBLG exhibits correlated states enabling emergent ferromagnetism and current-controlled magnetic switching. (a) R_{xx} vs. carrier density n and displacement field D, with filling relative to the moiré superlattice. (b) R_{xx} line cut shows resistance peaks at full and intermediate fillings. (c) Temperature-dependent hysteresis in R_{yx} vs. magnetic field. (d) R_{xy} hysteresis vs. applied current, indicating orbital magnetism. (e) Nonvolatile electrical writing/reading of a magnetic bit. Figure reprinted and Caption reproduced from references [325, 333] with permission from AAAS.

Chapter 3

Theoretical Background

Results presented within this thesis have been obtained from first-principle or ab-initio methods. This chapter will briefly introduce the first principle of materials modeling. In simple words, first-principle calculations are the ability to use quantum mechanics, the periodic table of elements, and computers to find the behavior of materials with the highest accuracy, plus predicting their behavior in the presence of different factors. This chapter introduces the many-body Scrodinger equation and next, the theory of Density Functional Theory (DFT) as one of the most prominent techniques in the first-principle approach. In the subsequent parts of this chapter, the construction method of vdW heterostructures and the effective k·p model are introduced, complemented by a brief introduction to magnetic interactions and transport methods.
The theoretical framework presented in this chapter is written based on the book *Materials Modelling Using Density Functional Theory: Properties and Predictions* by Feliciano Giustino [336].

3.1 Brief History of Computational Materials Modelling

Material modeling is the art of using mathematics to describe the behavior of materials on a microscopic scale. The first principle approach is a bottom-up model, which means that, in contrast to top-down approaches, the aim is to find the properties of materials without relying on empirical fitting parameters. Notably, some of our results, which will be discussed in detail in the following sections, are semi-empirical (e.g., van der Waals Grimme DFT-D2 correction). However, these corrections are for refining the model, and the overall structure of the first principle approach relies solely on one differential equation without using experimental results. Using quantum mechanics, which involves solving a complicated Schrödinger equation, a very general and powerful method, to compare predictions with reality. Using this approach, one can predict the behavior of simple materials like hydrogen and very complex materials like semiconductors or superconductors. However, as more atoms are added and the complexity of materials rises, the computational costs also increase, necessitating many supercomputers with many CPUs and substantial RAM. Besides the computational cost in this approach, another critical and challenging point is matching the predicted theoretical results with experimental results, which scientists are continually working to improve in terms of accuracy.

One of the standard techniques in the first principle calculation approach is Density Functional Theory, abbreviated as DFT. It is a very effective technique that covers a wide range of materials, from molecules to topological materials, by solving the Schrödinger equation. From a historical

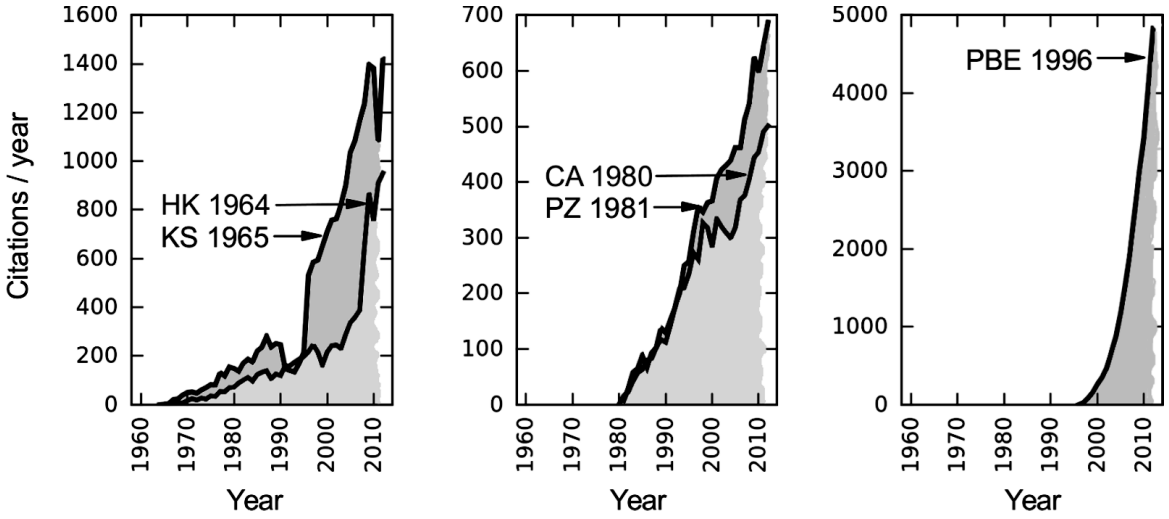

Figure 3.1. The number of citations per year for key works in the development of Density Functional Theory (DFT), including the foundational papers by Hohenberg and Kohn (1964) and Kohn and Sham (1965), as well as other contributions that established DFT—such as the works by Ceperley and Alder (1980), Perdew and Zunger (1981), and Perdew et al. (1996)—The statistical data were obtained from the Thomson Reuters Web of Science platform (http://apps.webofknowledge.com) and picture is from reference [336] with permission from Oxford University Press (License ID: 103668). Further reproduction or distribution is not permitted without written permission from the publisher.

point of view, the birth of Density Functional Theory (DFT) dates back to 1964, when Hohenberg and Kohn published their paper in the journal Physical Review titled "Inhomogeneous Electron Gas." The importance of DFT is evident in the sharp increase in the number of citations for the Hohenberg and Kohn (HK) paper, as well as for the Kohn-Sham (KS) approach and subsequent corrected methods, as shown in Figure (3.1).

Using DFT to take examples of materials predicted, modeled, or confirmed would be handy. For instance, Raty et al. used DFT to study nanoscale structures like detonation diamonds. They conducted atomic-scale calculations, simulated the temperature evolution of nanometer-sized diamonds, and found that the surfaces rearranged into a graphite-like structure. This led to the formation of 'bucky diamonds'—nanoparticles featuring a diamond core surrounded by a graphitic shell. Their DFT calculations matched experimental X-ray absorption spectra, confirming the presence of bucky diamonds. This example was about the importance of DFT in identifying new materials [337]. Another example is concerning the superconductivity materials. For this group of materials, the foundational BCS theory was established in 1957 by Bardeen, Cooper, and Schrieffer [338]. It explained the general principles of superconductivity but could not calculate superconducting properties like critical temperature using only the atomic number. However, DFT emerged as a powerful method to study conventional superconductors with high accuracy. For example, MgB_2 was discovered to superconduct below 39 K by Nagamatsu et al. in 2001 [339].

As it comes from Figure (3.2), Choi et al. in 2002 [340], using DFT calculations could predict accurately the heat capacity as a function of temperature, which is a key signature of the superconducting states. In the previous two examples, mainly the DFT's ability to understand the behavior of the existing materials was discussed; however, another most significant power is referred to the ability to predict the properties of the materials that have not yet been experimentally fabricated or even not discovered. For instance, Kang et al. modeled developing strategies to increase the battery

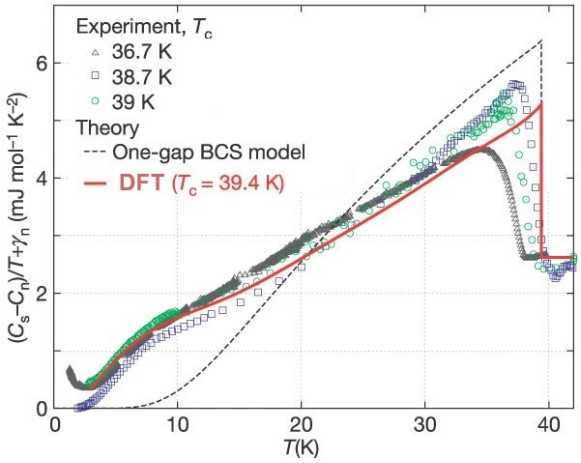

Figure 3.2. The measurements of experimental and DFT for the heat capacity of MgB_2. The graph is from reference [336] with permission from Oxford University Press License ID: 103668). Further reproduction or distribution is not permitted without written permission from the publisher.

electrode's charge and discharge rates using ab initio calculations [341]. Similarly, Greeley et al. used the DFT-based high-throughput screening to find over 700 binary surface alloys for catalytic activity and stability, which identifies BiPt as a superior electrocatalyst for hydrogen evolution and thus had a better performance than pure Pt in experimental tests [342].

The first principle approach, particularly DFT techniques, has a very long history of development. It began in 1964, but before that, there was a lot of effort to make this method better and more efficient. For instance, in 1965, pseudopotentials aimed to replace the complex interactions between electrons and the nucleus were introduced. As depicted in Figure (3.3), this development continued by including relativistic extensions in 1972. Then, in 1979, norm-conserving pseudopotentials were developed, and the Local Density Approximation (LDA) was introduced to find the exchange-correlation functional. Four years later, efforts were made to add the time-dependent part to solve the Schrödinger equation, followed by the introduction of Molecular Dynamic calculations the following year. Quasiparticle corrections for insulators were developed as an essential aspect of first principle calculations in 1986, and the Density Functional Perturbation theory was added a year later. The advancements in the quantum chemistry precision of XC [exchange and correlation energy] were created in 1988. In 1991, the Hubbard correction (DFT+U) was introduced to include Coulomb interactions, an essential correction in DFT. Generalized Gradient Approximation was added to the development of DFT in 1996 to go beyond localized electron density and increase accuracy. During these years, an enormous community effort was made to make better approximations involving many scientists and groups. For instance, in 2001, one of the crucial functionals, Hybrid functionals, was developed. At the time of writing this thesis, there is no universal parameter for the functionals, but recently, the accuracy and efficiency have been drastically increased using Machine Learning. So far, it has proven that Density Functional Theory (DFT) is a powerful tool to study and understand the behavior of materials at a wide range of structures and scales. In addition, this method has received significant citations from prominent scientists, which underlines its popularity. It is worth enumerating some of the reasons for this popularity:

1. **Universality**: DFT is a universal methodology that allows continuous applications in various

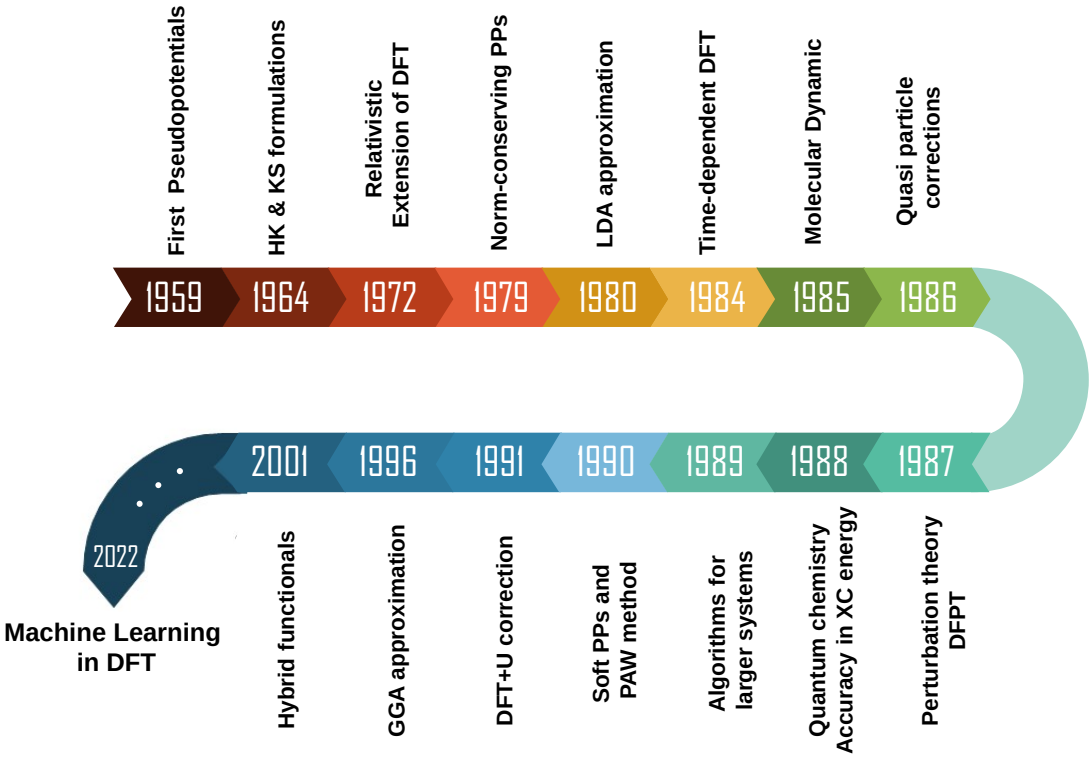

Figure 3.3. Density Functional Theory [DFT] Over Time

materials and avoids additional efforts through transferable expertise.

2. **Scalability**: DFT's ability is not limited to small molecules and ranges from simple structures like H_2 to very complex crystals with a high number of atoms, which helps researchers investigate the varying complexity levels.

3. **Simplicity**: The main equation of DFT, namely the Kohn-Sham one, is intuitive and clear, which connects elementary quantum mechanics to material science by assuming electrons as independent particles.

4. **Accuracy**: In contrast to the simplicity of the Kohn-Sham equations, the DFT is strongly accurate and is trustable to predict material properties, and the obtained results are highly close to the experimental measurements.

5. **Global Collaboration**: The popularity of DFT led to the development of a high standard open-source and commercial software, the creation of many online platforms to share information, and rapid development in terms of new ideas to improve this method.

6. **Good Starting Point**: Even though DFT is strong, it also has some limitations, such as inaccuracies in describing van der Waals interactions, red-shifted optical absorption spectra, and incorrect predictions for some materials like transition metal oxides. However, DFT for the mentioned materials is still valuable as a starting point for more refined calculations, often followed by post-DFT corrections to raise predictive capabilities.

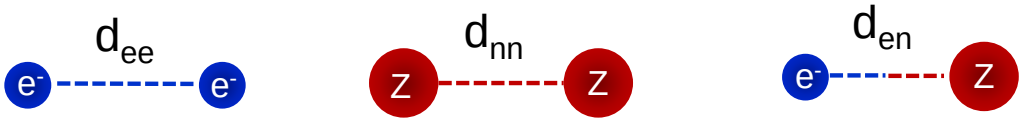

Figure 3.4. Electrostatic interaction between pairs of (d_{ee}) electron–electron, (d_{nn}) nucleus–nucleus, and (d_{en}) electron–nucleus.

Before finishing this section, I would like to mention a significant limitation of Density Functional Theory (DFT): its computational cost and weakness in handling extensive systems. Although one can understand and study the behavior of periodic materials using DFT with relatively high accuracy, for massive systems with a high number of atoms, DFT is still restricted and needs to be reformulated to enable calculations for such systems. At the time of writing this thesis, DFT codes are capable of predicting tens of thousands of atoms with the powerful resources of supercomputers. However, for some materials, such as proteins, millions of atoms are in minimal parts, making it unaffordable to calculate using the DFT method.

3.2 Many-body Schrödinger equation

This section briefly outlines the fundamental ingredients of Density Functional Theory (DFT), beginning with the Coulomb interaction and the formulation of the single - and many-body Schrödinger equations, followed by the main approximations required to make these equations solvable. Finally, the Hartree–Fock and Kohn–Sham formalisms are introduced as the conceptual foundation of DFT.

3.2.1 The Coulomb Interaction

A material system can be regarded as an ensemble of electrons and nuclei interacting through electrostatic forces, which can be symbolically expressed as:

$$\text{Material} = \text{Electrons} + \text{Nuclei}. \tag{3.1}$$

The stability of matter arises from the balance between attractive and repulsive Coulomb forces acting among charged particles. As illustrated in Figure (3.4), the electrostatic energies between different particle pairs separated by a distance d can be written as [343]:

$$E_{ee} = \frac{e^2}{4\pi\epsilon_0 d_{ee}}, \quad E_{nn} = \frac{Z^2 e^2}{4\pi\epsilon_0 d_{nn}}, \quad E_{en} = -\frac{Ze^2}{4\pi\epsilon_0 d_{en}}, \tag{3.2}$$

where e denotes the elementary charge, ϵ_0 is the vacuum permittivity, and Z is the nuclear charge number.

3.2.2 The Schrödinger Equation for Many-Body Systems

To describe the quantum behavior of particles, one must determine their wavefunction $\psi(\vec{r})$, defined at each spatial point $\vec{r} = x\hat{u}_x + y\hat{u}_y + z\hat{u}_z$. This is obtained by solving the time-independent Schrödinger equation [344]:

$$\left(\hat{H}_K + \hat{H}_P\right)\psi = E\psi, \tag{3.3}$$

where $\hat{H}_K$ and $\hat{H}_P$ represent the kinetic and potential energy operators, respectively, and E is the corresponding eigenvalue. The quantity $|\psi(\vec{r})|^2$ gives the probability density of finding the particle at position $\vec{r}$.

For a single electron in an external potential $V(\vec{r})$, the equation takes the form:

$$\left[\frac{\vec{p}^2}{2m_e} + V(\vec{r})\right]\psi(\vec{r}) = E\psi(\vec{r}), \tag{3.4}$$

where m_e is the electron mass and $\vec{P} = -i\hbar\nabla$, with $\nabla = \hat{u}_x\frac{\partial}{\partial x} + \hat{u}_y\frac{\partial}{\partial y} + \hat{u}_z\frac{\partial}{\partial z}$.

In systems containing multiple electrons, the Pauli exclusion principle restricts occupation of identical quantum states, implying that each spatial orbital can host at most two electrons of opposite spin. Consequently, electron–electron interactions modify both the potential $V(\vec{r})$ and the shape of $\psi(\vec{r})$, making the single-particle description insufficient.

For an N-electron, M-nucleus system, the full quantum state is described by a many-body wavefunction:

$$\Psi = \Psi(\vec{r}_1, \vec{r}_2, \ldots, \vec{r}_N; \vec{R}_1, \vec{R}_2, \ldots, \vec{R}_M), \tag{3.5}$$

whose squared modulus represents the probability density of finding electrons and nuclei in a specific configuration. To determine the probability of locating a particular electron (say, electron 1) at position $\vec{r}$, all other degrees of freedom must be integrated out:

$$P(\vec{r}_1 = \vec{r}) = \int |\Psi(\vec{r}, \vec{r}_2, \ldots, \vec{r}_N; \vec{R}_1, \ldots, \vec{R}_M)|^2 \, d\vec{r}_2 \ldots d\vec{r}_N d\vec{R}_1 \ldots d\vec{R}_M. \tag{3.6}$$

The total electron density, obtained by summing over all indistinguishable electrons, is then:

$$n(\vec{r}) = N \int |\Psi(\vec{r}, \vec{r}_2, \ldots, \vec{r}_N; \vec{R}_1, \ldots, \vec{R}_M)|^2 \, d\vec{r}_2 \ldots d\vec{r}_N d\vec{R}_1 \ldots d\vec{R}_M, \tag{3.7}$$

with normalization conditions:

$$\int |\Psi|^2 \, d\vec{r}_1 \ldots d\vec{r}_N d\vec{R}_1 \ldots d\vec{R}_M = 1, \qquad \int n(\vec{r}) \, d\vec{r} = N. \tag{3.8}$$

The total energy of the system is given by:

$$\left(\hat{H}_K + \hat{H}_P\right)\Psi = E_{\text{total}}\Psi, \tag{3.9}$$

where the kinetic energy operator includes contributions from both electrons and nuclei:

$$\hat{H}_K = -\sum_{i=1}^{N} \frac{\hbar^2}{2m_e}\nabla_i^2 - \sum_{I=1}^{M} \frac{\hbar^2}{2M_I}\nabla_I^2, \tag{3.10}$$

with ∇_i^2 acting on the coordinates of the ith particle:

$$\nabla_\alpha^2 \Psi = \frac{\partial^2 \Psi}{\partial x_\alpha^2} + \frac{\partial^2 \Psi}{\partial y_\alpha^2} + \frac{\partial^2 \Psi}{\partial z_\alpha^2}. \tag{3.11}$$

For the potential part, we can refer to the equations (3.2), and with this distinction, we account for all possible charge pairs in the system.

$$V_{ee} = \frac{1}{2} \sum_{i \neq j} \frac{e^2}{4\pi\epsilon_0} \frac{1}{|\vec{r}_i - \vec{r}_j|}; V_{nn} = \frac{1}{2} \sum_{I \neq J} \frac{e^2}{4\pi\epsilon_0} \frac{Z_I Z_J}{|\vec{R}_I - \vec{R}_J|}; V_{en} = -\sum_{i,I} \frac{e^2}{4\pi\epsilon_0} \frac{Z_I}{|\vec{r}_i - \vec{R}_I|}. \tag{3.12}$$

From (3.10), and equations (3.12), the time-independent Schrödinger equation can be rewritten as:

$$\begin{aligned} \Bigg[&- \sum_{i=1}^{N} \frac{\hbar^2}{2m_e} \nabla_i^2 - \sum_{I=1}^{M} \frac{\hbar^2}{2M_I} \nabla_I^2 + \frac{1}{2} \sum_{i \neq j} \frac{e^2}{4\pi\epsilon_0} \frac{1}{|\vec{r}_i - \vec{r}_j|} \\ &+ \frac{1}{2} \sum_{I \neq J} \frac{e^2}{4\pi\epsilon_0} \frac{Z_I Z_J}{|\vec{R}_I - \vec{R}_J|} - \sum_{i,I} \frac{e^2}{4\pi\epsilon_0} \frac{Z_I}{|\vec{r}_i - \vec{R}_I|} \Bigg] \Psi = E_{total} \Psi \end{aligned} \tag{3.13}$$

From the equation (3.13), we almost have all the information to study the behavior of the materials; however, to be more accurate, we need to include the time-dependent Schrödinger part, which we will not discuss, and this thesis results will be enough only for methods with solving the Time-independent Schrödinger equation. It is also noteworthy to mention that by solving the equation (3.13) and finding the lowest energy eigenstates, which, from now on, is called "ground-state" or in the abbreviation "GS" of the system, we can compute a wide range of equilibrium properties of materials, ranging from their elastic properties to enthalpies of formation, thermal characteristics, phase diagrams, and more. Even though solving this equation gives lots of information about the materials, it is very challenging and, in most cases, impossible to solve, even for simple systems. Therefore, some approximations are required to simplify the problem, which we will briefly discuss in the following subsections.

3.2.3 Clamped nuclei approximation

The equation (3.13) is generally very complicated, and as a first step, let us simplify it using atomic units. Accordingly, we introduce the so-called Hartree energy. As mentioned in the first part of this thesis, all the required quantities $\hbar$, m_e, m_p, e, and ϵ_0 are fundamental constants that do not vary with the specific material being considered. The equation (3.13), indeed, doesn't contain any empirical parameters, and all of the parameters are fundamental or can be come with estimation or data fitting procedure. Because of this, the mentioned equation is pointed to a first-principles approach. The electron orbital in the fundamental state of the Hydrogen atom has an average radius $a_0 \simeq 0.529\ A^\circ$. By substituting this value into equation (3.2), the average Coulomb energy (in absolute terms) for an electron-proton pair can be determined as:

$$E_{Ha} = \frac{e^2}{4\pi\epsilon_0 a_0} \tag{3.14}$$

where 'Ha' represents 'Hartree'. Similarly, the Coulomb energy for an electron-electron (e-e) pair and a proton-proton (n-n) pair at the same distance is also E_{Ha}; thus, it can be simplified the size of potential energies in equation (3.13) into the order of E_{Ha}. For the Kinetic energies, one can also use the semi-classical argument. We know the angular momentum in the fundamental form is provided by $m_e v a_0 = \hbar$, where v is the velocity of the electron and, similarly, the balance between the centrifugal force and the nuclear attraction in this orbit necessitates:

$$m_e \frac{v^2}{a_0} = \frac{e^2}{4\pi\epsilon_0 a_0^2} \tag{3.15}$$

It can be seen clearly, by combining the equations (3.14), and (3.15), that:

$$\frac{e^2}{4\pi\epsilon_0 a_0} = \frac{\hbar^2}{m_e a_0^2} \tag{3.16}$$

and it gives:

$$\frac{1}{2} m_e v^2 = \frac{1}{2} E_{Ha} \tag{3.17}$$

which shows that kinetic energy can also be written in the order of Hartree Energy. Thus, it is more convenient to divide every term in the equation (3.13) to the E_{Ha} to have a simplified and natural unit of energy:

(3.18)

$$\left[-\sum_i \frac{1}{2} {a_0}^2 \nabla_i^2 - \sum_I \frac{1}{2(M_I/m_e)} {a_0}^2 \nabla_I^2 + \frac{1}{2} \sum_{i \neq j} \frac{a_0}{|\vec{r}_i - \vec{r}_j|} \right.$$

$$\left. + \frac{1}{2} \sum_{I \neq J} Z_I Z_J \frac{a_0}{|\vec{R}_I - \vec{R}_J|} - \sum_{i,I} Z_I \frac{a_0}{|\vec{r}_i - \vec{R}_I|} \right] \Psi = E_{total}/E_{Ha} \Psi$$

The many-body Schrödinger equation in this form clearly shows that the notation can be significantly simplified by describing energies in units of E_{Ha}, distances in units of a_0, and masses in units of m_e. We use the following units unless we mention others:

$$\begin{gathered} 1 \text{ Ha} = 27.2114 \text{ eV} = 4.3597.\ 10^{-18} \text{ J}, \\ 1 \text{ bohr} = 0.529177 \text{ A} = 0.529177.10^{-10} \text{ m}, \\ 1 \text{ a.u. of mass} = 9.10938291.10^{-31} \text{ kg}, \end{gathered}$$

where 'a.u.' stands for the atomic unit. All of these units together are so-called Hartree atomic units. Therefore, we can use Hartree atomic units for equation (3.18), where four fundamental physical constants are set to 1 (dimensionless) to simplify the equation. They are electron mass (m_e), elementary charge (e), Reduced Planck's constant ($\hbar$), and Coulomb's constant ($\frac{1}{4\pi\epsilon_0}$). Now, we can re-write the equation (3.18) to the simplified version as the following form:

$$\boxed{\left[-\sum_i \frac{\nabla_i^2}{2} - \sum_I \frac{\nabla_I^2}{2M_I} - \sum_{i,I} \frac{Z_I}{|\vec{r}_i - \vec{R}_I|} + \frac{1}{2} \sum_{i \neq j} \frac{1}{|\vec{r}_i - \vec{r}_j|} + \frac{1}{2} \sum_{I \neq J} \frac{Z_I Z_J}{|\vec{R}_I - \vec{R}_J|} \right] \Psi = E_{tot} \Psi} \tag{3.19}$$

The equation (3.19) is more general and almost covers all the materials from gases to liquids to solids. Hence, this means that it is not only highly complicated to solve but also more or less useless. So, we need to start only with solids and molecules. Thus, one can, as a starting point, assume that nuclei are without any motion in known positions [it means they have clamped]. Simply put, according to the high mass of nuclei compared to the electrons, one can temporarily assume no motion for them. Also noteworthy is that the uncertainty principle doesn't allow us to assume nuclei are perfectly immobile in their equilibrium positions, $\Delta_x \Delta_P \geq \hbar$, and it should be taken into account their motion once the electronic structure is determined with concerning only the electrons contributions.

Assuming $M_I \to \infty$, one can simplify the equation (3.19) by setting $\sum_I \frac{1}{2}\frac{\nabla_I^2}{M_I} \cong 0$

$$\left[-\sum_i \frac{\nabla_i^2}{2} - \cancel{\sum_I \frac{\nabla_I^2}{2M_I}} - \sum_{i,I} \frac{Z_I}{|\vec{r}_i - \vec{R}_I|} + \frac{1}{2}\sum_{i\neq j} \frac{1}{|\vec{r}_i - \vec{r}_j|}\right]\Psi = \left[E_{tot} - \frac{1}{2}\sum_{I\neq J} \frac{Z_I Z_J}{|\vec{R}_I - \vec{R}_J|}\right]\Psi \tag{3.20}$$

$$E = E_{tot} - \frac{1}{2}\sum_{I\neq J} \frac{Z_I Z_J}{|\vec{R}_I - \vec{R}_J|} \tag{3.21}$$

Introducing the notation, the equation (3.19) can be rewritten as:

$$\left[-\sum_i \frac{\nabla_i^2}{2} - \sum_{i,I} \frac{Z_I}{|\vec{r}_i - \vec{R}_I|} + \frac{1}{2}\sum_{i\neq j} \frac{1}{|\vec{r}_i - \vec{r}_j|}\right]\Psi = E\Psi \tag{3.22}$$

At this stage, the main term requiring further consideration is the Coulomb interaction between electrons and nuclei. Following the Born–Oppenheimer approximation, the nuclei are assumed to remain fixed in space and thus their coordinates $\vec{R}_I$ act as external parameters, while the many-body wavefunction depends only on the electronic positions, i.e., $\Psi = \Psi(\vec{r}_1, \ldots, \vec{r}_N)$. Under this assumption, the electrostatic potential produced by the nuclei and experienced by an electron at position $\vec{r}$ is written as:

$$V_n(\vec{r}) = -\sum_I \frac{Z_I}{|\vec{r} - \vec{R}_I|}, \tag{3.23}$$

where Z_I denotes the nuclear charge of atom I. This approximation effectively removes explicit dependence on the nuclear coordinates in the electronic Hamiltonian. Consequently, the many-electron Schrödinger equation can be expressed as:

$$\boxed{\left[-\sum_i \frac{\nabla_i^2}{2} + \sum_i V_n(\vec{r}_i) + \frac{1}{2}\sum_{i\neq j} \frac{1}{|\vec{r}_i - \vec{r}_j|}\right]\Psi = E\Psi,} \tag{3.24}$$

which resembles the single-electron time-independent Schrödinger equation (3.4), but now accounts for electron–electron Coulomb repulsion. The total Hamiltonian, expressed in terms of the electronic coordinates, can therefore be written as:

$$\hat{H}(\vec{r}_1, \vec{r}_2, ..., \vec{r}_N)\Psi = \left[-\sum_i \frac{\nabla_i^2}{2} + \sum_i V_n(\vec{r}_i) + \frac{1}{2}\sum_{i\neq j} \frac{1}{|\vec{r}_i - \vec{r}_j|}\right]\Psi = E\Psi \tag{3.25}$$

leading to the many-electron eigenvalue equation:

$$\hat{H}(\vec{r}_1, \vec{r}_2, \ldots, \vec{r}_N)\Psi = E\Psi. \tag{3.26}$$

For comparison, the corresponding single-electron Hamiltonian introduced earlier in Eq. (3.4) can be expressed as:

$$\hat{H}_0 = -\frac{1}{2}\nabla^2 + V_n(\vec{r}). \tag{3.27}$$

The above formulation follows the standard treatment given in Giustino [336]. The equation (3.25) can be rewritten as:

$$\hat{H}(\vec{r}_1, \vec{r}_2, ..., \vec{r}_N)\Psi = \sum_i \left[\hat{H}_0(\vec{r}_i) + \frac{1}{2}\sum_{i\neq j}\frac{1}{|\vec{r}_i - \vec{r}_j|}\right]\Psi = E\Psi, \tag{3.28}$$

and finally, we have:

$$\hat{H}\Psi = E\Psi \tag{3.29}$$

3.2.4 Independent electrons approximation

We need to simplify the equation (3.25), which can be done by independent electron approximation. According to this approximation, electrons are free to move inside the fixed potential that the clamped nuclei have generated. Simply put, it means the electrons don't see each other, and by ignoring the interactions between electrons, this approximation reduces the issue's complexity to one that involves only one electron and an effective potential.

$$\sum_i \hat{H}_0(\vec{r}_i)\Psi = E\Psi, \tag{3.30}$$

and in light of the independence of electrons, the probability $|\Psi(\vec{r}_1, \vec{r}_2, ..., \vec{r}_N)|^2$ must given by the individual probability of each electron in their specified positions using $|\phi_i(\vec{r}_i)|^2$. At this point, we still don't know the function of ϕ; however, we guess it should be written as the solution of equation (3.30) as a product of individual ϕ:

$$|\Psi(\vec{r}_1, \vec{r}_2, ..., \vec{r}_N)|^2 = |\phi_1(\vec{r}_1)|^2.|\phi_2(\vec{r}_2)|^2. \ldots .|\phi_N(\vec{r}_N)|^2 = |\phi_1(\vec{r}_1).\phi_2(\vec{r}_2). \ldots .\phi_N(\vec{r}_N)|^2 \tag{3.31}$$

$$\Psi(\vec{r}_1, \vec{r}_2, ..., \vec{r}_N) = \phi_1(\vec{r}_1).\phi_2(\vec{r}_2). \ldots .\phi_N(\vec{r}_N) \tag{3.32}$$

For the Schrodinger equation in a single electron case, we can write the solution as:

$$\hat{H}_0(\vec{r})\phi_i(\vec{r}) = \epsilon_i\phi_i(\vec{r}), \tag{3.33}$$

where ϵ_1 is the smallest eigenvalues obtained from it, and ϵ_N is the biggest one ($\epsilon_1 < \epsilon_2 < ... < \epsilon_N$). Now, we should write it for simplified many electrons equation of (3.30).

$$\left[\sum_i \hat{H}_0(\vec{r}_i)\right]\phi_1(\vec{r}_1)...\phi_N(\vec{r}_N) = E\phi_1(\vec{r}_1)...\phi_N(\vec{r}_N), \tag{3.34}$$

Since single electron of
$\hat{H}_0(\vec{r}_1)$ acts only on the function of $\phi_1(\vec{r}_1)$,
$\hat{H}_0(\vec{r}_2)$ acts only on the function of $\phi_2(\vec{r}_2)$,
...
$\hat{H}_N(\vec{r}_N)$ acts only on the function of $\phi_N(\vec{r}_N)$. Therefore, we can rewrite the equation as follows:

$$\left[\hat{H}_0(\vec{r}_1)\phi_1(\vec{r}_1)\right]\phi_2(\vec{r}_2)\phi_3(\vec{r}_3)...\phi_N(\vec{r}_N) + \left[\hat{H}_0(\vec{r}_2)\phi_2(\vec{r}_2)\right]\phi_1(\vec{r}_1)\phi_3(\vec{r}_3)...\phi_N(\vec{r}_N) + ... \tag{3.35}$$

$$+ \left[\hat{H}_0(\vec{r}_N)\phi_N(\vec{r}_N)\right]\phi_1(\vec{r}_1)\phi_2(\vec{r}_2)...\phi_{N-1}(\vec{r}_{N-1}) = E\phi_1(\vec{r}_1)...\phi_N(\vec{r}_N)$$

And also we know:

$$\hat{H}_0(\vec{r}_i)\phi_i(\vec{r}_i) = \epsilon_i\phi_i(\vec{r}_i)$$

and for instance we have for the first electron

$$\hat{H}_0(\vec{r}_1)\phi_1(\vec{r}_1) = \epsilon_1\phi_1(\vec{r}_1)$$

and therefore, we can rewrite the equation (3.35) as follows:

$$\epsilon_1\phi_1(\vec{r}_1)\phi_2(\vec{r}_2)...\phi_N(\vec{r}_N) + \phi_1(\vec{r}_1)\epsilon_2\phi_2(\vec{r}_2)...\phi_N(\vec{r}_N) + ... = E\phi_1(\vec{r}_1)\phi_2(\vec{r}_2)...\phi_N(\vec{r}_N) \tag{3.36}$$

and finally,

$$E = \epsilon_1 + \epsilon_2 + ... + \epsilon_N \tag{3.37}$$

The obtained results show that the configuration with the lowest energy of the system is achieved by filling the lowest-energy eigenstates of the single-particle equation (equation (3.4)) with one electron per state, beginning with the lowest eigenvalues. In the following sections, we will call it the ground state of the energy. This aligns with our expectations of the solid-state physics [345]. Even though, We solved the equation (3.25) using independent electron approximation, however, there are two important weaknesses we cannot ignore. Firstly, according to Pauli's exclusion principle, the Ψ should change sign whenever two electron's sign is exchanged (e.g., swapping the r_1, and r_2), which equation (3.32) doesn't have that. The second one relates to the fact that the Coulomb term has been eliminated from the main equation (3.19), which should be addressed.

Exclusion Principle

The exclusion principle remarks that according to electrons being "fermions," the wavefunction for the many-body system (i.e., Ψ) should be changed in case of exchanging any electron variables. While the variable exchange is about both the position and the spin of electrons, one can, for simplicity, ignore the spin and conclude that two electrons cannot occupy the same electron state. Consider the following simple example: if we have two electrons, the wavefunction $\phi_1(\vec{r}_1)\phi_2(\vec{r}_2)$ with $\phi_1 \neq \phi_2$ doesn't satisfy this requirement; therefore, we cannot use equation (3.32). However, the wavefunction:

$$\Psi(\vec{r}_1, \vec{r}_2) = \frac{1}{\sqrt{2}}\left[\phi_1(\vec{r}_1)\phi_2(\vec{r}_2) - \phi_1(\vec{r}_2)\phi_2(\vec{r}_1)\right] \tag{3.38}$$

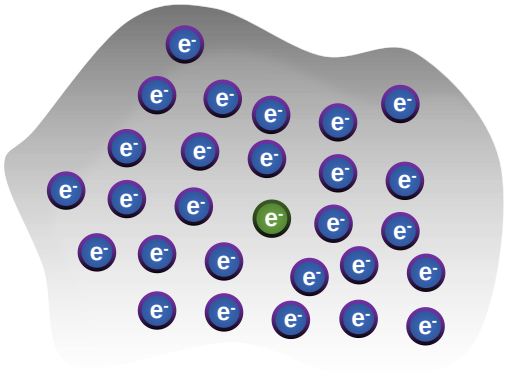

Figure 3.5. Schematic picture of how the other electrons interact with a single electron in average in the mean-filed approximation.

By direct substitution, one can find the $\Psi(\vec{r}_2, \vec{r}_1) = -\Psi(\vec{r}_1, \vec{r}_2)$. If we replace it in equation (3.30), the total energy ($E = \epsilon_1 + \epsilon_2$) comes from the terms on the right-handed side of the equation (3.38). Hence, all the linear combinations of such terms are also good solutions for the same energy. One can write the equation (3.38) by using a matrix determinate:

$$\Psi(\vec{r}_1, \vec{r}_2) = \frac{1}{\sqrt{2}} \begin{bmatrix} \phi_1(\vec{r}_1) & \phi_1(\vec{r}_2) \\ \phi_2(\vec{r}_1) & \phi_2(\vec{r}_2) \end{bmatrix}, \tag{3.39}$$

which is Slater determinant. We can construct this Slater determined for more electrons with this difference that we will have long rows and columns, and also the prefactor will change to $N!^{\frac{-1}{2}}$ for $N > 2$, to have the function correctly normalized: $\int |\Psi|^2 d\vec{r}_1 \dots d\vec{r}_N = 1$.

3.2.5 Mean-field Approximation

Until now, to solve the Schrodinger equation, we assumed a clamped nucleus approximation, i.e., the nuclei are not moving, and we can neglect their motion by putting zero for the terms of kinetic energy as well as the Coulomb interaction between electrons and nuclei. Next, we simplified the equation with the independent electron approximation, but in this case, we had inaccurate results. Therefore, the Mean-field Approximation can step in to avoid these drawbacks and limitations. According to the figure (3.5), one can assume many other electrons surround one electron. In such a case, instead of dealing with the complicated interactions of each electron individually, we approximate their collective influence as an averaged interaction, which is called Mean-field Approximation. Simply put, we are looking for the average influence of all other electrons on a single electron, and this is mathematically represented by "effective or Hubbard potential."

So, the question now arises as to whether a single-particle description can be maintained while incorporating the Coulomb repulsion in some manner. For a few moments, we can go to classical physics, and we know that a distribution of electronic charge, $n(\vec{r})$, will generate an electrostatic potential $\phi(\vec{r})$ through Poisson's equation [346]:

$$\nabla^2 \phi(\vec{r}) = 4\pi n(\vec{r}) \tag{3.40}$$

In Hartree units, all electrons within this electrostatic potential have potential energy given by $V_H(\vec{r}) = -\phi(\vec{r})$, named the 'Hartree Potential.' So, we have:

$$\nabla^2 V_H(\vec{r}) = -4\pi n(\vec{r}), \tag{3.41}$$

and from [346], we know the general solution for this equation is:

$$V_H(\vec{r}) = \int d\vec{r}\,' \, \frac{n(\vec{r}\,')}{|\vec{r} - \vec{r}\,'|}, \tag{3.42}$$

which indicates that in the infinitezimal volume $d\vec{r}\,'$ we have a charge $dQ = -n(\vec{r}\,')\, d\vec{r}\,'$, which causes a Coulomb potential at point $\vec{r}$ given by $\frac{dQ}{|\vec{r}-\vec{r}\,'|}$. As every electron in the system has the Hartree potential, we can rewrite the equation (3.33) as follows:

$$\left[-\frac{\nabla^2}{2} + V_n(\vec{r}) + V_H(\vec{r})\right] \phi_i(\vec{r}) = \epsilon_i \phi_i(\vec{r}) \tag{3.43}$$

$$n(\vec{r}) = \sum_i |\phi_i(\vec{r})|^2 \tag{3.44}$$

$$\nabla^2 V_H(\vec{r}) = -4\pi n(\vec{r}). \tag{3.45}$$

So, the new thing compared to the equation (3.33) is that now we have the Hartree potential in the Hamiltonian, and we included the Coulomb repulsion between electrons as well. Because the potential V_H represents the average potential felt by each electron, this method is referred to as the 'Mean-Field Approximation. In this formalism, we decreased the dimensions of the complicated 3N Schrodinger equation to N three-dimensional equations. To solve this, however, we need to calculate the equations (3.43) to (3.45) simultaneously, and they are so-called self-consistent calculations. Even though we have solutions using this method, the results lack sufficient accuracy for conducting quantitative studies of materials at the atomic scale. To solve this issue, we should include the elements of the theory, i.e., "exchange and correlation" potentials, which can be obtained through the integration from the equation (3.43) to (3.45), and we discuss it in details in next sections.

3.2.6 Beyond the Mean-filed approximation (Hartee-Fock approximation)

From the above follows, that if we ignore the electron's interactions with the Coulomb repulsion, the many-body wavefunction can be written as a Slater determinate, and single-particle Ψ can be found as the solutions of a simpler single-particle Schrodinger equation. We're ready to move on to improve it for the following reasons:
1- Even though the electrons' interactions are not too strong, they still interact. Therefore, it is still possible to seek a solution in the form of a Slater determinant. It means we need to find the $\phi_i(\vec{r}_i)$ in the equation (3.39) and it can be done using the 'Variational Principle'. This principle is a way of finding the best solution for one problem. This helps us to find or choose the option that gives the most favorable results: the shortest path, the lowest energy, etc. Let's think of the lowest energy of quantum state Ψ. The energy is coming as follows:

$$\hat{H}\Psi = E\Psi \rightarrow \int d\vec{r}_1 ... d\vec{r}_N \, \Psi^* \hat{H} \Psi = \int d\vec{r}_1 ... d\vec{r}_N \Psi^* E \Psi, \tag{3.46}$$

and we know $\int \Psi^* \Psi \, d\vec{r}_1 ... d\vec{r}_N = 1$; so we will have $E = \int d\vec{r}_1 ... d\vec{r}_N \, \Psi^* \hat{H} \Psi$ and we can rewrite it in Dirac notation:

$$E =< \Psi | \hat{H} | \Psi > . \tag{3.47}$$

It can be shown in detail, but we skip it here if we minimize E to the variations of the function $\phi_i(\vec{r})$ in the Slater determinate, it requires to have the orthonormal functions:

$$\frac{\partial E}{\partial \phi_i^*} = 0 \; ; \; \int \phi_i^*(\vec{r}) \phi_j(\vec{r}) \, d\vec{r} = \delta_{ij} \text{ where } \begin{bmatrix} = 1; & i = j \\ = 0; & i \neq j \end{bmatrix} \tag{3.48}$$

(where δ_{ij} is the Kronecker delta and is equal to 1 if $i = j$, 0 if $i \neq j$) and we obtained so-called Hartree-Fock equations [347]:

$$\left[-\frac{\nabla^2}{2} + V_n(\vec{r}) + V_H(\vec{r}) \right] \phi_i(\vec{r}) + \int d\vec{r}' \, V_X(\vec{r}, \vec{r}') \phi_i(\vec{r}') = \epsilon_i \phi_i(\vec{r}), \tag{3.49}$$

$$n(\vec{r}) = \sum_i |\phi_i(\vec{r})|^2, \tag{3.50}$$

$$\nabla^2 V_H(\vec{r}) = -4\pi n(\vec{r}). \tag{3.51}$$

If the above equations are compared with the equations (3.43) to (3.45), it can be figured out that there is an additional term, V_X:

$$V_X(\vec{r}, \vec{r}') = -\sum_j \frac{\phi_j^*(\vec{r}') \phi_j(\vec{r})}{|\vec{r} - \vec{r}'|}, \tag{3.52}$$

Two important points should be emphasized in the above equation:

- In the $V_X(\vec{r}, \vec{r}')$, we have supposed the same spins for electrons.
- $\sum_j$, this sum is over the occupied single-particle states.

Now, we are encountering two good and bad points for the Hartree-Fock equations: The former is that we could move from the "Classical" electrons in the Mean-Field approximation to the "Quantum" electrons here. The latter is that the current modifications introduce the non-local potential $V_X(\vec{r}, \vec{r}')$ in the single particle equations. The non-local potential means that electrons are not classical and like balls and they are wave-functions, these wave-functions depend not only on their position (e.g., at $\vec{r}$) but also on extra things like other electron's positions, which we call for instance at $\vec{r}_0$. So, the behavior of one electron not only depends on its position at $\vec{r}$ but also depends on another electron at $\vec{r}_0$ due to the Pauli exclusion principle. Remember, in this principle, the electrons are not allowed to be in the same state, and they move, and this move affects each other elections. This leads to a special interaction called "Fock exchange potential," which considers all electrons together (For more details about the derivation of equation (3.49), see Appendix A from the book [336]).

> **Why do we say "exchange"?** The origin of using the Hartree potential and, subsequently, Hartree-Fock potential was the fact that, when we exchanged the position of the electrons, the wave function was not changed, which, according to Pauli's exclusion principle, was wrong, and we had to consider it. In mean-field approximation (Hartree),

we included it, but it was only for the classical particles, and it was still not accurate. Hence, we used the Hartree-Fock method and used the Fock exchange potential to consider this issue.

3.2.7 Kohn–Sham equations

To summarize once more, we first replaced the full electron–electron interaction by an effective independent–particle description, thereby reducing the $3N$-dimensional many-electron problem to a set of one-electron equations. Next, we reintroduced the classical Coulomb repulsion through the Hartree potential, and accounted for the fermionic nature of electrons by including exchange effects. The remaining ingredient is the electron correlation, i.e., the residual many-body interaction beyond classical electrostatics and exchange. Because repulsion and the Pauli principle suppress the probability of finding two electrons near one another, this correlation cannot be neglected.

It is therefore convenient to augment the single-particle potential by a correlation term. Using a local representation for exchange (to avoid the nonlocal Fock operator), we write the one-electron equation as

$$\left[-\frac{\nabla^2}{2} + V_n(\vec{r}) + V_H(\vec{r}) + V_x(\vec{r}) + V_c(\vec{r})\right] \phi_i(\vec{r}) = \epsilon_i \, \phi_i(\vec{r}), \tag{3.53}$$

where

Recall (1): $V_n(\vec{r}) = -\sum_I \dfrac{Z_I}{|\vec{r} - \vec{R}_I|}$ (electron–nucleus Coulomb potential),

Recall (2): $\nabla^2 V_H(\vec{r}) = -4\pi \, n(\vec{r}), \qquad n(\vec{r}) = \sum_i |\phi_i(\vec{r})|^2,$

Recall (3): $V_H(\vec{r})$ (classical), $\qquad V_x(\vec{r})$, $V_c(\vec{r})$ (quantum contributions).

This heuristic route motivates the Kohn–Sham framework: the interacting system is mapped onto an auxiliary noninteracting system that reproduces the same ground-state density, while all many-body effects beyond the Hartree term are absorbed into an exchange–correlation (XC) potential. Details of the Kohn–Sham construction and the practical XC approximations used in this thesis are discussed in the following subsections.

3.3 Density Functional Theory (DFT)

In this section we address three questions:

1. How is the single-particle description, $\{\phi_i\}$, related to the many-body wavefunction Ψ?
2. Which equations do the orbitals ϕ_i satisfy?
3. How is the total energy E in Eq. (3.24) determined?

Density Functional Theory provides a unified answer to these questions within the Hohenberg–Kohn and Kohn–Sham formalisms.

3.3.1 Total energy of the electronic ground state

From the previous section,

$$E \;=\; \langle \Psi \mid \hat{\mathcal{H}} \mid \Psi \rangle \;=\; \int d\vec{r}_1 \ldots d\vec{r}_N \, \Psi^*(\vec{r}_1, \ldots, \vec{r}_N) \, \hat{\mathcal{H}} \, \Psi(\vec{r}_1, \ldots, \vec{r}_N), \tag{3.54}$$

with Hamiltonian

$$\hat{\mathcal{H}}(\vec{r}_1, \ldots, \vec{r}_N) = -\sum_i \frac{1}{2}\nabla_i^2 + \sum_i V_n(\vec{r}_i) + \frac{1}{2}\sum_{i \neq j} \frac{1}{|\vec{r}_i - \vec{r}_j|}. \tag{3.55}$$

The operator $\hat{\mathcal{H}}$ has the same form for all electronic systems; differences in material properties arise through the quantum state Ψ. In this sense, the energy is a functional of the many-body wavefunction,

$$E \;=\; \mathcal{F}[\Psi]. \tag{3.56}$$

The central result of DFT (Hohenberg–Kohn) is that, for the ground state, the total energy can be written as a functional of the electron density $n(\vec{r})$ alone:

$$E \;=\; \mathcal{F}[n]. \tag{3.57}$$

This is profoundly advantageous: whereas $\Psi(\vec{r}_1, \ldots, \vec{r}_N)$ depends on $3N$ variables, the density $n(\vec{r})$ depends only on three spatial variables, yet it suffices to determine the ground-state energy and observables that are functionals of n. (Excited states, in general, require information beyond the ground-state density and are not treated here.)

Summary

Ground state: $n(\vec{r}) \xrightarrow{\mathcal{F}} E, \qquad E = \mathcal{F}[n(\vec{r})].$

Excited states: $\Psi(\vec{r}_1, \ldots, \vec{r}_N) \xrightarrow{\mathcal{F}} E, \qquad E = \mathcal{F}[\Psi(\vec{r}_1, \ldots, \vec{r}_N)].$

3.3.2 Hohenberg–Kohn theorem

The foundation of Density Functional Theory rests on the Hohenberg–Kohn (HK) theorem, which establishes the central role of the electron density in determining the properties of a many-electron system. In its general form, the theorem can be expressed through three fundamental statements:

1. **Uniqueness:** The ground-state electron density $n(\vec{r})$ uniquely determines the external potential $V_n(\vec{r})$ (up to an additive constant). Consequently, all properties of the system, including the total energy, are unique functionals of $n(\vec{r})$; that is, $n \to V_n \to \Psi \to E$.
2. **Existence:** For a given external potential $V_n(\vec{r})$, there exists a corresponding many-body wavefunction Ψ that describes the ground state of the system.
3. **Variational principle:** Among all possible electron densities $n(\vec{r})$, the correct ground-state density minimizes the total energy functional. The true physical configuration is therefore the one that yields the lowest possible energy.

Combining these premises gives the general relationship

$$n(\vec{r}) \;\Rightarrow\; V_n(\vec{r}) \;\Rightarrow\; \Psi(\vec{r}_1,\ldots,\vec{r}_N) \;\Rightarrow\; E[n(\vec{r})],$$

or equivalently,

$$E = \mathcal{F}[n(\vec{r})],$$

where $\mathcal{F}$ represents a universal functional.

In essence, the HK theorem states that a quantum system can be completely characterized by its electron density rather than by its many-body wavefunction. This allows one to avoid the explicit solution of the full Schrödinger equation, focusing instead on $n(\vec{r})$ as the fundamental variable.

Proof outline. Among the three statements, the first—uniqueness of the mapping between $n(\vec{r})$ and $V_n(\vec{r})$—is the key nontrivial part and can be demonstrated by contradiction.

Let the kinetic and electron–electron interaction operators be:

$$\hat{T} = -\sum_i \frac{\nabla_i^2}{2}, \qquad \hat{W} = \frac{1}{2}\sum_{i\neq j} \frac{1}{|\vec{r}_i - \vec{r}_j|}.$$

Then the total energy is

$$E = \langle\Psi|\hat{H}|\Psi\rangle = \left\langle\Psi\middle|\sum_i V_n(\vec{r}_i)\middle|\Psi\right\rangle + \langle\Psi|\hat{T}+\hat{W}|\Psi\rangle. \tag{3.58}$$

Using Eq. (3.7), the expectation value can be rewritten in terms of the electron density:

$$E = \int n(\vec{r})\, V_n(\vec{r})\, d\vec{r} + \langle\Psi|\hat{T}+\hat{W}|\Psi\rangle. \tag{3.59}$$

Now, assume that two different external potentials, $V_n(\vec{r})$ and $V_n'(\vec{r})$, lead to the same ground-state electron density $n(\vec{r})$ but different ground-state wavefunctions Ψ and Ψ', with energies E and E', respectively.

Since Ψ is not the ground state of $\hat{H}'$, the Rayleigh–Ritz variational principle gives:

$$\langle\Psi|\hat{H}'|\Psi\rangle > E'. \tag{3.60}$$

Expanding the expectation value using Eq. (3.59),

$$\langle\Psi|\hat{T}+\hat{W}|\Psi\rangle + \int n(\vec{r}) V_n'(\vec{r})\, d\vec{r} > E'. \tag{3.61}$$

Subtracting the corresponding expression for E yields:

$$E - E' > \int n(\vec{r})\,[V_n(\vec{r}) - V_n'(\vec{r})]\, d\vec{r}. \tag{3.62}$$

Repeating the argument with primed and unprimed quantities exchanged gives:

$$E' - E > \int n(\vec{r})\,[V_n'(\vec{r}) - V_n(\vec{r})]\, d\vec{r}. \tag{3.63}$$

Adding the two inequalities leads to $0 > 0$, which is impossible. Thus, our initial assumption-that two distinct potentials produce the same ground-state density—is false. Therefore, the mapping between $n(\vec{r})$ and $V_n(\vec{r})$ is unique.

3.3.3 Kohn–Sham equations

The Hohenberg–Kohn framework guarantees that the ground–state energy can be written as a functional of the density $n(\vec{r})$, but it does not provide the functional in closed form. In practice, one proceeds by introducing the Kohn–Sham (KS) construction, which replaces the interacting system with an auxiliary noninteracting one chosen to reproduce the same ground-state density.

Comparing Eqs. (3.57) and (3.59), the *universal* functional can be defined as

$$\mathcal{F}[n] \;=\; \min_{\Psi \to n} \big\langle \Psi \big| \hat{T} + \hat{W} \big| \Psi \big\rangle, \tag{3.64}$$

so that the total energy reads

$$E[n] \;=\; \mathcal{F}[n] \;+\; \int n(\vec{r})\, V_n(\vec{r})\, d\vec{r}. \tag{3.65}$$

Kohn and Sham split $\mathcal{F}[n]$ into contributions that are convenient to evaluate plus a remainder:

$$\mathcal{F}[n] \;=\; T_s[n] \;+\; E_H[n] \;+\; E_{xc}[n], \tag{3.66}$$

where

$$T_s[n] = -\frac{1}{2} \sum_i \int \phi_i^*(\vec{r})\, \nabla^2\, \phi_i(\vec{r})\, d\vec{r}, \tag{3.67}$$

$$E_H[n] = \frac{1}{2} \iint \frac{n(\vec{r})\, n(\vec{r}\,')}{|\vec{r} - \vec{r}\,'|}\, d\vec{r}\, d\vec{r}\,', \tag{3.68}$$

and $E_{xc}[n]$ gathers *all* many–body effects not included in T_s and E_H (namely, exchange, correlation, and the difference between the true kinetic energy and T_s). The total energy functional becomes

$$E[n] \;=\; T_s[n] \;+\; \int n(\vec{r})\, V_n(\vec{r})\, d\vec{r} \;+\; E_H[n] \;+\; E_{xc}[n]. \tag{3.69}$$

Minimization of $E[n]$ with respect to n under the constraints of orthonormal orbitals $\{\phi_i\}$ and the density relation

$$n(\vec{r}) \;=\; \sum_i f_i\, |\phi_i(\vec{r})|^2, \tag{3.70}$$

leads (via Euler–Lagrange equations with Lagrange multipliers $\{\epsilon_i\}$) to the KS single–particle equations:

$$\left[\underbrace{-\frac{1}{2}\nabla^2}_{\textbf{Kinetic Energy}} \;+\; \underbrace{V_n(\vec{r})}_{\textbf{external nuclear potential}} \;+\; \underbrace{V_H(\vec{r})}_{\textbf{Hartree potential}} \;+\; \underbrace{V_{xc}(\vec{r})}_{\textbf{xc potential}} \right] \phi_i(\vec{r}) = \epsilon_i\, \phi_i(\vec{r}), \tag{3.71}$$

with the Hartree and exchange–correlation potentials defined by the functional derivatives

$$V_H(\vec{r}) = \frac{\delta E_H[n]}{\delta n(\vec{r})} = \int \frac{n(\vec{r}\,')}{|\vec{r}-\vec{r}\,'|}\, d\vec{r}\,', \qquad \text{equivalently } \nabla^2 V_H(\vec{r}) = -4\pi n(\vec{r}), \tag{3.72}$$

$$V_{xc}(\vec{r}) = \frac{\delta E_{xc}[n]}{\delta n(\vec{r})}. \tag{3.73}$$

Equations (3.71) must be solved self–consistently: starting from a trial density, one builds V_H and V_{xc}, solves the KS equations for $\{\phi_i\}$, updates $n(\vec{r})$, and iterates until convergence. The scheme is formally exact if the exact $E_{xc}[n]$ were known; in practice, E_{xc} is approximated (e.g., LDA, GGA, meta–GGA, hybrids), and the specific choices used in this thesis are detailed in the next subsection (see also Giustino [336]). Before going to the next section and discussing the approximations, I quote a related part of Kohn's Nobel Prize lecture in 1993:

> The Kohn-Sham theory may be regarded as the formal exactification of Hartree's theory. With the exact E_{xc} and V_{xc}, all many-body effects are, in principle, included. This directs attention to the functional $E_{xc}[n]$. The practical usefulness of ground-state DFT depends entirely on whether approximations for the functional $E_{xc}[n]$ could be found, which are at the same time sufficiently simple and sufficiently accurate.
> The text adapted from the Walter Kohn's Nobel lecture in 1999 - www.nobelprize.org

3.3.4 Exchange-correlation energy

Although the Kohn–Sham formulation provides an exact framework in principle, its practical implementation depends critically on the explicit form of the exchange–correlation (XC) functional $E_{xc}[n]$, which remains unknown. Accurate determination of the ground-state energy and density thus relies on approximate forms of this functional. Among these, the Local Density Approximation (LDA) and the Generalized Gradient Approximation (GGA) are the most widely used.

Local Density Approximation (LDA)

In the LDA, the exchange–correlation energy density at each spatial point is assumed to depend solely on the local value of the electron density. This approximation is conceptually simple, replacing the full nonlocal dependence with a local relation derived from the homogeneous electron gas (HEG) model.

Exchange and correlation in the homogeneous electron gas. For a uniform electron gas, the exchange energy per unit volume is analytically known [348, 349]:

$$E_x = -\frac{3}{4}\left(\frac{3}{\pi}\right)^{1/3} \int n^{4/3}(\vec{r})\, d\vec{r}. \tag{3.74}$$

The correlation energy, representing many-body interactions beyond exchange, is obtained numerically–commonly from Quantum Monte Carlo simulations [350] or parameterizations such as Perdew and Wang (1992) [351].

Application to real systems. Although real materials are not homogeneous, LDA assumes that the system can be divided into small regions where $n(\vec{r})$ varies slowly, treating each region as locally uniform. The total XC energy is then integrated over space:

$$E_{xc}^{\mathrm{LDA}}[n] = \int E_{xc}^{\mathrm{HEG}}[n(\vec{r})]\, d\vec{r}, \tag{3.75}$$

where E_{xc}^{HEG} denotes the exchange–correlation energy density of a homogeneous electron gas at density $n(\vec{r})$. The corresponding potential, used in the Kohn–Sham equations, is the functional derivative:

$$V_{xc}(\vec{r}) = \frac{\delta E_{xc}[n]}{\delta n(\vec{r})}. \tag{3.76}$$

For spin-polarized systems, the extension known as the Local Spin Density Approximation (LSDA) employs spin-dependent densities:

$$E_{xc}^{\mathrm{LSDA}}[n_\uparrow, n_\downarrow] = \int n(\vec{r})\, E_{xc}\big(n_\uparrow(\vec{r}), n_\downarrow(\vec{r})\big)\, d\vec{r}. \tag{3.77}$$

The LDA performs well for systems with nearly uniform charge densities but becomes less accurate when the density varies rapidly in space [348, 349, 352, 353].

Generalized Gradient Approximation (GGA)

To improve upon LDA, the Generalized Gradient Approximation incorporates not only the local density but also its spatial gradient, allowing a better description of inhomogeneous systems:

$$E_{xc}^{\mathrm{GGA}}[n] = \int n(\vec{r})\, E_{xc}\big(n(\vec{r}), \nabla n(\vec{r})\big)\, d\vec{r}. \tag{3.78}$$

For spin-polarized systems, this generalizes to:

$$E_{xc}^{\mathrm{SGGA}}[n_\uparrow, n_\downarrow] = \int n(\vec{r})\, E_{xc}\big(n_\uparrow, n_\downarrow, \nabla n_\uparrow, \nabla n_\downarrow\big)\, d\vec{r}. \tag{3.79}$$

The GGA family provides improved accuracy for a broad range of materials, from molecules to solids. Notable examples include Becke's exchange [354], the Lee–Yang–Parr correlation [355], and the Perdew–Burke–Ernzerhof (PBE) functional [356], the latter being one of the most widely adopted for solid-state and surface calculations. In this thesis, all density functional calculations were performed using the GGA–PBE approximation, which provides reliable results for two-dimensional materials [357].

3.3.5 Self-consistent field (SCF) procedure

In the preceding sections, we introduced the basic principles of Density Functional Theory and the Kohn–Sham (KS) equations, which in principle allow one to determine the total energy E and the ground-state electron density $n(\vec{r})$ of a material. The remaining question is how these equations are solved in practice. This is achieved through an iterative process known as the self-consistent field (SCF) cycle.

As illustrated schematically in Figure (3.6), the procedure begins with the external potential $V_n(\vec{r})$ originating from the atomic nuclei. A trial electron density $n^{(0)}(\vec{r})$ is then assumed, from which the corresponding Hartree and exchange–correlation potentials, $V_H(\vec{r})$ and $V_{xc}(\vec{r})$, are constructed. Together with $V_n(\vec{r})$, these define the total potential,

$$V_{\text{tot}}(\vec{r}) = V_n(\vec{r}) + V_H(\vec{r}) + V_{xc}(\vec{r}).$$

The KS equations are then solved as a single-particle eigenvalue problem:

$$\hat{H}_{\text{KS}}\,\phi_i(\vec{r}) = \epsilon_i\,\phi_i(\vec{r}),$$

yielding a set of orbitals $\{\phi_i\}$ and eigenvalues $\{\epsilon_i\}$. From the resulting orbitals, a new electron density is obtained via

$$n^{(1)}(\vec{r}) = \sum_i |\phi_i(\vec{r})|^2.$$

The newly computed density $n^{(1)}(\vec{r})$ is compared with the previous input $n^{(0)}(\vec{r})$. If the difference between successive iterations is within a specified tolerance (called Energy Tolerance), self-consistency is reached, and the ground-state density $n_0(\vec{r})$ is established. Otherwise, a new density–typically a linear combination of the old and new ones–is constructed, and the process is repeated until convergence. Once the SCF cycle converges, the total ground-state energy and related quantities can be evaluated. These results then serve as the starting point for the calculation of other material properties, such as band structures, forces, and vibrational spectra.

3.3.6 Limitations of the Density Functional Theory (DFT)

Even though we count lots of advantages for the DFT in materials behavior prediction, some limitations originated mainly from the exchange and correlation energy part. Some of them are listed in the following:

1. **Exchange-Correlation Functional Approximation:** After working a long time and lots of effort on making this more accurate term, there is still no universe and exact form of it, and it only relies on the approximations such as we have already discussed in the previous subsection. These approximations make the results inaccurate, and this is especially important when the systems include atoms with strong electron correlations like transition metals or rare-earth elements.
2. **Bandgap underestimation:** Pure DFT for the semiconductors and insulators underestimate the energy bandgap because KS equations do not include the true excitation energies and only are for the ground state energies. There are some advanced methods, such as GW or hybrid functional or DFT+U correction, which are needed in energy band gap predictions. In

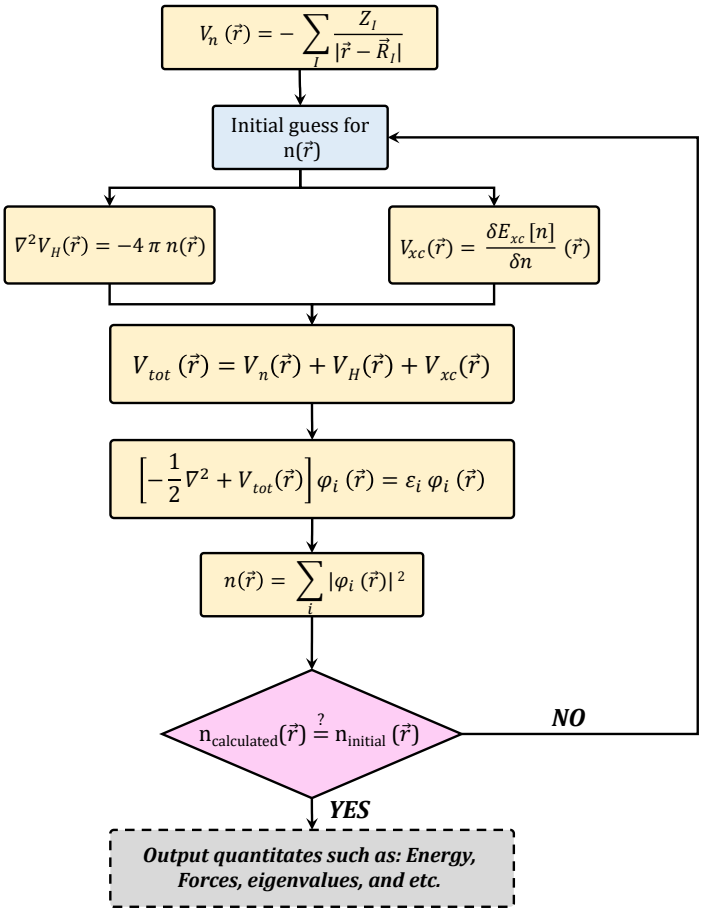

Figure 3.6. The schematic flowchart of the SCF procedure.

the next section, we briefly mention some of these approaches.

3. **van der Waals interaction:** In this thesis, we have worked on the Molecular structures and layered heterostructures, which include the weak van der Waals interactions, which in typical DFT is not considered. In the next section, we will address some of these corrections, such as DFTD2 and D3 corrections.

4. **Charge Transfer and Excited states:** As we have already discussed, DFT works basically on the ground-state energy, and when the systems have significant charge transfer or excited states, this is not captured very well. In this thesis, we have some results from the Magnons. We used the DFT and Heisenberg Hamiltonian to include the small excitation of the materials. We will describe the formulas in short in the following sections.

5. **Computational scaling:** Despite efficient approaches, DFT still struggles with extensive systems, complex surfaces, or even when using advanced functionals.

From the above list, we can conclude that the DFT has some limitations, and it is not an exact and universal utility to calculate the properties of materials, but still, it is a perfect starting point in

calculations. For instance, one can use DFT to predict the basic form of properties and, using some advanced techniques, correct the DFT and find more reliable results.

3.3.7 Basis sets and Pseudopotentials

Basis sets: So far, we figured out that the Schrodinger equation cannot be solved efficiently for all interacting electrons and nuclei in many-body systems. DFT could simplify this problem by transforming it into a practical single-particle problem using the KS equations where the electrons don't interact together and only move independently in an effective potential, V_{tot}, which includes the effect of all other electrons. Even though DFT simplified the Schrodinger equation, the exact form of eigenfunction,ϕ_i, to solve the KS equations is still unknown. We need it to find the electron density and, subsequently, use the SCF approach (as discussed in the previous subsection) to find the corresponding eigenvalues. One way is to use the expanded version of these eigenfunctions for the known parts called basis sets. Using the eigenfunctions as a combination of the basis sets, we approximate the eigenfunctions to the form that mathematically is understandable and subsequently solvable. Generally, the various types of basis sets used in DFT calculations can be divided into the common three groups [358]:

1. **Plane-Wave Basis sets:** This approach is appropriate mostly for periodic systems like crystals as it uses plane waves as basis functions. They have the advantage that they can easily adjust the periodic boundary conditions that inherently exist in most clean crystal solids. Another advantage is that this approach is more efficient in terms of computational cost for the periodic systems. However, to include properly the core electrons, they cannot capture them solely and usually require pseudopotentials, which consider electrons close to the core efficiently [359, 360, 361].
2. **Localized Basis Sets:** As it comes from the name of this approach, they are well-suited for materials with localized electronic states. In contrast to the Plave-wave method, which is mostly useful for delocalized structures, this is appropriate for systems with strong local interactions. This approach is often called Linear Combination of Atomic Orbitals (LCAO), and some of these methods are:
    - Linear combinations of Gaussian-type orbitals (GTOs)
    - Slater-type orbitals (STOs)
    - Numerical atomic orbitals (NAOs)
    - Linear combinations of pseudo atomic orbitals (LCPAOs)
3. **Augmented Basis Sets:** In general, this method is the combination of the plane waves with localized functions close to the atomic cores, which gives us more accurate results compared to both of the previous methods. On the other hand, these basis sets require high computational costs. some methods in this approach are [362, 363, 364, 365, 366, 367, 368]:
    - Augmented Plane Waves (APW)
    - Green's function Korringa, Kohn, and Rostoker method (KKR)
    - Muffin tin orbitals (MTOs)
    - Corresponding "L" (for linearized) methods

In this thesis, both the plane-wave (PW) and the linear combination of atomic orbitals (LCAO) methods were employed to solve the one-particle Kohn–Sham (KS) equations, depending on the structural and computational requirements of the system under study.

Plane-wave representation. In the plane-wave basis, each KS orbital $\psi_i(\vec{r})$ is expanded as a superposition of plane waves:

$$\psi_i(\vec{r}) = \sum_{\vec{G}} C_{i\vec{G}}\, e^{i(\vec{k}+\vec{G})\cdot\vec{r}}, \tag{3.80}$$

where $\vec{k}$ denotes the Bloch wavevector within the first Brillouin zone, $\vec{G}$ are reciprocal-lattice vectors, and $C_{i\vec{G}}$ are the expansion coefficients. The plane-wave basis naturally satisfies the periodic boundary conditions of crystalline solids. The completeness of this basis increases with the number of included plane waves, which is controlled by an energy cutoff E_{cut} that limits the kinetic energy of the components:

$$\frac{\hbar^2|\vec{k}+\vec{G}|^2}{2m_e} \leq E_{\text{cut}}. \tag{3.81}$$

A higher cutoff increases accuracy at the cost of computational effort, and E_{cut} is typically converged for each material.

LCAO representation. Complementary to the plane-wave approach, most of the calculations in this work were also performed using the LCAO method. Here, each KS orbital is written as a linear combination of localized atomic-like basis functions centered on the atoms:

$$\psi_i(\vec{r}) = \sum_{\mu} c_{i\mu}\, \phi_\mu(\vec{r} - \vec{R}_\mu), \tag{3.82}$$

where $\phi_\mu(\vec{r})$ are atomic orbitals–commonly Gaussian-type (GTO) or Slater-type (STO) functions–localized around atomic positions $\vec{R}_\mu$, and $c_{i\mu}$ are the expansion coefficients describing the contribution of each orbital to the total wavefunction. Because these basis functions are not orthogonal, the KS equations are transformed into a generalized eigenvalue problem,

$$Hc_i = \epsilon_i S c_i, \tag{3.83}$$

with Hamiltonian and overlap matrices defined as

$$H_{\mu\nu} = \langle\phi_\mu|\hat{H}|\phi_\nu\rangle, \qquad S_{\mu\nu} = \langle\phi_\mu|\phi_\nu\rangle. \tag{3.84}$$

The LCAO basis offers a compact representation particularly well-suited for systems with localized electronic states, while the plane-wave approach is generally advantageous for periodic solids and accurate total-energy calculations. In this thesis, both methods were applied depending on the symmetry, size, and electronic character of the systems considered.

Pseudopotentials: To have a good insight into the Pseudopotentials concept, it is worth having a summary from the beginning of the methodology we have discussed during this thesis till now. The primary purpose of this methodology part of the thesis is to find a way to obtain the properties of materials using the Schrödinger equation, followed by DFT and KS equations. The first step is finding the eigenfunctions through the SCF calculations in the KS framework. This approach's responsibility is transferring the many-body Schrödinger equation to a single-particle problem. Somehow, one can calculate the electron density $n(\vec{r})$ from the single-particle orbitals. However, one important challenge exists in the KS equations regarding the exchange-correlation

(XC) potential, which is difficult to calculate precisely because of the significantly complicated nature of the (valence) electrons correlation and exchange interactions. To solve the issue, we use some approximations like the Perdew-Burke-Ernzerhof (PBE) functional, which is part of the generalized gradient approximation (GGA) family, which is computationally balanced cost and accurate enough. Other functionals, such as LDA or hybrid functionals, are also adopted according to the specific systems. After XC potential, we still have a complexity with the effective potential $V_n(\vec{r})$, which describes the interactions among core electrons, valence electrons, and their mutual interactions. In quantum mechanics, we deal with atoms; each atom has its core electrons (the electrons are close to the nucleus) and valence electrons (those are far from the nucleus and have a main role in bonding and chemical reactions). During the chemical bonding or chemical interactions, the core electrons don't have significant changes and hence, it is possible to consider their effects in our calculations indirectly somehow instead of calculating their complex effect literally, this can be conducted by replacing them with the Psueodpotentials which are substitution of all interactions between them. Psueodpotentials are smoother and can save a lot of computational effort since we only focus on the valence electrons vital to obtaining the properties. Simply put, in the KS equations, the effective potential comprises the contributions of the external potential, Hartree term (e-e interactions), and the XC potentials. We need to consider all interactions among the core electrons and valence electrons which are complex and using the pseudopotentials (PPs) we can approximate them and only focus on the valence electrons which are critical to consider for us. To include the valence electrons in our calculation, somehow, we reduced the effect of the core electrons and their interactions with the valence electrons, and we can use several types of the Pseudopotentials [369, 370]:

1. **Norm-Conserving Pseudopotentials:** This type helps us to find an optimal cutoff distance from the atom where further out this distance, the norm (or total size) of the wavefunctions remains the same as it was with that cutoff. Simply, it means the interactions of the electrons outside of this distance are effectively approximated to ensure accuracy and no need for more details about the core electrons. However, it is worth mentioning that for this type, we need to include more basis sets (e.g., for more plane waves) to ensure their accuracy, which requires more computational costs.

2. **Ultrasoft Pseudopotentials:**This type relaxes the basis sets used in the norm concerning PPs, making them smoother and more efficient and reduces the number of the basis sets (e.g., plane waves), leading to lower computational costs.

3. **Projector Augmented Wave (PAW) Method:** This method combines the advantages of both mentioned types and balances accuracy and computational efficiency.

4. **Empirical Pseudopotentials:** In this method, instead of using the First principle parameters, we use the experimental results and, using fitting or other similar techniques, find the appropriate parameters for the interactions of the core and valence electrons. They are significantly efficient but are limited to specific structures and may not be universally applicable to all systems.

3.4 Advanced DFT approximations and corrections

3.4.1 DFT-D correction methods

In this thesis, several works are in stacking layers, which means we have multilayers on top of each other, and the number of them can be from 0 to the desired van der Waals heterostructure. Pure DFT generally does not include the van der Waals interactions (also called dispersion interactions), so the optimal distance between layers after DFT optimizations is not comparable with the experimental results. Hence, through the semi-empirical corrections by Grimme D2 [371] and D3 [372], one can include the long-range van der Waals interactions. These mentioned corrections are the methods that are added to the DFT calculations using the extra term in the energy to account for the van der Waals forces.

$$E_{DFT+D} = E_{DFT} + E_{disp} \tag{3.85}$$

Using the D2 and D3 corrections, we can add this E_{disp} to the main DFT energy.

D2 correction

In the D2 [371] correction, dispersion energy is considered two-body energy, and it can be represented by an attractive semi-empirical pair potential V^{PP} which accounts only for the lowest-order dispersion term:

$$E_{\text{disp}} = -S_6 \sum_{A<B} V^{\text{PP}}(Z_A, Z_B, R_{AB}), \tag{3.86}$$

where $Z_A(Z_B)$ and R_{AB} are the atomic numbers and interactions distance, respectively. The $S6$ is also a global scaling parameter, and it is a constant factor that is used to scale the dispersion energy term and ensure the calculated interactions are in agreement with the known experimental values. To do this, it is fitted (or calibrated) using a large set of molecules with known thermodynamical properties(e.g., bond energies, binding energies, ...) and depends on the XC functional employed, and eventually, the fitting ensures that the DFT-D2 method gives reliable and accurate results. the V^{PP} is given by:

$$V^{\text{PP}} = \frac{\sqrt{C_6^A C_6^B}}{R_{AB}^6} f(R_{AB}) \tag{3.87}$$

where

$$f(R_{AB}) = \frac{1}{1 + e^{-d_6\left[\frac{R_{AB}}{R_0^A + R_0^B} - 1\right]}} \tag{3.88}$$

is a damping function and C_6 and R_0 are different with elements. In our calculations, we set the d_6 equal to 20. Also it is noteworthy to mention that this D2 method not only considers the pairs of atoms between stacked layers (inter-layer) but also considers the intra-layer atoms. It finds all possible pairs and then sums them, then adds to the E_{DFT} term and gives the final energy term [371].

D3 correction

The D3 [372] correction includes both two and three body energies as dispersion energy:

$$E_{\text{disp}} = E^{(2)} + E^{(3)}. \tag{3.89}$$

Two body energy term:

The $E^{(2)}$ term include dispersion terms up to the 8^{th} order plus the 6^{th} order (i.e. $E^{(2)} = E_{D2} + 8^{th}$ order correction) :

$$E^{(2)} = -S_6 \sum_{A<B} V_6^{\text{PP}}(Z_A, Z_B, R_{AB}) - S_8 \sum_{A<B} V_8^{\text{PP}}(Z_A, Z_B, R_{AB}). \tag{3.90}$$

- $S_6 = 1$ for all elements.
- S_8 depended on the XC functional used.

6^{th} order of V^{PP}:

$$V_6^{\text{PP}} = \frac{C_6^{AB}}{R_{AB}^6} f_6(R_{AB}), \tag{3.91}$$

where

$$C_6^{AB} = \frac{\sum_i^{N_A} \sum_j^{N_B} C_{6,\text{ref}}^{AB} e^{-4[(n^A - n_i^A)^2 + (n^B - n_j^B)^2]}}{\sum_i^{N_A} \sum_j^{N_B} e^{-4[(n^A - n_i^A)^2 + (n^B - n_j^B)^2]}}, \tag{3.92}$$

8^{th} order of V^{PP}:

The pair potential for the 6^{th} order is given by:

$$V_8^{\text{PP}} = \frac{3C_{6,\text{ref}}^{AB} \left(\sqrt{Z_A} \frac{\langle r^4 \rangle_A}{\langle r^2 \rangle_A} \sqrt{Z_B} \frac{\langle r^4 \rangle_B}{\langle r^2 \rangle_B} \right)^{\frac{1}{2}}}{R_{AB}^8} f_8(R_{AB}). \tag{3.93}$$

The $C_{6,ref}^{AB}$ is calculated using the reference dispersion coefficients obtained from time-dependent Density functional theory and includes atomic coordination information (more details about the parameters in ref. [372]).

Three body energy term

This term is given by:

$$E^{(3)} = \sum_{A<B<C} V^{\text{TBP}}(Z_A, Z_B, Z_C, R_{AB}, R_{AC}, R_{BC}, \cos\theta_a, \cos\theta_b, \cos\theta_c), \tag{3.94}$$

where the three-body potential V^{TBP} is made with the two-body terms as a starting point:

$$V^{\text{TBP}} = f(\bar{R}_{ABC}) \frac{\sqrt{C_6^{AB} C_6^{AC} C_6^{BC}} (3 \cos\theta_a \cos\theta_b \cos\theta_c + 1)}{(R_{AB} R_{BC} R_{CA})^3}, \tag{3.95}$$

and

$$f(\bar{R}_{ABC}) = \frac{1}{1 + 6\left[\bar{R}_{ABC}/(\frac{4}{3}\bar{R}_0^{ABC})\right]^{-16}} \tag{3.96}$$

where the geometrically averaged radii are:

$$\bar{R}_{ABC} = (R_{AB}R_{BC}R_{CA})^{\frac{1}{3}} \qquad \text{and} \qquad \bar{R}_0^{ABC} = \left(R_0^{AB}R_0^{BC}R_0^{CA}\right)^{\frac{1}{3}}. \tag{3.97}$$

3.4.2 Bandgap correction methods (DFT+U)

The standard Density Functional Theory method, with its local XC approximations like LDA and GGA, has some weaknesses, particularly concerning estimating the correct energy bandgap. These weaknesses are as follows:

1. **Self-interaction:** In local approximation XC, the electrons can interact with themselves but it can prevent electrons from localizing properly, which should be corrected.
2. **Excited states:** The LDA and GGA description for the conduction band energy levels are often poor and usually underestimate the energy band gap compared to the experiments and must be corrected.

The mean-field Hubbard correction developed by Dudarev et al. [373] and Cococcioni et al. [374], often indicated by XC+U, DFT+U, LDA+U, or GGA+U, is a semi-empirical correction to improve the mentioned drawbacks regarding the energy bandgap. This can be done by adding an extra term to the exchange and correlation functional:

$$E_U = \frac{1}{2}\sum_{\mu} U_\mu (n_\mu - n_\mu^2). \tag{3.98}$$

- n_μ: number of electrons in a specific atomic shell (shell here stands, for example, the group of electrons with d-orbital)
- U_μ: The Hubbard U parameter for that shell, which quantifies the strength of the correction.

Effect of E_U:

- When a shell is fully occupied or empty (of electrons), the E_U becomes zero, which means there is no additional energy penalty.
- When a shell is partially filled, the E_U is non-zero and becomes positive ($E_U > 0$), and this situation encourages electrons to occupy these states or deplete them fully. This enhances the electron localization tendency and increases the energy band gap and, subsequently, leads to a better agreement with the experimental results.

The U value is often obtained using the empirical approach by fitting parameters with the experimental observations. However, some methods use the First principle calculations to estimate the U value, such as linear response theory with the function calculate Finite Difference Linear Response Hubbard U [374] or using the locally screened Coulomb correction (LSCC) approximation with the function calculate Local Screened Coulomb Correction Hubbard U [375]. Choosing the U is extremely sensitive, and it should be done cautiously since if the value of U is set too high, the

calculation might find several different ways the electrons could arrange themselves. These different arrangements are called "local minima" because the energy of the system is at a low point in multiple places, like being in different valleys on a landscape. Hence, an anisotropic initial electron state is required to avoid this issue, which means the starting point for the electron arrangement is uneven or direction-dependent and does not uniformly spread in all directions. Eventually, using this extra term in XC functional [denoted by XC + U], the pure DFT results can be treated much more precisely, particularly for materials with localized electrons, such as transition metal elements with partially filled d or f orbitals.

3.4.3 Spin-Orbit Coupling (SOC)

In this thesis, we have used a lot of the heavy elements, like Fe, Cr, Co, ..., and as their valence electrons are mostly inside the atomic cores, we need to include the relativistic contributions to the electronic structure. The standard time-independent Density Functional Theory describes only non-relativistic electrons moving in an external field built up by the atomic nuclei. The spin-orbit coupling has a relativistic effect, adding to the Kohn-Sham Hamiltonian and causing the splitting of electronic bands in many materials, from metals to semiconductors. So, for heavy elements like transition metal atoms, the spin-orbit coupling must be included, and in this thesis, we have calculated all these materials in the presence of spin-orbit coupling. To address this, fully relativistic Pseudopotentials have been adopted for our calculations.

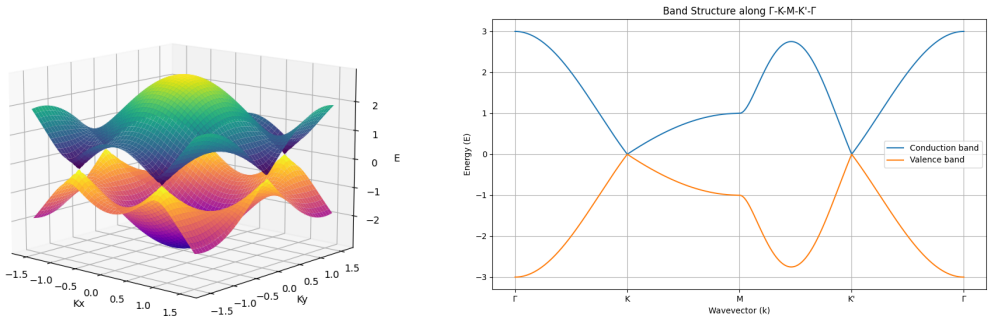

Figure 3.7. Band structure of pristine graphene from simple Tight-Binding model.

3.5 Tight-Binding and $\boldsymbol{k}\cdot\boldsymbol{p}$ model for graphene

Spin–orbit coupling (SOC) effects in graphene and related heterostructures are described here using a minimal tight-binding (TB) framework together with its low-energy $\boldsymbol{k}\cdot\boldsymbol{p}$ expansion around the Dirac points. When a substrate is present, the symmetry of pristine graphene (D_{6h}) is reduced to its maximal subgroup D_{3h}, which permits the emergence of three additional terms: (i) a staggered sublattice potential, (ii) a sublattice-dependent intrinsic SOC, and (iii) a Rashba SOC arising from the breaking of mirror symmetry σ_h.

In this formalism, the Pauli matrices $\hat{\sigma}_i$ act on the sublattice pseudospin space (A, B), $\hat{s}_i$ on the real spin space $(\uparrow, \downarrow)$, and the valley index $\tau = \pm 1$ distinguishes the inequivalent K and K' points. Wave vectors $\vec{k}$ are defined relative to the valley centers K_τ, and the reduced Planck constant is set to $\hbar = 1$ for convenience.

3.5.1 Minimal TB model and Dirac expansion

The nearest-neighbour TB Hamiltonian reads

$$\hat{H}_0(\vec{k}) = \begin{pmatrix} 0 & h(\vec{k}) \\ h^*(\vec{k}) & 0 \end{pmatrix}, \qquad h(\vec{k}) = -t \sum_{j=1}^{3} e^{i\vec{k}\cdot\vec{\delta}_j}, \tag{3.99}$$

with hopping t and nearest-neighbour vectors $\vec{\delta}_j$ on the honeycomb lattice. Linearizing near K/K' gives the standard Dirac form

$$\hat{H}_0^\tau(\vec{k}) = v\left(\tau\,\hat{\sigma}_x k_x + \hat{\sigma}_y k_y\right), \qquad v = \frac{\sqrt{3}}{2}\,a\,t, \tag{3.100}$$

where a is the lattice constant (Fermi velocity v can be fit to *ab initio*).

3.5.2 Symmetry-allowed perturbations (for D_{3h})

(i) Staggered potential. Breaking inversion symmetry by the substrate produces a mass term and this term is responsible for the orbital proximity-induced gap arising from the pseudospin symmetry

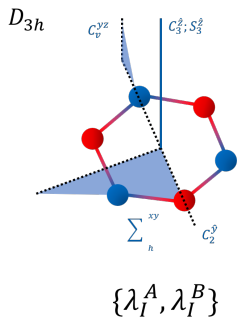

Figure 3.8. Maximal subgroup (D_{3h}) of the point group D_{6h} and the corresponding symmetry operations.

breaking: carbon atoms on sublattices A and B experience, on average, different crystalline fields due to the presence of magnetic substrate. This term takes the form [376, 377]:

$$\hat{H}_\Delta = \Delta\, \hat{\sigma}_z \otimes \hat{s}_0. \tag{3.101}$$

where Δ is the so-called staggered potential (effective orbital hybridization energy) on sublattices A and B.

(ii) Intrinsic SOC (sublattice dependent). Under D_{3h} symmetry the intrinsic SOC can differ on A and B (Figure (3.8)) and the effect of sublattice-dependent spin-conserving next-nearest neighbor spin-orbit interaction is described by the term [376, 377, 378]:

$$\hat{H}_I^\tau = \tau \left(\lambda_I^A\, \hat{\sigma}_+ + \lambda_I^B\, \hat{\sigma}_-\right) \otimes \hat{s}_z, \qquad \hat{\sigma}_\pm = \tfrac{1}{2}(\hat{\sigma}_z \pm \hat{\sigma}_0). \tag{3.102}$$

(For pristine D_{6h} graphene one has $\lambda_I^A = \lambda_I^B$ and $\Delta = 0$). $\lambda_I^{A/B}$ denotes the intrinsic spin-orbit parameter for the sublattices A/B, respectively.

(iii) Rashba SOC. When σ_h is broken (e.g. by a perpendicular field or substrate), the Rashba Hamiltonian in twisted graphene-based structures takes more general form [376, 377, 378, 379, 380, 381]:

$$\hat{H}_R^\tau = -\lambda_R \exp^{-i\frac{\phi_R}{2}\hat{s}_z} \left(\tau\hat{\sigma}_x \otimes \hat{s}_y + \hat{\sigma}_y \otimes \hat{s}_x\right) \exp^{i\frac{\phi_R}{2}\hat{s}_z}, \tag{3.103}$$

where λ_R describes the strength of the Rashba coupling, while the so-called Rashba angle, ϕ_R, governs the spin-momentum locking of electron spins and therefore plays an essential role in the current-induced spin polarization effect (also known as Rashba-Edelstein effect).

In turn, the effect of sublattice-dependent proximity-exchange interaction is taken into account by the following term[377, 382, 383]:

$$\hat{H}_{EX} = \left(\lambda_{EX}^A \hat{\sigma}_+ - \lambda_{EX}^B \hat{\sigma}_-\right) \otimes \hat{s}_z, \tag{3.104}$$

where $\lambda_{EX}^{A/B}$ are the sublattice dependent exchange coupling parameters. Finally, as the last term we need to add E_0, in which defines the position of the Dirac point with respect to the Fermi energy.

3.5.3 Working low-energy Hamiltonian

Collecting all eqautions (3.100)–(3.104), and allowing a fixed energy shift E_0 used for alignment with DFT bands, the model employed in this thesis is:

$$\hat{H}_\tau = \hat{H}_0^\tau + \hat{H}_\Delta + \hat{H}_I^\tau + \hat{H}_R^\tau + \hat{H}_{EX}^\tau + E_0\hat{\sigma}_0 \otimes \hat{s}_0, \tag{3.105}$$

$$\begin{aligned}\hat{H}_\tau = &\underbrace{v\left(\tau\,\hat{\sigma}_x k_x + \hat{\sigma}_y k_y\right)}_{\text{Dirac Term}} + \underbrace{\Delta\,\hat{\sigma}_z \otimes \hat{s}_0}_{\text{Mass Term}} \\ &+ \underbrace{\tau\left(\lambda_I^A\,\hat{\sigma}_+ + \lambda_I^B\,\hat{\sigma}_-\right) \otimes \hat{s}_z}_{\text{Intrinsic SOC Term}} - \underbrace{\lambda_R \exp^{-i\frac{\phi_R}{2}\hat{s}_z}\left(\tau\hat{\sigma}_x \otimes \hat{s}_y + \hat{\sigma}_y \otimes \hat{s}_x\right)\exp^{i\frac{\phi_R}{2}\hat{s}_z}}_{\text{Rashba SOC Term}} \qquad (3.106) \\ &+ \underbrace{\left(\lambda_{EX}^A\hat{\sigma}_+ - \lambda_{EX}^B\hat{\sigma}_-\right) \otimes \hat{s}_z}_{\text{Exchange Energy Term}} + \underbrace{E_0\hat{\sigma}_0 \otimes \hat{s}_0}_{\text{Energy Shift Term}} \quad . \qquad (3.107)\end{aligned}$$

All parameters $v, \Delta, \lambda_I^A, \lambda_I^B, \lambda_R, E_0$ are material-dependent and will be determined by fits to DFT data which has been discussed with all details in the chapter (7). A next-nearest-neighbour hopping t' may be included to capture particle–hole asymmetry but does not modify the leading SOC structure near K/K' and in our model has not been included.

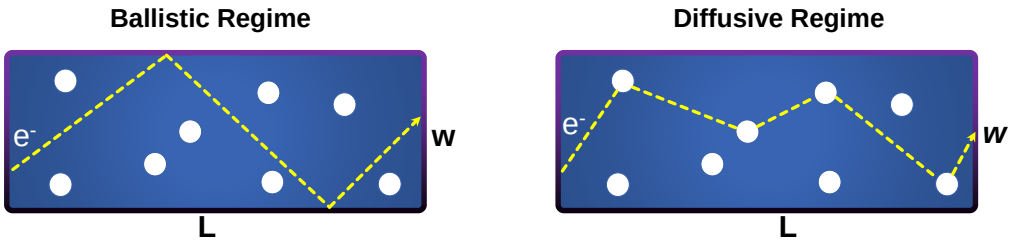

Figure 3.9. Schematic representation of electron transport in ballistic and diffusive regimes.

3.6 Electronic Transport

Ohm's law gives the electrical conductance, G, of bulk materials and is $G = \sigma\frac{A}{L}$. As illustrated in Ohm's law, G is related to the cross-sectional area (A), the length of the conductor (L), and the conductivity (σ), which is a material property of the conductor [384]. On the other hand, when the size of the conductor becomes comparable to the wavelength of the electrons, the classical Ohm's law is not the appropriate way to consider the electrical conductivity. A quantum mechanical description is needed to treat the motions of the electrons in terms of wave functions. In the electron transport in mesoscopic materials, we are dealing with the three characteristic lengths, and they are [385]:

- **Fermi wavelength (λ_F)**:This is de-Broglie wavelength for electrons at the Fermi energy (the highest energy level occupied by electrons at absolute zero temperature). When the materials have a size larger than λ_F, and the electrons are usually treated as particles. Still, for the smaller size (e.g., in terms of nanometers), the wave nature of electrons becomes important.
- **Phase relaxation length (L_ϕ):** This is the average distance between two successive inelastic scattering events. Between these scattering events the electron wave pattern is coherent. Coherency gets lost due to inelastic scattering.
- **Mean free path (L_m):** Mean free path is average distance between two successive scattering events, independently elastic or inelastic.

So, according to these length characteristics, one can divide the electron transport inside the materials into two main regimes as illustrated in Figure (3.9), and they are:

1. **Ballistic regime:** If the electrons move inside a material without collisions with anything and any loss, we can say the regime is ballistic. In this regime, the channel length and width are shorter than the mean free path of electrons (i.e., $L_m \gg L$ or w)
2. **Diffusive regime:** If the electrons travel inside a material, bumping into any defects, and they scatter in different directions, we can say the transport of the electrons is a diffusive regime. In this regime, the channel length and width are larger than the mean free path of electrons (i.e., $L_m \ll L$ or w)

During the last few years, electronic devices have become much smaller and have changed from micrometers to nanometers in size. Subsequently, the way electrons can move inside the materials also changes. This means that in devices with large sizes, electrons mostly scatter in their movement

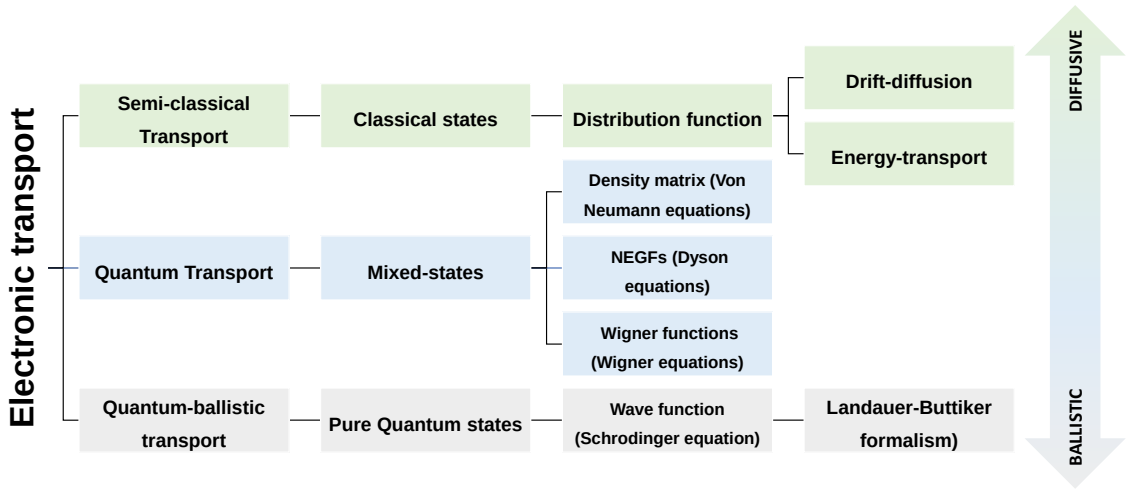

Figure 3.10. Different models to consider the electronic transport properties from the Diffusive regime to the Ballistic.

(diffusive transport), but in devices with small sizes, they move freely without any collisions (ballistic transport). For devices, where the active part between electrodes is nanometer-sized (it means the active part is much smaller than the electrodes), the traditional methods of modeling classical transport, like the Boltzmann equations, don't work anymore. When the size of the device is smaller than a certain key length, both scattering (diffusive regime) and the free movement (ballistic regime) of electrons happen simultaneously. However, the transition between them is gradual and requires more advanced models to consider [386, 387]. Several models exist for the transport of electrons, and each one has its limitations and advantages. The classifications of the different models for the different regimes are shown in Figure (3.10). In the following subsections, we will discuss **Landauer-Büttiker theory** and **Non-equilibrium Green Function Method (NEGF)** briefly.

3.6.1 Landauer Method: equilibrium transport

The Landauer method was introduced in 1970 to described electronic transport in nanoscale systems [388]. This method is usually adopted for systems in which the phase coherence is preserved, like nanowires, molecular junctions, and quantum dots. The main idea of this theory is to conceptualize electronic transport as a scattering problem. The system in this model has three parts: Two large reservoirs (leads or electrodes) and one middle scattering part. We assume all scattering events in the channel are elastic and dissipation processes can only take place in the leads. A conductor scatters the electrons coming from the left lead and then merge to the opposite lead. The model assumes the leads are in thermal and electrochemical equilibrium and characterized by a Fermi-Dirac distribution. The scattering region (conductor) characterized by a transmission coefficient

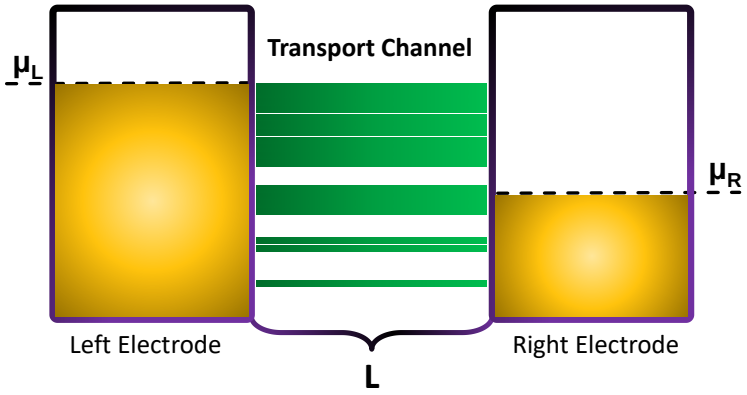

Figure 3.11. Schematic representation of the 1D transport problem where the current is flowing in the transport channel between two electrochemical potentials located at the left and right.

$T(E)$ also measures the probability of an injected electron through the left lead and absorbed by the right one. As shown in Figure (3.11), the conductor has been connected to two reservoirs at the different chemical potentials μ_L (left) and μ_R (right). When the electric current (I) flows inside the system, it can be given by the number of electrons transmitted from the left to the right electrode:

$$I = \frac{2e}{h} \int_{-\infty}^{\infty} T(E) \left[f_L(E) - f_R(E) \right] \mathrm{d}E \tag{3.108}$$

where the $T(E)$ is the transmission probability of an electron with the specified energy level E, and the $f_L(E)$, and $f_R(E)$ are the Fermi-Dirac distribution functions for the left and right electrodes, respectively.

$$f(E) = \frac{1}{1 + e^{\frac{E-\mu}{k_B T}}}. \tag{3.109}$$

Using the linear response regime, due to the small magnitude of the difference in chemical potential ($\mu_L - \mu_R = eV$) with the V as an applied bias, the I can be approximated as [389]:

$$f_L(E) - f_R(E) \approx -eV \frac{\partial f}{\partial E} \tag{3.110}$$

At low temperatures, $\frac{\partial f}{\partial E}$ is like a δ-function at the Fermi energy E_F and the current could be simplified to:

$$I = \frac{2e^2}{h} T(E_F) V \tag{3.111}$$

and form Ohm's law, $R = \frac{V}{I}$, and the conductance is inverse of the resistance, and it is given by:

$$G = \frac{2e^2}{h} T(E_F). \tag{3.112}$$

The equations clearly show the conductance is quantized of the $2e^2/h$, which this G is known as the quantum conductance whenever the $T(E) = 1$ (i.e., perfect transmission). However, if there are some potential barriers in the channel, the backscattering of the electrons causes the $T(E_F) < 1$ and conductance to decrease. Till now, we assumed that our systems are at low temperatures, but we know it is not possible in real applications, and we need to consider the finite temperature. At finite temperatures, the step-like nature of the Fermi-Dirac distribution becomes smoother, and it can be introduced in the equation (3.108). Next, the conductance can be calculated by integrating over $T(E)$, and the temperature-smeared derivative of the Fermi-Dirac distribution:

$$G(T) = \frac{2e^2}{h} \int_{-\infty}^{\infty} T(E)(-\frac{\partial f}{\partial E})dE. \tag{3.113}$$

These equations can be extended to multichannel systems where the total conductance is given by the sum of all channel's contributions:

$$G = \frac{2e^2}{h}\Sigma_n T_n(E_F), \tag{3.114}$$

where T_n is the transmission probability for the n-th mode. The extension of the Landauer formula to the multichannel case is essential for understanding the transport in systems with multiple electronic states (conduction channels) that participate in the conduction, e.g., in nanotubes, graphene, semiconductor nanowires, etc. Later, the Landauer formalism was developed by Büttiker et al. [390], and is an extended model providing a more comprehensive framework of transport problems. In this model, multiple electrodes have been studied where electrons can flow in and out through different independent channels.

3.6.2 Non-equilibrium Green's function formalism

Another method for modeling the quantum transport properties in the nano-scale devices is Non-equilibrium Green's function formalism, which for the first time was proposed in 1959 by Martin and Schwinger to use the Green's function (GF) for the many-body quantum systems [391]. Indeed, the main work regarding this approach is back to two papers by Meir et al. [392] and Lake et al. [393]. The NEGF method has some key strengths that make it a practical theory in the transport properties of the devices; some of them are: (1) This approach uses the same theory for source, drain, and scattering regions; (2) it is using the first-principle calculations like DFT to determine the electronic structure of the scattering region under the finite bias of source and drain, (3) the electron-electron interactions as an essential part of the nanoscale systems is included through the self-energy, (4) the NEGF method is a suitable tool for the large-scale systems since it uses the localized basis functions which means it focuses only on a small and important part of the materials instead of considering whole the system simultaneously. These mentioned advantages led to the implementation of the NEGF combined with DFT to make a device and investigate its transport properties [386, 394, 395, 396, 397]. A typical device includes three parts: left and right electrodes and the central region. We use the "screening approximation", which means the main scattering part (central region) is calculated in full detail, while the electrodes are uniform. This approximation works well, especially in situations where the current through the system is small, so the electrons in electrodes can be treated as if there's no significant disturbance, and one can assume

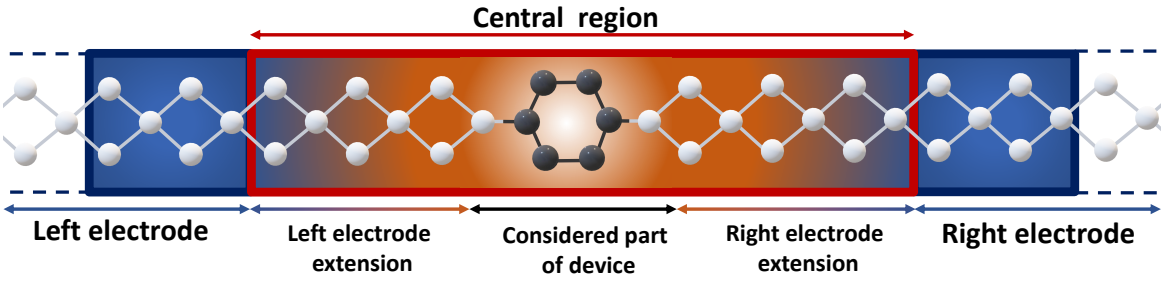

Figure 3.12. Schematic illustration of the device considered in the NEGF methods.

the electrodes are regular and periodic without needing full details of calculations. The schematic illustration in Figure (3.12) shows how the electrodes extended into the central region to avoid any disturbances coming from the scattering part [e.g., here we have simple benzene]. In typical devices, the electrodes are at equilibrium, which means the electrons in the left and right electrodes are in a periodic boundary condition with a well-behaved distribution. Using the standard electronic structure calculations, their properties can be determined. The main challenge comes up when the electron distribution in the central region is not equilibrium due to the interaction within both electrodes. In our calculations, we assume the system has reached a steady state, meaning the electron density remains constant in time for the central region. This electron density is due to the filled eigenstates of the system, and as the left and right electrodes have a voltage difference, they have different chemical potentials. So, we need to calculate their contributions to the total $n(\vec{r})$ separately in the central region:

$$n(\mathbf{r}) = n^L(\mathbf{r}) + n^R(\mathbf{r}). \tag{3.115}$$

The contribution of electronic states from the left and right electrodes can be obtained through the calculation of scattering states, which describe how electrons propagate between the electrodes and the central region of the device.

As illustrated schematically in Figure (3.13), a scattering state originating in one electrode (e.g., the right) traverses the central region and contributes to the charge density on the opposite side. The electron densities associated with the left and right electrodes can be expressed as a sum over all occupied scattering states:

$$n^L(\vec{r}) = \sum_\alpha |\psi_\alpha(\vec{r})|^2 f\left(\frac{\varepsilon_\alpha - \mu_L}{k_B T}\right), \qquad n^R(\vec{r}) = \sum_\alpha |\psi_\alpha(\vec{r})|^2 f\left(\frac{\varepsilon_\alpha - \mu_R}{k_B T}\right), \tag{3.116}$$

where f is the Fermi–Dirac distribution, $\mu_{L/R}$ are the chemical potentials, and T denotes the temperature of the electrodes. The scattering states are constructed by matching Bloch states in the electrodes—where translational symmetry holds—with the wavefunctions in the central region obtained from the stationary Schrödinger equation $(H - \varepsilon)\psi = 0$.

Although one can describe the transport using the extended Landauer formalism, it is computationally more efficient to employ the non-equilibrium Green's function (NEGF) framework [394], which provides an equivalent but more general formulation. In NEGF, the electronic density matrix is divided into contributions from the two electrodes:

$$D = D^L + D^R. \tag{3.117}$$

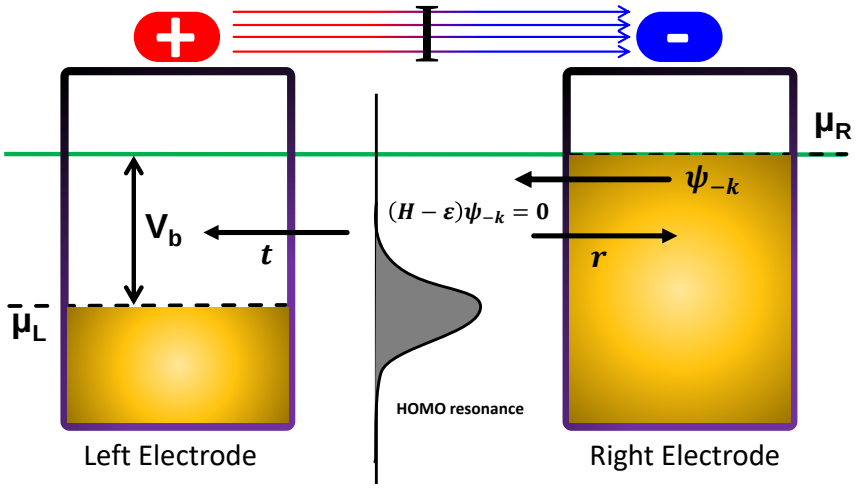

Figure 3.13. Electron distribution in the considered two-terminal device. Each electrode maintains an equilibrium Fermi distribution but with different chemical potentials such that $\mu_R - \mu_L = eV_b$. Electrons flow from right to left and are scattered by the central region.

The left-electrode contribution is given by

$$D^L = \int \rho^L(\varepsilon)\, f\left(\frac{\varepsilon - \mu_L}{k_B T_L}\right) d\varepsilon, \qquad \rho^L(\varepsilon) = \frac{1}{2\pi} G(\varepsilon)\, \Gamma^L(\varepsilon)\, G^\dagger(\varepsilon), \tag{3.118}$$

where $\rho^L(\varepsilon)$ is the spectral density matrix. Here, $G(\varepsilon)$ is the retarded Green's function and Γ^L describes the coupling of the central region to the left electrode,

$$\Gamma^L = i\left[\Sigma^L - (\Sigma^L)^\dagger\right], \tag{3.119}$$

with Σ^L being the corresponding electrode self-energy. Despite the current flow leading to a non-equilibrium state in the central region, each electrode remains in local equilibrium and is characterized by its Fermi function $f(\varepsilon, \mu_{L/R}, T_{L/R})$.

Analogously, the right-electrode terms are written as

$$D^R = \int \rho^R(\varepsilon)\, f\left(\frac{\varepsilon - \mu_R}{k_B T_R}\right) d\varepsilon, \qquad \rho^R(\varepsilon) = \frac{1}{2\pi} G(\varepsilon)\, \Gamma^R(\varepsilon)\, G^\dagger(\varepsilon), \tag{3.120}$$

where

$$\Gamma^R = i\left[\Sigma^R - (\Sigma^R)^\dagger\right]. \tag{3.121}$$

Retarded Green's function. The retarded Green's function encapsulates the electronic response of the device and is defined as

$$G(\varepsilon) = \left[(\varepsilon + i\delta_+)S - H\right]^{-1}, \tag{3.122}$$

where δ_+ is a small positive infinitesimal ensuring convergence, S is the overlap matrix, and H is the Hamiltonian of the device. For transport calculations, we require only the Green's function of

the central (scattering) region, which includes the effect of the electrodes through their self-energies $\Sigma^{L/R}$. These self-energies incorporate the boundary conditions imposed by the semi-infinite leads and determine how the electrodes modify the electronic structure and transmission of the central region:

$$G(\varepsilon) = [(\varepsilon + i\delta_+)S - H - \Sigma^L(\varepsilon) - \Sigma^R(\varepsilon)]^{-1}. \tag{3.123}$$

To obtain the $G(\epsilon)$, we need to invert the matrix of the central region's Hamiltonian, which this matrix is stored in a sparse format and uses the $O(N)$ algorithm. The reason for this is that when the size of the system is large, the inversion will be too big, and it would be more efficient to select only the non-zero part (or important part of the central region inverted matrix), which helps save computational costs [397].

Self-Energy: This is the part that describes the effect of the electrodes on the central region, and it can be calculated in different ways:

1. **Direct Self-Energy:** Uses exact diagonalization of the Hamiltonian. This method is accurate, but it is slow as it uses the exact diagonalization of the Hamiltonian. [398].
2. **Recursion Self-Energy:** It is fast in some systems and not efficient for all as it is an iterative scheme and solves the problem step-by-step and using the results of the previous step for the new step. [399].
3. **Sparse Recursion Self-Energy:** Same as the recursion method but optimized for memory use by exploiting matrix sparsity.
4. **Krylov Self-Energy:** The fastest method is this, but it doesn't have very high accuracy and, for most sensitive materials, cannot be accurate. [400, 401].

Complex Contour Integration The density matrix in NEGF is given by the energy integral, which should be calculated using complex contour integration and divided into two parts: equilibrium and non-equilibrium state integration.

For equilibrium states:

- **Semi Circle Contour:** Uses a semi-circular contour for efficient computation and is the most efficient way of calculations.
- **Ozaki Contour:** Uses the residue theorem and a continued-fraction representation of the Fermi–Dirac distribution. This method is stable, but it takes more time than a semi-circle contour.

For non-equilibrium states:

- **Real Axis Contour:** This is done along the real axis and is the most demanding part for large biases.

Finally, for small biases, we can choose the fast single contour, and for high biases and more stable but slow cases, we choose the double contour.

Spill-in Terms Even though the central region's density matrix D_{CC} is calculated using the Green's function and from the electron density equation (i.e., $n(\mathbf{r}) = \sum_{ij} D_{ij}\phi_i(\mathbf{r})\phi_j(\mathbf{r})$), however, the boundary condition of the regions close to the central region is necessary to calculate to have proper results in edges (i.e., $D_{LL}, D_{LC}, D_{CR}, D_{RR}$).

Effective potential After calculating the non-equilibrium density, we then calculate the effective potential, which is the sum of the XC part and electrostatic Hartree potential. The XC part depends on the local electron density and is easy to obtain, but the Hartree potential requires solving the Possion equation using the boundary condition from the electrodes as it is:

$$\mu_R - \mu_L = eV_b. \tag{3.124}$$

Total Energy and Forces For device systems, which are open and allow charge flow, the energy is described by the grand canonical potential:

$$\Omega[n] = \varepsilon[n] - e\,N_L\,\mu_L - e\,N_R\,\mu_R, \tag{3.125}$$

Where N_L and N_R are the electron numbers from the left and right electrodes. The forces on atoms are derived as:

$$\mathbf{F}_i = -\frac{\partial\Omega[n]}{\partial\mathbf{R_i}}. \tag{3.126}$$

Using the forces calculations, we can understand the mechanical stability of the system, ensure self-consistency in the calculations, perform dynamic simulations, and increase the interactions in device systems.

Transmission Coefficient Once the self-consistent density matrix is calculated, the transmission coefficient, $T(\epsilon)$, gives the probability that electrons at a given energy pass through the device:

$$T(\varepsilon) = \sum_k t_k^\dagger t_k \delta(\varepsilon - \varepsilon_k), \tag{3.127}$$

where the t_k is transmission amplitude, and using it, we define the fraction of a scattering state k that propagates through a device. Alternatively, the $T(E)$ can also be calculated using the retarded Green's function:

$$T(\varepsilon) = G(\varepsilon)\Gamma^L(\varepsilon)G^\dagger(\varepsilon)\Gamma^R(\varepsilon). \tag{3.128}$$

Electrical Current Now having the $T(E)$, one can easily calculate the electric current:

$$I(V_L, V_R, T_L, T_R) = \frac{e}{h}\sum_\sigma \int T_\sigma(E)\left[f\left(\frac{E-\mu_R}{k_B T_R}\right) - f\left(\frac{E-\mu_L}{k_B T_L}\right)\right] dE, \tag{3.129}$$

here:

- f: the Fermi function
- $T_{L/R}$: the electron temperatures of the left/right electrode
- $T_\sigma(E)$: the transmission coefficient for the spin component σ.
- $\mu_L = E_F^L - eV_L$,
- $\mu_R = E_F^L - eV_R$,

and the chemical potential related to the bias is given by:

$$\mu_R - \mu_L = eV_{bias}, \tag{3.130}$$

thus

$$V_{bias} = V_L - V_R. \tag{3.131}$$

As a final note of this topic, the Fermi levels in the (3.130) are assumed to be the same since we are supposed to have the same material for both electrodes. However, if the electrodes have different materials, the $E_F^L \neq E_F^R$ should be considered in the calculation by shifting the Fermi level of one of the electrodes (usually the right electrode) to ensure they match when there's no applied voltage.

Chapter 4

Silicene nanosheets under strain and Cr-doping

4.1 Reprint of article [P1]

On the subsequent pages, we append a reprint with permission:

[P1] **M.A. Jafari**, A.A. Kordbacheh, A. Dyrdał

Electronic and magnetic properties of silicene monolayer under bi-axial mechanical strain: First principles study

Journal of Magnetism and Magnetic Materials 554 (2022): 169260.

DOI: 10.1016/j.jmmm.2022.169260

[1]Copyright on any research article published in the Journal of Magnetism and Magnetic Materials is retained by the author(s). The authors grant Elsevier a license to publish the article and identify it as the original publisher. Authors also grant any third party the right to use the article freely, as long as the integrity of the work is maintained and the original authors, citation details, and publisher are identified. If the article is published as Open Access, it may be available under a Creative Commons license, allowing for wider reuse and distribution.

4.1.1 Introduction and aims

After graphene's emergence in the field of 2D materials, new avenues were opened in electronic, spintronic, and quantum technologies. Despite graphene being an outstanding material due to its electrical, thermal, and mechanical properties, the lack of energy bandgap restricts its application in semiconductor devices that require a switchable on-off state [402, 403]. This limitation of graphene forced the researchers to look for alternative 2D materials that can overcome the mentioned limitations. Silicene, the silicon-based counterpart of graphene, showed great potential as an up-and-coming candidate owing to its inherent compatibility with the existing silicon technology and unique structural and electronic characteristics [404]. In contrast to the graphene with a flat planar sp^2, silicene has a buckled hexagonal lattice structure as a result of the sp^3 hybridization of silicon atoms. This buckling not only allows for an intrinsic spin-orbit coupling (SOC) but also makes its band structure highly sensitive to external perturbations like mechanical strain. In the pristine form, silicene has a small SOC-induced energy band gap where its electronic properties are highly tunable. Applying the uni/bi-axial strain on the monolayer of silicene can lead to significant modifications in the electronic dispersion, including the shifts of Dirac cones away from the high symmetry points in the Brillouin zone, anisotropic modifications of the carrier velocities, and even strain-induced band gap opening or closure [405].

In addition to strain, chemical doping is also a powerful tool to modify the properties of 2D materials. Introducing magnetic impurities, like Chromium (Cr), into the silicene lattice can drastically change both the electronic and magnetic behavior of the system. The hybridization between the 3d orbitals of Cr and the silicon orbitals in silicene can lead to various behaviors, such as the transition between metallic, half-metallic, and semiconducting states, as well as the induction of finite magnetic moments that are strongly sensitive to the lattice deformations. The interplay between doping and strain simultaneously makes the possibility of engineering materials' band structure where even small changes in the atomic configuration or external strain can shift the balance between competing electronic phases [406, 407].

In this chapter, I present results that have been published in the paper [P1]. My work on this topic has been motivated by the need to understand and control the above-mentioned phenomena for the development of next-generation nanoelectronic and spintronic devices. My study mainly focuses on how biaxial mechanical strain affects the electronic and magnetic properties of Cr-doped silicene. On the other hand, by systematically investigating the different doping configurations like monomer, horizontal dimer, and vertical dimer substitution, we have obtained the strain-induced modifications on the monolayer of silicene. The DFT results show that strain not only modulates the overlap of atomic orbitals and changes the effective hopping parameters between silicon atoms, but it also affects the hybridization with the doped Cr 3d states. Subsequently, one can see the various electronic phases, including the opening or closing of the band gap and tuning the magnetic moment, which are essential in tunable device performance. Moreover, the practical aspects of this work are emphasized by recent experimental advances in the synthesis and manipulation of silicene on various substrates. Controlled deposition and doping techniques combined with the application of mechanical strain using substrate engineering or external forces have opened the possibility for the precise design of material properties. Having comprehensive knowledge concerning these effects at a fundamental level is essential for bridging the gap between theoretical and real-world applications [408]. In summary, the results that I obtained show the essential aspects of the effect of combined Cr-doping and mechanical strain in silicone. The results not

only contribute to the fundamental understanding of 2D material physics but also open a way for designing the silicon-based nanoelectronic and spintronic devices with appropriate functionalities.

4.1.2 Methods

The results discussed in [P1] I obtained based on Density Functional Theory [DFT]. The calculations were conducted using the Quantum ATK code package. I used the Perdew–Burke–Ernzerhof (PBE) generalized gradient approximation for the exchange and correlation part. The supercell of silicone nanosheet I considered is 4×4 with doped Cr-atoms with different horizontal monomer and dimer substitutions and dimer adatoms. The biaxial strain is applied across the x and y lattice directions, and the amount, according to the stability of the structures, is between -6% *and* $+8\%$.

4.1.3 Main results

In this paper, I show that Cr-doped silicene has a significant role in modifying the electronic and magnetic properties. This behavior is much more extensive when we put the doped materials under biaxial strain. Due to mechanical strain, Cr-doped silicene exhibits the semimetal-to-metal transition in the monomer configuration. The silicene preserves its metallic behavior for horizontal dimer substitutions with slight changes in the electronic band structure under strain. The remarkable alternations are due to vertical dimer doping, where an energy band gap of approximately 0.13 eV in the band structure without strain disappears under both compressive and tensile strains. Moreover, the magnetic moments are strongly strain-dependent, and prominent changes occur in the HDimer-doped silicene, particularly under compressive strain. These modifications, which are experimentally accessible, make these materials possible candidates for magnetic field-sensitive nanodevices.

Journal of Magnetism and Magnetic Materials 554 (2022) 169260

Contents lists available at ScienceDirect

Journal of Magnetism and Magnetic Materials

journal homepage: www.elsevier.com/locate/jmmm

Research articles

Electronic and magnetic properties of silicene monolayer under bi-axial mechanical strain: First principles study

M.A. Jafari [a], A.A. Kordbacheh [b], A. Dyrdal [a,*]

[a] Department of Mesoscopic Physics, ISQI, Faculty of Physics, Adam Mickiewicz University, ul. Uniwersytetu Poznańskiego 2, 61-614 Poznań, Poland
[b] Department of Physics, Iran University of Science and Technology, 16846-13114 Tehran, Iran

ARTICLE INFO

Keywords:
Density functional theory
Silicene
Strain
Electronic properties
Magnetic properties

ABSTRACT

Mechanical control of electronic and magnetic properties of 2D Van-der-Waals heterostructures gives new possibilities for further development of spintronics and information-related technologies. Using the density functional theory, we investigate the structural, electronic and magnetic properties of silicene monolayer with substituted Chromium atoms and under a small biaxial strain ($-6\% < \epsilon < 8\%$). Our results indicate that the Cr-doped silicene nanosheets without strain have magnetic metallic, half-metallic or semiconducting properties depending on the type of substitution. We also show that the magnetic moments associated with the monomer and vertical dimer substitutions change very weakly with strain. However, the magnetic moment associated with the horizontal dimer substitution decreases when either compressive or tensile strain is applied to the system. Additionally, we show that the largest semiconductor band-gap is approximately 0.13 eV under zero strain for the vertical Cr-doped silicene. Finally, biaxial compressive strain leads to irregular changes in the magnetic moment for Cr vertical dimer substitution.

1. Introduction

Two-dimensional (2D) crystals are currently of great interest for both applied and fundamental research. The most prominent example of this kind materials is graphene. However, the class of 2D materials is very large and is continuously growing. It contains single-layered materials such as those belonging to the group IV of the periodic table (silicene, germanene and stanene) and to the group V (arsenene, antimonene, bismuthene), as well as layered 2D materials like Transition Metal Dichalcogenides and MXenes. Among them silicene seems to be a promising material due to its compatibility with existing silicon-based electronic devices. Because of sp3 hybridization, silicene is the 2D buckled hexagonal lattice of silicon atoms, and is considered as a one of alternative materials to graphene [1–5]. Research activities on silicene significantly increased after its successful synthesis under UHV conditions on several substrates, like for instance on Ag(111), ZrB2(0001), MoS2(0001), and Ir(111) [6–10]. Silicene displays several interesting characteristics, which have been revealed by recent experimental and theoretical investigations. These include for instance: (i) a remarkable spin–orbit coupling parameter, that leads to the energy gap of 1.5 meV [11–13] at the Dirac point, which is much larger than that in graphene (24 μeV) [2,14,15]; (ii) electrically tunable bandgap; (iii) the phase transition from a spin Hall topological insulator to a band insulator [16]; (iv) the strain-induced tunable bandgap [17–19], and (v) promising electric and thermoelectric characteristics [20–26]. The energy gap in silicene makes it promising for applications, however the realization of stabile monolayer of silicene is still problematic [27]. For example, to achieve high on-to-off current ratios and a perfect switching capability, the material exploited for Field-Effect-Transistors (FETs) is usually required to have a fairly large bandgap [10], significantly larger than that mentioned above for silicene.

Electronic and magnetic properties of silicene can be tuned by impurities, i.e., magnetic atoms built into the monolayer structure. Importantly, recent achievements of nanotechnology enable precise arrangements of impurities (including regular lattices), so by doping one can modify electronic properties in a controllable way. The single-side adsorption of alkali metal atoms on silicene has been reported to give rise to a bandgap of approximately 0.5 eV [28,29], that is much larger than that due to intrinsic spin–orbit interaction. If both sides of the single-layer silicene have been saturated with hydrogen atoms, the formed composite system has been shown to be a kind of a nonmagnetic semiconductor [30]. Based on the previous studies, the ferromagnetic characteristics of silicene can be attributed to the single-side hydrogenation [31].

Strain engineering enables external control of electronic characteristics of semiconductor heterostructures and nanomaterials. This

* Corresponding author.
E-mail address: adyrdal@amu.edu.pl (A. Dyrdal).

https://doi.org/10.1016/j.jmmm.2022.169260
Received 2 August 2021; Received in revised form 9 February 2022; Accepted 9 March 2022
Available online 19 March 2022
0304-8853/

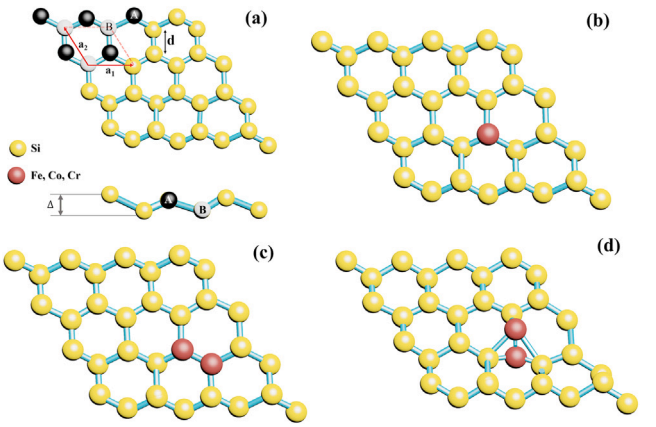

Fig. 1. (a) Hexagonal crystal structure of silicene, with d being the atom spacing and Δ denoting the buckling parameter. The unit cell is indicated by he red dashed lines, and the basis consists of two Si atoms, labelled with A and B. (b–d) Types of impurity substitutions: monomer (b), horizontal dimer (c), and vertical dimmer (d).

technique is widely applied to nano-electro-mechanical and nano-opto-mechanical systems, as well as to MOSFETs [32,33]. In turn, the in-plane strain in silicene leads to a modification of the electronic structure and its transport characteristics [34,35].

An important question is whether a significant gap in the spectrum of silicene can be induced by the strain, especially at low values of strain. If this is the case, tunable silicene devices would be of great practical importance. According to earlier density functional theory (DFT) calculations, a gap in the spectrum of silicene can be open under arbitrary uniaxial strain. Its magnitude varies non-monotonically with the strain. These findings were supported by other ab-initio (without empirical parameters and from first principles) calculation [36]. For similar strain magnitudes, however, the two gap calculations were not in agreement. Recently, Pereira et al. [37] have questioned the accuracy of those conclusions by applying the Tight Binding (TB) approach. According to their findings, a spectral gap can only be achieved for +20% uniaxial deformations. Furthermore, this effect highly depends on the deformation route regarding the rudimentary lattice. The aforementioned findings are in accordance with the studies of Hasegawa et al. [38], indicating that there is a robust gapless Dirac spectrum with regard to arbitrary and not extremely large changes in the nearest neighbour hopping parameters. Moreover, employing the TB model, Wunsch et al. [39] found that the semi-metallic phase appears for hopping parameter expansion.

The results of ab-initio calculations [40] are in agreement with the gapless situation presented in [41]. The inconsistency between various ab-initio calculations ware partially related to the fact that due to strain the Dirac points shift from the high symmetry points of the Brillouin zone. This resulted in arriving at the wrong conclusion that a bandgap is achievable for any strain. In addition, Faccio et al. also performed DFT research and calculated the impact of ≈2% strain in silicene nanoribbon [41]. Keeping in mind that mechanical strain can substantially change the physical properties of silicene, we have performed detailed ab-initio calculations of the magnetic and electronic characteristics of silicene with inserted dimers and monomers of Cr atoms. Then, we have analysed the influence of a biaxial strain for up to ≈±8% deformations. We have shown that magnetic and electronic characteristics of silicene with substitutional impurity atoms can be easily controlled by various kinds of strains (i.e., substrate-induced strains or external mechanical forces). It is worth to note, that the gap due to strain and doping is significantly larger than the gap induced by the intrinsic spin–orbit interaction in undoped and unstrained silicene.

2. Methodology and strain-dependent structural properties

To study electronic and magnetic properties of silicene under mechanical strain we have used the DFT method [42] within the Perdew–Burke–Ernzerhof (PBE) generalized gradient approximation (GGA) [43] form of the exchange–correlation functional, as implemented in the QuantumATK code package ver. S-2021.06 [44,45]. The PseudoDojo collection of optimized norm-conserving Vanderbilt (ONCV) pseudopotentials and ultra-basis set have been used for the optimization of structures and for further calculations [46]. For the Brillouin zone integration we have taken 8 × 8 × 1 Monkhorst–Pack k-points in self-consisting calculation (SCF), and the mesh cut-off of energy has been set to 450 Ry. Structures ware relaxed until the forces on each atom were less than 0.05 eV/Å and relative convergence for the Self-Consistent Field (SCF) energy is reached until 10^{-5} eV/Å . We have used 15 Å vacuum region to prevent interaction of two neighbouring layers along the c-axis [47–49].

The atomic structure of silicene should be characterized before modelling the electronic structure [50]. The first structure optimization process for a single layer of Si was reported by Takeda and Shiraishi [51]. By analogy to graphite, they defined a hexagonal lattice for Si atoms (with a periodicity perpendicular to the plane with a large vacuum layer of minimally 10 Å), and then varied the in-plane lattice constant and positions of the basis atoms (Fig. 1(a)) inside the unit cell, while keeping constant the imposed D3d symmetry [52]. According to their results, the buckled structure has a lower total energy, with a local minimum for $a = 3.855$ Å and a deformation angle of 9.9°, when compared to the energy of a flat structure [50].

In the present study, the 4 × 4 monolayer of silicene was characterized systematically (thus the unit cells were repeated up to four times in the x and y directions) using DFT [53]. The Si atom bounded to three nearest neighbour surrounding Si atoms with the Si–Si bond length of 2.28 Å and lattice parameter a of 3.84 Å was assumed prior to structural relaxation. The optimized lattice parameter, $a = 3.86$ Å, correlates quite well with other data, even though the standard GGA functional method overestimates it. The buckling parameter Δ is 0.46 Å, which is also consistent with other studies [54–58].

In this paper we analyse three different types of substitution in silicene monolayer by Chromium adatoms as presented in Fig. 1. These are: (i) monomer substitution, where one Si atom in the supercell is substituted by Cr atom (3.2% substitution), as presented in Fig. 1(b); (ii) horizontal dimer (HDimer) substitution with two neighbouring Si atoms substituted by Cr atoms (6.25% substitution), see Fig. 1(c); (iii) vertical dimer (VDimer) substitution, where one Si atom is replaced by two Cr atoms (3.2% substitution), as shown in Fig. 1(d). These three structures were modelled within the optimized 4 × 4 supercell geometries, and we analysed behaviour of the electronic and magnetic properties with the strain.

The strain is defined as a deformation resulting from external loads or forces, that may be calculated by the following equation: $\epsilon = \Delta a/a_0$ with $\Delta a = a - a_0$, where a is the lattice parameter of the strained silicene and $a_0 = 3.86$ Å is the lattice constant of the unstrained silicene [34,36,59]. The model of strained unit cell for the tensile and compression strains is achieved by varying the lattice constant along the lattice vectors by the following substitution $a \rightarrow \epsilon a$. Accordingly, the uniaxial tensile strain or compression ($\Delta a \gtrless 0$ respectively) is realized by modification of the lattice constant in the x direction, that is by modification of the lattice vector $\mathbf{a}_1$ (mechanical force applied along the lattice vector $\mathbf{a}_1$), whereas the biaxial tensile or compressive strain is described by modification of both $\mathbf{a}_1$ and $\mathbf{a}_2$ lattice vectors (forces are oriented along both lattice vectors).

The presence of biaxial strain affects the buckling parameter, Δ, as well as the Cr–Si and Cr–Cr bonds in the silicene monolayer with monomer and dimer substitutions, respectively. Fig. 2 presents the basic parameters of the relaxed structures as a function of strain and also for all the substitutions under consideration.

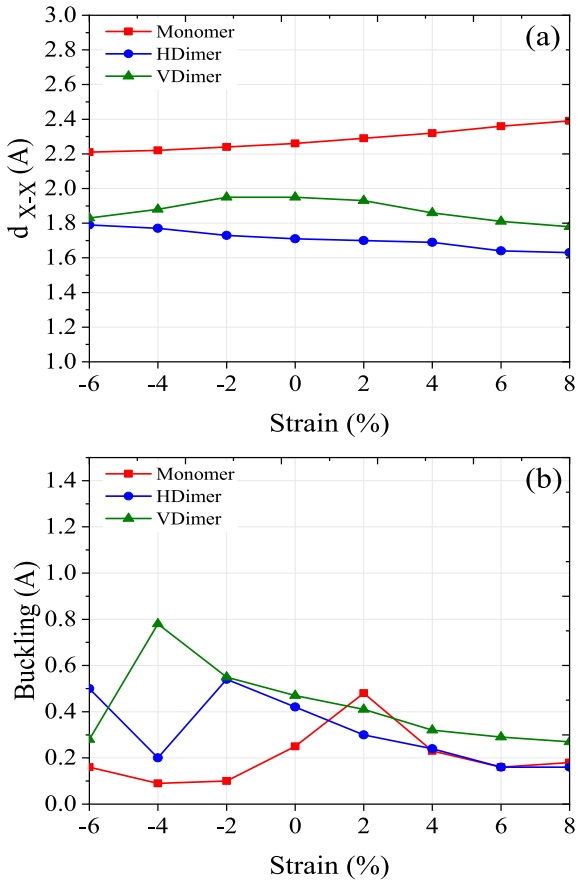

Fig. 2. Variation of the Cr–Si and Cr–Cr bond lengths, d_{X-X} (Fig. 2.(a)), as well as of the buckling parameter (b) under the biaxial tensile and compressive strain for the monomer, horizontal dimer, and vertical dimer substitutions.

For the monomer substitution (see Fig. 2(a)), the bond length between Cr and Si atoms, $d_{\mathrm{Cr-Si}}$, slightly increases with the strain. However, there is no clear universal behaviour of the buckling parameter with strain, though one can see that this parameter reaches a maximum for a specific strain equal 2%, and then decreases with increasing magnitude of either tensile or compressive strain.

For the silicene with HDimer substitution, the tensile strain reduces monotonically the bond length $d_{\mathrm{Cr-Cr}}$ and the buckling parameter. However, for the compressive strain one observes increase of the bond length for Cr–Cr dimers. In turn, the buckling parameter for Cr–Cr HDimers varies nonmonotonously with the magnitude of compressive strain, i.e., it reaches a minimum at some magnitude of the strain, see Fig. 2(b).

In turn, for the VDimer substitution, the strain only very slightly affects the bound lengths reducing it when the strain takes absolute values larger than 2%. The corresponding buckling parameter decreases with increasing tensile strain and increases with increasing magnitude of the compressive strain up to 4%, where it reaches a maximal value, and then decreases with a further increase of the magnitude of compressive strain.

At this point, one should note that high strain values are experimentally difficult to obtain [36,60–64]. The recent reports about graphene-like monoatomic crystals indicate that the strain around 4% can be relatively easily obtained. Accordingly, in this paper we have restricted our considerations to the strain ranging from −6% to 8%.

Table 1
Band gap (eV) changing for Cr substitution during the biaxial strain and applied spin–orbit interaction.

Strain (%)	−6%	−4%	−2%	0%	2%	4%	6%	8%
Monomer-Cr	0	0	0	0	0	0	0	0
HDimer-Cr	0.1	0	0	0	0	0	0	0
VDimer-Cr	0	0	0.12	0.13	0	0.05	0	0

3. Strain-dependent electronic and magnetic properties

It is well known that strain has a significant impact on electronic and magnetic properties of 2D crystals [65–69]. One of the consequences of the strain in 2D crystal is the electronic bandgap engineering, i.e., strain-induced bandgap opening [20] or a direct–indirect–direct bandgap transition in green phosphorene [70,71].

Fig. 3 presents the band structures of strained and unstrained silicene doped with Cr for the three different types of substitution (Monomer, HDimer and VDimer), as discussed in Section 2. The band structure has been calculated along the high-symmetry points of the Brillouin zone, i.e., along the Γ-M–K–Γ path. In turn, Table 1 collects information about the band gap in silicene under strain and with different types of Cr substitution. The electronic band structure of undoped silicene monolayer under strain is presented in Appendix A. Here one needs to remind, that strain in undoped silicene does not open a gap. A small gap appears only due to spin–orbit interaction. When neglecting this interaction, the gap in undoped silicene remains equal to zero (at the Dirac points), see also Fig. 5 in Appendix A. Apart from this, due to hybridization of the 3d-impurity states and those of pure silicene, the band structure becomes remarkably modified by doping. Each state of the doped system includes in general contributions due to 3d-transition metals as well as due to silicon atoms. To show this explicitly, we have presented the so-called *fat-bands* structure, where the two contributions are indicated explicitly with different colours. In Appendix B we present *fat-bands* calculated for silicene monolayer doped with Cr-atoms (i.e., the band structure projected over orbitals of Silicone and Chromium atoms). The corresponding results are shown in Fig. B.6, and from this figure one can estimate whether a particular band contributes to conductivity or not. If it is due to impurities only and is dispersionless around the Fermi level, it does not contribute to conductivity. If however it is dispersive around the Fermi level, then even though the silicon contribution is small, it contributes to conductivity. These features have been taken into account when determining the band gaps. In Appendix B we show the *fat-bands* for silicene with Cr-Monomers, Cr-HDimers and Cr-VDimers.

The silicene with Cr-monomers is either metallic or semimetallic, with the Fermi energy crossing the valence bands. In the presence of compressive strain the energy gap becomes opened in the spectrum above the Fermi energy, while the Fermi level is still inside the valence bands. In the presence of tensile strain the system moves from semimetallic to metallic one. In turn, for silicene with Cr-HDimer substitution, the electronic structure is only slightly affected by the strain. The most promising effect of strain on the electronic structure can be observed for silicene monolayer with Cr-VDimer substitution. Without strain the system is a semiconductor with the energy gap equal 0.13 eV. Applying compressive strain one can close the energy gap and move the Fermi level to the valence bands. The tensile strain, in turn, leads to reduction of the energy gap for the 4% strain, and leads to its complete closure for strain ≥6 %.

Our calculations also reveal the impact of biaxial strain on the magnetic characteristics of the silicene monolayer doped with the specified above Monomers, HDimers and VDimers of Cr atoms. The corresponding results are presented in Fig. 4, where spin polarization of silicene monolayer doped with Cr atoms is shown as a function of strain (the three types of substitution are presented). Situations in the presence of spin–orbit interaction and that in the absence of spin–orbit coupling are

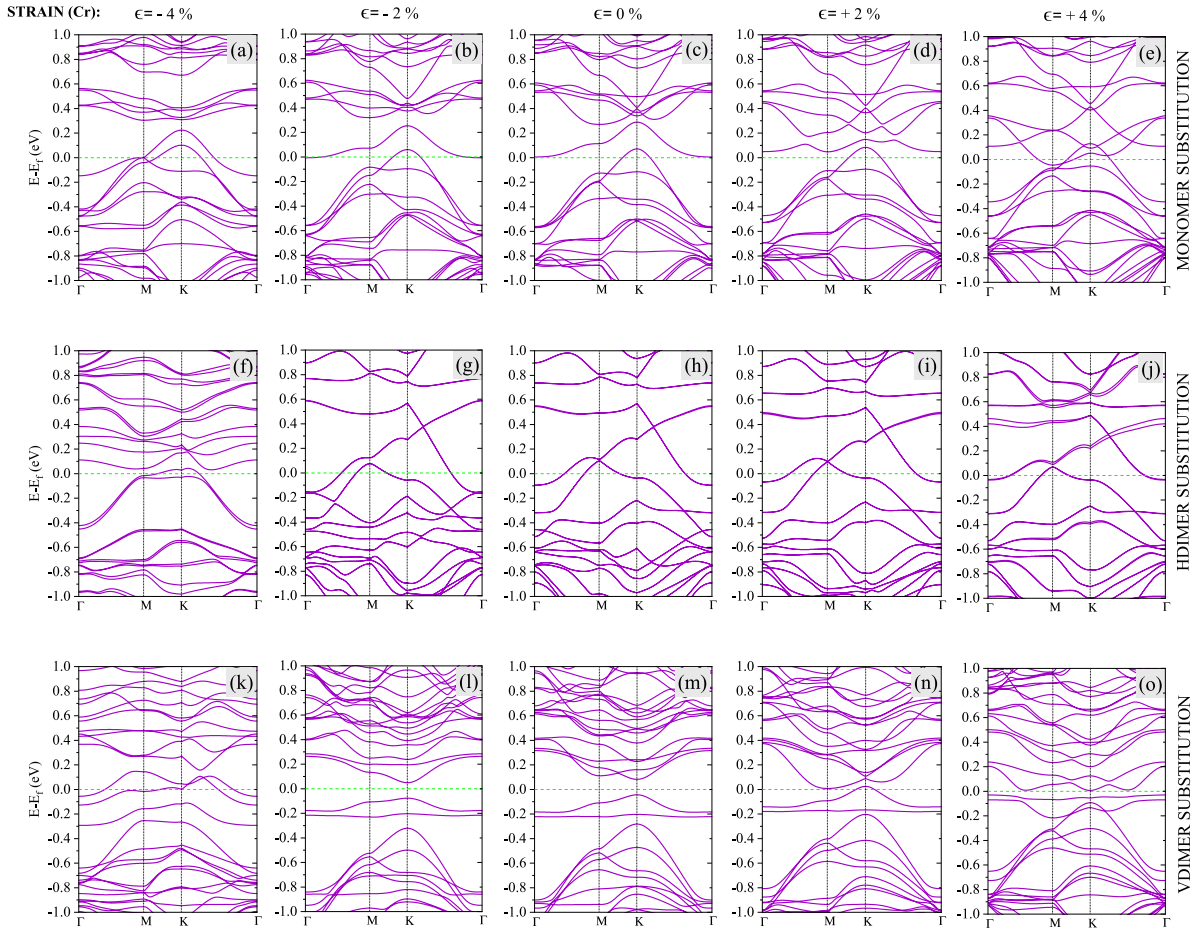

Fig. 3. The electronic energy spectrum of silicene under selected values of biaxial strain (from −4% to +4%) in the presence of spin–orbit interaction, and for Cr doping with the three types of substitution: (a–e) monomer, (f–j) HDimer, and (k–o) VDimer.

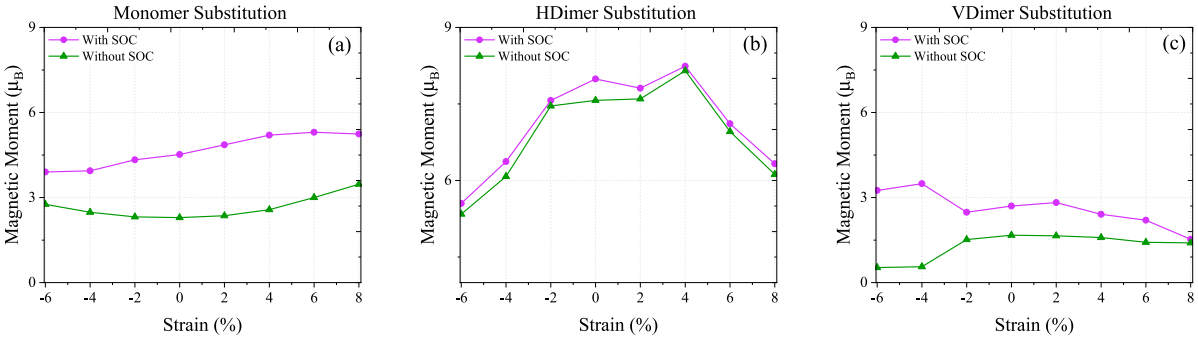

Fig. 4. Magnetic moment behaviour as a function of the applied biaxial strain for the Cr substitution obtained based on calculations with and without spin–orbit coupling (SOC). The green curves (no SOC) correspond to the collinear calculations discussed in Appendix C.

shown there. In the latter case, the calculation procedure is described in Appendix C. For silicene with the Cr-monomers, the magnetic moment varies monotonously with the strain when the spin–orbit coupling is included, while in its absence, the magnetic moment increases with the magnitude of strain, both tensile and compressive. Moreover, the difference between these two situations is relatively large. In turn, for the case of Cr-HDimer, the magnetic moment decreases with the compressive and tensile strain, and the difference between the cases with and without spin–orbit interaction is small. For the silicene monolayer doped with Cr-VDimers, the magnetic moment only weakly depends on the strain for strain larger than −4%, and the difference between the case with and without spin–orbit interaction is small except the strain below −4%, where this difference is relatively large. It is worth noting that the largest magnetic moment for the unstrained system is for silicene monolayer with Cr-HDimers, where the changes in the magnetic moment due to strain are also most pronounced.

4. Conclusions

In this work we presented detailed study of electronic and magnetic properties of silicene doped with Cr atoms in one of the three doping

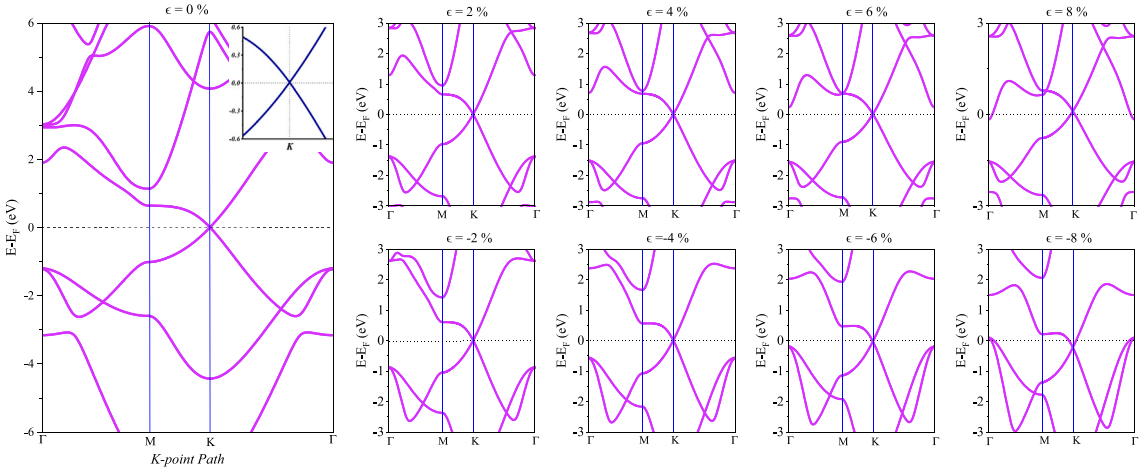

Fig. 5. The electronic band structure of undoped silicene monolayer under biaxial strain from −8% to +8% and in the absence of spin–orbit interaction.

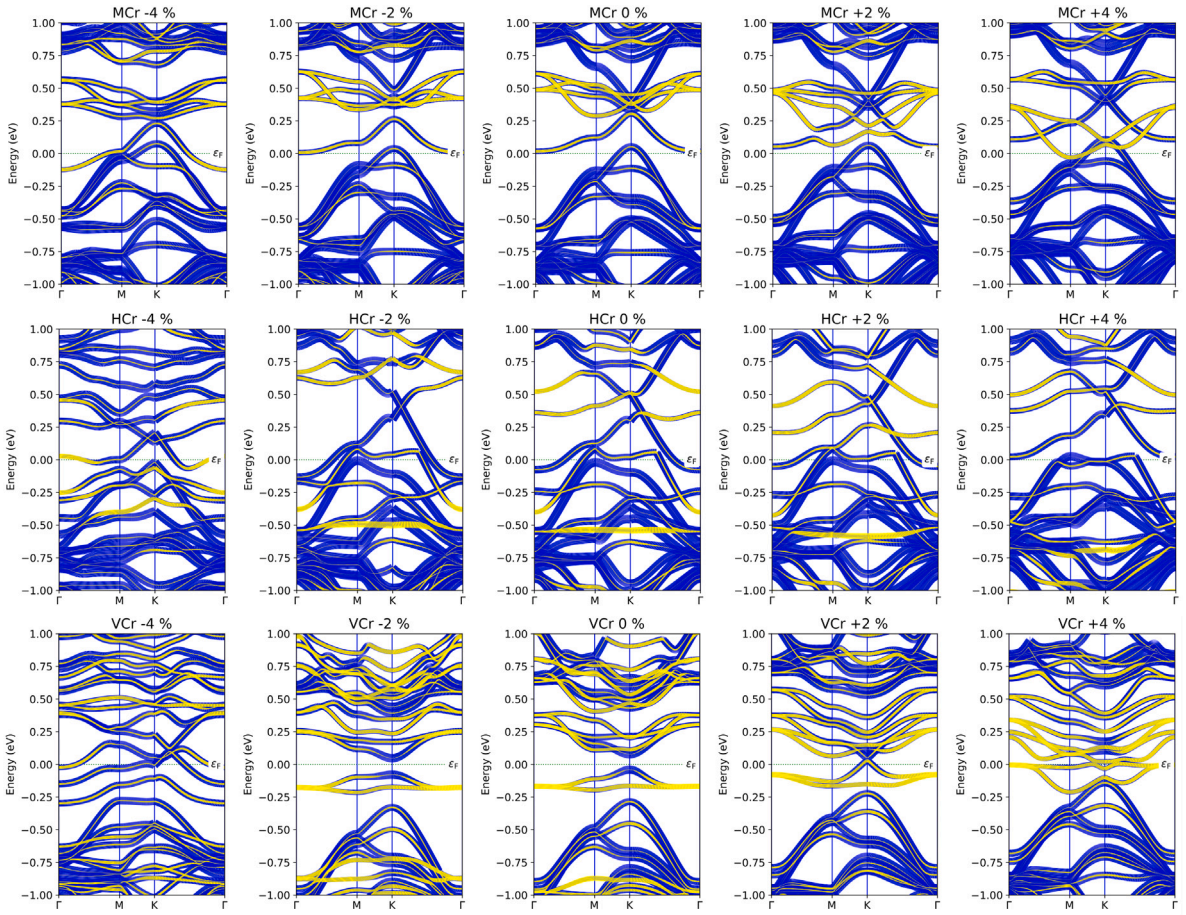

Fig. B.6. A fat-band representation is used to indicate the projected weights in a silicene monolayer with substituted Chromium atoms in the (top) monomer, (middle) HDimer, and (bottom) VDimer forms. The yellow and blue colors represent the transition metal and silicon atoms contributions, respectively.

schemes, i.e., monomer, HDimer, and VDimer substitutions. Numerical results based on the DFT calculations clearly show that the way of substitution may substantially change the structural, electronic and magnetic behaviour of the silicene under strain. The interplay of doping and strain may be used to engineer band gap, and thus also character of transport properties from metallic to half-metallic or semiconducting. Such a strain-induced engineering of transport properties is important from the practical point of view as it may be used in various spintronics and/or logic devices. It is expected, that controlling current and magnetic state with a strain opens new route for nanoelectronics of future generation.

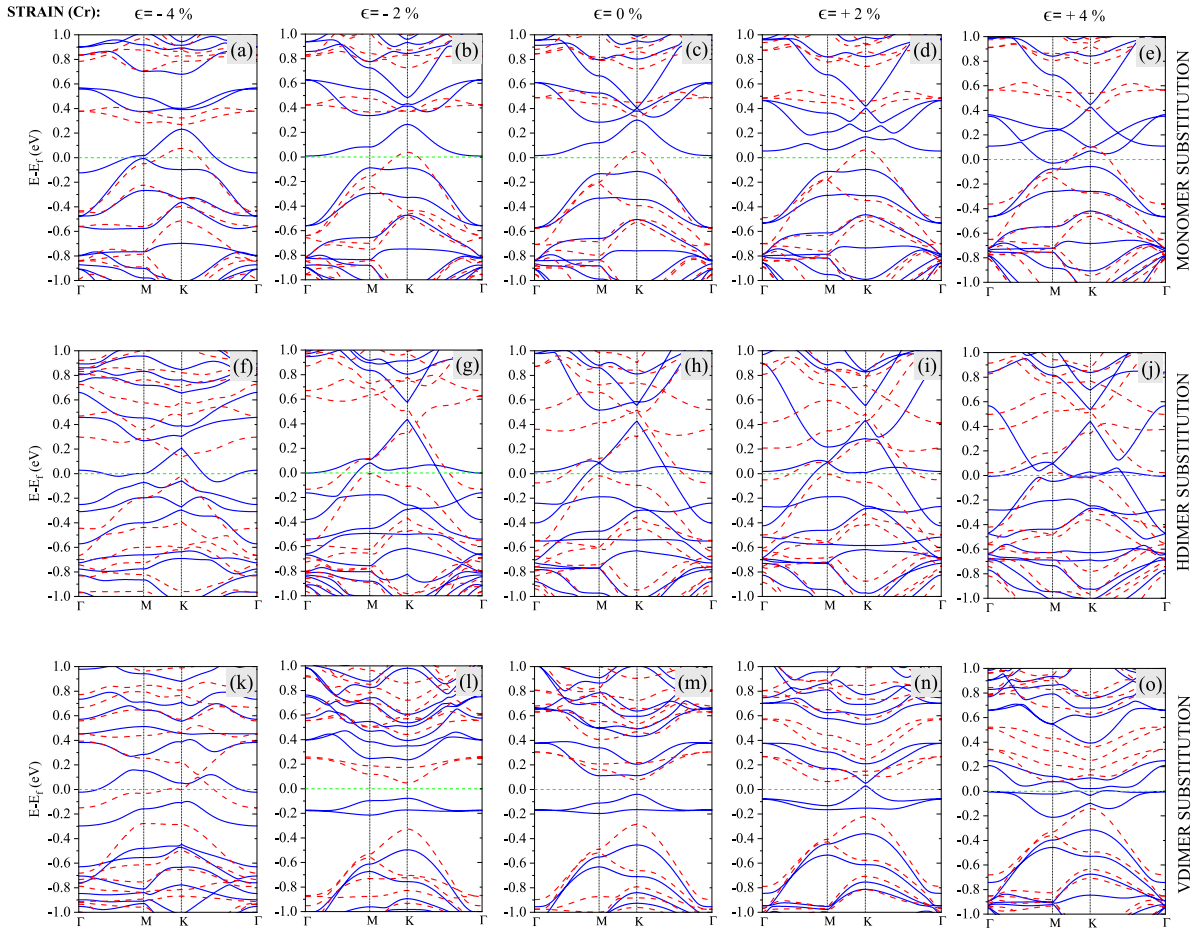

Fig. C.7. The electronic energy spectrum of silicene under selected values of biaxial strain, from −4% to +4%, for Cr doping in case of three types of substitution: (a–e) monomer, (f–j) HDimer, and (k–o) VDimer. The solid (blue) and dashed (red) lines correspond to the spin-up and spin-down, respectively.

Declaration of competing interest

The authors declare that they have no known competing financial interests or personal relationships that could have appeared to influence the work reported in this paper.

Acknowledgments

We thank Prof. J. Barnaś for valuable discussions and reading this manuscript. This work has been supported by the Norwegian Financial Mechanism 2014–2021 under the Polish–Norwegian Research Project NCN GRIEG "2Dtronics" no. 2019/34/H/ST3/00515.

Appendix A. The electronic band structure of undoped silicene

To understand the interplay of the effects due to strain and doping, it is advisory to analyse the impact of strain on the undoped silicene. In Fig. 5 we present the electronic structure of pure silicene monolayer subject to a biaxial strain from −8% to +8%, and in the absence of spin–orbit coupling. It is evident, that the strain has a significant a impact on the band structure. However, the band gap remains zero as in the absence of strain. The valence and conduction bands tough each other at the Dirac K points, independently of the strain, which preserves semimetallic behaviour of the system with increasing strain, either tensile or compressive. The strain does not open a gap, however, it modifies asymmetry of the Dirac cones.

Appendix B. The fat-band structures

As already mentioned above, due to hybridization of the 3d-impurity states and those of pure silicene, the band structure becomes remarkably modified by doping. Each state of the doped system includes then, in general, contributions from the 3d-transition metals as well as due to the silicon atoms. We show this explicitly in Fig. B.6, where the two contributions are indicated with different colours for silicene monolayer doped with Cr-atoms. We show there the fat-bands for Cr-Monomers, Cr-HDimers and Cr-VDimers. From this figure one can evaluate whether a particular band contributes to transport or not, and this was taken into account when determining the band gaps presented in Table 1.

Appendix C. The electronic band structure of silicene doped by Cr atoms from collinear calculations

In this section we present electronic spectrum of silicene monolayer doped by Cr atoms in the presence of biaxial strain. As before we consider the three types of substitutions discussed in the main text. The electronic structure has been obtained from collinear (spin polarized) calculations. This procedure is applicable in the absence of spin–orbit interaction, where spin-up and spin-down states are well defined. Fig. C.7 presents the corresponding electronic band dispersions, where the solid blue and dashed red lines correspond to the spin-up and spin-down states, respectively.

References

[1] A. Bernard, et al., Appl. Phys. Lett. 96 (2010) 18.
[2] H. Enriquez, et al., J. Phys.: Condens. Matter 24 (2012) 31.
[3] B. Feng, et al., Nano Lett. 12 (7) (2012) 3507.
[4] B. Lalmi, et al., Appl. Phys. Lett. 97 (2010) 22.
[5] Li Tao, et al., Nature Nanotechnol. 10 (2015) 227.
[6] A. Kumar, P.K. Ahluwalia, Physica B 419 (2013).
[7] A. Kumar, P.K. Ahluwalia, Eur. Phys. J. B 85 (2012) 6.
[8] A. Kumar, P.K. Ahluwalia, Mater. Chem. Phys. 135 (2012) 2–3.
[9] A. Kumar, P.K. Ahluwalia, Physica B 407 (2012) 24.
[10] Yuliang Mao, et al., J. Phys.: Condens. Matter 30 (2018) 36.
[11] S.-H. Chen, J. Magn. Magn. Mater. 405 (2016) 317.
[12] S. Chowdhury, D. Jana, Rep. Progr. Phys. 79 (2016) 12.
[13] N. Ding, et al., RSC Adv. 7 (2017) 17.
[14] N.D. Drummond, V. Zolyomi, V.I. Fal'Ko, Phys. Rev. B 85 (2012) 075423.
[15] M. Ezawa, Phys. Rev. Lett. 109 (2012) 055502.
[16] A. Dyrdal, J. Barnaś, Phys. Status Solidi RRL 6 (2012) 340.
[17] M. Gmitra, et al., Phys. Rev. B 80 (2009) 235431.
[18] Xi-Xi Guo, et al., Appl. Surf. Sci. 341 (2015) 69.
[19] Zhi-Xin Guo, et al., Phys. Rev. B 87 (2013) 235435.
[20] M. Wierzbicki, J. Barnaś, R. Swirkowicz, Phys. Rev. B 91 (2015) 165417.
[21] M. Wierzbicki, J. Barnaś, R. Świrkowicz, J. Phys.: Condens. Matter 27 (2015) 485301.
[22] I. Weymann, M. Zwierzycki, S. Krompiewski, Phys. Rev. B 96 (2017) 115452.
[23] S. Krompiewski, J. Magn. Magn. Mater. 534 (2021) 168036.
[24] S. Krompiewski, G. Cuniberti, Phys. Rev. B 96 (2017) 155447.
[25] N. Ghasemi, A.A. Kordbacheh, M. Berahman, J. Magn. Magn. Mater. 473 (2019) 306.
[26] M. Jafari, A.A. Kordbacheh, S. Mahdian, N. Ghasemi, Physica E 117 (2020) 113855.
[27] T. Low, F. Guinea, M.I. Katsnelson, Phys. Rev. B 83 (2011) 19.
[28] X.-L. Zhang, L.-F. Liu, Wu-M. Liu, Sci. Rep. 3 (2013) 2908.
[29] Guy Le Lay, Nature Nanotechnol. 10 (2015) 202.
[30] G. Cao, Y. Zhang, J. Cao, Phys. Lett. A 379 (2015) 1475.
[31] P. Zhang, et al., Phys. Lett. A 376 (2012) 1230.
[32] M. Chu, et al., Annu. Rev. Mater. Res. 39 (2009) 203.
[33] M.L. Lee, et al., J. Appl. Phys. 97 (2005) 011101.
[34] R. Qin, et al., AIP Adv. 2 (2012) 022159.
[35] M. Farokhnezhad, M. Esmaeilzadeh, K. Shakouri, Phys. Rev. B 96 (2017) 205416.
[36] B. Mohan, A. Kumar, P.K. Ahluwalia, Physica E 61 (2014) 40.
[37] V.M. Pereira, A.H. Castro Neto, N.M.R. Peres, Phys. Rev. B 80 (2009) 045401.
[38] Y. Hasegawa, et al., Phys. Rev. B 74 (2006) 033413.
[39] B. Wunsch, F. Guinea, F. Sols, New J. Phys. 10 (2008) 103027.
[40] M. Farjam, H. Rafii-Tabar, Phys. Rev. B 80 (2009) 167401.
[41] R. Faccio, et al., Condens. Matter 21 (2009) 285304.
[42] S. Grimme, et al., J. Chem. Phys. 132 (2010) 154104.
[43] S. Grimme, J. Comput. Chem. 27 (2006) 1787.
[44] Synopsys QuantumATK code package: https://www.synopsys.com/silicon/quantumatk.html.
[45] Søren Smidstrup, et al., J. Phys.: Condens. Matter 32 (2020) 015901.
[46] M.J. van Setten, et al., Comput. Phys. Comm. 226 (2018).
[47] M. Ernzerhof, G.E. Scuseria, J. Chem. Phys. 110 (1999) 5029.
[48] M.T. Yin, Marvin L. Cohen, Phys. Rev. B 25 (1982) 7403.
[49] K. Burke, J. Chem. Phys. 136 (2012) 150901.
[50] L.C. Lew Yan Voon, Chin. Phys. B 24 (2015) 087309.
[51] K. Takeda, K. Shiraishi, Phys. Rev. B 50 (1994) 14916.
[52] L.C. Lew Yan Voon, Physical properties of silicene, in: M. Spencer, T. Morishita (Eds.), Silicene, in: Springer Series in Materials Science, vol. 235, Springer, Cham, 2016.
[53] S. Kansara, S.K. Gupta, Y. Sonvane, Comput. Mater. Sci. 141 (2018) 235.
[54] S. Lebegue, O. Eriksson, Phys. Rev. B 79 (2009) 115409.
[55] T. Björkman, J. Chem. Phys. 141 (2014) 074708.
[56] J.-A. Yan, et al., Phys. Rev. B 91 (2015) 245403.
[57] Z. Ni, Zeyuan, et al., Nano Lett. 12 (2012) 113.
[58] G. Liu, et al., Europhys. Lett. 99 (2012) 17010.
[59] P.T. Kaloni, Y.C. Cheng, U. Schwingenschlögl, J. Appl. Phys. 113 (2013) 104305.
[60] T.M.G. Mohiuddin, et al., Phys. Rev. B 79 (2009) 205433.
[61] Georgia Tsoukleri, et al., Small 5 (2009) 2397.
[62] M. Huang, et al., Nano Lett. 10 (2010) 4074.
[63] S. Bertolazzi, J. Brivio, A. Kis, ACS Nano 5 (2011) 9703.
[64] M.V. Fischetti, S.E. Laux, J. Appl. Phys. 80 (1996) 2234.
[65] R. Roldán, et al., Condens. Matter 27 (2015) 313201.
[66] X. Wang, et al., Nano Lett. 15 (2015) 5969.
[67] C. Si, Z. Sun, F. Liu, Nanoscale 8 (2016) 3207.
[68] Z. Khatibi, A. Namiranian, S.F.K.S. Panahi, Physica B 565 (2019) 33.
[69] Z. Khatibi, A. Namiranian, F. Parhizgar, Diam. Relat. Mater. 92 (2019) 228.
[70] X. Peng, Q. Wei, A. Copple, Phys. Rev. B 90 (2014) 085402.
[71] Ch. Shao, et al., Nanoscale Microscale Thermophys. Eng. 21 (2017) 201.

Chapter 5

Electronic and magnetic properties of V-based TMDCs

5.1 Introduction and aims

Two-dimensional transition metal dichalcogenides (2D-TMDCs) are such a versatile class of 2D materials due to the variety of electronic phases and tunable magnetic properties. As discussed in detail in section 2.2.2, TMDCs are described by the formula MX_2, where M represents a transition metal (such as Mo, W, Nb, or V) and X is a chalcogen (S, Se, or Te). To date, writing this thesis, there are around 70 combinations of Transition metal elements with the chalcogenides [95], and among them, V-based TMDCs have attracted more attention due to their intrinsic magnetic behavior and potential applications in spintronics, quantum computing, and nanoelectronic devices [153]. The primary interest in van der Waals (vdW) magnetic materials was related to the discovery of the long-range ferromagnetism in atomically thin crystals such as CrI_3 and $Cr_2Ge_2Te_6$. This led to more research on other vdW systems where magnetism might be either inherent or induced by external perturbations. V-based dichalcogenides, VX_2 (X = S, Se, Te), can be in different polymorphs, particularly in the trigonal prismatic (2H) and the octahedral (1T or T) phases. These polymorphs are not only different in their atomic coordination but also in their electronic correlations and magnetic orders. For example, the T-phase, which is characterized by octahedral coordination of sulfur atoms around vanadium atoms, has shown interesting electronic results, offering promising prospects for new magnetic devices. From an experimental perspective, there are advanced methods in synthesis and exfoliation that allow the isolation of the monolayer and bilayer of TMDCs. Such ultrathin layers show properties that can significantly change from their bulk counterparts. For instance, while most of the TMDCs are non-magnetic in bulk form, monolayer or bilayer of V-based dichalcogenides can show ferromagnetic or antiferromagnetic behavior depending on the number of layers, the stacking arrangement, and the strength of the interlayer interactions. Moreover, external factors like mechanical strain can tailor their electronic band structure, magnetic anisotropy energy, exchange interactions, and Curie temperatures.

In this thesis, I have performed a comprehensive theoretical analysis of the electronic and magnetic properties of 2D Vanadium-based TMDCs (VX_2 with X = S, Se, and Te). The results of this study are included in the articles [P2 and P3]. In the article [P2], I investigated these materials in the H-phase. A detailed DFT calculations combined with effective spin Hamiltonian approaches were used to investigate the band structures, exchange interactions, and magnetic anisotropies in both monolayer and bilayer of VX_2. The study emphasized that while the magnetic ground state of monolayers is generally ferromagnetic, bilayers may exhibit antiferromagnetic interlayer coupling, making them natural candidates for 2D spin-valve devices, which we will discuss in chapter 6. Furthermore, the obtained results showed the influence of the interplay between Coulomb correlations (Hubbard U term) and spin-orbit coupling on the shapes of the magnetic and electronic behavior of these materials. In the article [P3], I study how tensile and compressive strains can significantly modify the electronic band structure and magnetic anisotropy of the monolayer and bilayer VS_2 in T-phase. Key parameters like exchange coupling constants and Curie temperature have been found to be highly sensitive to the applied strain, which suggests that strain engineering can be an essential way of tuning the magnetism in such inherent systems. Together, these studies involve the understanding of how intrinsic properties and external perturbations (such as strain) are essential in the electronic and magnetic characteristics of vanadium-based TMDCs. The main aim in this direction of my study is to establish principles for next-generation 2D spintronic devices based on V-based TMDCs. Showing the strain-dependent modification of band gaps,

magnetic moments, and exchange interactions, we provide a framework that not only deepens the fundamental understanding of 2D magnetism in TMDCs but also helps in experimental efforts toward engineering materials with desired functionalities.

5.2 Reprint of article [P2]

On the subsequent pages, we append a reprint with permission:

[P2] **Mirali Jafari**, Wojciech Rudziński, Józef Barnaś, Anna Dyrdał

Electronic and magnetic properties of 2D vanadium-based transition metal dichalcogenides

Journal of Scientific Reports 13.1 (2023): 20947

DOI: 10.1038/s41598-023-48141-1

[1]Copyright on any research article in open access (OA) journals published by Springer Nature is retained by the author(s). Authors grant Springer Nature a license to publish the article and identify itself as the original publisher. Authors also grant any third party the right to use the article freely if its integrity is maintained and its original authors, citation details, and publisher are identified. OA articles in Springer Nature journals are predominantly published under Creative Commons Attribution v4.0 International license (CC BY), according to Global Open Research Support.

Performing this work, I aimed to determine the ground-state magnetic configuration of VX_2 materials in both mono- and bi-layers of Vanadium-based TMDCs. I achieved this by evaluating how the phase structure and inter-layer coupling can influence the magnetic properties of the materials, such as magnetic anisotropy energy or Heisenberg exchange coupling parameters.

5.2.1 Methods

I have used Density Functional Theory (DFT) using Quantum ATK code packages combined with other post-processing codes like Vampire. The GGA+U method was applied to better capture the electron-electron correlation effects in Vanadium atoms. To include van der Waals interactions between layers and the intralayer atomics, we have used the Grimme DFTD2 correction. The ground state for each VX_2 structure has been calculated as the total energy difference between two FM and AFM spin configurations. Using the Force theorem, the magnetic anisotropy energy (MAE) has been calculated, and other parameters like exchange coupling constants were computed using the original Liechtenstein-Katsnelson-Antropov-Gubanov (LKAG) [191] method and using the TB2J code package [409]. Magnon spectra have been calculated using DFT calculations and compared with analytical spin-wave theory. I have used Vampire code [410] for magnetic dynamic properties like hysteresis loop or estimation of Curie temperature.

5.2.2 Main results

- **Atomic structure:** The structures have both H- and T-phases, so we have chosen the Hexagonal phases in this research. After optimization, each structure shows changes in its geometry due to the chalcogen's atomic number, the interatomic distances between atoms, and, eventually, the lattice constant of the structure. Among the investigated structures, bilayer VTe_2 shows the largest interlayer spacing, attributed to the larger atomic radius of tellurium compared to sulfur and selenium. These minor changes from monolayer to bilayer and different chalcogen sizes directly change the electronic and magnetic behavior.
- **Electronic Band Structure:**Using the DFT, the spin-resolved band structures have been calculated for all VX_2 configurations. The choice of chalcogen significantly modifies the energy band gap and the system's behavior. For instance, the monolayer of VS_2 is ferromagnetic and a semiconductor with a 0.35 eV gap (within GGA+U approximation). However, the bilayer of this material with the same ground state is half-metallic, exhibiting spin-polarized electronic states at the Fermi level — a key feature desirable for spintronic applications. In contrast, bilayer VSe_2 reveals antiferromagnetic coupling between monolayers with a notable semiconducting energy band gap. The monolayer of Vanadium di-telluride is also half-metallic, while the bilayer shows metallic behavior. A wide range of properties for various numbers of layers and different X atoms in the VX_2 structure, is promising platform for electronic devices.
- **Magnetic Anisotropy Energy (MAE):** The MAE results show an easy-plane anisotropy for all investigated structures, where energy required for out-of-plane (perpendicular) magnetization is higher for the bilayer than for monolayers. The trend depends on the increasing atomic number of the chalcogen, which correlates with bond lengths, where VS_2 has the weakest MAE and VTe_2 has the strongest. Understanding the MAE orientation is one of the key

points in designing devices that require specific in-plane or out-of-plane magnetization.

- **Curie-Temperature and hysteresis loop:** The Curie temperatures (T_C) in our research have been calculated using two different methods, namely, mean-field approximation and Monte Carlo simulations. Monolayer, VS_2 with the highest J, has the Curie temperature well above the room temperature and has potential in practical applications. In case of bilayers, the Curie temperatures decrease slightly due to the interlayer interactions. Still, in the case of VSe_2, it remains significant, making it a good candidate for the 2D spin-valve component. From the hysteresis loops, one can observe the remarkable coercivity differences among the different VX_2 materials, where the VS_2 has the highest coercivity.
- **Spin-wave excitations:** The spin-wave excitations in VX_2 bilayers have been calculated using DFT and compared with analytical spin-wave theory methods, and both results agree. The effect of interlayer coupling and exchange interactions is essential in defining magnon energy.

scientific reports

Check for updates

OPEN

Electronic and magnetic properties of 2D vanadium-based transition metal dichalcogenides

Mirali Jafari[1], Wojciech Rudziński[1], Józef Barnaś[1,2] & Anna Dyrdał[1]✉

In this paper, electronic and magnetic properties of monolayers and bilayers of Vanadium-based transition metal dichalcogenides VX_2 (X = S, Se, Te) in the H phase are investigated theoretically using methods based on DFT calculations as well as analytical methods based on effective spin Hamiltonians. The band structure has been computed for all systems, and then the results have been used to determine exchange parameters and magnetic anisotropy constants. These parameters are subsequently used for the determination of the Curie temperatures, hysteresis curves, and energy of spin-wave excitations. In the latter case, we compare analytical results based on effective spin Hamiltonian with those determined numerically by Quantum ATK software and find a good agreement. The determined Curie temperature for VTe_2 monolayers and bilayers is below the room temperature (especially that for bilayers), while for the other two materials, i.e. for VS_2 and VSe_2, it is above the room temperature, in agreement with available experimental data.

Van-der-Waals (vdW) magnetic materials are currently of great interest as they are considered as future materials for building two-dimensional (2D) electronic and spintronic devices, including atomically thin spin valves, nonvolatile memory elements, and gates for information processing. The most fascinating aspects of the physics observed in van-der-Waals materials are the magnetism and magnetic phase transitions emerging in monolayers and in a few layers of these 2D crystals. The discovery of ferromagnetism in single layers of CrI_3[1] and $Cr_2Ge_2Te_6$[2] initiated an enormous interest in magnetic 2D vdW crystals. These crystals now serve as a large platform for basic research on 2D magnetism, and additionally allow to mimic the physics of ideal Ising, Kitaev or Heisenberg models and magnetic phase transitions induced by external gate voltages or strain. The magnetic ground state of 2D vdW crystals depends, among others, on their crystallographic phase, stacking geometry, and possible twisting of adjacent monolayers. The current worldwide interest in magnetic vdW crystals follows not only from their novel and interesting physics, but also from their potential for applications (e.g. in quantum computing, topological magnonics, spintronics, optoelectronics, and others)[3].

Recently, two main groups of magnetic vdW materials have been focusing great attention: transition metal trihalides, with CrI_3 being thought of as a prototype of 2D magnetic crystal, and magnetic transition metal dichalcogenides (TMDCs). In this paper, we focus on Vanadium-based dichalcogenides, VX_2 (X = S, Se, and Te). Two different polymorphs of VX_2 materials are currently known; the trigonal prismatic crystallographic structure (2H, D3h) and the octahedral (1T, D3d) one[4–6], as presented schematically in Fig. 1. Additionally, a distorted octahedral ($1T_d$) phase has been identified[7]. These materials consist of monolayers of VX_2, that are weakly coupled by van der Waals forces and therefore can be easily exfoliated down to a single monolayer or a few-layer form. A monolayer of VX_2 material consists of a hexagonal atomic plane of Vanadium atoms, that is sandwiched between two chalcogen (X) atomic planes. However, the positions of X atoms are different in different phases. The corresponding unit cell includes one Vanadium atom and two chalcogen atoms. In the case of bilayers (BLs) of the hexagonal 2H phase, the V (X) atoms of the top layer are above the X (V) atoms of the bottom layer. In turn, in the bilayers of the T1 phase, the V atoms of the top layer are above the V atoms of the bottom layer. This can be clearly seen in the top and side views of the bilayers, shown in Fig. 1.

While there are several theoretical studies on the monolayers and bilayers of VX_2 materials in the 2H phase[8,9], and these materials were successfully synthesized in the bulk and multilayer forms[6], VSe_2 and VTe_2 in the trigonal (1T) phase have been synthesized only in the monolayer form.[10–13]. Therefore, in this paper, we present the results of our detailed analysis of the monolayers and bilayers of Vanadium-based transition metal dichalcogenides, VX_2 (where X = S, Se, Te), in the H-phase only. In the beginning, we focus on electronic properties, especially on the

[1]Department of Mesoscopic Physics, ISQI, Faculty of Physics, Adam Mickiewicz University in Poznań, ul. Uniwersytetu Poznańskiego 2, 61-614 Poznań, Poland. [2]Institute of Molecular Physics, Polish Academy of Sciences, ul. M. Smoluchowskiego 17, 60-179 Poznań, Poland. ✉email: adyrdal@amu.edu.pl

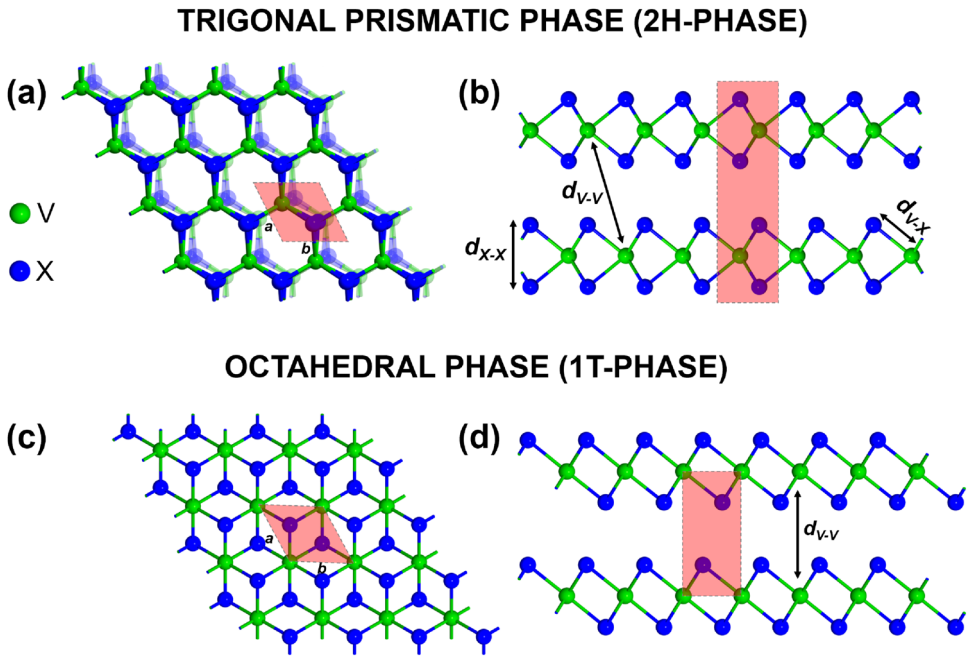

Figure 1. Schematic structure of the 2H phase of VX_2 monolayer and bilayer structures. Top (**a**) and side (**b**) views, as well as the elementary units are shown. Various bondlengths are also indicated in (**b**). For comparison, the top and side views of the T-phase bilayer are also shown in (**c**) and (**d**).

band structures of these materials. Then, we evaluate the basic magnetic parameters, like magnetic moments of Vanadium atoms, exchange parameters, and magnetic anisotropy constants. These parameters are subsequently used in the simulations of Curie temperature, magnetic hysteresis curves, and spin wave excitations. Details of the methods used in calculations are described in section METHOD.

We also note that though there is relatively broad literature on TMDCs, their behavior, especially in the monolayer and bilayer forms, is still under discussion. This concerns even the magnetic ground state as numerical results based on DFT calculations depend on many approximations and assumptions. Our results present a contribution to this discussion—especially our investigation of bilayers with antiferromagnetic coupling between the two monolayers is of particular interest, as such bilayers are natural candidates for 2D spin valves.

Results

Atomic structure

Figure 1a and b show respectively the top and side views of the atomic structure in a bilayer of H-phase dichalcogenides VX_2. Each Vanadium atom is surrounded by six nearest-neighbour chalcogen atoms, and the corresponding lattice parameters a and b (see Fig.1a) are equal, $a = b$, in honeycomb structures. The structural lattice parameters and bondlengths after optimization are presented in Table 1 for both monolayers and bilayers.

From this table follows that there is no significant change in the lattice parameters when the number of layers increases from N = 1 to N = 2. However, when the atomic number of chalcogen atoms increases, the lattice constant increases as well. Additionally, the bondlengths between Vanadium and X atoms (d_{V-X}) and between the chalcogenide atoms (d_{X-X}) also increase with the increasing atomic number of chalcogen atoms. The obtained results are in very good agreement with earlier studies[8,14]. From Table 1 also follows, that the bondlengths are rather weakly modified when the number of layers N increases from 1 to 2, similarly as in the case of lattice

VX_2	N	a [Å]	d_{V-V} [Å]	d_{V-X} [Å]	d_{X-X} [Å]
VS_2	1	3.17159	-	2.36	2.98
	2	3.17147	6.30	2.36	2.97
VSe_2	1	3.31934	-	2.49	3.20
	2	3.31971	6.66	2.49	3.19
VTe_2	1	3.59006	-	2.72	3.53
	2	3.59069	7.15	2.71	3.52

Table 1. Optimized lattice constants a, and the bondlengths d_{V-X}, d_{V-V}, and d_{X-X} between various atoms, as defined in Fig. 1. N indicates the number of layers, N = 1 for monolayers and N = 2 for bilayers.

parameters, where the change is only 0.31%. However, the changes associated with different X atoms can be up to 12.91% and are quite significant. This is a consequence of the increasing radius of atomic orbitals with increasing atomic number, which in turn leads to increasing bondlengths and subsequently weaker bonding in VTe_2 as compared to VS_2. The intralayer distance between two nearest-Vanadium atoms is remarkably different from the interlayer one. The optimized structures, including also the Van-der-Waals correction, show that the largest interlayer distance is for VTe_2 while the lowest distance is for VS_2.

Electronic bandstructure

Before calculating spin-resolved electronic band structures of the VX_2 (X = S, Se, and Te) monolayers and bilayers, one needs to determine first the corresponding magnetic ground states. Therefore, for each system we calculated its total energy in three different spin configurations: non-magnetic (NM), ferromagnetic (FM), and antiferromagnetic (AFM). In all calculations, the NM state was the most unstable one. Then, we calculated the total energy difference between the FM and AFM states, $\Delta E = E_{AFM} - E_{FM}$. The negative sign of ΔE indicates that the AFM state is stable, while the positive sign shows the FM state is stable. The obtained ground states for all systems under consideration are given in Table 2. From these data follows that all the monolayers have a ferromagnetic ground state. However, for the bilayer structures, different materials may have different ground states. The total energy in the antiferromagnetic spin configuration of VS_2 is larger than that in the ferromagnetic case, so the ground state is FM. On the contrary, for VSe_2 and VTe_2, we found that magnetic moments of the two V atomic planes are arranged antiferromagnetically in the ground state, i.e. the interlayer exchange coupling is antiferromagnetic, in agreement with other works[9,15–18].

From the DFT calculations, we have determined the magnetic moments of Vanadium atoms for all the systems under consideration. These moments have been calculated within the GGA approximation with Coulomb correction U included, referred to in the following as the GGA + U approximation. The Hubbard parameter U describes the on-site Coulomb interaction between electrons, and the impact of finite U on electronic spectrum in VX_2 dichalcogenides was already studied in the relevant literature. Especially, Ref. [19] gives clear arguments that U = 2 is an appropriate approximation for VX_2 materials. Following this paper, as well as other relevant pulications [8,20–22], we assumed U = 2 eV in our numerical calcuations. The obtained magnetic moments of Vanadium are presented in Table 2. From this table and also from other calculations (not shown here) follows that the Vanadium ion preserves absolute value of its magnetic moment when the number of layers varies from one to two—independently of the approximation used in calculations. However, the Coulomb correlation U leads to a slightly larger magnetic moment in comparison to that obtained in the GGA calculations with and without spin-orbit coupling (SOC) included. From our calculations follows that the magnetic moment of V ion in monolayers is the lowest one for VS_2, where is equal to 1.267 μ_B (μ_B is the Bohr magneton). In turn, in VSe_2 and VTe_2 it is 1.435 μ_B and 1.679 μ_B, respectively.

Figure 2 shows the electronic band structures of the monolayers and bilayers of VX_2 along the high symmetry points in the Brillouin zone. For both, monolayers and bilayers, the calculations are based on the GGA + U approximation, and additionally we also show there the band structures in the GGA approximation with spin-orbit interaction included (GGA + SOC approximation). From comparison of the results for GGA (not shown) and GGA + SOC approximations follows that the spin-orbit interaction does not lead to significant modifications in the band structure. This is also consistent with the results obtained in Ref. [8].

In the case of band structures calculated in the GGA+SOC approximation, we distinguish in Fig. 2 contributions from the V and X atoms. Generally, these results demonstrate that the main contribution to the bands near the Fermi level comes from the Vanadium atoms. As illustrated in Fig. 2, in the VS_2 monolayers and bilayers, the orbital d_{z^2} of Vanadium has a large contribution to the valance band maximum (VBM) near the Γ point, while for the conduction band minimum (CBM) the Vanadium d_{xy} orbital dominates at the M point. A similar situation happens also in the monolayers and bilayers of VSe_2, but with the contribution of $d_{x^2-y^2}$ orbitals of Vanadium dominating for the VBM at the K point and a combination of the d_{z^2} and d_{xy} orbitals dominating for the CBM at the M point. Regarding the VTe_2, the mixture of d_{yz} and d_{xz} states of Vanadium dominates for the VBM at the Γ point, while the d_{z^2} and d_{xy} orbitals dominate for the CBM around the M point.

Basic features of the electronic structure obtained in the GGA+U and GGA+SOC approximations, especially the bandgaps, are listed in Table 2. From this table follows that in the GGA+U approximation, the ferromagnetic VS_2 monolayers display semiconducting behaviour (with the gap of 0.35 eV), while the bilayers are then half-metallic due to a finite density of states at the Fermi level in the spin-up band. In turn, in the GGA + SOC calculations, both monolayers and bilayers have metallic properties. In the case of VSe_2, both monolayers and bilayers reveal semiconducting behaviour with the gaps in the GGA + U calculations equal to 0.55 eV for the monolayers and 0.50 eV for the bilayers. This behaviour also appears in the GGA + SOC calculations, but with the band gaps reduced to 0.29 eV and 0.17 eV for the monolayers and bilayers, respectively. However, the monolayers of VTe_2 display half-metallic behaviour in the GGA + U calculations, while the bilayers are then metallic. In the GGA + SOC calculations, both monolayers and bilayers are semiconducting with narrow gaps equal to 0.11 eV for the monolayer and 0.10 eV for the bilayer structures.

When comparing results of various approximations, we arrived at the conclusion that including spin-orbit coupling (SOC) does not make significant quantitative changes in the band structure, though some qualitative differences may appear due to spin mixing induced by SOC. We verified that GGA + SOC calculations give results which are quantitatively and also qualitatively similar to those obtained in the GGA approximation (not shown). From Ref. [8] follows that the results of GGA+U+SOC calculations are quantitatively similar to those of GGA + U. In turn, including Coulomb correlation U into calculations may lead to remarkable changes in the electronic spectrum, especially in the band gaps. From the above observations one may conclude that when calculating properties that do not originate from SOC, the approximation GGA + U seems to be the appropriate one. In

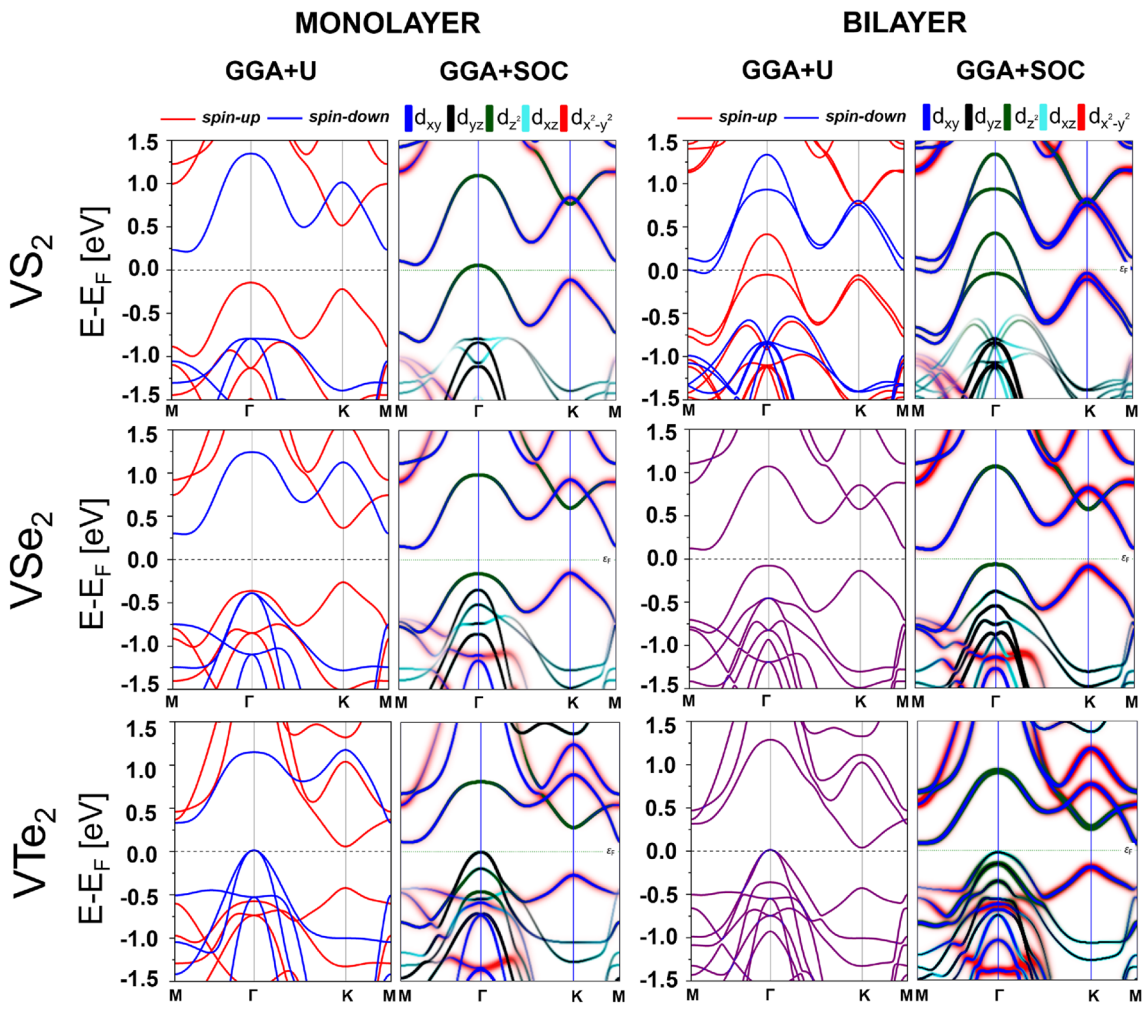

Figure 2. Spin-resolved band structures for the monolayers (first and second columns from left) and bilayers (third and fourth columns from left) of VX_2 (X = S, Se, Te) in the GGA+U approximation (first and third columns) and GGA + SOC approximation (second and fourth columns) where *d*—orbital-decomposition is added to visualize contributions of the Vanadium orbitals near the Fermi energy E_F.

VX_2	N	Ground state	Magnetic moment of V [μ_B]	Bandgap [eV]	
			GGA + U	GGA + U	GGA + SOC
VS_2	1	FM	1.267	0.35	Metallic
	2	FM	1.228	Half-metal	Metallic
VSe_2	1	FM	1.435	0.55	0.29
	2	AFM	1.437	0.50	0.17
VTe_2	1	FM	1.679	Half-metal	0.11
	2	AFM	1.709	Metallic	0.10

Table 2. Calculated ground states, magnetic moments (absolute values) of V atoms, and energy band gaps. N indicates the number of layers.

turn, when a particular property (like for instance. magnetic anisotropy) originates from SOC, then in the first approximation GGA + SOC is sufficient.

Magnetic anisotropy energy

Magnetic anisotropy energy (MAE) is an important parameter that determines the magnetisation orientation in the ground-state. This anisotropy originates from the spin-orbit coupling and can be calculated from the energy difference between relevant spin orientations using the force theorem. This theorem allows one to evaluate MAE using non-self-consistent band energies, and in general, it is defined as follows[23–25]:

$$MAE = \sum_i f_i(\theta_1, \phi_1)\epsilon_i(\theta_1, \phi_1) - \sum_i f_i(\theta_0, \phi_0)\epsilon_i(\theta_0, \phi_0), \quad (1)$$

where $f_i(\theta, \phi)$ refers to the occupation factor for the band i (i includes also k-point index), with (θ, ϕ) and $\epsilon_i(\theta, \phi)$ describing the spin orientation and the corresponding band energy, respectively. In this paper, we focus on the perpendicular (out-of-plane) and in-plane anisotropies. When the system is magnetically isotropic (or nearly isotropic) in the plane, then the perpendicular anisotropy is defined as $MAE = E_{[100]} - E_{[001]}$ (or $MAE = E_{[010]} - E_{[001]}$), with the x, y axes in the layer plane and the z axis perpendicular to the layer. Thus, positive value of MAE corresponds to the perpendicular easy axis, while negative value to the perpendicular hard axis, i.e. to easy-plane anisotropy.

Table 3 shows MAE (per unit cell) for the materials considered in this paper. The perpendicular MAE for the monolayer of VS_2, VSe_2, and VTe_2 is − 0.2276 meV, − 0.7143 meV, and − 1.9431 meV, respectively. The MAE of the bilayers, is approximately twice as large as that of the corresponding monolayer. The calculations show, that MAE has a negative sign for the monolayers and bilayers, which indicates that the anisotropy is of easy-plane type. The dependence of MAE on the polar angle (angle between magnetization orientation and axis perpendicular to the layer plane) is shown in Fig. 3 for all the systems under consideration.

As presented in Table 3, we have also determined the in-plane easy-axis MAE which is defined as the difference between two in-plane magnetization directions namely, $MAE = E_{[100]} - E_{[010]}$. Because of the symmetry of the studied systems, this anisotropy is negligibly small, of an order of micro/nano eV, which indicates its insignificant role in the magnetization processes, though it determines the magnetization orientation in the zero temperature limit. We note, that our calculations are for unstrained structures. It is however known that external strain has a significant impact on the magnetic anisotropy, and can remarkably change the anisotropy constants.

Exchange parameters, Curie temperature and hysteresis loops

A very important parameter, especially when one considers application possibilities, is the Curie temperature T_C. In this paper, we evaluate T_C of VX_2 monolayers and bilayers within two different methods: the mean-field

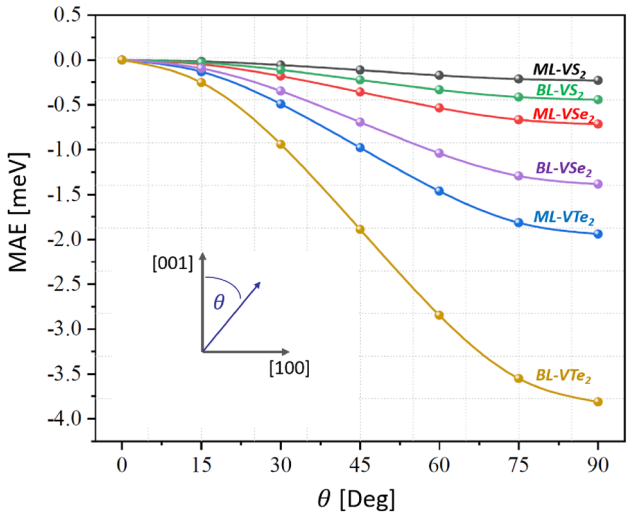

Figure 3. Angular dependence of the magnetic anisotropy energy per unit cell, MAE, of monolayers (ML) and bilayers (BL) of V-based TMDs. The anisotropy energy is shown as a function of the polar angle θ for the azimuthal angle equal to 0 (see the inset for the definition of θ).

		MAE		*J*$_{ij}$ [meV]		
VX_2	N	Perpendicular [meV]	In-plane [neV]	J_1	J_2	J_{int}
VS_2	1	− 0.22	3.58	25.68	− 2.13	–
	2	− 0.44	− 0.12	26.67	− 1.63	0.50
VSe_2	1	− 0.71	− 15.28	19.52	− 0.94	–
	2	− 1.38	− 10.69	18.60	− 1.15	− 0.05
VTe_2	1	− 1.93	− 35.79	9.84	− 0.78	–
	2	− 3.81	18.93	8.69	− 0.66	− 0.11

Table 3. Calculated perpendicular and in-plane magnetic anisotropy energy (MAE) per unit cell within the GGA + SOC approximation, and the exchange coupling parameters J_1, J_2, J_{int} within the GGA + U approximation.

approximation (MFA)[26] and the Monte–Carlo (MC) simulations. The corresponding calculations are based on the Heisenberg spin Hamiltonian with classical spins:

$$H = -\sum_{i,j} J_{ij} S_i . S_j - K \sum_i (S_i^z)^2, \tag{2}$$

where J_{ij} is the exchange coupling constant between V atoms located in the sites i and j, S_i is the local spin vector on the atom i, while K is the easy-plane magnetic anisotropy constant, $K < 0$. The anisotropy constant K is determined by the above calculated MAE. We take into account only the exchange coupling J_{ij} between nearest neighbours, J_1, and next-nearest-neighbours, J_2, for the intralayer interactions. In the case of bilayer structures, we also include interlayer coupling J_{int}. All the exchange parameters have been determined using the energy mapping method[27]. Contrary to the other methods, where results rely on the total energy analysis, in this method one calculates the exchange constant for a particular wave vector q using the magnetic force theorem (for more details see Ref. [26]). Table 3 shows all the exchange constants for the monolayers and bilayers of the materials under consideration, obtained in the GGA + U approximation. From this table follows that the largest exchange parameters are for VS_2, and the smallest ones for VTe_2. For the bilayers we have also determined the exchange parameter J_{int} between the two monolayers and found J_{int} =0.5 meV, -0.05 meV, and -0.11 meV for VS_2, VSe_2, and VTe_2, respectively. Positive and negative signs of J_{int} correspond to the FM and AFM interlayer coupling, respectively.

The Curie temperature, T_C, of a ferromagnet is a temperature at which the average magnetic moment becomes equal to zero due to random thermal fluctuations of the local magnetic moment orientations. With the obtained exchange parameters, the Curie temperature could be estimated using the mean field approximation method (MFA) as follows:[26]

$$T_C^{\mathrm{MFA}} = \frac{2}{3k_B} \sum_{j\mathbf{R} \neq i\mathbf{0}} J_{i\mathbf{0},j\mathbf{R}}, \tag{3}$$

where $J_{i\mathbf{0}j\mathbf{R}}$ stands for the exchange coupling parameter between the atom at site i in the main considered primitive cell (labeled with 0) and the atom at site j in a different unit cell displaced from the central one by the lattice vector $\mathbf{R}$. To find the Curie temperatures in the MFA, listed in Table 4, we performed GGA+U calculations up to the third nearest neighbours. Interestingly, the results reveal Curie temperatures close to or beyond the room temperature for most of the analyzed structures. In general, the mean-field approximation overestimates T_C when compared to experiment and other methods. This appears because the mean-field approximation neglects the role of magnetic fluctuations in the system, which in 2D are relatively large. However, T_C^{MFA} can be considered as the upper limit of Curie temperature, and we show it in Table 4 for comparison.

To get more realistic values of T_C, we used the atomistic Vampire code package[28,29] as well as the magnetic moments, MAE, exchange parameters J_1, J_2, and J_{int} obtained from the DFT calculations, and simulated magnetization vs. temperature for VX_2 monolayers and bilayers within the Monte Carlo metropolis algorithm[30,31]. The results are shown in Fig.4. To fit the magnetisation versus temperature curve, Fig. 4a and c, the Curie–Bloch equation in the classical limit was used:

$$M(T) = M_s \left(1 - \frac{T}{T_C}\right)^{\beta}, \tag{4}$$

where T is the temperature and T_C is the Curie temperature, while β is the critical exponent, which is generally different for different materials. As follows from Table 4, the Curie temperature determined by the Monte–Carlo calculations is lower than that in the mean field approximation. Anyway, all the results show that the highest T_C is for VS_2 and the lowest one is for VTe_2 materials. This difference originates from the corresponding difference in exchange coupling parameters J_1 and J_2.

Other important characteristics of magnetic materials are the relevant hysteresis loops. These loops reveal magnetization reversal processes in an external magnetic field and therefore contain information on the magnetic ground state and possible magnetic phase transitions induced by the magnetic field. In Fig. 4b and d we present the hysteresis curves for the monolayers and bilayers of VX_2.

In the simulation procedure, the system is slowly cooled down until the temperature reaches the desired value in the presence of a magnetic field H = 1T applied in the plane of the system and along the in-plane easy-axis (corresponding to a very small anisotropy). Then, the obtained spin configuration in the last step of cooling is used as the initial configuration for calculating the hysteresis curve.

Because individual monolayers are ferromagnetic, shapes of the hysteresis loops of all monolayers in Fig. 4 are similar and typical for ferromagnetic layers. As follows from Fig. 4, hysteresis loops for bilayers are similar to those for the corresponding monolayers, which indicates that the antiferromagnetic interlayer coupling does not play an important role in the hysteresis curves. This is because interlayer coupling is relatively small. For VTe_2, e.g, the energy of interlayer coupling corresponds roughly to 10 K and is much smaller than the temperature for which the hysteresis curves were calculated (50 K) and also significantly smaller than the corresponding anisotropy energy (around 38 K). An interesting feature of the hysteresis loops is the coercivity, which is the largest for VS_2 and smallest for VTe_2, just opposite to the behavior of easy-plane anisotropy constant, which is the largest for VTe_2 and smallest for VS_2. The stronger anisotropy, the more fixed is the magnetic moment to the layer plane. Accordingly, magnetization rotation is in the layer plane, where in-plane anisotropy is very small.

VX_2	N	T_C [K]		
		MFA	MC	β
VS_2	1	438.72	289.45	0.48
	2	446.95	333.06	0.39
VSe_2	1	434.01	249.69	0.46
	2	416.97	229.10	0.41
VTe_2	1	296.39	126.61	0.38
	2	268.44	119.57	0.39

Table 4. Curie temperature T_C obtained within the mean field approximation (MFA) and Monte–Carlo (MC) simulations, as well as the corresponding power factor β.

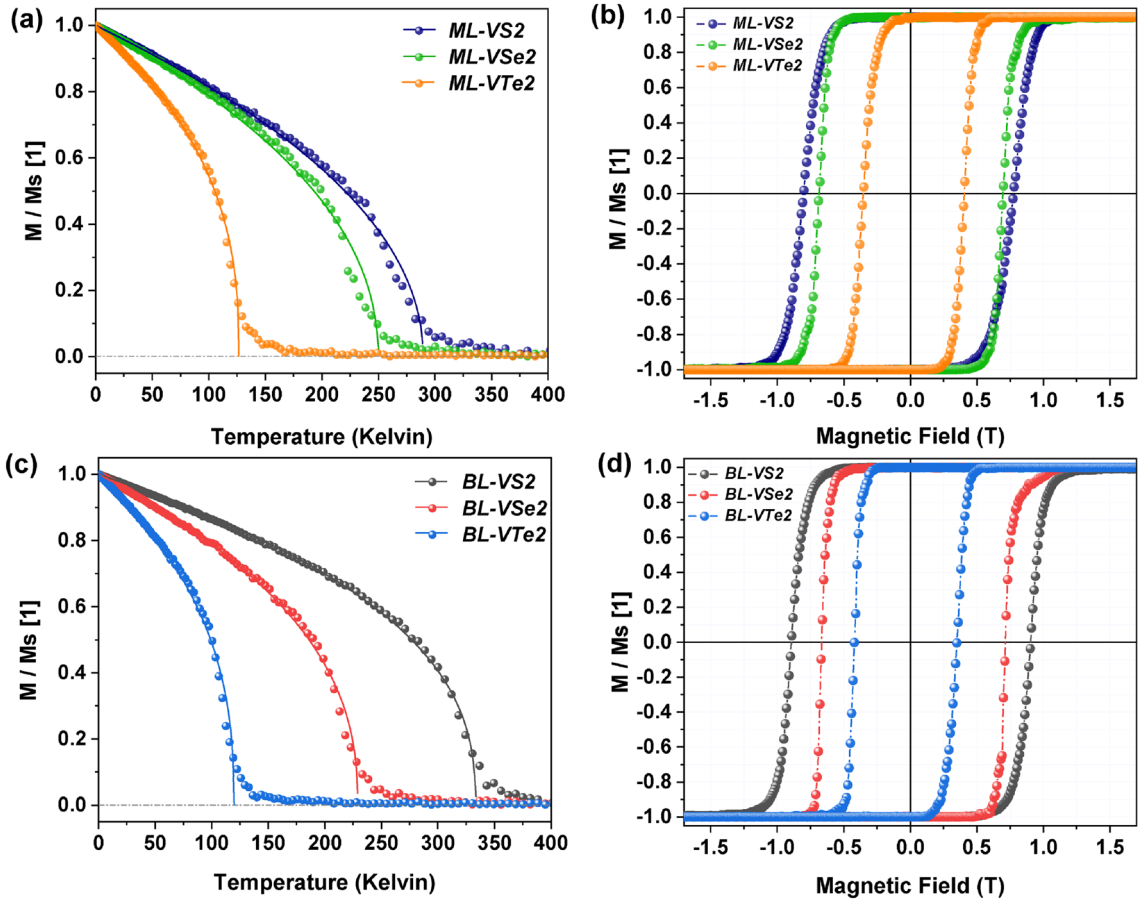

Figure 4. Magnetization normalized to the saturation magnetization M_s as a function of temperature within the Monte Carlo simulations for monolayers (**a**) and bilayers (**c**) of VX_2, and the corresponding hysteresis curves (**b**, **d**).

Dynamic properties: magnon spectra

Having found the exchange and anisotropy parameters, determined from the calculated band structures, one can calculate the energy (frequency) of the collective excited states of the magnetic moments (spins), known as spin waves or magnons. We have determined the spectra of spin waves using the corresponding code implemented into the Quantum ATK package. Dispersion curves of these modes in bilayers along basic orientations in the Brillouin zone are shown in Fig. 5 (right column), where these spectra are compared with the corresponding spectra obtained analytically, with the parameters taken from DFT calculations. The energy of spin waves determined from the analytical model in the whole Brillouin zone is presented in the left column of Fig. 5 for all the three systems considered in this paper.

The analytical calculations are based on the effective spin Hamiltonian (2), generalized by including the in-plane anisotropy:

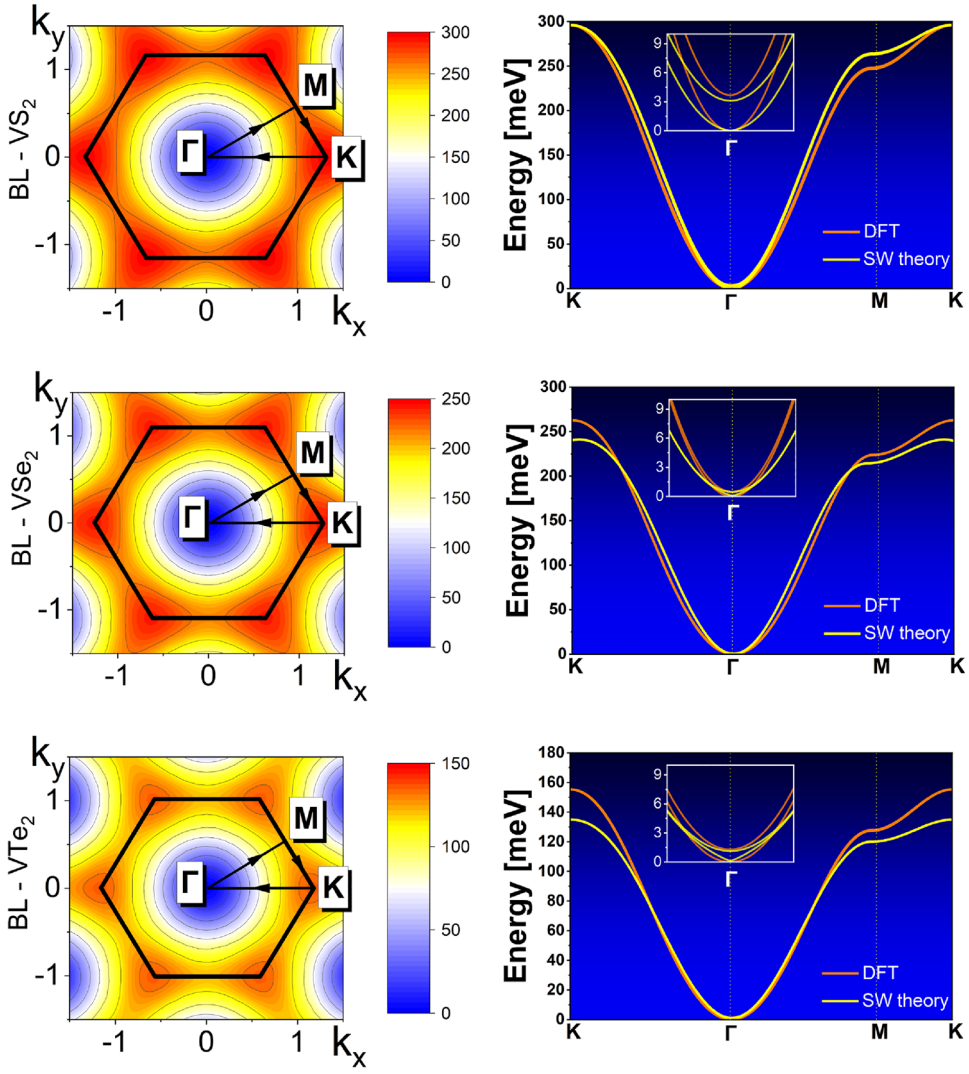

Figure 5. (Right panel) Magnon spectra in the VX_2 bilayers (X = S, Se, Te). The red lines correspond to the numerically calculated spectra using the ATK package, while the yellow lines present the spectra obtained from the analytical model. The insets show the spectra in the vicinity of the Brillouin zone center (Γ point), where splitting of the modes can be clearly seen. (Left panel) Density plots representing analytically calculated energy of spin waves in the whole Brillouin zone.

$$H = -\sum_{i,j} J_{ij} S_i \cdot S_j - K \sum_i (S_i^z)^2 - K_y \sum_i (S_i^y)^2. \tag{5}$$

Here, apart from the easy-plane anisotropy ($K < 0$), there is also a weak in-plane easy-axis anisotropy along the axis y, with K_y being the relevant anisotropy constant, $K_y > 0$. This anisotropy constant is very small in the systems under consideration (see Table 3) and does not lead to significant features in the spectra. Additionally, in the analytical model the exchange interaction is limited to the intralayer and interlayer nearest-neighbours. The intralayer (ferromagnetic) and interlayer (antiferromagnetic) exchange parameters between Vanadium atoms are taken from DFT calculations and are adapted to the spin 1/2 model (spin of Vanadium atoms). Due to the easy-plane anisotropy, the magnetic moments of vanadium atoms in equilibrium are oriented within the atomic planes. The magnon modes are determined by assuming small deviations of the spin moments from their ground state orientation. Then, the spin operators are transformed into the local magnon operators using Hollstein-Primakoff transformation. The local-magnon Hamiltonian is finally diagonalized by the Fourier transformation followed by the Bogolibov transformation. More details on this procedure will be presented elsewhere[32].

Figure 5 shows the energy of spin waves in all the bilayer systems studied in this paper. Each monolayer separately supports one magnon branch, as the monolayer contains only one magnetic atom in the elementary unit cell. Therefore, in the case of bilayers, there are two spin-wave modes, which slightly differ in energy due to coupling between the monolayers. In the absence of magnetic field and in-plane anisotropy (which is extremely small in the systems under consideration), the energy of the lower branch vanishes at the Γ point ($\boldsymbol{k} = 0$) for all three systems, while the energy of the second mode in the Γ point is nonzero, and the gap between these two

modes is generally determined by the interlayer exchange coupling and easy-plane magnetic anisotropy. This gap is very small and can not be distinguished in the main parts of the spectra in Fig. 5, but it is well resolved in the insets presenting the zoomed-out areas around the Γ points. This gap is clearly visible there for both analytical and computational spectra.

From Fig. 5 follows that the agreement between the modes calculated by the ATK package and by the analytical model based on some effective spin Hamiltonian is quite satisfactory. The largest deviations occur for VTe_2, and especially at the Brillouin zone boundaries. It is obvious that the spectra obtained by these two approaches may differ due to some differences in the models. For instance, the ATK code includes the influence of further neighbours which is not taken into account in the analytical model. Despite this, the agreement is satisfactory. In addition, a comparison of the spectra obtained numerically with the analytical ones allows to prove the proper behaviour of the numerical spectra near the Γ point of the Brillouin zone.

Discussion

The van der Waals magnetic materials are expected to have a big impact on the development of future nanoelectronics and nanospintronics. These materials can be easily achieved in atomically thin layers, which makes them ideal building elements for novel two-dimensional electronics/spintronic devices. The studied monolayers and bilayers of Vanadium-based dichalcogenides, especially of VS_2 and VSe_2, are magnetic also at room temperatures and moderately above. Therefore, they can be considered as being prospective ones for certain applications. However, for real practical applications, the Curie temperatures should be still higher.

The antiferromagnetically exchange-coupled bilayers of the studied materials can be considered as natural spin-valves, in which the two monolayers have opposite magnetic moments at zero field. External field can rotate these moments from antiparallel to parallel configuration and this may be associated with a resistance change. Alternatively, one can build spin-valves by connecting two stripes of the two-dimensional ferromagnetic material with a stripe of two-dimensional nonmagnetic material. In fact, there are various possible architectures of the spin valves based on van der Waals materials. Unfortunately, the interlayer exchange coupling in vanadium-based TMDs is rather small, of the order of 1 meV. Accordingly, spin valves based on these materials can work at low temperatures, of the order of 10 K. For most of practical applications, however, one needs spin valves working at room temperatures. Therefore, further research on the already known materials, as well as a search for novel materials with better characteristics, is still required.

Method

DFT calculations

All the first-principles calculations in this paper have been performed in the framework of Density Functional Theory (DFT) using the *Quantum ATK* code package (version 2021.06-SP2)[33], which is based on Hohenberg-Kohn theorem[34] as well as the Kohn–Sham equations[35]. To expand the wave function, the SG15 collection of optimized norm-conserving Vanderbilt (ONCV) pseudopotentials with the Ultra Linear Combination of Atomic Orbitals (LCAO-U)[36] basis set has been employed. We used the generalized-gradient approximation (GGA) in the formalism of Perdew–Burke–Ernzerhof (PBE) for the exchange-correlation interaction of electrons[37]. The energy mesh-cutoff of 600 eV within the total energy convergence criteria of 1×10^{-6} eV (10^{-8} eV for the magnetic anisotropy energy calculations) for each primitive cell has been performed. The two-dimensional Brillouin zone was sampled by a Γ-centered Monkhorst–Pack method[38] using the k-point grid of $30 \times 30 \times 1$. All studied structures have been fully optimized and minimized until the force on each atom is smaller than 0.02 eV/Å. To avoid any artificial interaction between image layers along the non-periodic directions, we employed at least 25 and 30 Angstroms vacuum layers for monolayer and bilayer structures, respectively. Moreover, to optimize the lattice parameters as well as the bondlengths, we have included a weak and non-local van der Waals (vdW) interaction between the layers in bilayer structures of VX_2 materials. Using the so-called dispersion interactions, inter-layer bondlengths are decreased and the layers are not able to bind strongly and are separated. In our calculations, we used the semi-empirical corrections by Grimme DFT-D2[39]. To the electron-electron correlation effect of the localized 3*d* orbitals of Vanadium (V), we implemented the DFT+U calculations, in which the *U* term refers to the effective potential of the onsite Coulomb interaction for the V-3d electrons[40].

Static magnetic properties

To obtain magnetization as a function of temperature, and estimate Curie Temperature we have used the *Vampire* code based on the Monte Carlo metropolis algorithm (MC). For the MC calculations, we selected a $l \times l$ where $l = 120$ is the number of repeated units of the supercell with the periodic boundary conditions in all directions. We also used 10000 equilibrium steps followed by 10000 averaging steps.

Data availability

All relevant data are included in the article.

Code availability

The calculations were performed using the Quantum ATK code package (version 2021.06-SP2), Vampire packages, and Wolfram Mathematica.

Received: 31 July 2023; Accepted: 22 November 2023
Published online: 28 November 2023

References

1. Huang, B. *et al.* Layer-dependent ferromagnetism in a van der Waals crystal down to the monolayer limit. *Nature* **546**, 270–273. https://doi.org/10.1038/nature22391 (2017).
2. Gong, C. *et al.* Discovery of intrinsic ferromagnetism in two-dimensional van der Waals crystals. *Nature* **546**, 265–269. https://doi.org/10.1038/nature22060 (2017).
3. Wang, Q. H. *et al.* The magnetic genome of two-dimensional van der Waals materials. *ACS Nano* **16**, 6960–7079. https://doi.org/10.1021/acsnano.1c09150 (2022).
4. Chhowalla, M. *et al.* The chemistry of two-dimensional layered transition metal dichalcogenide nanosheets. *Nat. Chem.* **5**, 263–275. https://doi.org/10.1038/nchem.1589 (2013).
5. Feng, J. *et al.* Metallic few-layered VS_2 ultrathin nanosheets: High two-dimensional conductivity for in-plane supercapacitors. *J. Am. Chem. Soc.* **133**, 17832–17838. https://doi.org/10.1021/ja207176c (2011).
6. Zhang, H., Liu, L.-M. & Lau, W.-M. Dimension-dependent phase transition and magnetic properties of VS_2. *J. Mater. Chem. A* **1**, 10821–10828. https://doi.org/10.1039/C3TA12098H (2013).
7. Bastos, C. M., Besse, R., Da Silva, J. L. & Sipahi, G. M. Ab initio investigation of structural stability and exfoliation energies in transition metal dichalcogenides based on ti-, v-, and mo-group elements. *Phys. Rev. Mater.* **3**, 044002. https://doi.org/10.1103/PhysRevMaterials.3.044002 (2019).
8. Fuh, H.-R. *et al.* Newtype single-layer magnetic semiconductor in transition-metal dichalcogenides VX_2 (X= S, Se and Te). *Sci. Rep.* **6**, 1–11. https://doi.org/10.1038/srep32625 (2016).
9. Jafari, M., Wawrzyniak-Adamczewska, M., Stagraczyński, S., Dyrdal, A. & Barnaś, J. Spin valve effect in two-dimensional VSe_2 system. *J. Magn. Magn. Mater.* **548**, 168921. https://doi.org/10.1016/j.jmmm.2021.168921 (2022).
10. Boscher, N. D., Blackman, C. S., Carmalt, C. J., Parkin, I. P. & Prieto, A. G. Atmospheric pressure chemical vapour deposition of vanadium diselenide thin films. *Appl. Surf. Sci.* **253**, 6041–6046. https://doi.org/10.1016/j.apsusc.2007.01.002 (2007).
11. Lavela, P. *et al.* VSe_2- ySy electrodes in lithium and lithium-ion cells. *J. Appl. Electrochem.* **27**, 1207–1211 (1997).
12. Thompson, A., Scanlon, J. & Symon, C. The electrochemical reaction of li with VSe_2 and implications on the ionicity of intercalation compounds. *Solid State Ionics* **1**, 47–57. https://doi.org/10.1016/0167-2738(80)90021-1 (1980).
13. Vinokurov, A., Tyurin, A., Emelina, A., Gavrichev, K. & Zlomanov, V. Thermodynamic properties of VTe_2. *Inorg. Mater.* **45**, 480–485. https://doi.org/10.1134/S0020168509050045 (2009).
14. Ma, Y. *et al.* Evidence of the existence of magnetism in pristine VX_2 monolayers (X = S, Se) and their strain-induced tunable magnetic properties. *ACS Nano* **6**, 1695–1701. https://doi.org/10.1021/nn204667z (2012).
15. Gong, S.-J. *et al.* Electrically induced 2d half-metallic antiferromagnets and spin field effect transistors. *Proc. Natl. Acad. Sci.* **115**, 8511–8516. https://doi.org/10.1073/pnas.1715465115 (2018).
16. Li, A. *et al.* Coupling stacking orders with interlayer magnetism in bilayer H-VSe_2. *Chin. Phys. Lett.* **37**, 107101. https://doi.org/10.1088/0256-307X/37/10/107101 (2020).
17. Feng, S. & Mi, W. Strain and interlayer coupling tailored magnetic properties and valley splitting in layered ferrovalley 2H-VSe_2. *Appl. Surf. Sci.* **458**, 191–197. https://doi.org/10.1016/j.apsusc.2018.07.070 (2018).
18. Rassekh, M., He, J., Shayesteh, S. F. & Palacios, J. J. Remarkably enhanced curie temperature in monolayer CrI_3 by hydrogen and oxygen adsorption: A first-principles calculations. *Comput. Mater. Sci.* **183**, 109820. https://doi.org/10.1016/j.commatsci.2020.109820 (2020).
19. Fuh, H.-R., Chang, K.-W., Hung, S.-H. & Jeng, H.-T. Two-dimensional magnetic semiconductors based on transition-metal dichalcogenides VX_2 (X= S, Se, Te) and similar layered compounds Vi_2 and $Co(OH)_2$. *IEEE Magn. Lett.* **8**, 1–5. https://doi.org/10.1109/LMAG.2016.2621720 (2017).
20. Fuh, H.-R., Yan, B., Wu, S.-C., Felser, C. & Chang, C.-R. Metal-insulator transition and the anomalous hall effect in the layered magnetic materials VS_2 and VSe_2. *N. J. Phys.* **18**, 113038. https://doi.org/10.1088/1367-2630/18/11/113038 (2016).
21. Isaacs, E. B. & Marianetti, C. A. Electronic correlations in monolayer VS_2. *Phys. Rev. B* **94**, 035120. https://doi.org/10.1103/PhysRevB.94.035120 (2016).
22. Karbalaee Aghaee, A., Belbasi, S. & Hadipour, H. Ab initio calculation of the effective coulomb interactions in MX_2 (M = Ti, V, Cr, Mn, Fe, Co, Ni; S = S, Se, Te): Intrinsic magnetic ordering and Mott phase. *Phys. Rev. B* **105**, 115115. https://doi.org/10.1103/PhysRevB.105.115115 (2022).
23. Blanco-Rey, M., Cerdá, J. I. & Arnau, A. Validity of perturbative methods to treat the spin–orbit interaction: Application to magnetocrystalline anisotropy. *N. J. Phys.* **21**, 073054. https://doi.org/10.1088/1367-2630/ab3060 (2019).
24. Błoński, P. & Hafner, J. Density-functional theory of the magnetic anisotropy of nanostructures: An assessment of different approximations. *J. Phys. Condens. Matter* **21**, 426001. https://doi.org/10.1088/0953-8984/21/42/426001 (2009).
25. Daalderop, G., Kelly, P. & Schuurmans, M. First-principles calculation of the magnetocrystalline anisotropy energy of Iron, Cobalt, and Nickel. *Phys. Rev. B* **41**, 11919. https://doi.org/10.1103/PhysRevB.41.11919 (1990).
26. Pajda, M., Kudrnovskỳ, J., Turek, I., Drchal, V. & Bruno, P. Ab initio calculations of exchange interactions, spin-wave stiffness constants, and curie temperatures of Fe, Co, and Ni. *Phys. Rev. B* **64**, 174402. https://doi.org/10.1103/PhysRevB.64.174402 (2001).
27. Liechtenstein, A. I., Katsnelson, M., Antropov, V. & Gubanov, V. Local spin density functional approach to the theory of exchange interactions in ferromagnetic metals and alloys. *J. Magn. Magn. Mater.* **67**, 65–74 (1987).
28. Evans, R. F. *et al.* Atomistic spin model simulations of magnetic nanomaterials. *J. Phys. Condens. Matter* **26**, 103202. https://doi.org/10.1088/0953-8984/26/10/103202 (2014).
29. Evans, R. *Vampire Software Package Version 4.0*. http://vampire.york.ac.uk (2016).
30. Muller-Krumbhaar, H. & Binder, K. *Monte Carlo Methods in Statistical Physics* 261 (Springer, 1979).
31. Newman, M. E. & Barkema, G. T. *Monte Carlo Methods in Statistical Physics* (Clarendon Press, 1999).
32. Rudziński, W., Barnaś, J. & Dyrdał, A. Spin waves in bilayers of transition-metal dichalcogenides. http://arxiv.org/abs/2307.13414 (2023).
33. Smidstrup, S. *et al.* First-principles Green's-function method for surface calculations: A pseudopotential localized basis set approach. *Phys. Rev. B* **96**, 195309. https://doi.org/10.1103/PhysRevB.96.195309 (2017).
34. Hohenberg, P. & Kohn, W. Inhomogeneous electron gas. *Phys. Rev.* **136**, B864. https://doi.org/10.1103/PhysRev.136.B864 (1964).
35. Kohn, W. & Sham, L. J. Self-consistent equations including exchange and correlation effects. *Phys. Rev.* **140**, A1133. https://doi.org/10.1103/PhysRev.140.A1133 (1965).
36. Hamann, D. Optimized norm-conserving vanderbilt pseudopotentials. *Phys. Rev. B* **88**, 085117. https://doi.org/10.1103/PhysRevB.88.085117 (2013).
37. Perdew, J. P., Burke, K. & Ernzerhof, M. Generalized gradient approximation made simple. *Phys. Rev. Lett.* **77**, 3865. https://doi.org/10.1103/PhysRevLett.77.3865 (1996).
38. Monkhorst, H. J. & Pack, J. D. Special points for Brillouin-zone integrations. *Phys. Rev. B* **13**, 5188. https://doi.org/10.1103/PhysRevB.13.5188 (1976).
39. Grimme, S. Semiempirical GGA-type density functional constructed with a long-range dispersion correction. *J. Comput. Chem.* **27**, 1787–1799. https://doi.org/10.1002/jcc.20495 (2006).
40. Dudarev, S. L., Botton, G. A., Savrasov, S. Y., Humphreys, C. & Sutton, A. P. Electron-energy-loss spectra and the structural stability of Nickel Oxide: An LSDA+U study. *Phys. Rev. B* **57**, 1505. https://doi.org/10.1103/PhysRevB.57.1505 (1998).

Acknowledgements
This work has been supported by the Norwegian Financial Mechanism under the Polish-Norwegian Research Project NCN GRIEG, project No. 2019/34/H/ST3/00515, '2Dtronics'.

Author contributions
A.D. initiated and supervised the study, M.J. performed first principles calculations, W.R. performed analytical calculations of magnon spectra. A.D., J.B. performed analysis and contributed to discussions. M.J., J.B. and A.D. wrote the manuscript. All authors reviewed the manuscript.

Competing interests
The authors declare no competing interests.

Additional information
Correspondence and requests for materials should be addressed to A.D.

Reprints and permissions information is available at www.nature.com/reprints.

Publisher's note Springer Nature remains neutral with regard to jurisdictional claims in published maps and institutional affiliations.

5.3 Reprint of article [P3]

On the subsequent pages, we append a reprint with permission:

[P3] **Mirali Jafari**, Anna Dyrdał

Effect of strain on the electronic and magnetic properties of bilayer T-phase VS_2: A first-principles study

Journal of Magnetism and Magnetic Materials

DOI: 10.1016/j.jmmm.2023.171618

[2]Copyright on any research article published in the Journal of Magnetism and Magnetic Materials is retained by the author(s). The authors grant Elsevier a license to publish the article and identify it as the original publisher. Authors also grant any third party the right to use the article freely, as long as the integrity of the work is maintained and the original authors, citation details, and publisher are identified. If the article is published as Open Access, it may be available under a Creative Commons license, allowing for wider reuse and distribution.

My primary motivation for this work concerned the need for comprehensive work on the influence of strain on the electronic and magnetic properties of VS_2 bilayer in its thermodynamically stable phase, that is, the T-phase. In this study, the bilayer configurations provide additional degrees of freedom through interlayer coupling, enabling new opportunities for tuning magnetic properties in device applications. This paper aims to understand the essential behavior of electronic and magnetic behaviors, such as ground state, magnetic anisotropy, exchange coupling between magnets, and Curie temperature, which enhance the practical aspects of the T-phase of VS_2 in nanoscale device applications.

5.3.1 Methods

I performed my calculations using the Density Functional Theory [DFT] as implemented in the Quantum ATK code package with correction methods, including Coulomb interactions [DFT+U] and spin-orbit coupling. Biaxial strain is applied from -10% to $+10\%$ on the bilayer of VS_2, after examining the structure stability for different strain values leading to changes in structure, electronic, and magnetic properties. Magnetic anisotropy energy has been calculated using force theorem methods, and Curie temperatures have been estimated using the mean field approximation and random phase approximation method under different compressive and tensile strains.

5.3.2 Main results

The results obtained in this work show that compressive strain generally enhances the magnetic moment, primarily due to the strengthening of the vanadium–sulfur bonding under compression. At the same time, the magnetic moment is reduced when the biaxial strain is tensile. While VS_2 is a metallic material at zero strain, a small energy band gap appears under tensile strain. Magnetic anisotropy energy shows the preferred in-plane orientations, which, under tensile strain, is much more pronounced, while in compressive strain, it tends to vanish close to the isotropic level. The exchange coupling parameters show the ferromagnetic order at zero strain, and the Curie temperature is close to room temperature. The exchange coupling changes from FM to AFM for higher strain values, especially under compressive strains.

Journal of Magnetism and Magnetic Materials 589 (2024) 171618

Contents lists available at ScienceDirect

Journal of Magnetism and Magnetic Materials

journal homepage: www.elsevier.com/locate/jmmm

Research article

Effect of strain on the electronic and magnetic properties of bilayer T-phase VS_2: A first-principles study

Mirali Jafari *, Anna Dyrdał

Department of Mesoscopic Physics, ISQI, Faculty of Physics, Adam Mickiewicz University, ul. Uniwersytetu Poznańskiego 2, 61-614 Poznań, Poland

ARTICLE INFO

Keywords:
VS_2
Trigonal phase
Density Functional Theory (DFT)
Strain
Electronic and magnetic properties

ABSTRACT

Using the Density Functional Theory (DFT) calculations, we determined the electronic and magnetic properties of a T-phase VS_2 bilayer as a function of tensile and compressive strain. First, we determine the ground state structural parameters and then the band structure, magnetic anisotropy, exchange parameters, and Curie temperature. Variation of these parameters with the strain is carefully analyzed and described. The easy-plane anisotropy, which is rather small in the absence of strain, becomes remarkably enhanced by tensile strain and reduced almost to zero by compressive strain. We also show that the exchange parameters and the Curie temperature are remarkably reduced for the compressive strains below roughly −4%.

1. Introduction

Two-dimensional (2D) transition metal dichalcogenides (TMDs) represent a wide class of materials, that have been extensively investigated recently as they are of highly promising potential for applications in nanoelectronic and optoelectronic devices [1–8]. Generally, TMDs correspond to a general chemical formula, MX_2, where M denotes a transition metal element, such as Mo, W, Nb, and V, while X stands for a chalcogen element, like S, Se, and Te. Currently, over 40 different TMDs are known, including metallic, semiconducting, and superconducting ones [9–13]. Notably, the 2D layered TMDs display distinct physical properties, when compared with their bulk counterparts — especially in the context of band structures [14]. Several experimental methods and techniques are currently known, which allow to obtain monolayers of various TMDs, including mechanical exfoliation techniques, liquid exfoliation methods, and chemical vapor deposition (CVD). These techniques collectively facilitate the successful production of various TMD-monolayers, increasing thus our understanding of these interesting materials [3,15,16].

Typically, layers of vanadium (V) based TMDs exist in two structural phases, namely the 2H phase characterized by trigonal prismatic coordination, and the 1T phase with octahedral coordination [2,17]. Most primitive TMDs lack magnetic properties, which hinders their suitability for applications relying on magnetism. Nevertheless, inducing magnetic properties in these materials is feasible with various techniques, such as doping with various point defects, adsorption of non-metal elements, or exploiting edge effects [18–23]. For instance, the formation of triple vacancies in single-layer MoS_2 has been proposed as a tool to generate a net magnetic moment, whereas other defects related to Mo and S atoms do not affect the non-magnetic ground state [24]. In MoS_2 nanoribbons, the interplay of defects and adsorption can be used for tuning between non-magnetic and magnetic states, depending on the type of defects introduced and the specific sites where the adatoms are adsorbed. However, extending this ability to other TMD materials has proven to be intricate, as the induced magnetic properties are highly dependent on the nature of defects, edge states, and position of dopants, which leads to significant experimental challenges.

On the other hand, computational studies can be used to elucidate the physical properties of TMDs, down to single monolayers. Indeed, such calculations show that monolayers of VX_2 (where X = S and Se) exhibit intriguing ferromagnetic behavior, providing thus evidence of magnetic properties of pristine 2D monolayers [25]. This insight opens new avenues for the fabrication of ferromagnetic TMDs without resorting to doping with point defects, non-metal element adsorption, or external forces like tensile strain. Encouraged by these theoretical predictions, researchers successfully synthesized ultrathin VS_2 nanosheets with less than five S–V–S atomic layers, using a modified all-in-solution method. The corresponding experimental results confirmed the presence of a room temperature ferromagnetism (FM) in the ultrathin VS_2 nanosheets, accompanied by a very weak antiferromagnetism (AFM). [26,27]

In our study, we have chosen the T-phase of VS_2 for detailed investigation, mainly due to its unique and fascinating electronic properties. The T-phase, characterized by octahedral sulfur coordination around vanadium atoms, presents a promising avenue for exploring

* Corresponding author.
E-mail addresses: mirali.jafari@amu.edu.pl (M. Jafari), adyrdal@amu.edu.pl (A. Dyrdał).

https://doi.org/10.1016/j.jmmm.2023.171618
Received 22 September 2023; Received in revised form 4 December 2023; Accepted 7 December 2023
Available online 10 December 2023
0304-8853/

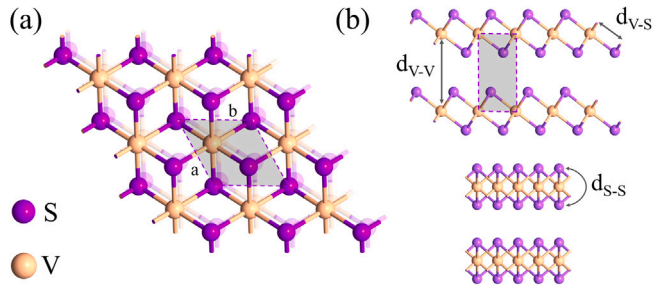

Fig. 1. Schematic structure of bilayer of T-VS_2 for (a) Top, (b) Side perspectives in which ($a = b$) shows the hexagonal lattice constants, (d_{V-V}) is the inter-layer distance between Vanadium atoms, (d_{V-S}) is the bond length of Vanadium atoms with the surrounded Sulfur atoms, (d_{S-S}) is the distance between Sulfur atoms in each layer.

new phenomena in two-dimensional materials. The T phase is different from its more commonly studied 2H-phase counterpart and exhibits distinctive intrinsic electronic correlations. It is worth noting, that the band structure of the T-phase offers new application possibilities in spintronics and quantum computing [26,28]. To get an insight into the fundamental properties of VS_2, we have decided to investigate the effects of bi-axial strain [29,30] on the VS_2 bilayer configuration. This choice is supported by the following arguments. Firstly, the bilayer structures reveal interlayer interactions and display electronic phenomena that are absent in single-layer counterparts [31,32]. Secondly, bilayer structures are experimentally accessible and are suitable for device applications. Their potential to tailor electronic and magnetic properties makes them interesting for both fundamental and applied research [33–35]. The remaining part of this paper is structured as follows: Section 2 provides an overview of the methodology and computational techniques employed. Section 3 elaborates on the findings derived from the computational analysis. Finally, Section 4 encapsulates the concluding remarks.

2. Computational details

The first-principles calculations were performed using the Density Functional Theory (DFT) and the Quantum ATK code package (version 2021.06-SP2) [36]. The calculations were based on the Hohenberg–Kohn theorem [37] and Kohn–Sham [38] equations, and utilized the SG15 collection of optimized norm-conserving Vanderbilt (ONCV) pseudopotentials with Ultra Linear Combination of Atomic Orbitals (LCAO-Ultra) basis set [39]. The exchange–correlation interaction of electrons was described using the Perdew–Burke–Ernzerhof (PBE) generalized-gradient approximation (GGA) [40]. The calculations were performed with a converged energy cutoff of 500 Ry and the total energy convergence criteria of 10^{-6} eV, with higher criteria of 10^{-8} eV for magnetic anisotropy energy calculations. The two-dimensional Brillouin zone was sampled using a Γ-centered Monkhorst–Pack method [41] with a k-point grid of 25 × 25 × 1. All structures were fully optimized until the force on each atom was less than 0.02 eV/Å. To avoid artificial interaction between image layers, vacuum layers of 25 Angstroms were introduced. Additionally, a weak and non-local van der Waals (vdW) interaction was included in bilayer structures of VS_2 material to optimize lattice parameters and bond lengths. The dispersion interactions were accounted for using Grimme DFT-D2 semi-empirical corrections [42]. All structures were fully optimized in the presence of Hubbard U parameter (U = 2 eV), where GGA+U was employed to consider the electron–electron correlation effect of the localized $3d$ orbitals of Vanadium (V) [43].

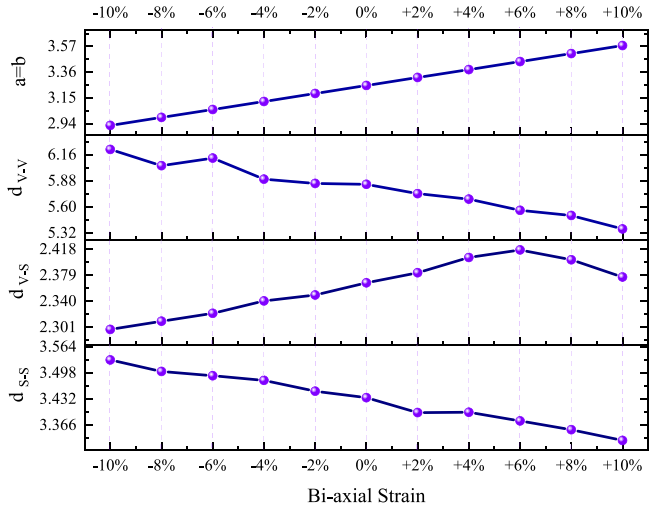

Fig. 2. Geometry changes of T-VS_2 bilayer under the bi-axial strain from −10% to +10%. Here we show the lattice parameter ($a = b$), the inter-layer distance between Vanadium atoms (d_{V-V}), the bond length of Vanadium atoms with the surrounded Sulfur atoms (d_{V-S}), and the distance between Sulfur atoms in each layer (d_{S-S}).

3. Results and discussions

3.1. Structural properties

The T-phase vanadium disulfide (VS_2) is a van der Waals layered material, in which an individual monolayer consists of a single layer of vanadium atoms sandwiched between two layers of sulfur atoms, as shown schematically in Fig. 1. The lattice structure of T-phase VS_2 is hexagonal, with each vanadium atom being surrounded by six nearest-neighbor sulfur atoms. The lattice constants of the unit cell in the T-phase VS_2 are denoted by a and b, which are equal in honeycomb structures, i.e., $a = b$.

As illustrated in Fig. 2, the distance between two Vanadium atoms located in different monolayers in a bilayer, d_{V-V}, exhibits a non-monotonic dependence on the bi-axial strain, increasing smoothly with increasing compressive strain from 0% to −10%, and decreasing with increasing tensile strain from 0% to 10%. A weak but noticeable nonmonotonic behavior appears within the range of −4% to −8% of compressive strain, where a relatively fast increase appears in the range of −4% to −6%, followed by a decrease in the range of −6% to −8% of compressive strain. This general tendency in the behavior of d_{V-V} with strain can be attributed to the competition between the increasing repulsive forces between the Vanadium atoms under compression and the decreasing attractive forces under tension. The nonmonotonic behavior in the above mentioned range of compressive strains may be due to the occurrence of an energy barrier that needs to be overcome for further compression.

The bond length between Vanadium and Sulfur atoms (d_{V-S}) is found to be sensitive to the direction and magnitude of the applied strain. The d_{V-S} exhibits a smooth decrease with increasing compressive strain from 0% to −10%. Under compressive strain, the compression of the lattice constants enhances the covalent interactions between Vanadium (V) and Sulfur (S) atoms, resulting in a decrease in the bond length between them. Conversely, under tensile strain, the elongation of the lattice constants weakens the covalent interactions between the V and S atoms, resulting in an increase in the bond length between them. However, under tensile strain, d_{V-S} exhibits a non-monotonic variation; it increases for the tensile strain up to 6%, and then smoothly decreases at the higher values of the tensile strains. This anomalous behavior can be explained by the evolution of the electronic structure of the VS_2 bilayer under strain, which alters the hybridization of the

Table 1
Energy band gap of the structure (E_{Gap}), spin magnetic moment (MM), and magnetic anisotropic energy (MAE) under bi-axial strain.

Strain [%]		−10	−8	−6	−4	−2	0	2	4	6	8	10
E_{Gap} [eV]	GGA+U	Metal	Metal	Metal	Metal	Metal	Metal	Metal	Metal	Metal	Half-Metal	Metal
	GGA+SOC	Metal	Metal	Metal	Metal	Metal	Metal	Metal	0.06	Metal	0.0004	Metal
MM [μ_B]	GGA+U	0.336	0.593	0.887	1.27	1.43	1.56	1.61	1.66	1.72	1.80	1.91
	GGA+SOC	0.001	0.000	0.002	0.03	0.54	0.83	1.16	1.28	1.33	1.38	1.45
MAE [meV]		0	0	0	−0.0001	−0.0335	−0.0610	−0.226	−0.225	−0.210	−0.213	−0.17

orbitals involved in the V–S bond. Specifically, the tensile strain can induce a weakening of the V–S bond due to the destabilization of the 3d orbital of the Vanadium atom, leading to an initial elongation of d_{V-S}. However, at higher tensile strains, the hybridization of the V–S orbitals changes, leading to a stabilization of the 3d orbital of the Vanadium atom and a subsequent contraction of d_{V-S}.

The distance between Sulfur atoms, d_{S-S}, is also observed to vary monotonically with increasing compressive and tensile strain, increasing with increasing compressive strain, and decreasing with increasing tensile strain. This trend is due to the changes in the electrostatic interaction between the Sulfur atoms and the Vanadium atoms in the VS_2 bilayer, which are influenced by the changes in the inter-layer distance and the electronic structure of the bilayer.

3.2. Static electronic and magnetic properties

3.2.1. Electronic bandstructure

To obtain the spin-resolved electronic band structure, we need to determine first the ground state. In the case of the T-phase of VS_2, finding the ground state is challenging due to the Coulomb interaction. It has been shown that the ground state of this material can alternate between antiferromagnetic (AFM) and ferromagnetic (FM), when the Coulomb interaction is taken into consideration. This variation in the ground state makes it important to determine where the magnetic moment is predominantly localized. This is especially important when calculating exchange integrals. In this work, we have found that the magnetic moment becomes localized mainly on the vanadium (V) atoms. To determine the most stable geometry of the T-VS_2 bilayer, we calculated the total energy of FM and AFM configurations for different values of U (ranging from 0 to 3). We fully optimized the structure without the Coulomb interaction ($U = 0$), and found that it had an AFM ground state. Structures with U greater than or equal to 1 were found to be FM. We then optimized the structure for U ranging from 1 to 3, and selected the optimized structure with $U = 2$ eV, based on its stability which was determined by changes in the lattice parameters and bond lengths, in agreement with earlier works [44,45]. Using this value of U, we calculated all other relevant properties. We employed the DFT calculations to investigate the spin-resolved bandstructure of the bilayer of T-VS_2 under bi-axial strain with and without SOC. Our findings, summarized in Table 2, reveal that the unstrained structure exhibits metallic behavior, which is preserved under all compressive strains examined. However, we observe a significant change in the material's behavior at strains of +4% and +8%, which is attributed to the introduction of SOC. Specifically, the opening of a bandgap at these strains leads to the transition of the bilayer of T-VS_2 from a metal to a very weak semiconductor. In addition, we computed the spin magnetic moment for each strain using GGA+U and GGA+SOC methods. Fig. 3 shows the variation of the spin magnetic moment under different strains. Our results demonstrate that the spin magnetic moment increases under the tensile strain, while it decreases under the compressive strain. Moreover, at higher compressive strains, the magnetization of the structure nearly disappears. This behavior could be due to the weakening of the interlayer interaction and the distortion of the crystal lattice. As the lattice compression increases, the magnetic moment decreases until it reaches a critical point where the magnetic order disappears.

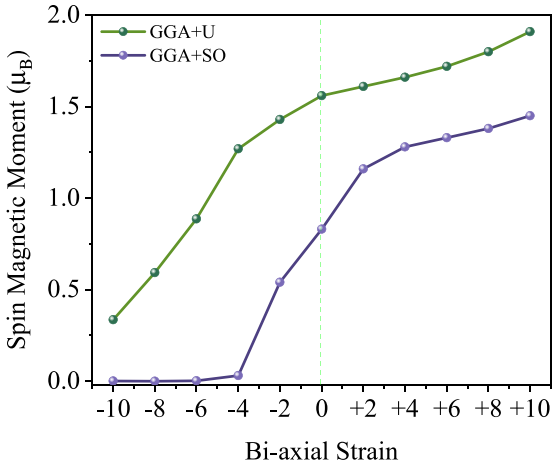

Fig. 3. Spin Magnetic Moment (MM) as a function of applied bi-axial strain.

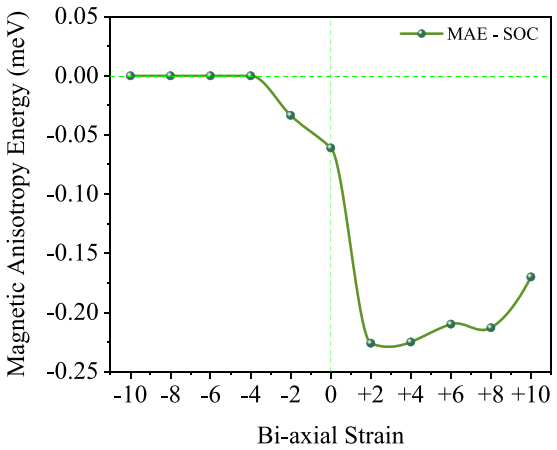

Fig. 4. Magnetic Anisotropy Energy changes during the applied bi-axial strain from −10% to +10%.

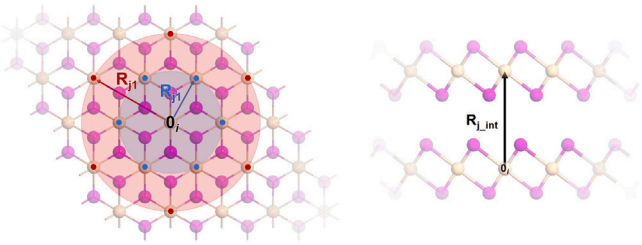

Fig. 5. Schematic representation of the nearest (J_1, blue) and next-nearest (J_2, red) neighbors surrounding the central Vanadium atom (labeled as 0) in the $T-VS_2$ bilayer. The right panel presents a side view emphasizing interlayer atoms (J_{int}.).

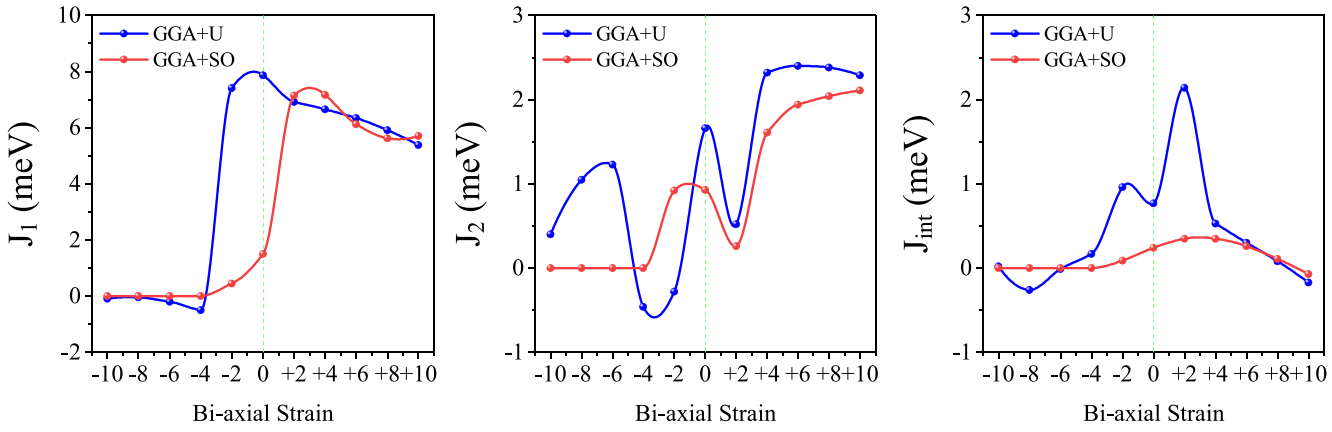

Fig. 6. Exchange coupling constants as a function of applied bi-axial strain from −10% to +10%.

Table 2
Changes in the exchange parameters J_1, J_2, and J_{int} under the bi-axial strain.

Strain [%]		−10	−8	−6	−4	−2	0	2	4	6	8	10
J_1 [meV]	GGA+U	−0.09	−0.04	−0.20	−0.50	7.41	7.86	6.92	6.65	6.34	5.91	5.38
	GGA+SOC	0	0	0	0	0.45	1.51	7.15	7.17	6.12	5.62	5.70
J_2 [meV]	GGA+U	0.40	1.05	1.23	−0.46	−0.28	1.66	0.52	2.32	2.40	2.38	2.29
	GGA+SOC	0	0	0	0	0.92	0.93	0.26	1.61	1.94	2.04	2.11
J_{int} [meV]	GGA+U	0.02	−0.26	−0.01	0.17	0.96	0.77	2.14	0.53	0.30	0.08	−0.17
	GGA+SOC	0	0	0	0	0.09	0.24	0.35	0.35	0.26	0.11	−0.07

3.2.2. Magnetic anisotropy energy

Magnetic anisotropy energy (MAE) plays a crucial role in determining the ground state magnetization orientation and can be calculated using the force theorem by evaluating the energy difference between relevant spin orientations. In this paper, we focus on the perpendicular anisotropy, which is defined as the energy difference between magnetizations along two specific crystallographic orientations. More precisely, the perpendicular anisotropy is defined as MAE = $E_{[100]} - E_{[001]}$ (or MAE = $E_{[010]} - E_{[001]}$, when the system is magnetically isotropic or near isotropic in the plane), where the positive value of MAE corresponds to the perpendicular easy axis, while the negative value to the perpendicular hard axis, i.e. to the easy-plane anisotropy. Our results, as illustrated in Fig. 4, show that the pure T-VS_2 structure without any strain exhibits a relatively small easy-plane magnetic anisotropy, which increases under the tensile strain due to the increase in crystal field splitting. In contrast, under compressive strain, the easy-plane magnetic anisotropy decreases and becomes close to zero, then for the strain below $\leq -4\%$ is roughly equal to zero. This result can be attributed to the decrease in crystal field splitting, which makes the system more isotropic.

3.3. Exchange parameters, curie temperature

When investigating magnetic properties of materials, the density functional theory (DFT) technique is commonly used as it gives reliable results. This technique allows to determine material parameters, like zero-temperature magnetization and magnetic ordering. Additionally, DFT enables calculation of the exchange parameters which enter Heisenberg spin Hamiltonian — commonly used to determine the Curie temperature, spin wave dispersions, and others. The Heisenberg exchange Hamiltonian can be written as:

$$H = -\sum_{i \neq j} J_{ij} \hat{e}_i \hat{e}_j \tag{1}$$

Here, $\hat{e}_i$ represents the normalized local spin vector on atom i, and J_{ij} stands for the Heisenberg exchange coupling constant. We utilized the Liechtenstein–Katsnelson–Antropov–Gubanov formula (LKAG formula)

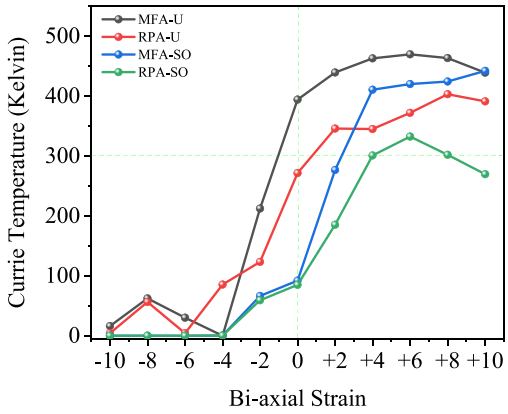

Fig. 7. The estimated Curie temperature in the Mean Field Approximation (MFA) and Random Phase Approximation (RPA) under bi-axial strain.

[46] to determine the Heisenberg intra-layer exchange coupling constants between the nearest-neighbors (J_1) and next nearest-neighbors (J_2), as well as for the inter-layer coupling (J_{int}). To compute the exchange coupling matrix element $J_{0i,Rj}$, which describe the interaction between atom i in the central unit cell (labeled 0) and atom j in a different unit cell displaced from the central one by a lattice vector R, as shown in Fig. 5, the real-space Green's function method is employed [46], as implemented in the ATK package.

Our results for the clean and unstrained structure show that both J_1 and J_2 are positive, indicating that the magnetic interactions between the nearest and next nearest neighbors are ferromagnetic. The parameter J_{int} is also positive, indicating that the magnetic interaction between spins in different layers is ferromagnetic, too. Furthermore, we found that J_1 is the largest coupling parameter, J_2 is smaller than J_1, and J_{int} is the smallest from the set of the three determined coupling constants.

Our calculations of the Heisenberg exchange coupling constants for the bilayer of T-phase VS_2 reveal several interesting behaviors. First, we find that both GGA+U and GGA+SOC methods yield similar behavior

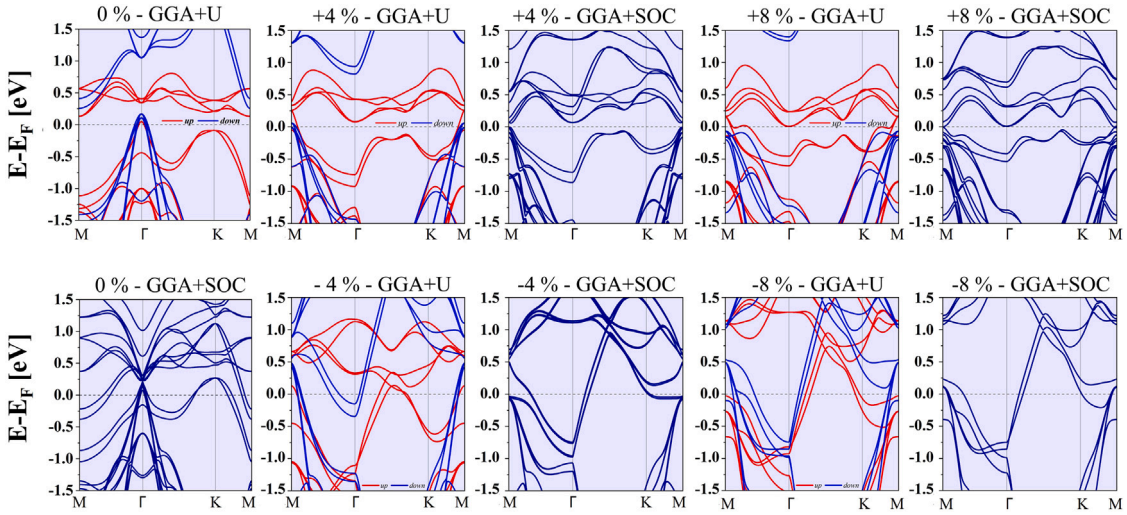

Fig. A.8. Spin-resolved band structures for the Bilayer T-phase of VS2 in the GGA+U and GGA+SOC approximations.

for J_1, but with some differences in magnitude. Specifically, the J_1 values obtained from both methods are remarkably different at zero strain, with the GGA+U value being larger than the GGA+SOC value. This can be attributed to the fact that the GGA+U method tends to overestimate the strength of the Coulomb interaction, leading to larger values of the exchange coupling constants. However, at higher tensile strains, the J_1 values obtained from GGA+U and GGA+SOC calculations converge, and the difference between them becomes smaller. This behavior can be explained by a combination of strain-induced changes in the electronic structure, spin polarization, and crystal structure of the bilayer. As the magnitude of the tensile strain increases, the crystal lattice becomes more distorted, which leads to a modification of the exchange pathways and a consequent change in the magnetic properties of the system. Additionally, the spin–orbit coupling becomes more significant at higher strains, leading to a more pronounced influence on the magnetic properties of the system. These changes in the electronic structure and spin polarization can lead to J_1 obtained from GGA+U and GGA+SOC more similar at higher tensile strains. In the case of compressive strains, we observed that both GGA+U and GGA+SOC result in a decrease in J_1 due to the crystal lattice distortion caused by the compressive strain, which in turn leads to a change in the magnetic properties of the system. Notably, we found that at the strain of −4%, the sign of J_1 obtained from GGA+U calculations changes to antiferromagnetic coupling, whereas the value obtained from GGA+SOC approaches zero. This can be explained by the tendency of the GGA+U method to overestimate the Coulomb interaction strength, leading to larger values of the exchange coupling constants and its sign change. In contrast, the GGA+SOC method includes the spin–orbit coupling, which can suppress the exchange interaction and can result in smaller values of the exchange parameters. We observed a similar trend for the next nearest neighbor exchange coupling constant (J_2), with both GGA+U and GGA+SOC showing fluctuations in their magnitude. From Fig. 6, it can be clearly seen that the magnitude of J_2 fluctuates due to the changes in the crystal structure under strain. Interestingly, in the presence of Hubbard corrections, we observe the sign change of J_2 from FM to AFM and the from AFM to FM under compressive strain.

Finally, we also evaluated the inter-layer exchange coupling constant (J_{int}), which determines the ground state of the bilayer structure of T-VS_2. From Fig. 6 follows that the inter-layer exchange coupling constant sharply increases at strains of ±2%, indicating the preference of the ferromagnetic coupling in this range of strains. However, for higher tensile and compressive strains, the inter-layer exchange coupling constant decreases, indicating the tendency towards antiferromagnetic coupling at larger strains (at 10% for tensile strain and −6% to −8% for compressive strain). This behavior can be attributed to the interplay between changes in the crystal structure and the electronic and magnetic properties of the system.

Having found the exchange parameters, one can determine the Curie temperature. To do this we use the Mean Field Approximation (MFA) and the Random Phase Approximation (RPA). In the Mean Field Approximation, spins are treated based on an average interaction field, and any correlations beyond the nearest neighbors are disregarded. The MFA allows to find a simple expression. In the first approximation only J_1, J_2 and J_{int} are taken into account and the Curie temperature (T_c) can be then calculated as:

$$T_c = \frac{2}{3k_B}\left(Z_1 J_1 + Z_2 J_2 + Z_{int} J_{int}\right), \tag{2}$$

where k_B is the Boltzmann constant, while $Z_1 = 6$, $Z_2 = 6$, and $Z_{int} = 1$ denote the respective numbers of the nearest neighbors, next-nearest neighbors, and interlayer nearest neighbors atoms. In turn, the Random Phase Approximation (RPA) takes into account fluctuations in the spin orientations and incorporates correlations beyond the mean field. This approximation offers a more precise estimation of the Curie temperature. However, the RPA involves solving a system of coupled equations that take into account the spin correlation functions, resulting in a more intricate expression for T_c. The pure structure of the bilayer of T-VS_2 has T_c close to or beyond the room temperature for GGA+U in the MFA and RPA methods, respectively. However, this value is lower for the GGA+SOC calculations.

Using the ATK code, we have calculated the Curie temperature for the different strains and the results are listed in Table 3. We note that the ATK in general also includes small contributions from exchange couplings between further neighbors. The T_c plot as a function of biaxial strain exhibits a similar trend to that of the exchange parameters, as shown in Fig. 7. Under tensile strain, the Curie temperature shows an increasing tendency. However, at higher tensile strains, it slightly decreases, which can be attributed to the interplay between the changes in electronic structure, spin interactions, and lattice distortions. In turn, the Curie temperature under compressive strains decreases, as anticipated from the corresponding J_1 and J_2 interactions. The decrease in Curie's temperature continues until certain points where it becomes very low or even vanishes.

4. Summary and conclusions

In this paper, we have analyzed the influence of biaxial compressive and tensile strains on the electronic and magnetic properties of a bilayer of T-VS_2. The bilayer structure seems to be interesting for applications,

Table 3
Curie temperature (T_c) obtained by MFA and RPA methods for different applied bi-axial strains.

Strain [%]		−10	−8	−6	−4	−2	0	2	4	6	8	10
MFA	GGA+U	16.2	62.3	30.1	–	212.4	394.2	439.5	463.0	469.8	463.5	439.1
	GGA+SOC	0	0	0	0.3	66.5	92.1	276.8	410.7	420.1	424.3	442.1
RPA	GGA+U	4.3	56.4	4.3	85.5	123.3	271.5	345.9	345.1	372.1	403.2	391.3
	GGA+SOC	0	0	0	0.3	59.2	85.0	185.4	301.0	332.5	302.5	269.6

as it reveals the properties of a natural spin valve [13,47–49]. We have determined the strain-induced changes in the structural parameters, electronic band structure, magnetic anisotropy, exchange parameters, and Curie temperature.

An interesting effect is that easy-plane magnetic anisotropy is enhanced for tensile strains and reduced almost to zero for compressive strains. This anisotropy in unstrained structures is rather small, so the tensile strain can be used to enhance the corresponding anisotropy parameter. Similarly, the compressive strain also reduces other magnetic properties, like magnetic moments of Vanadium, exchange parameters, and Curie temperature, which are strongly suppressed at higher compressive strains.

CRediT authorship contribution statement

Mirali Jafari: Conceptualization, Formal analysis, Investigation, Methodology, Software, Visualization, Writing – original draft, Writing – review & editing. **Anna Dyrdał:** Conceptualization, Data curation, Formal analysis, Funding acquisition, Investigation, Methodology, Project administration, Supervision, Validation, Writing – original draft, Writing – review & editing.

Declaration of competing interest

The authors declare that they have no known competing financial interests or personal relationships that could have appeared to influence the work reported in this paper.

Data availability

Data will be made available on request.

Acknowledgment

This work has been supported by the Norwegian Financial Mechanism 2014–2021 under the Polish-Norwegian Research Project NCN GRIEG "2Dtronics" no. 2019/34/H/ST3/00515.

Appendix. Band structures

To have a dipper insight into the impact of strain on electronic properties, we have also calculated the electronic band structures of both strained and unstrained structures. The numerical calculations were performed within the Generalized Gradient Approximation with Hubbard U correction (GGA+U) scheme, as well as in the Generalized Gradient Approximation with Spin–Orbit Coupling (GGA+SOC) method. The band structures for strain levels of −8%, −4%, 0%, +4%, and +8% are shown in Fig. A.8, and the corresponding band gaps are given in Table 1. This figure and data in the Table 1 clearly show that the electronic structure changes remarkably under the external stain.

References

[1] W. Xiong, C. Xia, J. Du, T. Wang, X. Zhao, Y. Peng, Z. Wei, J. Li, Electrostatic gating dependent multiple-band alignments in a high-temperature ferromagnetic Mg (OH) $2/VS_2$ heterobilayer, Phys. Rev. B 95 (24) (2017) 245408, http://dx.doi.org/10.1103/PhysRevB.95.245408.
[2] M. Kan, B. Wang, Y.H. Lee, Q. Sun, A density functional theory study of the tunable structure, magnetism and metal-insulator phase transition in VS_2 monolayers induced by in-plane biaxial strain, Nano Res. 8 (2015) 1348–1356, http://dx.doi.org/10.1007/s12274-014-0626-5.
[3] Q.H. Wang, K. Kalantar-Zadeh, A. Kis, J.N. Coleman, M.S. Strano, Electronics and optoelectronics of two-dimensional transition metal dichalcogenides, Nature Nanotechnol. 7 (11) (2012) 699–712, http://dx.doi.org/10.1038/nnano.2012.193.
[4] K.F. Mak, C. Lee, J. Hone, J. Shan, T.F. Heinz, Atomically thin MoS_2: a new direct-gap semiconductor, Phys. Rev. Lett. 105 (13) (2010) 136805, http://dx.doi.org/10.1103/PhysRevLett.105.136805.
[5] D. Xiao, G.-B. Liu, W. Feng, X. Xu, W. Yao, Coupled spin and valley physics in monolayers of MoS_2 and other group-VI dichalcogenides, Phys. Rev. Lett. 108 (19) (2012) 196802, http://dx.doi.org/10.1103/PhysRevLett.108.196802.
[6] K.F. Mak, K. He, C. Lee, G.H. Lee, J. Hone, T.F. Heinz, J. Shan, Tightly bound trions in monolayer MoS_2, Nat. Mater. 12 (3) (2013) 207–211, http://dx.doi.org/10.1038/nmat3505.
[7] C.-Y. Wang, G.-Y. Guo, Nonlinear optical properties of transition-metal dichalcogenide MX_2 (M=Mo, W; X=S, Se) monolayers and trilayers from first-principles calculations, J. Phys. Chem. C 119 (23) (2015) 13268–13276, http://dx.doi.org/10.1021/acs.jpcc.5b01866.
[8] S. Bertolazzi, J. Brivio, A. Kis, Stretching and breaking of ultrathin MoS_2, ACS Nano 5 (12) (2011) 9703–9709, http://dx.doi.org/10.1021/nn203879f.
[9] E. Marseglia, Transition metal dichalcogenides and their intercalates, Int. Rev. Phys. Chem. 3 (2) (1983) 177–216, http://dx.doi.org/10.1080/01442358309353343.
[10] J.A. Wilson, A. Yoffe, The transition metal dichalcogenides discussion and interpretation of the observed optical, electrical and structural properties, Adv. Phys. 18 (73) (1969) 193–335, http://dx.doi.org/10.1080/00018736900101307.
[11] M. Chhowalla, H.S. Shin, G. Eda, L.-J. Li, K.P. Loh, H. Zhang, The chemistry of two-dimensional layered transition metal dichalcogenide nanosheets, Nat. Chem. 5 (4) (2013) 263–275, http://dx.doi.org/10.1038/nchem.1589.
[12] J.N. Coleman, M. Lotya, A. O'Neill, S.D. Bergin, P.J. King, U. Khan, K. Young, A. Gaucher, S. De, R.J. Smith, et al., Two-dimensional nanosheets produced by liquid exfoliation of layered materials, Science 331 (6017) (2011) 568–571, http://dx.doi.org/10.1126/science.1194975.
[13] M. Jafari, M. Wawrzyniak-Adamczewska, S. Stagraczyński, A. Dyrdal, J. Barnaś, Spin valve effect in two-dimensional VSe_2 system, J. Magn. Magn. Mater. 548 (2022) 168921, http://dx.doi.org/10.1016/j.jmmm.2021.168921.
[14] D. Jariwala, V.K. Sangwan, L.J. Lauhon, T.J. Marks, M.C. Hersam, Emerging device applications for semiconducting two-dimensional transition metal dichalcogenides, ACS Nano 8 (2) (2014) 1102–1120, http://dx.doi.org/10.1021/nn500064s.
[15] B. Radisavljevic, A. Radenovic, J. Brivio, V. Giacometti, A. Kis, Single-layer MoS_2 transistors, Nature Nanotechnol. 6 (3) (2011) 147–150, http://dx.doi.org/10.1038/nnano.2010.279.
[16] C. Lee, Q. Li, W. Kalb, X.-Z. Liu, H. Berger, R.W. Carpick, J. Hone, Frictional characteristics of atomically thin sheets, Science 328 (5974) (2010) 76–80, http://dx.doi.org/10.1126/science.1184167.
[17] H. Zhang, L.-M. Liu, W.-M. Lau, Dimension-dependent phase transition and magnetic properties of VS_2, J. Mater. Chem. A 1 (36) (2013) 10821–10828, http://dx.doi.org/10.1039/C3TA12098H.
[18] R. Shidpour, M. Manteghian, A density functional study of strong local magnetism creation on MoS_2 nanoribbon by sulfur vacancy, Nanoscale 2 (8) (2010) 1429–1435, http://dx.doi.org/10.1039/B9NR00368A.
[19] J. He, K. Wu, R. Sa, Q. Li, Y. Wei, Magnetic properties of nonmetal atoms absorbed MoS_2 monolayers, Appl. Phys. Lett. 96 (8) (2010) http://dx.doi.org/10.1063/1.3318254.
[20] Z. Wang, K. Zhao, H. Li, Z. Liu, Z. Shi, J. Lu, K. Suenaga, S.-K. Joung, T. Okazaki, Z. Jin, et al., Ultra-narrow WS_2 nanoribbons encapsulated in carbon nanotubes, J. Mater. Chem. 21 (1) (2011) 171–180, http://dx.doi.org/10.1039/C0JM02821E.
[21] Y. Li, Z. Zhou, S. Zhang, Z. Chen, MoS_2 Nanoribbons: high stability and unusual electronic and magnetic properties, J. Am. Chem. Soc. 130 (49) (2008) 16739–16744, http://dx.doi.org/10.1021/ja805545x.

[22] Y. Ma, Y. Dai, M. Guo, C. Niu, B. Huang, Graphene adhesion on MoS_2 monolayer: An ab initio study, Nanoscale 3 (9) (2011) 3883–3887, http://dx.doi.org/10.1039/C1NR10577A.

[23] Y. Ma, Y. Dai, M. Guo, C. Niu, J. Lu, B. Huang, Electronic and magnetic properties of perfect, vacancy-doped, and nonmetal adsorbed $MoSe_2$, $MoTe_2$ and WS_2 monolayers, Phys. Chem. Chem. Phys. 13 (34) (2011) 15546–15553, http://dx.doi.org/10.1039/C1CP21159E.

[24] J. Xiao, X. Wang, X.-Q. Yang, S. Xun, G. Liu, P.K. Koech, J. Liu, J.P. Lemmon, Electrochemically induced high capacity displacement reaction of PEO/MoS_2/graphene nanocomposites with lithium, Adv. Funct. Mater. 21 (15) (2011) 2840–2846, http://dx.doi.org/10.1002/adfm.201002752.

[25] Y. Ma, Y. Dai, M. Guo, C. Niu, Y. Zhu, B. Huang, Evidence of the existence of magnetism in pristine VX_2 monolayers (X=S, Se) and their strain-induced tunable magnetic properties, ACS Nano 6 (2) (2012) 1695–1701, http://dx.doi.org/10.1021/nn204667z.

[26] J. Feng, X. Sun, C. Wu, L. Peng, C. Lin, S. Hu, J. Yang, Y. Xie, Metallic few-layered VS_2 ultrathin nanosheets: high two-dimensional conductivity for in-plane supercapacitors, J. Am. Chem. Soc. 133 (44) (2011) 17832–17838, http://dx.doi.org/10.1021/ja207176c.

[27] S.A. Patil, N.K. Shrestha, H.T. Bui, V.D. Chavan, D.-k. Kim, S.F. Shaikh, M. Ubaidullah, H. Kim, H. Im, Solvent modulated self-assembled VS_2 layered microstructure for electrocatalytic water and urea decomposition, Int. J. Energy Res. 46 (6) (2022) 8413–8423, http://dx.doi.org/10.1002/er.7651.

[28] M. Kan, J. Wang, X. Li, S. Zhang, Y. Li, Y. Kawazoe, Q. Sun, P. Jena, Structures and phase transition of a MoS_2 monolayer, J. Phys. Chem. C 118 (3) (2014) 1515–1522, http://dx.doi.org/10.1021/jp4076355.

[29] Y. Zhou, Z. Wang, P. Yang, X. Zu, L. Yang, X. Sun, F. Gao, Tensile strain switched ferromagnetism in layered NbS_2 and $NbSe_2$, Acs Nano 6 (11) (2012) 9727–9736, http://dx.doi.org/10.1021/nn303198w.

[30] M. Jafari, A. Kordbacheh, A. Dyrdal, Electronic and magnetic properties of silicene monolayer under bi-axial mechanical strain: First principles study, J. Magn. Magn. Mater. 554 (2022) 169260.

[31] X. Liu, A.P. Pyatakov, W. Ren, Magnetoelectric coupling in multiferroic bilayer VS_2, Phys. Rev. Lett. 125 (24) (2020) 247601, http://dx.doi.org/10.1103/PhysRevLett.125.247601.

[32] R.Z. Dong, Comparative studies on VS_2 bilayer and VS_2 /graphene heterostructure as the anodes of li ion battery, Key Eng. Mater. 894 (2021) 61–66, http://dx.doi.org/10.4028/www.scientific.net/kem.894.61.

[33] G. Duvjir, J. Kim, B. Tsermaa, B.K. Choi, Y.J. Chang, Lattice dynamics driven by tunneling current in 1T structure of bilayer VSe_2, J. Korean Phys. Soc. 77 (2020) 1031–1034.

[34] T. Kawakami, K. Sugawara, T. Kato, T. Taguchi, S. Souma, T. Takahashi, T. Sato, Electronic states of multilayer $VTe2$: Quasi-one-dimensional Fermi surface and implications for charge density waves, Phys. Rev. B 104 (4) (2021) 045136.

[35] R. Wu, Q. Tao, J. Li, W. Li, Y. Chen, Z. Lu, Z. Shu, B. Zhao, H. Ma, Z. Zhang, et al., Bilayer tungsten diselenide transistors with on-state currents exceeding 1.5 milliamperes per micrometre, Nat. Electron. 5 (8) (2022) 497–504.

[36] S.r. Smidstrup, D. Stradi, J. Wellendorff, P.A. Khomyakov, U.G. Vej-Hansen, M.-E. Lee, T. Ghosh, E. Jónsson, H. Jónsson, K. Stokbro, First-principles green's-function method for surface calculations: A pseudopotential localized basis set approach, Phys. Rev. B 96 (19) (2017) 195309, http://dx.doi.org/10.1103/PhysRevB.96.195309.

[37] P. Hohenberg, W. Kohn, Inhomogeneous electron gas, Phys. Rev. 136 (3B) (1964) B864, http://dx.doi.org/10.1103/PhysRev.136.B864.

[38] W. Kohn, L.J. Sham, Self-consistent equations including exchange and correlation effects, Phys. Rev. 140 (4A) (1965) A1133, http://dx.doi.org/10.1103/PhysRev.140.A1133.

[39] D. Hamann, Optimized norm-conserving vanderbilt pseudopotentials, Phys. Rev. B 88 (8) (2013) 085117, http://dx.doi.org/10.1103/PhysRevB.88.085117.

[40] J.P. Perdew, K. Burke, M. Ernzerhof, Generalized gradient approximation made simple, Phys. Rev. Lett. 77 (18) (1996) 3865, http://dx.doi.org/10.1103/PhysRevLett.77.3865.

[41] H.J. Monkhorst, J.D. Pack, Special points for Brillouin-zone integrations, Phys. Rev. B 13 (12) (1976) 5188, http://dx.doi.org/10.1103/PhysRevB.13.5188.

[42] S. Grimme, Semiempirical GGA-type density functional constructed with a long-range dispersion correction, J. Comput. Chem. 27 (15) (2006) 1787–1799, http://dx.doi.org/10.1002/jcc.20495.

[43] S.L. Dudarev, G.A. Botton, S.Y. Savrasov, C. Humphreys, A.P. Sutton, Electron-energy-loss spectra and the structural stability of nickel oxide: An LSDA+ U study, Phys. Rev. B 57 (3) (1998) 1505, http://dx.doi.org/10.1103/PhysRevB.57.1505.

[44] H.-R.F. Fuh, C.-R. Chang, Y.-K. Wang, R.F.L. Evans, R.W. Chantrell, H.-T. Jeng, Newtype single-layer magnetic semiconductor in transition-metal dichalcogenides VX_2 ($X = S, Se$ and Te), Scientific Reports 7 (6) (2016) 32625, http://dx.doi.org/10.1038/srep32625.

[45] M. Jafari, W. Rudziński, J. Barnaś, A. Dyrdał, Electronic and magnetic properties of 2d vanadium-based transition metal dichalcogenides, Scientific Reports 12 (2023) 20947, http://dx.doi.org/10.1038/s41598-023-48141-1.

[46] A.I. Liechtenstein, M. Katsnelson, V. Antropov, V. Gubanov, Local spin density functional approach to the theory of exchange interactions in ferromagnetic metals and alloys, J. Magn. Magn. Mater. 67 (1) (1987) 65–74.

[47] E. Elahi, G. Dastgeer, P.R. Sharma, S. Nisar, M. Suleman, M.W. Iqbal, M. Imran, M. Aslam, A. Imran, A brief review on the spin valve magnetic tunnel junction composed of 2D materials, J. Phys. D: Appl. Phys. (2022).

[48] C. Long, T. Wang, H. Jin, H. Wang, Y. Dai, Stacking-independent ferromagnetism in bilayer VI_3 with half-metallic characteristic, J. Phys. Chem. Lett. 11 (6) (2020) 2158–2164.

[49] B. Wu, R. Quhe, J. Yang, S. Liu, J. Shi, J. Lu, H. Du, High-performance spin filters and spin field effect transistors based on bilayer VSe_2, Adv. Theory Simul. 4 (2) (2021) 2000238.

Chapter 6

Spin-Valve Systems Based on vdW Heterostructures

6.1 Reprint of article [P4]

On the subsequent pages, we append a reprint with permission:

[P4] **M.A. Jafari**, M. Wawrzyniak-Adamczewska, S. Stagraczyński, A. Dyrdał, J. Barnaś

Spin valve effect in two-dimensional VSe_2 system

Journal of Magnetism and Magnetic Materials 548 (2022): 168921.

DOI: 10.1016/j.jmmm.2021.168921

[1]Copyright on any research article published in the Journal of Magnetism and Magnetic Materials is retained by the author(s). The authors grant Elsevier a license to publish the article and identify it as the original publisher. Authors also grant any third party the right to use the article freely, as long as the integrity of the work is maintained and the original authors, citation details, and publisher are identified. If the article is published as Open Access, it may be available under a Creative Commons license, allowing for wider reuse and distribution.

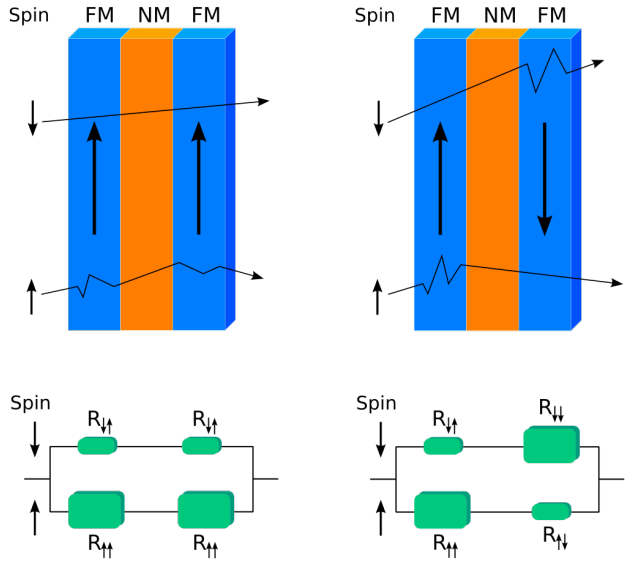

Figure 6.1. Schematic representation of spin valve GMR effect. Copyright-Guillom, Wikimedia commons, 2006, distributed under GFDL license.

6.1.1 Introduction and aims

Spintronics, or spin electronics, has become an outstanding field in modern physics and technology. The electron spin degree of freedom in spintronics plays a prominent role, in addition to its charge, in developing advanced electronic devices. One of the most well-known spintronics devices is the spin-valve. Spin-valves act based on the principle of spin-dependent electronic transport and allowed the discovery of the Giant Magnetoresistance (GMR) effect. The discovery and theoretical formulation of GMR by Albert Fert and Peter Grünberg in 1988 laid the foundation for spintronic applications and led to a paradigm shift in data storage and sensor technologies [411, 412]. However, the extensive and complete theory of spin-valve structures was developed later in 1990 by Józef Barnaś and Robert Camley, whose models provided a deeper understanding of spin-dependent scattering mechanisms in layered magnetic structures [413, 414, 415]. As shown in Figure (6.1), the configuration of a spin valve system includes two ferromagnetic (FM) layers separated by a non-magnetic (NM) metallic spacer, where the magnetization of one FM layer is pinned while the other remains free to switch under an external magnetic field. The electrical resistance of the system depends on the relative orientation of the magnetization between the two FM layers. When the magnetizations are parallel, electron scattering in one spin channel is minimized, leading to a low-resistance state. In contrast, an antiparallel alignment results in a higher resistance state.

Experimental evidence of GMR and spin valves was first shown in Fe/Cr multilayers by Baibich et al. (1988) and Binasch et al. (1989), which confirms the resistance modulation predicted by theory. These early experimental results showed that the presence of an NM spacer and its thickness can significantly change the magnetoresistance effects with oscillatory coupling between the FM layers. Later, works by Dieny et al. (1991) led to the development of practical spin-valve structures where a

metallic spacer exists and is applicable for technological applications. Various fabrication techniques, such as sputtering deposition, molecular beam epitaxy (MBE), and electrodeposition, have been used to refine the spin-valve structures. Modern spin-valves use novel interface engineering methods to raise performance and stability [416, 417]. Thanks to the emergence of spin-valve systems, many technological innovations were introduced. The most spectacular examples are hard disk drive (HDD) read heads introduced by IBM in 1997, which led to a significant increase in data storage densities [417]. Another prominent application is the Magnetoresistive Random-Access Memory (MRAM), where spin valves are fundamental components for non-volatile high-speed memory. Beyond traditional data storage, spin valve applications extend to biosensing applications, where their sensitivity to external magnetic fields enables the detection of biomolecules in medical diagnostics. Additionally, spintronic logic device advances have opened the way for energy-efficient computing architectures, including neuromorphic systems and quantum spintronic devices [418, 419].

Recently, spin valve magnetoresistance has attracted much attention, especially in antiferromagnetically coupled metallic 2D materials [420]. Among them, vdW magnetic crystals have been shown as promising candidates for constructing vdW spin valves. In particular, V-based dichalcogenides such as VSe_2 are unique because of the interplay between strong in-plane ferromagnetic coupling and weak interlayer antiferromagnetic coupling that produces a spin valve architecture. A single monolayer of VSe_2 consists of a hexagonal array of vanadium atoms sandwiched by two layers of selenium atoms. While some studies suggest that neighbouring vanadium atoms can exhibit ferromagnetic exchange within a monolayer, the nature of interlayer magnetic coupling remains sensitive to the environment and is often considered antiferromagnetic under specific stacking and thickness conditions. This intrinsic arrangement in vdW is analogous to the spin valves in metallic thin films. The various geometries lead to different interlayer exchange coupling and electronic structures, and subsequently influence the spin-dependent transport properties. By applying an external magnetic field, one can force a transition from the equilibrium antiferromagnetic (AP) configuration to a ferromagnetic (P) state that leads to a measurable change in electrical resistance. This intrinsic spin valve effect, without the need for complex multilayer fabrication, gives the opportunity to design next-generation spintronic devices.

In summary, my main motivation for the article [P4] was the concept of electronic device design that can be smaller. Traditional spin valve systems are made of thicker ferromagnetic and non-magnetic metallic thin films. Therefore, this natural property of the VSe_2 bilayer leads to intrinsic vdW spin valve systems without requiring extra layers. Consequently, the intrinsic spin valve behavior in VSe_2 bilayers allows for more compact and efficient device designs [153, 421, 422]. Accordingly, in this work, I provide comprehensive first-principles calculations of the spin valve effects in the 2D VSe2 bilayer system. We determined the electronic structure by DFT and its combination with nonequilibrium Green's function formalism and Landauer transport theory. We calculated the ballistic conductance in both the parallel and antiparallel magnetic configurations. Moreover, our results were extended to the investigation of thermal and thermoelectric properties.

6.1.2 Methods

To simulate the spin valve systems in this research, I used the Density Functional Theory [DFT] combined with the NEGF method for the transport properties (full theoretical background is presented in sections 3.3, and 3.6.2). The designed devices were calculated in the ballistic transport

regime using the Quantum ATK – LCAO software package (more details about this code are in section 7.1.3). The electronic and magnetic properties and thermal conductance were modeled for the 1D nanoribbon in ferromagnetic and antiferromagnetic states.

6.1.3 Main results

The most important findings presented in [P4] are listed below with emphasis on the difference between the VSe_2 bilayer in the H- and T-phases:

1. In both H and T phases, the VSe_2 bilayer exhibits a high sensitivity to magnetic alignment changes. In the H-phase, the change in in-plane resistance created by switching from an antiferromagnetic to a ferromagnetic configuration is more remarkable than in the T-phase, though the T-phase also shows the spin-valve effect with a smaller magnetoresistance ratio. The results suggest that the H-phase is much more suitable for applications in energy conversion devices.
2. According to the figure of merit (ZT) analysis, the thermoelectric efficiency in the H-phase of the VSe_2 bilayer is more viable for applications in energy conversion devices than the T-phase. This shows that the selection of the material phase is crucial in designing the spintronic and thermoelectric devices.
3. One of the limitations of the VSe_2 is its magnetic instability at raised temperatures due to the destabilization of the antiferromagnetic configuration at high temperatures. Therefore, one can overcome this problem by developing stable, high-temperature, two-dimensional spin valve systems, which are crucial for practical applications. This can be achieved by combining it with insulating magnetic materials, which leads to the stabilization of magnetic configurations.

Journal of Magnetism and Magnetic Materials 548 (2022) 168921

Contents lists available at ScienceDirect

Journal of Magnetism and Magnetic Materials

journal homepage: www.elsevier.com/locate/jmmm

Research articles

Spin valve effect in two-dimensional VSe_2 system

M.A. Jafari [a], M. Wawrzyniak-Adamczewska [a], S. Stagraczyński [a], A. Dyrdal [a,*], J. Barnaś [a,b]

[a] Department of Mesoscopic Physics, ISQI, Faculty of Physics, Adam Mickiewicz University, ul. Uniwersytetu Poznańskiego 2, 61-614 Poznań, Poland
[b] Institute of Molecular Physics, Polish Academy of Sciences, ul. Mariana Smoluchowskiego 17, 60-179 Poznań, Poland

ARTICLE INFO

Keywords:
Van-der-Waals materials
Dichalcogenides
Magnetoresistance
Spin valves

ABSTRACT

Vanadium based dichalcogenides, VSe_2, are two-dimensional materials in which magnetic Vanadium atoms are arranged in a hexagonal lattice and are coupled ferromagnetically within the plane. However, adjacent atomic planes are coupled antiferromagnetically. This provides new and interesting opportunities for application in spintronics and data storage and processing technologies. A spin valve magnetoresistance may be achieved when magnetic moments of both atomic planes are driven to parallel alignment by an external magnetic field. The resistance change associated with the transition from antiparallel to parallel configuration is qualitatively similar to that observed in artificially layered metallic magnetic structures. Detailed electronic structure of VSe_2 was obtained from DFT calculations. Then, the ballistic spin-valve magnetoresistance was determined within the Landauer formalism. In addition, we also analyze thermal and thermoelectric properties. Both phases of VSe_2, denoted as H and T, are considered.

1. Introduction

Spin-valve magnetoresistance is a phenomenon that has been observed first in antiferromagnetically exchange-coupled metallic Fe/Cr/Fe bilayers and superlattices [1,2]. In the simplest case, magnetic moments of the two magnetic Fe layers are oriented in opposite orientations (in the film plane), while an external in-plane magnetic field drives the moments to parallel configuration. The electrical resistance of such a system decreases during the rotation of the moments from antiparallel to parallel configurations. This resistance drop is known as the spin-valve magnetoresistance (or equivalently giant magnetoresistance) [1–3]. The phenomenon turned out to be very useful for practical applications as sensors of weak magnetic fields in hard-disc drives [4]. Many various realizations of spin valves have been proposed in recent years, including vertically magnetized ultrathin layered metallic systems, tunnel junctions [5], magnetic single-electron transistors [6], molecular junctions [7,8], and others. In all cases there are two magnetic elements (usually electrodes), whose magnetic moments can be rotated in a controllable way from antiparallel to parallel configurations.

Further miniaturization of nanoelectronics and spintronics devices, especially in view of recent developments in the information storage and processing technologies, stimulates search for novel materials that can be used to construct new spin-values. An interesting and promising solutions rely on novel two-dimensional crystals, especially on van der Waals magnetic materials, like for instance Vanadium Dichalcogenides VSe_2 [9–14]. The key property of such materials is a weak van-der-Waals coupling between different atomic planes, so one can easily produce materials with well controlled number of atomic planes, down to single atomic monolayers [15–18]. A single monolayer of VSe_2 consists of one atomic plane of vanadium atoms and two atomic sheets of Se atoms, that are shifted in opposite directions out of the atomic plane of V atoms. The Vanadium atoms in a single monolayer form a hexagonal lattice with ferromagnetic exchange coupling between nearest neighbors. Exchange coupling between next-nearest-neighbors is antiferromagnetic and is negligibly small. This leads to a strictly 2D ferromagnetic system. Adjacent monolayers of VSe_2 are coupled *via* van-der-Waals forces, and the V-atoms in different planes are exchange-coupled antiferromagnetically. Thus, a bilayer of VSe_2 with antiferromagnetic interlayer coupling is conceptually similar to a metallic spin valve with two magnetic layers coupled through a nonmagnetic spacer due to antiferromagnetic indirect exchange coupling of RKKY-type. Such an interaction is antiferromagnetic in certain regions of the nonmagnetic spacer thicknesses. It is clear now, that bilayer of VSe_2 is a natural atomically thin spin valve. In the ground state magnetic moments of both V-planes are oriented in opposite orientations perpendicular to the planes. Relatively weak external magnetic field normal to the planes drives the magnetic moments of both atomic planes to parallel orientations, exactly like in conventional metallic spin valves. In this paper we show that this rotation of magnetic moments from antiparallel to parallel configuration is associated with a resistance change, i.e. there is a spin-valve magnetoresistance like

* Corresponding author.
E-mail address: adyrdal@amu.edu.pl (A. Dyrdal).

https://doi.org/10.1016/j.jmmm.2021.168921
Received 20 August 2021; Received in revised form 24 November 2021; Accepted 25 November 2021
Available online 18 December 2021

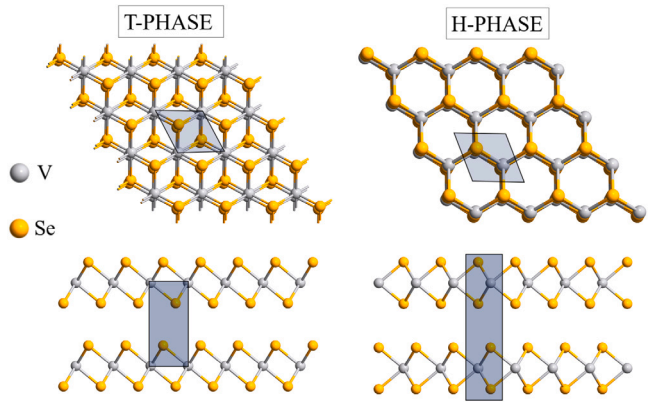

Fig. 1. Atomic structure of the 2D VSe_2 bilayer in the T (left side) and H (right side) crystallographic phases. The upper parts show slightly tilted top views, while the bottom parts show the corresponding side views. Primitive unit cells are also marked by the shaded areas. In the T-phase bilayer the Vanadium atoms are one above the other (AA stacking), while in the H-phase bilayer the stacking is of AB type.

in metallic systems. In general, the spin-valve magnetoresistance can be defined for current flowing in plane of the system (so-called CIP geometry) as well as when it flows perpendicularly to the planes (CPP geometry). In this paper we restrict considerations to the case when current flows in the 2D planes, i.e., we consider the CIP geometry.

To do this we calculate first the electronic structure of VSe_2 bilayer. Then, from the total energy calculations, we confirm that magnetic moments of the two V atomic planes are arranged antiferromagnetically in the ground state (i.e. the interlayer exchange coupling is antiferromagnetic), in agreement with literature [13,19,20]. Since VSe_2 bilayer exists in two different staking configurations, so-called H and T phases (see Fig. 1), we consider both of them. In the H phase the Vanadium atoms in different planes are one above the other [21], while in the T phase they are displaced and each V atom has three nearest neighbors in the adjacent Vanadium plane [10]. For both phases we calculate transport characteristics in the ballistic transport regime. To find conductance, we calculate transmission coefficient and then use the Landauer [22] formula to find conductance. From the conductance in both parallel (ferromagnetic) and antiparallel (antiferromagnetic) configurations we determine magnitude of the magnetoresistance as a function of the position of Fermi level. In practice, this position can be generally controlled externally (e.g. by a gate voltage). We also calculate an electronic contribution to the heat conductance and the corresponding thermal magnetoresistance. In addition, we also determine the thermoelectric efficiency [23,24]. More details on numerical method are in Section 2. Numerical results on electronic band structure and transport characteristics (magnetoresistance) are given in Section 3 and Section 4, respectively. In turn, final conclusions are in Section 5.

2. Numerical method

For transport analysis we take a nanoribbon of VSe_2 bilayer with a finite width, and assume that the central part of the nanoribbon represents our system, while the left and right parts of the nanoribbon play the role of electrodes. To find transport properties we calculate first electronic structure of the nanoribbon, from which we determine the transmission function and subsequently all transport characteristics. In this paper, the electronic structure – and thus also transport properties – are determined from first principle calculations within the framework of Density Functional Theory (DFT) [25] and nonequilibrium Green's functions (NEGFs) as implemented in the Quantum ATK-LCAO code package [26]. Within this approach, the generalized gradient approximation of Perdew–Burke Ernzerhof [27] is used to describe the exchange–correlation functional for the electrons. Moreover, an appropriate semi-empirical modeling correction known as Grimme DFT-D2 approximation [28] was used to deal with the weak interlayer van der Waals interaction. The PseudoDojo collection of optimized norm-conserving Vanderbilt (ONCV) pseudopotentials and ultra basis set were used to optimize the structures and study the electronic properties [29]. The Brillouin zone sampling was adopted using $12 \times 12 \times 1$ and $1 \times 1 \times 300$ Monkhorst–Pack grid for the electronic and transport calculations, respectively, and the mesh cut-off energy was set to 600 Ry. Furthermore, the force per atom less than 10^{-3} eV/Å was minimized through the standard Conjugate-Gradients (CG) method. In addition, relative convergence for the Self-Consistent Field (SCF) energy is reached until 10^{-5} eV/Å.

We limit further analysis of transport characteristics to the ballistic transport and linear response regime. Using methods implemented in Quantum ATK + NEGF package [30], one finds the transmission function $\mathcal{T}(\varepsilon)$, $\mathcal{T}(\varepsilon) = \sum_\sigma \mathrm{Tr}\left\{\Gamma_{L,\sigma}(\varepsilon)\mathcal{G}^R_\sigma(\varepsilon)\Gamma^R_\sigma(\varepsilon)\mathcal{G}^A_\sigma(\varepsilon)\right\}$. Here $\mathcal{G}^{R/A}_\sigma(\varepsilon)$ denotes retarded and advanced Green's functions of the central region, $\Gamma_{L/R,\sigma}(\varepsilon)$ is the line-width broadening matrix due to spin-dependent coupling between the central scattering and left/right electrode respectively, and σ is the spin index. According to the Landauer–Buttiker formula, the electric current in nonequilibrium situation is given as: $I = \frac{e}{h}\int d\varepsilon \mathcal{T}(\varepsilon)\left[f_L(\varepsilon,\mu,T) - f_R(\varepsilon,\mu,T)\right]$, where $f_{L/R}(\varepsilon,\mu,T)$ is the Fermi–Dirac distribution function for the left/right electrode respectively (μ and T are the corresponding chemical potential and temperature). In equilibrium case (linear response), temperatures and chemical potentials of both electrodes are equal, $T_L = T_R = T$ and $\mu_L = \mu_R = \mu$, respectively, and transport parameters are determined by the kinetic coefficients L_n defined as follows:

$$L_n(\mu,T) = -\frac{1}{h}\int d\varepsilon \mathcal{T}(\varepsilon)(\varepsilon-\mu)^n \frac{\partial f(\varepsilon,\mu,T)}{\partial \varepsilon} \tag{1}$$

for $n = 0, 1, 2$. Accordingly, the linear electrical conductance G can be calculated as $G = e^2 L_0$, while the electronic contribution to the thermal conductance, κ_{el}, and Seebeck coefficient (thermopower), S, are then given by the formulas: [31–33]:

$$\kappa_{el} = \frac{1}{T}\left[L_2 - \frac{L_1^2}{L_0}\right], \tag{2}$$

$$S = -\frac{1}{eT}\frac{L_1}{L_0}. \tag{3}$$

As a result, the corresponding figure of merit can be written in the following form:

$$ZT = \frac{S^2 G}{\kappa_{el}} T. \tag{4}$$

In general, the denominator in the above equation for ZT should also include the phonon contribution. As our main interest was in spin valves, the figure of merit was calculated only with the electronic contribution to the heat conductivity, just to evaluate the upper limit of ZT. Any phonon contribution reduces the magnitude of ZT, though at low temperatures the phonon contribution is small and the electronic term dominates, so Eq. 4 describes reasonably well the parameter ZT at low temperatures. At higher temperatures, however, one should include the phonon term in realistic calculations.

3. Electronic band structure: 2D system

The bulk form of VSe_2 exists in two polymorphs, namely in the trigonal prismatic structure (2H, D3 h) and in the octahedral (1T, D3d) structure. Atomic configuration of the T-phase and H-phase bilayers of VSe_2 is shown in Fig. 1. Note, in the case of T bilayers the stacking is of AA type, while for H bilayers it is of AB type. Accordingly, in the T-phase bilayer the Vanadium atoms are one above the other, while the H-phase bilayer consists of two hexagonal atomic layers with an AB stacking, in which the V (Se) atoms of the top layer cover the Se

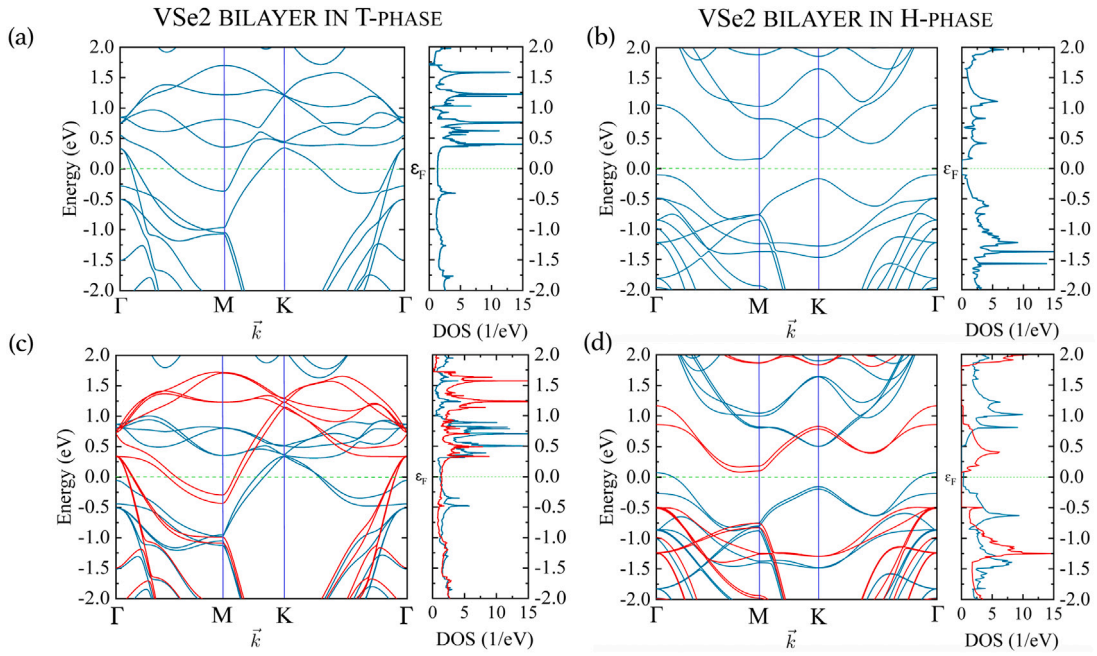

Fig. 2. Electronic structure of the 2D VSe_2 bilayer in the T (a,c) and H (b,d) crystallographic phases for the antiferromagnetic (a,b) and ferromagnetic (c,d) configurations of the magnetic moments of both vanadium atomic planes, and for the Coulomb parameter $U = 0$. The electronic structure in the ferromagnetic state is spin-dependent, while that in the antiferromagnetic state is spin degenerate. The corresponding density of states for both magnetic configurations is also shown on the right side. In the H phase, the ferromagnetic state is metallic, while a narrow gap appears in the antiferromagnetic state. In the T phase, both states are metallic.

(V) atoms of the bottom layer [34,35]. This can be clearly seen in the side views of the bilayers shown in the bottom parts of Fig. 1.

Based on available literature, we assume a sufficiently strong exchange coupling of ferromagnetic type within atomic planes of Vanadium atoms [19–21], and focus only on the exchange coupling between adjacent atomic planes of VSe_2. To verify equilibrium magnetic configuration we calculate the electronic structure and total energy per unit cell in the parallel configuration (ferromagnetic state) and antiparallel one (antiferromagnetic state). The spin-resolved electronic structure of the 2D VSe_2 bilayer in the T and H configurations is shown in Fig. 2 for both ferromagnetic and antiferromagnetic states. In the T phase, both antiferromagnetic (Fig. 2(a)) and ferromagnetic (Fig. 2(c)) states are metallic. In turn, the ferromagnetic state in the H phase is metallic (Fig. 2(d)), while there is a narrow indirect gap in the antiferromagnetic state (Fig. 2(b)). The corresponding density of states per unit energy is also shown in Fig. 2 for both magnetic states and both T and H phases. This density in the H phase clearly reveals a gap at the Fermi level of a neutral system in the antiferromagnetic state.

From the total energy calculations one can evaluate interlayer exchange coupling and determine magnetic configuration in the ground state. In both T and H phases, the total energy in the ferromagnetic state is larger than that in the antiferromagnetic state, thus the ground state in both phases is antiferromagnetic. The corresponding antiferromagnetic exchange coupling parameter is pretty small, of an order of a few meV [13]. Accordingly, the antiferromagnetic state becomes destabilized at relatively low temperatures. For practical realizations one would need materials with antiferromagnetic state stable at higher temperatures. This can be forced externally, for instance by exchange coupling to adjacent insulating magnetic layers with different coercive fields, so one can reach antiparallel and parallel configurations at higher temperatures and in appropriate external magnetic fields.

4. Electron transport in a nanoribbon: spin-valve magnetoresistance

In the linear response regime the conductance and ballistic magnetoresistance are determined by the transmission coefficient at the Fermi energy. Generally, the Fermi energy (chemical potential) can be tuned by a gate voltage. In Fig. 3(a,b) we show the transmission coefficient for a nanoribbon in both ferromagnetic and antiferromagnetic states and for the T (a) and H (b) phases. The corresponding linear ballistic magnetoresistance as a function of the energy E for both T and H phases is shown in Fig. 3(c,d). Note, E can be considered as a chemical potential or Fermi energy, and the Fermi energy of a pristine (neutral) material corresponds to $E = 0$. The magnetoresistance is defined quantitatively as the ratio of resistance difference in the two magnetic states normalized to the sum of both resistances, $\mathrm{MR} = (R_{AP} - R_P)/(R_{AP} + R_P) = (G_P - G_{AP})/(G_P + G_{AP})$, where $R_{AP}(R_P)$ stands for the resistance in the antiparallel (parallel) state, while $G_{AP}(G_P)$ is the corresponding conductance. The magnitude of magnetoresistance is relatively small at the Fermi level of neutral (pristine) systems, up to 10 percent. As one can see, the magnitude of magnetoresistance varies with position of E (chemical potential) taking at maximum about 20% in the T phase and 60% in the H phase. Moreover, it acquires positive as well as negative values. The magnetoresistance is shown there for three different temperatures, and as one can note, the increasing temperature smooths the dependence on the energy.

Similarly to the spin-valve magnetoresistance phenomenon described above, one may also define the thermal magnetoresistance (TMR) effect [36], which reflects the fact that also electronic contribution to the heat conductance depends on the magnetic state, and thus the heat conductance changes with rotation from antiferromagnetic state to the ferromagnetic one. This thermal magnetoresistance may be defined in a similar way as the electrical one, $\mathrm{TMR} = (\kappa_P - \kappa_{AP})/(\kappa_P + \kappa_{AP})$, where κ_{AP} and κ_P are the corresponding electronic contributions to the heat conductances in the antiparallel and parallel configurations. The thermal magnetoresistance in the linear response is shown in Fig. 4(a,b) for both T and H phases. Similarly as MR, the magnitude of thermal magnetoresistance depends on the energy E (chemical potential, Fermi level), taking positive as well as negative values. The thermal magnetoresistance is shown there for three different temperatures, and one can note that the increasing temperature smooths the dependence on the Fermi energy, similarly as in the case of MR.

Temperature gradient applied to the system generates a charge current. This phenomenon is known as the Seebeck effect [37], and

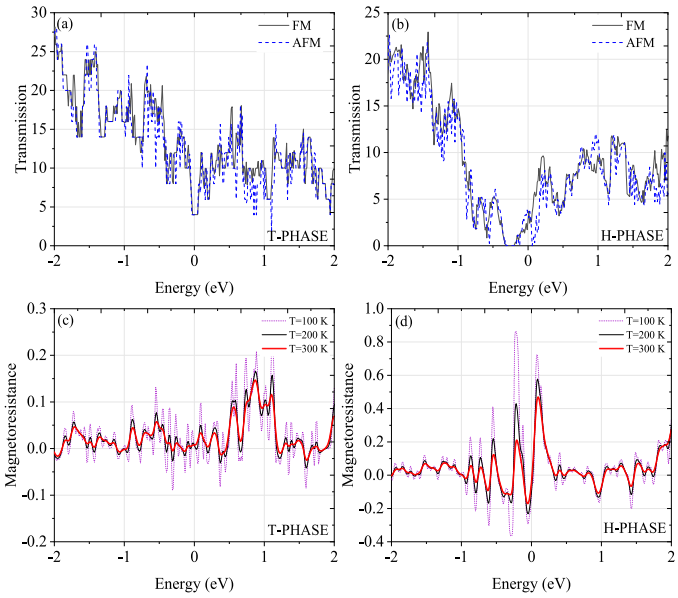

Fig. 3. Total transmission coefficient in the ferromagnetic and antiferromagnetic states for the T (a) and H (b) phases, and the corresponding spin-valve magnetoresistance, (c) and (d), as a function of the energy E for indicated temperatures. The energy E can be considered as an externally tuneable Fermi energy (or chemical potential). Fermi energy of a neutral (pristine) material corresponds to $E = 0$.

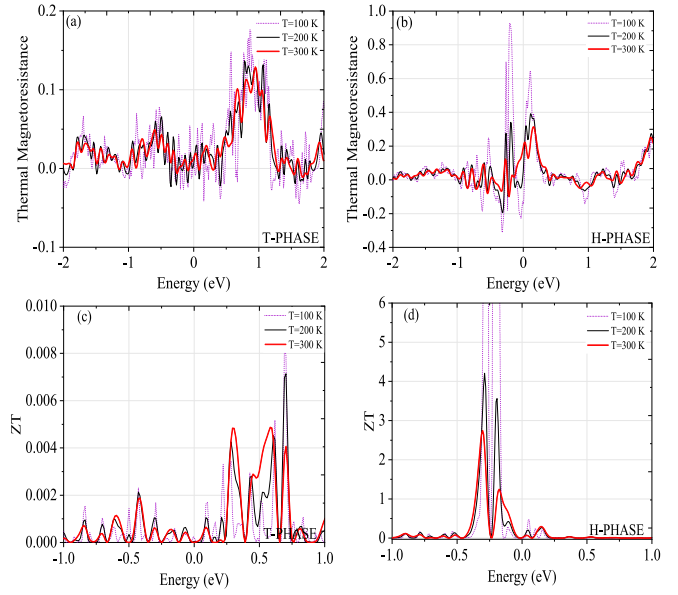

Fig. 4. Thermal magnetoresistance as a function of energy in the T (a) and H (b) phases. The corresponding thermoelectric efficiency (figure of merit) ZT is shown in (c) and (d).

is of high interest for thermoelectric applications [38–40]. In the linear response, the Seebeck coefficient (thermopower) is given by Eq. (3). The corresponding thermoelectric efficiency ZT (figure of merit) is shown for both phases in Fig. 4(c,d). As one can note, ZT is very small for the T phase but is remarkably higher for the H phase. Thus, only the H phase may be of some interest for thermoelectric applications. Since the current in ferromagnetic states is spin polarized due to spin-dependent electronic structure, one may also define spin thermoelectric phenomena [40–42]. This problem, however, is not considered in this paper.

5. Summary and conclusions

We have analyzed numerically magnetoresistance in spin-valves based on 2D van-der-Waals magnetic materials. As an example we have taken a bilayer of Vanadium dichalcogenide VSe_2. Each atomic monolayer of the VSe_2 bilayer is ferromagnetic, but different monolayers are coupled antiferromagnetically. Thus, the equilibrium configuration is antiferromagnetic, and external magnetic field can rotate magnetic moments of the two monolayers from antiparallel to parallel state. This rotation is accompanied by a resistance change for in-plane transport. Such a behavior is qualitatively similar to that in metallic spin valves. Similar resistance change can be also observed for current flowing perpendicularly to the atomic planes. We have also analyzed the corresponding thermal magnetoresistance and thermoelectric phenomenon. The latter effect is rather small in the T phase, while it can be remarkable in the H phase, especially when tuning the Fermi level below that of pristine material.

We also note that such free standing spin valves can work at low temperatures. This is because magnetism of these materials is not stable at higher temperatures. To reach any real application, one needs materials with magnetism at higher temperatures (with stronger ferromagnetic exchange coupling within the planes and larger antiferromagnetic exchange coupling between the atomic planes). Fortunately, owing to recent progress in synthesis of novel 2D materials, one may believe that these expectations will be fulfilled in new materials.

Declaration of competing interest

The authors declare that they have no known competing financial interests or personal relationships that could have appeared to influence the work reported in this paper.

Acknowledgments

This work has been supported by the Norwegian Financial Mechanism 2014–2021 under the Polish-Norwegian Research Project NCN GRIEG “2Dtronics” no. 2019/34/H/ST3/00515.

References

[1] M.N. Baibich, J.M. Broto, A. Fert, F.N. Van Dau, F. Petroff, P. Etienne, G. Creuzet, A. Friederich, J. Chazelas, Giant magnetoresistance of (001) Fe/(001) Cr magnetic superlattices, Phys. Rev. Lett. 61 (21) (1988) 2472.

[2] G. Binasch, P. Grünberg, F. Saurenbach, W. Zinn, Enhanced magnetoresistance in layered magnetic structures with antiferromagnetic interlayer exchange, Phys. Rev. B 39 (7) (1989) 4828.

[3] J. Barnaś, A. Fuss, R.E. Camley, P. Grünberg, W. Zinn, Novel magnetoresistance effect in layered magnetic structures: Theory and experiment, Phys. Rev. B 42 (13) (1990) 8110.

[4] B. Dieny, V.S. Speriosu, S.S.P. Parkin, B.A. Gurney, D.R. Wilhoit, D. Mauri, Giant magnetoresistive in soft ferromagnetic multilayers, Phys. Rev. B 43 (1) (1991) 1297.

[5] S. Yuasa, T. Nagahama, A. Fukushima, Y. Suzuki, K. Ando, Giant room-temperature magnetoresistance in single-crystal Fe/MgO/Fe magnetic tunnel junctions, Nature Mater. 3 (12) (2004) 868–871.

[6] J. Barnaś, A. Fert, Magnetoresistance oscillations due to charging effects in double ferromagnetic tunnel junctions, Phys. Rev. Lett. 80 (5) (1998) 1058.

[7] L. Zhu, K.L. Yao, Z.L. Liu, Molecular spin valve and spin filter composed of single-molecule magnets, Appl. Phys. Lett. 96 (8) (2010) 82115.

[8] S. Krompiewski, R. Gutiérrez, G. Cuniberti, Giant magnetoresistance of multiwall carbon nanotubes: Modeling the tube/ferromagnetic-electrode burying contact, Phys. Rev. B 69 (15) (2004) 155423.

[9] W.Y. Tong, C.G. Duan, Electrical control of the anomalous valley Hall effect in antiferrovalley bilayers, Npj Quant. Mater. 2 (1) (2017) 1–6, http://dx.doi.org/10.1038/s41535-017-0051-6.

[10] F. Li, K. Tu, Z. Chen, Versatile electronic properties of VSe2 bulk, few-layers, monolayer, nanoribbons, and nanotubes: A computational exploration, J. Phys. Chem. C 118 (36) (2014) 21264–21274.

[11] H.-R. Fuh, B. Yan, S.-C. Wu, C. Felser, C.-R. Chang, Metal-insulator transition and the anomalous Hall effect in the layered magnetic materials VS2 and VSe2, New J. Phys. 18 (11) (2016) 113038.

[12] H.-R. Fuh, C.-R. Chang, Y.-K. Wang, R.F.L. Evans, R.W. Chantrell, H.-T. Jeng, Newtype single-layer magnetic semiconductor in transition-metal dichalcogenides VX 2 (X=S, Se and Te), Sci. Rep. 6 (1) (2016) 1–11.
[13] S.J. Gong, C. Gong, Y.Y. Sun, W.Y. Tong, C.G. Duan, J.H. Chu, X. Zhang, Electrically induced 2D half-metallic antiferromagnets and spin field effect transistors, Proc. Natl. Acad. Sci. USA 115 (34) (2018) 8511–8516, http://dx.doi.org/10.1073/pnas.1715465115.
[14] Q. Jiang, W. Xia, T. Xu, W. Liu, X. Shen, Y. Guo, M. Ye, S. Qiao, Independent spin polarized valence electronic states in VSe2 from charge density wave transition, J. Electron. Spectros. Relat. Phenomena 238 (2020) 146868.
[15] K.S. Burch, D. Mandrus, J.G. Park, Magnetism in two-dimensional van der waals materials, Nature 563 (7729) (2018) 47–52, http://dx.doi.org/10.1038/s41586-018-0631-z.
[16] G. Aivazian, Z. Gong, A.M. Jones, R.L. Chu, J. Yan, D.G. Mandrus, C. Zhang, D. Cobden, W. Yao, X. Xu, Magnetic control of valley pseudospin in monolayer WSe 2, Nat. Phys. 11 (2) (2015) 148–152, http://dx.doi.org/10.1038/nphys3201, http://arxiv.org/abs/1407.2645.
[17] W. Zhao, B. Dong, Z. Guo, G. Su, R. Gao, W. Wang, L. Cao, Colloidal synthesis of VSe 2 single-layer nanosheets as novel electrocatalysts for the hydrogen evolution reaction, Chem. Commun. 52 (59) (2016) 9228–9231.
[18] M. Bayard, M.J. Sienko, Anomalous electrical and magnetic properties of vanadium diselenide, J. Solid State Chem. 19 (4) (1976) 325–329.
[19] A. Li, W. Zhou, J. Pan, Q. Xia, M. Long, F. Ouyang, Coupling stacking orders with interlayer magnetism in bilayer H-VSe2, Chinese Phys. Lett. 37 (10) (2020) 107101.
[20] S. Feng, W. Mi, Strain and interlayer coupling tailored magnetic properties and valley splitting in layered ferrovalley 2H-VSe2, Appl. Surf. Sci. 458 (2018) 191–197.
[21] M. Esters, R.G. Hennig, D.C. Johnson, Dynamic instabilities in strongly correlated VSe2 monolayers and bilayers, Phys. Rev. B 96 (23) (2017) 235147, http://dx.doi.org/10.1103/PhysRevB.96.235147.
[22] R. Landauer, Electrical resistance of disordered one-dimensional lattices, Phil. Mag. 21 (172) (1970) 863–867, http://dx.doi.org/10.1080/14786437008238472, URL https://doi.org/10.1080/14786437008238472.
[23] M. Hatami, G.E.W. Bauer, Q. Zhang, P.J. Kelly, Thermoelectric effects in magnetic nanostructures, Phys. Rev. B 79 (17) (2009) 174426.
[24] L. Gravier, S. Serrano-Guisan, F. Reuse, J.-P. Ansermet, Thermodynamic description of heat and spin transport in magnetic nanostructures, Phys. Rev. B 73 (2) (2006) 24419.
[25] J. Taylor, H. Guo, J. Wang, Ab initio modeling of quantum transport properties of molecular electronic devices, Phys. Rev. B 63 (24) (2001) 245407.
[26] S. Smidstrup, D. Stradi, J. Wellendorff, P.A. Khomyakov, U.G. Vej-Hansen, M.-E. Lee, T. Ghosh, E. Jónsson, H. Jónsson, K. Stokbro, First-principles Green's-function method for surface calculations: A pseudopotential localized basis set approach, Phys. Rev. B 96 (19) (2017) 195309.
[27] J.P. Perdew, K. Burke, M. Ernzerhof, Generalized gradient approximation made simple, Phys. Rev. Lett. 77 (18) (1996) 3865.
[28] S. Grimme, Semiempirical GGA-type density functional constructed with a long-range dispersion correction, J. Comput. Chem. 27 (15) (2006) 1787–1799.
[29] M.J. van Setten, M. Giantomassi, E. Bousquet, M.J. Verstraete, D.R. Hamann, X. Gonze, G.-M. Rignanese, The PseudoDojo: Training and grading a 85 element optimized norm-conserving pseudopotential table, Comput. Phys. Comm. 226 (2018) 39–54.
[30] M. Palsgaard, T. Markussen, T. Gunst, M. Brandbyge, K. Stokbro, Efficient first-principles calculation of phonon-assisted photocurrent in large-scale solar-cell devices, Phys. Rev. Appl. 10 (1) (2018) 14026.
[31] K. Uchida, T. Nonaka, T. Kikkawa, Y. Kajiwara, E. Saitoh, Longitudinal spin seebeck effect in various garnet ferrites, Phys. Rev. B 87 (10) (2013) 104412.
[32] Y.-S. Liu, X. Zhang, J.-F. Feng, X.-F. Wang, Spin-resolved Fano resonances induced large spin Seebeck effects in graphene-carbon-chain junctions, Appl. Phys. Lett. 104 (24) (2014) 242412.
[33] Y.S. Liu, X.F. Yang, F. Chi, M.S. Si, Y. Guo, A proposal for time-dependent pure-spin-current generators, Appl. Phys. Lett. 101 (21) (2012) 213109.
[34] S. Manzeli, D. Ovchinnikov, D. Pasquier, O.V. Yazyev, A. Kis, 2D transition metal dichalcogenides, Nat. Rev. Mater. 2 (8) (2017) 1–15.
[35] A.A. Wasey, S. Chakrabarty, G. Das, Quantum size effects in layered VX2 (X=S, Se) materials: Manifestation of metal to semimetal or semiconductor transition, J. Appl. Phys. 117 (6) (2015) 064313.
[36] O. Tsyplyatyev, O. Kashuba, V.I. Fal'ko, Thermally excited spin current and giant magnetothermopower in metals with embedded ferromagnetic nanoclusters, Phys. Rev. B 74 (13) (2006) 132403.
[37] H.J. Goldsmid, et al., Introduction to Thermoelectricity, Vol. 121, Springer, 2010.
[38] Y. Dubi, M. Di Ventra, Thermospin effects in a quantum dot connected to ferromagnetic leads, Phys. Rev. B 79 (8) (2009) 81302.
[39] S.R. Boona, R.C. Myers, J.P. Heremans, Spin caloritronics, Energy Environ. Sci. 7 (3) (2014) 885–910.
[40] K.-i. Uchida, H. Adachi, T. Kikkawa, A. Kirihara, M. Ishida, S. Yorozu, S. Maekawa, E. Saitoh, Thermoelectric generation based on spin Seebeck effects, Proc. IEEE 104 (10) (2016) 1946–1973.
[41] R. Świrkowicz, M. Wierzbicki, J. Barnaś, Thermoelectric effects in transport through quantum dots attached to ferromagnetic leads with noncollinear magnetic moments, Phys. Rev. B 80 (19) (2009) 195409.
[42] K. Zberecki, M. Wierzbicki, J. Barnaś, R. Swirkowicz, Thermoelectric effects in silicene nanoribbons, Phys. Rev. B 88 (11) (2013) 115404.

Chapter 7

Exchange and spin-orbit proximity driven topological and transport phenomena in twisted graphene/CrI_3 heterostructures

7.1 Preprint of article [P5]

On the subsequent pages, we append a preprint with permission:

[P5] **M.A. Jafari**, M. Gmitra, and A. Dyrdał,

Exchange and spin-orbit proximity driven topological and transport phenomena in twisted graphene/CrI_3 heterostructures

arXiv preprint arXiv:2509.11670 (2025)

DOI: 10.48550/arXiv.2509.11670

7.1.1 Introduction and aims

When graphene is placed on magnetic materials, it experiences, among others, a proximity exchange interaction which leads to the opening of energy band gap in the graphene spectrum and can induce spin-polarized states. [423, 424]. The proximity effects lead to additional terms in the Hamiltonian and, consequently, to additional degrees of freedom for spintronics applications.[423, 425]. The presence of spin-dependent transport phenomena due to proximity effects have been confirmed experimentally using magneto-transport studies and Kerr rotation measurements[426, 427]. One of the interesting examples is the investigation of the proximity effects by placing graphene on magnetic insulators. Recent studies have shown that strong magnetization can be induced in graphene by proximity to substrates like CrI_3. For instance, Zhang *et al.* [428] showed that by compressing the distance between graphene and CrI_3, the Dirac points of graphene can be tuned into the band gap of CrI_3. This leads to the appearance of strong magnetic exchange splitting and to the realization of Chern insulating states. Complementary to this work, Farooq and Hong [429] demonstrated that an external electric field could switch the valley splitting in graphene/CrI_3 systems providing electrical possibility of control the valley degrees of freedom. Very recently, the role of the twist angle between vdW layers in the heterostructure has been found to be of essential attention, and this field is called the twistronics. The twistronics is important since even a slight rotation between two 2D layers can significantly change the interlayer hybridization and, consequently, the proximity-induced interactions. There are several theoretical studies on graphene coupled to TMDCs demonstrating that the magnitude and types of induced SOC are highly sensitive to the twist angle. For instance, Naimer *et al.* [430] have investigated how the twist angle can modulate the proximity SOC in graphene/TMDCs heterostructures, which shows that maximum spin splitting can be achieved at an intermediate angle (typically around 20°). Additionally, Zollner *et al.* [267] performed a Density Functional Theory-based investigation on the twist-angle dependent proximity SOC in graphene/TMDCs structures. They found that for Mo-based TMDCs, the proximity valley-Zeeman SOC exhibits a maximum at around 15°–20° and vanishes at 30°, while for W-based TMDCs, there is an almost linear decrease in proximity valley-Zeeman SOC when twisting from 0° to 30°. These studies collectively indicate the critical role of twisting and enhances the motivation to study more in this area and work on the proximity effects of graphene on other 2D materials like transition metal halides.

In this chapter, we studied comprehensively the twisted-graphene/CrI_3 vdW heterostructures (see Figure (7.1)) using the combination of Density Functional Theory (DFT) calculations with an effective $k{\cdot}p$ model. The main aim of this work is to consider the twisted graphene on CrI_3 monolayer as a tunable platform where proximity exchange and spin–orbit coupling effects reshape the Dirac bands and enable topological and valley-dependent transport. Our results show that the Dirac cones of graphene can be placed in the insulator gap of CrI_3 and give the possibility of having transport properties of graphene in the proximity to magnetic CrI_3. Additionally, the results indicate that not only does the twist angle serve as an additional tuning parameter to enhance the weak intrinsic SOC in graphene, but it also controls the interplay between Valley-Zeeman and Rashba SOC. These results are interesting in opening up new ways for designing spintronic and valleytronic devices based on 2D heterostructures, where both magnetic and spin-orbit properties can be tuned through geometrical alignment.

7.1.2 Main results

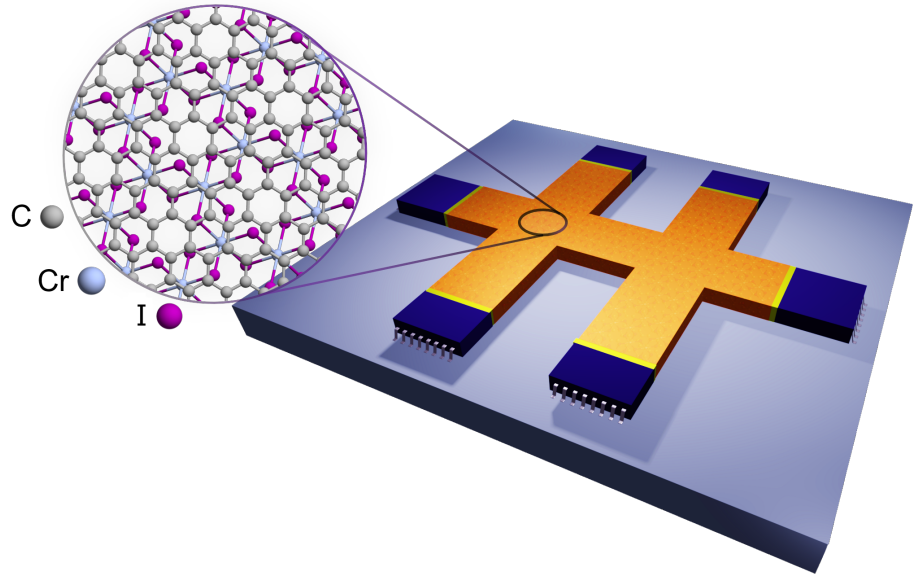

Figure 7.1. Schematic illustration of the studied spintronic device made by graphene/CrI_3.

The most important findings presented in [P5] are the following:

1. **Twist-angle engineering:** With an appropriate twist of graphene layer relative to the fixed CrI_3 layer ($\varphi \approx 10.89°$), one can position graphene's low-energy states in the band gap of CrI_3. Moreover, one observes that the graphene low-energy bands are spin splitted and gapped.
2. **Quantum anomalous Hall (QAH) state:** The twisted graphene/CrI_3 heterostructure can host a quantum anomalous Hall insulating phase. Magnetic proximity coupling from the CrI_3 substrate induces spin splitting in graphene's electronic bands and opens a topologically nontrivial energy gap. When the Fermi level lies within this gap, the system behaves as a Chern insulator, exhibiting quantized Hall conductance and vanishing longitudinal resistance—remarkably, in the absence of any external magnetic field.
3. **Valley-contrasting transport effects:** Due to the breaking of time-reversal symmetry, spatial inversion symmetry, and pseudospin symmetry the certain forms of spin-orbital and exchange proximity effects lead to the different band gap widths at the K and K' points. This allows external fields or gating to selectively close the band gap at one valley while keeping it open at the other valley. Consequently, a valley Hall effect as well as a valley Nernst effect is predicted, which highlights the potential for valley-selective electronic and thermoelectric applications in the twisted graphene/CrI_3 system.
4. **Strain-tunable topological phase transitions:** Finally, we showed that applying mechanical bi-axial strain on the CrI_3 monolayer, rather than applying it on the graphene monolayer, provides the topological and magnetic phase transition. Our results demonstrate that the magnetic ground state of the heterostructure is changed from the ferromagnetic to antiferromagnetic one. Additionally, this magnetic phase change has a profound impact on graphene's

band topology, i.e., the non-trivial insulating phase is changed to the topologically trivial one. Hence, the presence of strain can tune the topological properties of the heterostructure.

Exchange and spin-orbit proximity driven topological and transport phenomena in twisted graphene/CrI_3 heterostructures

M. Jafari[1*], M. Gmitra[2,3], A. Dyrdał[1*]
[1]*Faculty of Physics and Astronomy, ISQI, Adam Mickiewicz University in Poznań, ul. Uniwersytetu Poznanskiego 2, 61-614 Poznań, Poland*
[2]*Institute of Physics, Pavol Jozef Safarik University in Kosice, 04001 Kosice, Slovakia*
[3]*Institute of Experimental Physics, Slovak Academy of Sciences, 04001 Kosice, Slovakia*
(Dated: September 16, 2025)

We present results of comprehensive first-principles and kp-method studies of electronic, magnetic, and topological properties of graphene on a monolayer of CrI_3. First, we identify a twist angle between the graphene and CrI_3, that positions the graphene Dirac cones within the bandgap of CrI_3. Then, we derive the low-energy effective Hamiltonian describing electronic properties of graphene Dirac cones. Subsequently, we examine anomalous and valley Hall conductivity and discuss possible topological phase transition from a quantum anomalous Hall insulator to a trivial insulating state, concomitant a change in the magnetic ground state of CrI_3. These findings highlight the potential of strain engineering in two-dimensional van der Waals heterostructures for controlling topological and magnetic phases.

INTRODUCTION

Since the discovery of graphene [1], there has been remarkably rapid progress in synthesizing two-dimensional (2D) materials, assembling them into van der Waals (vdW) heterostructures, and in their functionalization [2–7]. Over the past two decades, advances in fabrication of vdW materials coincided with the discovery of novel phenomena and topological phases driven by the choice of 2D crystals and intentional twisting of layers. [3, 8–18]. In addition, vdW heterostructures offer exceptional tune-ability by electric and magnetic fields, mechanical forces, and temperature, making them a unique platform for both fundamental research—spanning solid-state physics, magnetism, quantum transport, and optics, as well as for emerging applications in spintronics, data storage, quantum technologies, sensors, and beyond [11, 19–22].

Within the rapidly growing family of van der Waals materials, graphene-based vdW heterostructures remain the most intensively studied. When combined with semiconducting transition metal dichalcogenides (TMDCs) [23–29], graphene exhibits strong spin–orbit proximity effects, leading to spin-to-charge conversion phenomena such as the spin Hall effect and current-induced spin polarization. In turn, graphene on ferromagnetic layers exhibits proximity-induced exchange effects, showing the anomalous Hall effect up to room temperature and the quantum anomalous Hall state when the Fermi level is within the band gap [30–37].

Graphene also seems to be an ideal platform for developing the twistronics [38–42]. Twist-angle-dependent spin–orbit proximity effects in graphene on TMDCs have been explored both theoretically and experimentally. [43–51]. Apart from this, twist-angle-tunable magnetism and magnetic proximity effects are currently attracting considerable attention. In multilayer graphene systems, that can serve as orbital Chern insulators, the electric-field control of magnetic states has been experimentally demonstrated. [52]. Moreover, a twist-angle-induced magnetism in twisted bilayer WSe_2 has been reported, recently [53]. Twisting has also been shown to induce nonrelativistic spin splitting in antiferromagnetically coupled bilayers and to generate large transverse spin currents under external electric fields without spin-orbit coupling [54]. Interestingly, altermagnetism has recently been observed in twisted magnetic van der Waals bilayers, opening a new avenue in altermagnetic spintronics, with twist-angle-controlled large spin currents [55]. The twist angle also provides a new degree of freedom to tune the proximity exchange coupling in graphene deposited on magnetic van der Waals crystals, controlling both its strength and its character from ferromagnetic to antiferromagnetic [36, 56].

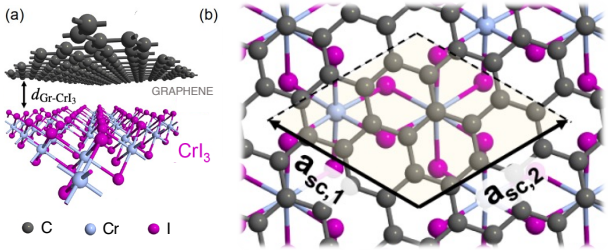

FIG. 1. Structural model of the t-Gr/CrI_3 heterostructure: (a) side view and (b) top view, with the corresponding supercell outlined.

Transition metal trihalides are among the most intensively studied magnetic van der Waals crystals [18, 57]. Cr-based trihalides, CrX_3 (X = I, Cl, Br), are insulating, exfoliable 2D magnets, whose magnetic interactions depend strongly on stacking. Their magnetic ground state and anisotropy energy – both in monolayers and multilayers – can be tuned by magnetic and electric fields or by strain and pressure [58–61].

The electronic and magnetic properties of single- and bilayer graphene/CrX_3 heterostructures have recently been investigated both theoretically and experimentally [62–64]. It has been shown that electronic states of graphene overlap and strongly hybridize with CrI_3 orbitals [64]. However, the application of gate voltage can drastically change the elec-

tronic band structure, shifting graphene electronic states to the bandgap of CrI_3. The hydrostatic pressure applied to graphene/CrI_3 can have a similar effect [65]. Importantly, pressure and gate voltage allow controlling the bandgap width in electronic states of graphene [66]. Moreover, the above-mentioned first-principles results indicate valley-contrasting physics in graphene deposited on CrI_3.

The ferromagnetic proximity exchange effect in graphene on CrI_3 makes graphene a Chern insulator with quantized anomalous Hall conductivity, when the chemical potential is within the energy gap. The ability to control its electronic and topological properties by external means, such as gate voltage and pressure – together with the system's intrinsic valley-contrasting physics – makes graphene/CrI_3 a compelling platform for exploring new topologically nontrivial phases and phenomena.

In this paper, we propose an alternative way to shift the electronic states of graphene into the bandgap of CrI_3 in graphene/CrI_3 (Gr/CrI_3) heterostructures. We have found that the twist of the graphene layer with respect to the CrI_3 layer by the angle $\Theta = 10.89°$ places the graphene Dirac cones close to the Fermi level. The low-energy electronic states of the twisted graphene on CrI_3 (t-Gr/CrI_3) reveal a band inversion – a characteristic signature of systems with nontrivial topological order. Indeed, we found that the system is a Chern insulator with quantized anomalous Hall conductivity when all valence bands are occupied. Furthermore, we analyse in this paper the behavior of selected transport characteristics, including the anomalous and valley Hall effects and the anomalous and valley Nernst effects. We also consider the effect of lateral biaxial strain on CrI_3, which can induce a magnetic phase transition to an antiferromagnetic ground state, accompanied by a topological phase transition to a trivial insulating phase. Our results show the possibility of controlling the band structure in graphene-based heterostructures *via* the twist angle. In turn, the interplay of twisting and mechanical strain in twisted graphene-based heterostructures provides a new route towards tunable topological spintronics.

STRUCTURE AND FIRST-PRINCIPLES MODELLING

Structure model of the considered t-Gr/CrI_3 heterostructure is shown in Fig. 1, where Fig. 1(a) shows the side view, while Fig. 1(b) presents the top view of the heterostructure, with the corresponding supercell outlined. The lattice parameter of pristine graphene is equal to 2.46 Å, while that of CrI_3 is 6.92 Å. To perform first-principles calculations using the Bloch theorem, we define commensurate supercells for the heterostructures. Accordingly, using the coincidence lattice method, we consider below the system geometry and determine parameters of the supercells suitable for density functional theory (DFT) calculations. Then, we briefly outline technical details of the DFT calculations, and – at the end of this section – we present and discuss the electronic band structure and magnetic properties of the t-Gr/CrI_3 heterostructure.

TABLE I. Structural and computational parameters for the studied systems.

Θ	(n,m)	(n',m')	N	$\varepsilon_{\mathrm{Gr}}$ [%]	n_k	a_{sc} [Å]	d [Å]	GS
0°	(5,0)	(1,1)	74	−2.60	8	11.99	3.4901	FM
10.89°	(2,1)	(1,0)	22	+6.27	12	6.92	3.4829	FM

Supercell Geometry

We have performed first-principles calculations for both untwisted and twisted heterostructures consisting of graphene on CrI_3 monolayer. To construct the relevant supercell, we use the coincidence lattice method [67–70]. Assuming that $\mathbf{a}_{1,2}$ are the vectors defining the primitive unit cell of graphene, and $\mathbf{b}_{1,2}$ are the vectors defining the primitive unit cell of CrI_3, one can define their supercells by the vectors $\mathbf{a}^{(n,m)}_{sc,1,2}$, and $\mathbf{b}^{(n',m')}_{sc,1,2}$, respectively:

$$\mathbf{a}^{(n,m)}_{sc,1} = n\,\mathbf{a}_1 + m\,\mathbf{a}_2, \qquad \mathbf{a}^{(n,m)}_{sc,2} = \hat{R}_\theta\,\mathbf{a}^{(n,m)}_{sc,1} \tag{1}$$

$$\mathbf{b}^{(n',m')}_{sc,1} = n'\,\mathbf{b}_1 + m'\,\mathbf{b}_2, \quad \mathbf{b}^{(n',m')}_{sc,2} = \hat{R}_{\theta'}\,\mathbf{b}^{(n',m')}_{sc,1} \tag{2}$$

where $\{n,m,n',m'\} \in \mathbb{Z}$, while $\hat{R}_\theta$ and $\hat{R}_{\theta'}$ are the rotation matrices by the angle $\theta := \measuredangle(\mathbf{a}_1,\mathbf{a}_2)$ and $\theta' := \measuredangle(\mathbf{b}_1,\mathbf{b}_2)$ respectively. As both graphene and CrI_3 form the hexagonal lattices, with the lattice constant $a = |\mathbf{a}_1| = |\mathbf{a}_2|$ and $b = |\mathbf{b}_1| = |\mathbf{b}_2|$, respectively, one can choose $\theta = \theta' = 60\,\mathrm{deg}$. Accordingly, the relative twist angle of the supercell with respect to the primitive unit cell for graphene is given by the formula

$$\Theta = \theta_0 - \arctan\left(\frac{\sqrt{3}m'}{2n'+m'}\right) - \arctan\left(\frac{\sqrt{3}m}{2n+m}\right), \tag{3}$$

where θ_0 is the initial orientation between lattices that in our case is 30°.

In order to construct the commensurate supercells for the whole vdW heterostructure, as required for periodic DFT calculations, one needs to construct the individual supercells in a way that $a^{(n,m)}_{sc} \approx b^{(n',m')}_{sc}$, and then to apply a mechanical strain to one of the supercells to fulfil the condition $a^{(n,m)}_{sc} = b^{(n',m')}_{sc}$. We consider two supercell geometries: in the first case, the graphene monolayer is placed directly on top of a CrI_3 monolayer without any twist; in the second case, the graphene monolayer is twisted by the angle of $\Theta = 10.89°$ on the fixed monolayer of CrI_3. Table I collects the parameters defining lattice vectors of the supercells, the number of atoms constituting the supercells, and the calculated biaxial strain applied to graphene.

Computational details

The first-principles calculations were performed within density-functional theory (DFT) [71]. The exchange–correlation energy was treated in the

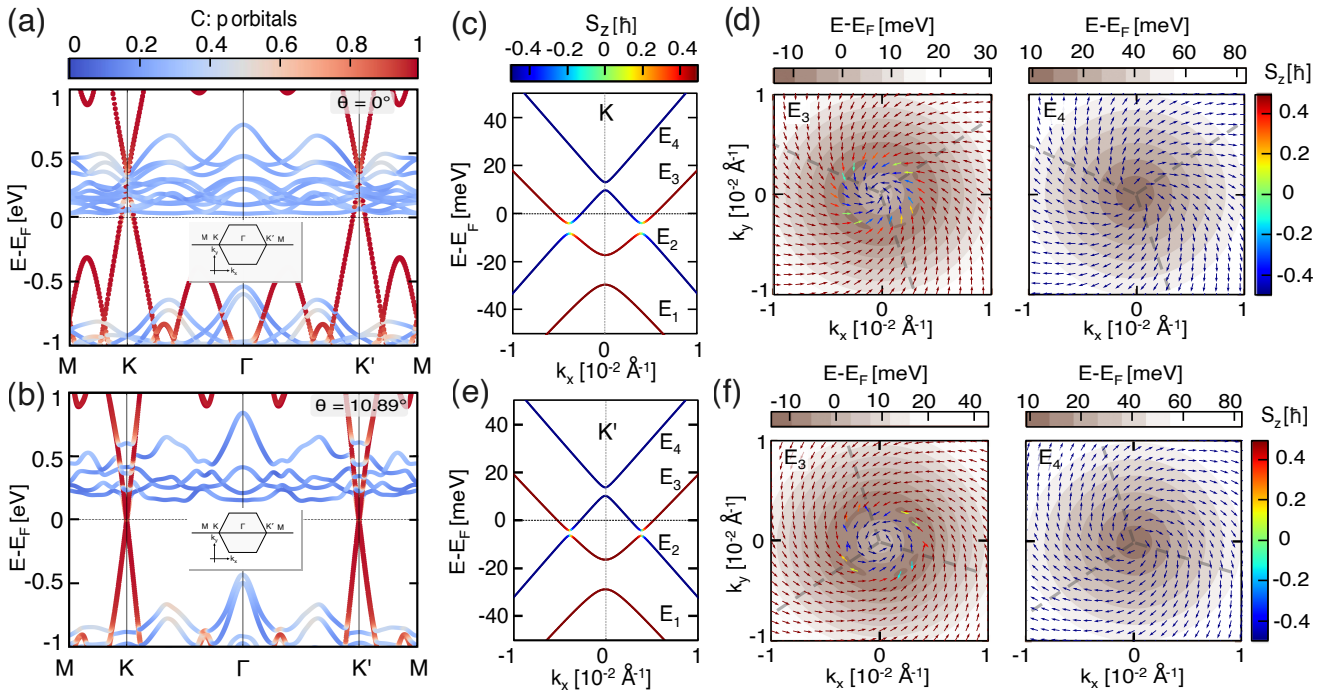

FIG. 2. Band structure of Gr/CrI_3 from DFT calculations. (a),(b) The band structure along the M–K–Γ–K'–M path for Θ = 0° (a), and Θ = 10.89° (b). The colour scale presents the weighted contribution of Carbon p orbitals to each band. (c),(e) Band structures of t-Gr/CrI_3 zoomed on graphene electronic states around the K and K' points of the Brillouin zone. The colour scale represents the corresponding spin S_z expectation value. (d),(f) In-plane spin expectation values in the wavevector space, plotted in the vicinity of the K and K' points (the point $(k_x, k_y) = (0, 0)$ defines K/K' point, respectively).

generalized-gradient approximation (GGA) using the Perdew–Burke–Ernzerhof (PBE) functional [72]. A plane-wave basis was employed together with scalar-relativistic projector-augmented-wave (PAW) pseudopotentials [73] as implemented in the Quantum Espresso package [74]. To account for spin–orbit coupling (SOC), we used fully relativistic PAW datasets. The kinetic-energy cutoff for wave-functions was set to 70 Ry, whereas the charge-density energy cutoff was set to 500 Ry. Long-range interactions between graphene and the CrI_3 monolayer was described using the Grimme DFT-D2 dispersion correction [75]. Electronic occupations followed a Marzari-Vanderbilt smearing with width $k_B T$ = 0.0005 Ry [76]. In turn, on-site electron correlations for the Cr 3d states were included via the DFT+U (U = 3 eV) approach of Cococcioni [77]. To eliminate interactions between periodic images along the c axis, a vacuum spacing of 25 Å has been added. Finally, Brillouin-zone integrations have been performed employing a uniform $n_k \times n_k \times 1$ k-point mesh, with the n_k values for each geometry listed in Table I.

Electronic and magnetic properties of Gr/CrI_3 heterostructure

Pristine CrI_3 is a ferromagnet with the easy axis oriented perpendicularly to the monolayer plane. The magnetic anisotropy energy (MAE) is defined as the difference in total energy between the out-of-plane and in-plane magnetization orientations: $MAE = E_{[100]} - E_{[001]}$. For the pristine CrI_3 monolayer we found MAE_{CrI_3} = 0.869 meV, that is in good agreement with other literature data [58, 65]. However, deposition of graphene on CrI_3 leads to a remarkable decrease in MAE, and we found $MAE_{Gr/CrI3}(\Theta = 0°)$ = 0.476meV for the untwisted Gr/CrI_3 structure, and $MAE_{tGr/CrI_3}(\Theta = 10.89°)$ = 0.71546 meV for the twisted structure. This indicates that the electronic states of graphene on CrI_3 are influenced by both proximity-induced exchange field and spin-orbit coupling, which lift the degeneracy of the graphene p-states and deforms the Dirac cones in the K and K' points.

Figures 2(a,b) show the band structure of Gr/CrI_3 obtained from DFT calculations, plotted along the high-symmetry path M–K–Γ–K'–M in the Brillouin zone, and for the twist angles Θ = 0° (a) and Θ = 10.89° (b), respectively. The presented data correspond to the tensile strain ε = +6.27% applied to graphene (and zero strain, $\varepsilon_{CrI_3} = 0$, on CrI_3) to ensure commensurability of the DFT calculations. For the untwisted heterostructure, Fig. 2(a), the graphene Dirac cones merge with the electronic band of CrI_3. In turn, for the twisted structure, the Dirac cones are shifted to the bandgap of CrI_3, see Fig. 2(b). Figures 2(c,e) present the low-energy electronic states of graphene in the vicinity of the K and K' Dirac points, modified by the proximity effects. In graphene deposited on

CrI_3, the time-reversal symmetry, spatial inversion symmetry, and sublattice (pseudospin) symmetry are broken. Consequently, one observes the interplay between exchange field, spin-orbit coupling, and staggered potential, which altogether lead to spin splitting and anticrossing of the bands and to a finite band gap. These proximity effects will be elaborated in more detail in the subsequent section. To complete the DFT results, in Figures 2(d,f) we show the spin expectation values, corresponding to the states shown in Figures 2(c,d). The most important feature of the results shown in Figures 2 (c - f) is the inverted band structure — a hallmark of nontrivial topological properties. Moreover, one can also note the valley-contrasting behaviour, i.e., the bandgap at the K point is 4.15 meV whereas at the K' point it is 2.15 meV.

LOW-ENERGY EFFECTIVE MODEL

The electronic states of proximitized graphene can be described within an effective tight-binding Hamiltonian that incorporates the symmetries of local atomic orbitals [78]. In the vicinity of the graphene K and K' points, this Hamiltonian can be expanded according to the standard $\mathbf{k}\cdot\mathbf{p}$ method. As a result, the physics of the low-energy electronic states of graphene can be described by an effective low-energy $\mathbf{k}\cdot\mathbf{p}$ Hamiltonian, whose explicit matrix form can be determined by taking into account the relevant symmetry arguments and also features of the DFT band structure. When expressed in terms of the Pauli matrices acting in the sublattice, $\hat{\sigma}_\alpha$, and spin, $\hat{s}_\alpha$ subspaces ($\alpha = \{0, x, y, z\}$, with $\alpha = 0$ corresponding to the identity 2×2 matrix), this Hamiltonian takes the form [43, 44, 46, 78–82]:

$$\hat{H}_\tau = \hat{H}_0^\tau + \hat{H}_\Delta + \hat{H}_I^\tau + \hat{H}_R^\tau + \hat{H}_{EX}^\tau + E_0\hat{\sigma}_0\otimes\hat{s}_0, \qquad (4)$$

where $\tau = \pm 1$ corresponds to the K/K' valley, respectively. The first term describes the low-energy states of pristine graphene [78, 80]:

$$\hat{H}_0^\tau = v\left(\tau\hat{\sigma}_x k_x + \hat{\sigma}_y k_y\right), \qquad (5)$$

with the parameter $v = at\frac{\sqrt{3}}{2}$ defining the Fermi velocity, and determined by the lattice constant a and nearest neighbour hopping parameter t. The second term is responsible for the orbital proximity-induced gap arising from the pseudospin symmetry breaking: carbon atoms on sublattices A and B experience, on average, different crystalline fields due to the presence of CrI_3. This term takes the form [78, 80]:

$$\hat{H}_\Delta = \Delta\hat{\sigma}_z\otimes\hat{s}_0, \qquad (6)$$

where Δ is the so-called staggered potential (effective orbital hybridization energy) on sublattices A and B. The effect of sublattice-dependent spin-conserving next-nearest neighbor spin-orbit interaction is described by the term [78–80]:

$$\hat{H}_I^\tau = \tau\left(\lambda_I^A\hat{\sigma}_+ + \lambda_I^B\hat{\sigma}_-\right)\otimes\hat{s}_z \qquad (7)$$

TABLE II. The parameters defining the effective low-energy Hamiltonian of tGr/CrI_3, obtained from fitting to the DFT data.

a [Å]	t [eV]	E_0 [meV]	Δ [meV]	λ_I^A [meV]	λ_I^B [meV]	λ_R [meV]	ϕ_R [rad]	λ_{EX}^A [meV]	λ_{EX}^B [meV]
2.62	2.02	-5.7	5.7	0.8	-0.99	1.65	3.75	16.01	20.79

where $\hat{\sigma}_\pm = (\hat{\sigma}_z \pm \hat{\sigma}_0)/2$, and $\lambda_I^{A/B}$ denotes the intrinsic spin-orbit parameter for the sublattices A/B, respectively. Due to the spatial inversion symmetry breaking, the Rashba spin-orbit interaction appears in the system and tilts electrons' spin out of the plane. The Rashba Hamiltonian in twisted graphene-based structures takes more general form [43, 44, 46, 78–80]:

$$\hat{H}_R^\tau = -\lambda_R \exp^{-i\frac{\phi_R}{2}\hat{s}_z}\left(\tau\hat{\sigma}_x\otimes\hat{s}_y + \hat{\sigma}_y\otimes\hat{s}_x\right)\exp^{i\frac{\phi_R}{2}\hat{s}_z}, \qquad (8)$$

where λ_R describes the strength of the Rashba coupling, while the so-called Rashba angle, ϕ_R, governs the spin-momentum locking of electron spins and therefore plays an essential role in the current-induced spin polarization effect (also known as Rashba-Edelstein effect). In turn, the effect of sublattice-dependent proximity-exchange interaction is taken into account by the following term[80–82]:

$$\hat{H}_{EX} = \left(\lambda_{EX}^A\hat{\sigma}_+ - \lambda_{EX}^B\hat{\sigma}_-\right)\otimes\hat{s}_z, \qquad (9)$$

where $\lambda_{EX}^{A/B}$ are the sublattice dependent exchange coupling parameters. Finally, in the last term of Eq. (4), E_0 defines the position of the Dirac point with respect to the Fermi energy.

All parameters of Hamiltonian (4) can be obtained through a fitting procedure, in which the eigenstates of the $\mathbf{k}\cdot\mathbf{p}$ Hamiltonian are compared with the DFT-calculated electronic states of graphene around the K and K' points. In parallel with the band-structure fitting, the spin projections of electrons in the graphene electronic states are also matched to the DFT results. Table II collects all the parameters obtained for tGr/CrI_3 by the fitting procedure. Figure 3 presents the electronic band structure and spin components in the vicinity of Dirac points, and shows a very good agreement between the effective model and DFT calculations. The effective exchange coupling constants are about two orders of magnitude larger than in graphene/$MnPSe_3$ [82] and one order of magnitude larger than in graphene/$Cr_2Ge_2Te_6$ [36]. In turn, the intrinsic SOC and Rashba SOC parameters are comparable to those reported in semiconducting TMDCs [45, 49].

TOPOLOGICAL PROPERTIES AND SELECTED TRANSPORT CHARACTERISTICS

Berry curvature and Chern number

Figures 2(c),(e) reveal the inverted band structure of twisted graphene on CrI_3, indicating nontrivial topological properties

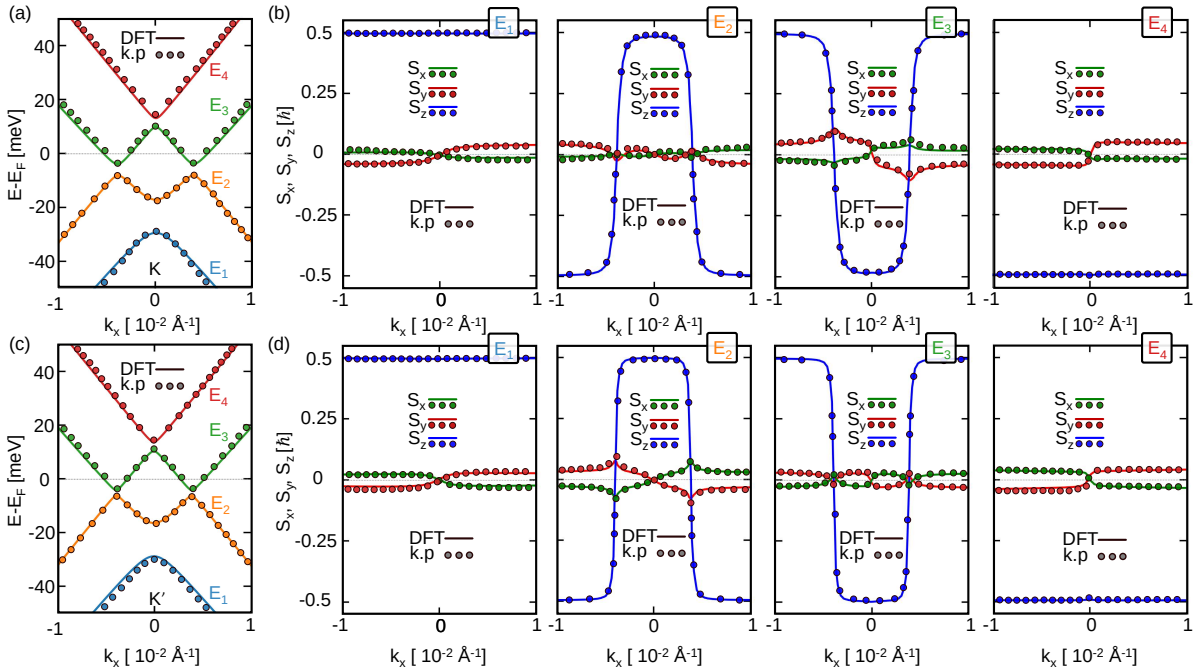

FIG. 3. Electronic band structure of tGr/CrI_3 as well as the S_x, S_y, and S_z components of spin expectation values in the vicinity of the K and K' points. Solid lines represent the DFT results, while the dots correspond to the results obtained from the $\mathbf{k}\cdot\mathbf{p}$ model Hamiltonian.

of the heterostructure. To analyse this issue in more details, we determine the Berry curvature, $\Omega^n_{\mathbf{k}}$, and Chern number, n_{Ch}. The Berry curvature corresponding to the n-th band can be obtained directly from the following formula [83–88]:

$$\mathbf{\Omega}_{\mathbf{k}n} = \nabla_{\mathbf{k}} \times \langle \Psi_{\mathbf{k}n} | i\nabla_{\mathbf{k}} | \Psi_{\mathbf{k}n} \rangle, \tag{10}$$

where $|\Psi_{\mathbf{k}n}\rangle$ is the basis function, i.e., the eigenfunction of the $\mathbf{k}\cdot\mathbf{p}$ Hamiltonian (4) or the cell-periodic Bloch state in the case of tight-binding or the first-principles calculations. Note that in the 2D system the Berry curvature has only the z component, $\mathbf{\Omega}_{\mathbf{k}n} = (0, 0, \Omega_{\mathbf{k}n})$. The Berry connection integrated over fully-occupied bands defines the Chern number [84, 86]:

$$n_{Ch} = \frac{1}{2\pi} \sum_{\substack{n \\ \text{occ.}}} \int d^2\mathbf{k}\, \Omega_{\mathbf{k}n} \tag{11}$$

Note that in the case of a low-energy Hamiltonian, one needs to take into account the contribution from the two inequivalent K points, thus the Chern number calculated within the $\mathbf{k}\cdot\mathbf{p}$ model is:

$$n_{Ch} = \sum_{\tau=\pm 1} n^{\tau}_{Ch} \tag{12}$$

and n^{τ}_{Ch} is defined by the Eq. (11) with Berry Curvature $\Omega^{\tau}_{\mathbf{k}n}$ calculated for the τ-th valley.

Figure 4(a) presents the total Berry curvature of the t-Gr/CrI_3 heterostructure, calculated from the DFT data for the fully occupied valence bands, i.e, for the Fermi level inside the energy gap of graphene. The Berry curvature was obtained from maximally localized Wannier functions using the WANNIER90 package [89, 90] and the post-processing tools of WANNIERTOOLS[91]. The Berry curvatures for individual valence bands, calculated within the low-energy effective Hamiltonian, are shown in Fig. 4(b,c) together with their sum (total Berry curvature). These results demonstrate not only the excellent agreement between the fitted $\mathbf{k}\cdot\mathbf{p}$ model and the DFT calculations, but also confirm that our low-energy Hamiltonian accurately captures the topological properties of the t-Gr/CrI_3 heterostructure.

The total Berry curvature for fully occupied valence exhibits nonzero peaks around the K and K' points, where the graphene electronic states are located. Importantly, in consequence of time-reversal symmetry breaking, the peaks at the K and K' valleys have the same sign. The interplay between the proximity-induced exchange field and Rashba spin–orbit coupling opens an energy gap, which is further modulated by the staggered potential and intrinsic valley-Zeeman-type SOC. As a result, the insulating state in the t-Gr/CrI_3 heterostructure is topologically nontrivial. When the Fermi level is in the energy gap, the system is a Chern insulator, i.e., it hosts the quantum anomalous Hall (QAH) phase. Indeed, the Chern numbers calculated for the K and K' valleys are identical, $n^{\mathrm{K}}_{\mathrm{Ch}} = n^{\mathrm{K}'}_{\mathrm{Ch}} = -1$, giving a total Chern number for the fully occupied valence bands of $n_{\mathrm{Ch}} = -2$. The same result is obtained directly from DFT calculations for the Chern number of the fully occupied valence bands. This is in agreement with earlier results on the topological properties of graphene on magnetic substrates [82, 92–95].

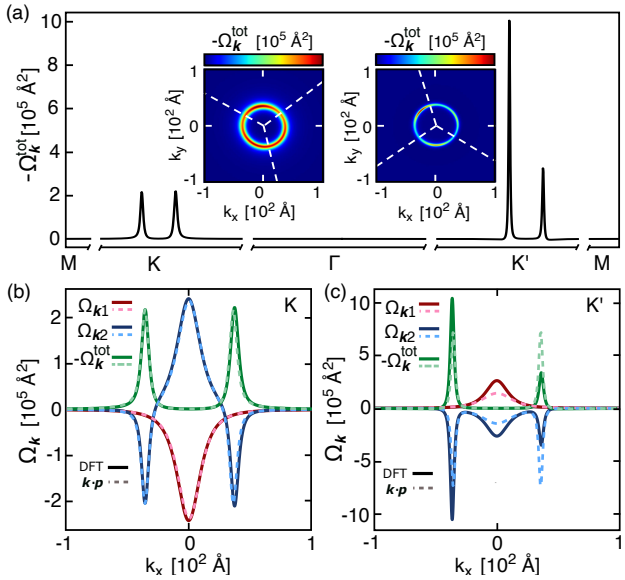

FIG. 4. Berry curvature of the t-Gr/CrI3 heterostructure for fully occupied valence bands. (a) DFT results obtained from maximally localized Wannier functions. (b),(c) Berry curvatures of individual valence bands of graphene and their sum obtained from the fitted low-energy model for the K (b) and K' (c) points.

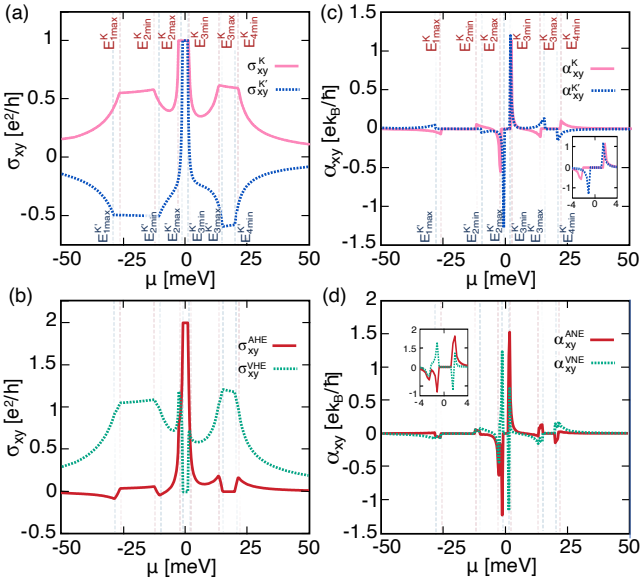

FIG. 5. (a) The intrinsic contributions to the transverse conductivity, $\sigma_{xy}^{\mathrm{K/K'}}$, from the K and K' valleys, respectively. (b) Anomalous Hall conductivity, $\sigma_{xy}^{\mathrm{AHE}}$, and the valley Hall conductivity, $\sigma_{xy}^{\mathrm{VHE}}$, plotted as a function of the chemical potential, calculated from the effective model. (c) Contributions to the transverse thermal conductivity, $\alpha_{xy}^{\mathrm{K/K'}}$, from the K and K' valleys, respectively. (d) Anomalous Nernst effect, $\alpha_{xy}^{\mathrm{ANE}}$, and valley Nernst effect, $\alpha_{xy}^{\mathrm{VNE}}$, plotted as a function of the chemical potential. The $\mu = 0$ is set at the position of Dirac point, i.e., $\mu \to \mu - E_0$.

Anomalous and valley Hall effect

The t-Gr/CrI_3 heterostructure exhibits Berry-phase-induced anomalous Hall effect (AHE). In the clean limit, the corresponding anomalous Hall conductivity can be found based on the Thouless-Kohmoto-Nightingale-Nijs (TKNN) theory [84–87]:

$$\sigma_{xy}^{\mathrm{AHE}} = -\frac{e^2}{h}\sum_n \int \frac{d^2\mathbf{k}}{2\pi}\Omega_{\mathbf{k}n} f(E_{\mathbf{k}n}), \tag{13}$$

where the conductivity tensor σ_{xy} is the ratio of charge current density flowing in the x-direction as a system response to the external electric field applied in the y-direction ($\sigma_{xy} \equiv j_x/E_y$) and $f(E_{\mathbf{k}n})$ is the Fermi-Dirac distribution function for the n-th band. Note that in the case of the $\mathbf{k}\cdot\mathbf{p}$ model, this expression should be treated as a sum of the contributions from both valleys (i.e., from K and K' points). Accordingly, $\sigma_{xy}^{\mathrm{AHE}}$ should read $\sigma_{xy}^{\mathrm{AHE}} \equiv \sigma_{xy}^{\mathrm{K}} + \sigma_{xy}^{\mathrm{K'}}$, as in this case $\Omega_{\mathbf{k}n} = \Omega_{\mathbf{k}n}^{\mathrm{K}} + \Omega_{\mathbf{k}n}^{\mathrm{K'}}$.

The valley-contrasting behaviour of the band structure suggests the presence of a nonzero valley Hall effect (VHE) [94, 96–98]. This phenomenon follows directly from the valley-dependent anomalous velocity generated in an external electric field. Specifically, for a given band, the anomalous velocity components of electrons have opposite directions in the two valleys, as the corresponding Berry curvatures at the K and K' points have opposite signs. Consequently, electrons (or holes) from the two valleys are deflected toward opposite edges of the sample. The valley Hall conductivity is defined as

$$\sigma_{xy}^{\mathrm{VHE}} = \sigma_{xy}^{\mathrm{K}} - \sigma_{xy}^{\mathrm{K'}}. \tag{14}$$

Importantly, in t-Gr/CrI_3 we have found that the bandgaps at the K and K' points differ by about 2 meV. In such a case, the bandgap can be closed selectively (via external magnetic field or gate voltage) at one valley while remains open at the other one, realizing a valley-dependent bandgap closing. Otherwise, by tuning the chemical potential, one can obtain a current associated solely with the electronic states of a single valley.

Figure 5(a) shows the Hall conductivities associated with the K and K' points, whereas Fig. 5(b) presents their sum, i.e. the anomalous Hall conductivity, $\sigma_{xy}^{\mathrm{AHE}}$, and their difference, that is the valley Hall conductivity $\sigma_{xy}^{\mathrm{VHE}}$ – all presented as a function of the chemical potential. For chemical potentials within the gap (around $\mu = 0$), the anomalous Hall conductivity achieves the quantized and universal value $\sigma_{xy}^{\mathrm{AHE}} = 2e^2/h$. This quantization follows directly from the Chern number of the fully occupied valence bands of graphene, $n_{\mathrm{Ch}} = -2$. Outside the gap, the anomalous Hall conductivity rapidly decreases with increasing absolute value of the chemical potential. The kinks observed for both positive and negative chemical potentials correspond to the crossing of the valence and conduction band extrema at K and K' points, as indicated in Fig. 5. Furthermore, the asymmetry of the anomalous Hall

conductivity with respect to the sign of the chemical potential reflects both particle–hole asymmetry and the inequivalence of the band extrema at the K and K' points.

The VHE is absent, when the chemical potential is within the bandgap. However, when the chemical potential crosses the first conduction-band minimum ($E_{3\mathrm{min}}$) or the valence-band maximum ($E_{2\mathrm{max}}$), the valley Hall conductivity exhibits a sharp peak, then decreases to a local minimum and increases again to its maximum value, when the chemical potential crosses the first conduction-band extremum ($E_{3\mathrm{max}}$) or the upper valence-band minimum ($E_{2\mathrm{min}}$), respectively. In the energy window between the local maximum of the first conduction band ($E_{3\mathrm{max}}$) and minimum of the second conduction band ($E_{4\mathrm{min}}$), as well as between the local minimum of the upper valence band ($E_{2\mathrm{min}}$) and the maximum of the lower valence band ($E_{1\mathrm{max}}$), we observe a plateau in the valance Hall conductivity

Here, we should note that a modern theoretical framework for orbital effects has been proposed recently, suggesting that the valley Hall effect should, at some stage, be more rigorously described in terms of the orbital Hall effect [99]. Since the aim of this work is to highlight the potential of t-Gr/CrI_3 as an interesting platform for spintronics, we decided not to pursue this direction here. The orbital Hall effect in proximitized graphene has been discussed, for example, in [100–103], and will be addressed in the context of graphene on magnetic substrates in future work.

Anomalous and valley Nernst effect

The Berry curvature is also responsible for transport phenomena driven by a temperature gradient in the system. One example is the anomalous Nernst effect (ANE), the thermal counterpart of the anomalous Hall effect. By analogy with the valley Hall effect, one can also define the valley Nernst effect (VNE). Both kinetic coefficients can be calculated from the following expressions:

$$\alpha_{xy}^{\mathrm{ANE}} = \alpha_{xy}^{\mathrm{K}} + \alpha_{xy}^{\mathrm{K}'}, \tag{15}$$

$$\alpha_{xy}^{\mathrm{VNE}} = \alpha_{xy}^{\mathrm{K}} - \alpha_{xy}^{\mathrm{K}'}, \tag{16}$$

where

$$\alpha_{xy}^{\tau} = \frac{ek_B}{\hbar}\sum_n \int \frac{d^2\mathbf{k}}{(2\pi)^2}\Omega_{\mathbf{k}n}^{\tau} S_{\mathbf{k}n}^{\tau}. \tag{17}$$

In the above equation $S_{\mathbf{k}n}$ is the entropy density of electrons, defined as:

$$S_{\mathbf{k}n}^{\tau} = -f(E_{\mathbf{k}n}^{\tau})\ln(f(E_{\mathbf{k}n}^{\tau})) - (1-f(E_{\mathbf{k}n}^{\tau}))\ln(1-f(E_{\mathbf{k}n}^{\tau})). \tag{18}$$

Figure 5(c) presents the transverse thermal conductivity calculated for the K and K' points, respectively, whereas

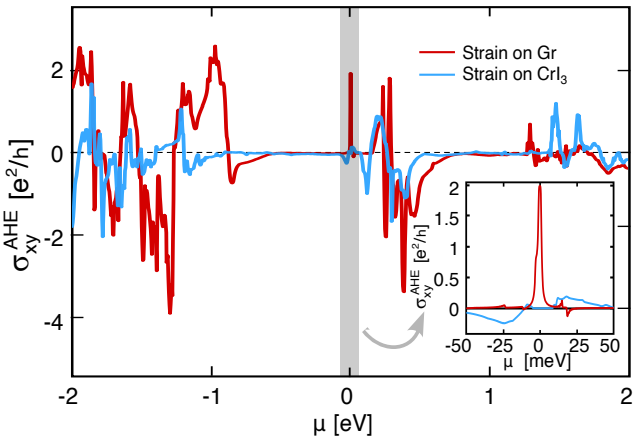

FIG. 6. (a) Anomalous Hall conductivity calculated based on DFT data for t-Gr/CrI_3 when biaxial strain is applied only to graphene (red line) and when it is applied only to the CrI_3 monolayer. The $\mu = 0$ is set at the position of the Dirac point, i.e., $\mu \to \mu - E_0$.

Fig 5(d) presents the variation of ANE and VNE with chemical potential. Both characteristics exhibit sharp peaks at the chemical potential crossing the band extrema. Accordingly, measurements of the anomalous or valley Hall effect, as well as of the anomalous or valley Nernst effect, allow for determination of both the bandgap width and the band splitting in proximitized graphene.

EFFECT OF STRAIN

The electronic, topological, and magnetic properties of van der Waals materials are highly susceptible to mechanical strain [104–107]. It has been demonstrated that both the magnetic anisotropy energy and magnetic ground state of CrI_3 mono- and bi-layers can be modified by applying biaxial strain or gate voltage [59, 60]. Accordingly, biaxial strain also modifies the net magnetization and the magnetic ground state of the t-Gr/CrI_3 heterostructure. These changes can be simply observed experimentally by the anomalous Hall conductivity measurement. In Fig. 6, we present the anomalous Hall conductivity of the t-Gr/CrI_3 heterostructure, calculated from DFT data using the Wannier90 package, for the two possible supercells that ensure commensurability between graphene and CrI_3 unit cells, as required for first-principles simulations. The red curves in Fig. 6(a) and (b) correspond to the structure discussed throughout this work, in which biaxial strain is applied to the graphene monolayer while the CrI_3 monolayer remains unstrained. In this case, the system is in a ferromagnetic ground state and exhibits topologically nontrivial behavior, with a quantized anomalous Hall conductivity when the chemical potential lies within the energy gap. By contrast, the blue curves represent results for a supercell in which biaxial tensile strain of $\epsilon_{CrI_3} = -5.90\%$ is applied to the CrI_3 layer, while the graphene remains unstrained. In this situation, we have found that the structure is in an antiferromagnetic ground state, in

agreement with previous studies reporting a magnetic phase transition under strain of -5.5% [58, 65]. Importantly, the magnetic phase transition results in a strong modification of the proximity effects on the graphene electronic states. Consequently, t-Gr/CrI_3 becomes a trivial insulator with vanishing anomalous Hall conductivity when the chemical potential lies within the bandgap. We should note that the applied tensile strain is large and may cause the system to become unstable. This issue could potentially be mitigated by stabilizing the structure on a substrate or through encapsulation. However, such considerations (requiring DFT modelling of Gr/CrI_3 together with an additional substrate or encapsulating material) are beyond the scope of this work. Here, our objective was to emphasize the potential of magnetic van der Waals heterostructures for electronic and spintronic quantum devices, in which a strain-induced change in the quantum anomalous Hall conductivity from two conductance quanta to zero can encode logical "1" and "0," respectively.

DISCUSSION AND CONCLUSIONS

In this work, we provided a comprehensive analysis of the electronic, magnetic, and topological properties of graphene deposited on CrI_3. First, we have found the twist angle at which the graphene Dirac cones are positioned within the energy gap of CrI_3. Next, we have derived the low-energy effective Hamiltonian describing properties of the proximitized graphene, which accurately captures the low-energy physics of the t-Gr/CrI_3 heterostructure. We have also confirmed that the system is Chern insulator and reveals quantized anomalous Hall conductivity, when the chemical potential is placed inside the energy gap. We have analysed the intrinsic anomalous and valley Hall effect as well as anomalous and valley Nernst effects. Characteristic kinks in the AHE/VHE (or sharp peaks in the ANE/VNE), that appear when the chemical potential is shifted from the energy gap into the first valence or conduction band, and when it crosses the edge of the second valence or conduction band, allow for determining the bandgap width and band splitting in proximitized graphene directly from transport measurements.

Another important feature of t-Gr/CrI_3 is the valley-contrasting behaviour of graphene Dirac cones. We have shown that the difference in the energy gap of the unbiased structure at the K and K' valleys is approximately 2 meV. Accordingly, one can simply tune these gaps with an external gating or magnetic field. In such a case, the bandgap closes selectively at one valley, while remaining open at the other valley, enabling valley-dependent bandgap engineering and single-valley transport controlled by the chemical potential. We have also highlighted the potential of magnetic van der Waals heterostructures for quantum electronic and spintronic devices, where strain can switch the quantum anomalous Hall conductivity between two conductance quanta and zero, encoding logical "1" and "0," respectively.

We should also stress that in this article, we have presented transport coefficients that do not depend on the Rashba angle, ϕ_R. The electronic states of twisted graphene on CrI_3 exhibit a large Rashba angle, $\phi_R = 3.75, \mathrm{rad}$ (approximately 215°), as shown in Fig. 2(e) and (f). The Rashba angle substantially affects the nonequilibrium spin polarization, a phenomenon known also as the unconventional Rashba-Edelstein effect. A nonzero Rashba angle originates from the breaking of the in-plane mirror symmetry and results in spin–momentum locking, in which the electron spin expectation value acquires a finite radial component alongside the more commonly observed orthogonal component. Consequently, the nonequilibrium spin polarization has two in-plane components; one perpendicular and one parallel to the external electric field, as it was reported for graphene on transition metal dichalcogenides [45, 47, 49, 51, 108]. In turn, it is also well known that in magnetic systems with strong spin-orbit coupling, the nonequilibrium spin polarization can possess all three components (depending on the magnetization orientation) [99, 109–112]. Accordingly, the nonequilibrium spin polarization emerging in t-Gr/CrI_3 will have various contributions that may, in slightly different ways, induce spin dynamics in the CrI_3 layer. A detailed theory of Rashba-Edelstein effect and spin-orbit torques in twisted graphene on ferromagnetic layers is discussed elsewhere [113].

ACKNOWLEDGMENTS

M.J. and A.D. acknowledges the supported by the National Science Centre (NCN), Poland within the Norwegian Financial Mechanism under the Polish-Norwegian Research Project GRIEG '2Dtronics', project no. 2019/34/H/ST3/00515.

M.G. acknowledges funding by the EU NextGenerationEU through the Recovery and Resilience Plan for Slovakia under the project No. 09I05-03-V02-00071, and the Ministry of Education, Research, Development and Youth of the Slovak Republic, provided under Grant No. VEGA 1/0104/25, Slovak Research and Development Agency under Contract No. SK-SRB-23-0033, and the Slovak Academy of Sciences project IMPULZ IM-2021-42.

* adyrdal@amu.edu.pl; mirali.jafari@amu.edu.pl

[1] K. S. Novoselov, A. K. Geim, S. V. Morozov, D.-e. Jiang, Y. Zhang, S. V. Dubonos, I. V. Grigorieva, and A. A. Firsov, science **306**, 666 (2004).
[2] A. K. Geim and I. V. Grigorieva, Nature **499**, 419 (2013).
[3] C. Gong and X. Zhang, Science **363**, eaav4450 (2019).
[4] J. Kim, O. Song, Y. S. Cho, M. Jung, D. Rhee, and J. Kang, ACS Materials Au **2**, 382 (2022).
[5] A. Castellanos-Gomez, X. Duan, Z. Fei, H. R. Gutierrez, Y. Huang, X. Huang, J. Quereda, Q. Qian, E. Sutter, and P. Sutter, Nature Reviews Methods Primers **2**, 58 (2022).
[6] R. Bian, C. Li, Q. Liu, G. Cao, Q. Fu, P. Meng, J. Zhou, F. Liu, and Z. Liu, National Science Review **9**, nwab164 (2021).
[7] J. Qi, Z. Wu, W. Wang, K. Bao, L. Wang, J. Wu, C. Ke, Y. Xu,

and Q. He, International Journal of Extreme Manufacturing **5**, 022007 (2023).
[8] A. Soumyanarayanan, N. Reyren, A. Fert, and C. Panagopoulos, Nature **539**, 509 (2016).
[9] Y. Tokura, M. Kawasaki, and N. Nagaosa, Nature Physics **13**, 1056 (2017).
[10] C. Bao, P. Tang, D. Sun, and S. Zhou, Nature Reviews Physics **4**, 33 (2022).
[11] H. Kurebayashi, J. H. Garcia, S. Khan, J. Sinova, and S. Roche, Nature Reviews Physics **4**, 150 (2022).
[12] P. Törmä, S. Peotta, and B. A. Bernevig, Nature Reviews Physics **4**, 528 (2022).
[13] Q. H. Wang, A. Bedoya-Pinto, M. Blei, A. H. Dismukes, A. Hamo, S. Jenkins, M. Koperski, Y. Liu, Q.-C. Sun, E. J. Telford, H. H. Kim, M. Augustin, U. Vool, J.-X. Yin, L. H. Li, A. Falin, C. R. Dean, F. Casanova, R. F. L. Evans, M. Chshiev, A. Mishchenko, C. Petrovic, R. He, L. Zhao, A. W. Tsen, B. D. Gerardot, M. Brotons-Gisbert, Z. Guguchia, X. Roy, S. Tongay, Z. Wang, M. Z. Hasan, J. Wrachtrup, A. Yacoby, A. Fert, S. Parkin, K. S. Novoselov, P. Dai, L. Balicas, and E. J. G. Santos, ACS Nano **16**, 6960 (2022).
[14] G. Zhang, H. Wu, L. Zhang, L. Yang, Y. Xie, F. Guo, H. Li, B. Tao, G. Wang, W. Zhang, and H. Chang, Small **18**, 2204380 (2022).
[15] A. Fert, R. Ramesh, V. Garcia, F. Casanova, and M. Bibes, Rev. Mod. Phys. **96**, 015005 (2024).
[16] W. Ren, P. Bøggild, J. Redwing, K. Novoselov, L. Sun, Y. Qi, K. Jia, Z. Liu, O. Burton, J. Alexander-Webber, S. Hofmann, Y. Cao, Y. Long, Q.-H. Yang, D. Li, S. H. Choi, K. K. Kim, Y. H. Lee, M. Li, Q. Huang, Y. Gogotsi, N. Clark, A. Carl, R. Gorbachev, T. Olsen, J. Rosen, K. S. Thygesen, D. K. Efetov, B. S. Jessen, M. Yankowitz, J. Barrier, R. K. Kumar, F. H. L. Koppens, H. Deng, X. Li, S. Dai, D. N. Basov, X. Wang, S. Das, X. Duan, Z. Yu, M. Borsch, A. C. Ferrari, R. Huber, M. Kira, F. Xia, X. Wang, Z.-S. Wu, X. Feng, P. Simon, H.-M. Cheng, B. Liu, Y. Xie, W. Jin, R. R. Nair, Y. Xu, Q. Zhang, A. K. Katiyar, J.-H. Ahn, I. Aharonovich, M. C. Hersam, S. Roche, Q. Hua, G. Shen, T. Ren, H.-B. Zhang, C. M. Koo, N. Koratkar, V. Pellegrini, R. J. Young, B. Qu, M. Lemme, and A. J. Pollard, The 2D Materials Roadmap (2025), arXiv:2503.22476 [cond-mat.mtrl-sci].
[17] X. Sun, M. Suriyage, A. R. Khan, M. Gao, J. Zhao, B. Liu, M. M. Hasan, S. Rahman, R.-s. Chen, P. K. Lam, and Y. Lu, Chemical Reviews **124**, 1992 (2024).
[18] B. Zhang, P. Lu, R. Tabrizian, P. X. L. Feng, and Y. Wu, npj Spintronics **2**, 6 (2024).
[19] E. Y. Vedmedenko, R. K. Kawakami, D. D. Sheka, P. Gambardella, A. Kirilyuk, A. Hirohata, C. Binek, O. Chubykalo-Fesenko, S. Sanvito, B. J. Kirby, J. Grollier, K. Everschor-Sitte, T. Kampfrath, C.-Y. You, and A. Berger, Journal of Physics D: Applied Physics **53**, 453001 (2020).
[20] H. Yang, S. O. Valenzuela, M. Chshiev, S. Couet, B. Dieny, B. Dlubak, A. Fert, K. Garello, M. Jamet, D.-E. Jeong, K. Lee, T. Lee, M.-B. Martin, G. S. Kar, P. Sénéor, H.-J. Shin, and S. Roche, Nature **606**, 663 (2022).
[21] J. T. Gish, D. Lebedev, T. W. Song, V. K. Sangwan, and M. C. Hersam, Nature Electronics **7**, 336 (2024).
[22] C. Becher, W. Gao, S. Kar, C. D. Marciniak, T. Monz, J. G. Bartholomew, P. Goldner, H. Loh, E. Marcellina, K. E. J. Goh, T. S. Koh, B. Weber, Z. Mu, J.-Y. Tsai, Q. Yan, T. Huber-Loyola, S. Höfling, S. Gyger, S. Steinhauer, and V. Zwiller, Materials for Quantum Technology **3**, 012501 (2023).
[23] M. Gmitra and J. Fabian, Phys. Rev. B **92**, 155403 (2015).
[24] M. Gmitra, D. Kochan, P. Högl, and J. Fabian, Phys. Rev. B **93**, 155104 (2016).
[25] A. W. Cummings, J. H. Garcia, J. Fabian, and S. Roche, Phys. Rev. Lett. **119**, 206601 (2017).
[26] T. S. Ghiasi, J. Ingla-Aynés, A. A. Kaverzin, and B. J. van Wees, Nano Letters **17**, 7528 (2017).
[27] J. H. Garcia, M. Vila, A. W. Cummings, and S. Roche, Chem. Soc. Rev. **47**, 3359 (2018).
[28] T. Wakamura, F. Reale, P. Palczynski, M. Q. Zhao, A. T. C. Johnson, S. Guéron, C. Mattevi, A. Ouerghi, and H. Bouchiat, Phys. Rev. B **99**, 245402 (2019).
[29] T. S. Ghiasi, A. A. Kaverzin, P. J. Blah, and B. J. van Wees, Nano Letters **19**, 5959 (2019).
[30] A. G. Swartz, P. M. Odenthal, Y. Hao, R. S. Ruoff, and R. K. Kawakami, ACS Nano **6**, 10063 (2012).
[31] H. X. Yang, A. Hallal, D. Terrade, X. Waintal, S. Roche, and M. Chshiev, Phys. Rev. Lett. **110**, 046603 (2013).
[32] S. Su, Y. Barlas, J. Li, J. Shi, and R. K. Lake, Phys. Rev. B **95**, 075418 (2017).
[33] A. Hallal, F. Ibrahim, H. Yang, S. Roche, and M. Chshiev, 2D Materials **4**, 025074 (2017).
[34] D. V. Averyanov, I. S. Sokolov, A. M. Tokmachev, O. E. Parfenov, I. A. Karateev, A. N. Taldenkov, and V. G. Storchak, ACS Applied Materials & Interfaces **10**, 20767 (2018).
[35] J. Wu, F. Liu, M. Sasase, K. Ienaga, Y. Obata, R. Yukawa, K. Horiba, H. Kumigashira, S. Okuma, T. Inoshita, and H. Hosono, Science Advances **5**, eaax9989 (2019).
[36] K. Zollner and J. Fabian, Phys. Rev. Lett. **128**, 106401 (2022).
[37] S. Pandey, S. Hettler, R. Arenal, C. Bouillet, A. R. Moghe, S. Berciaud, J. Robert, J.-F. m. c. Dayen, and D. Halley, Phys. Rev. B **108**, 144423 (2023).
[38] J. Liu, Z. Ma, J. Gao, and X. Dai, Phys. Rev. X **9**, 031021 (2019).
[39] S. Carr, S. Fang, and E. Kaxiras, Nature Reviews Materials **5**, 748 (2020).
[40] F. He, Y. Zhou, Z. Ye, S.-H. Cho, J. Jeong, X. Meng, and Y. Wang, ACS nano **15**, 5944 (2021).
[41] M. Liu, L. Wang, and G. Yu, Advanced Science **9**, 2103170 (2022).
[42] D. Aggarwal, R. Narula, and S. Ghosh, Journal of Physics: Condensed Matter **35**, 143001 (2023).
[43] Y. Li and M. Koshino, Phys. Rev. B **99**, 075438 (2019).
[44] A. David, P. Rakyta, A. Kormányos, and G. Burkard, Phys. Rev. B **100**, 085412 (2019).
[45] T. Naimer, K. Zollner, M. Gmitra, and J. Fabian, Phys. Rev. B **104**, 195156 (2021).
[46] C. G. Péterfalvi, A. David, P. Rakyta, G. Burkard, and A. Kormányos, Phys. Rev. Res. **4**, L022049 (2022).
[47] S. Lee, D. J. P. de Sousa, Y.-K. Kwon, F. de Juan, Z. Chi, F. Casanova, and T. Low, Phys. Rev. B **106**, 165420 (2022).
[48] A. Pezo, Z. Zanolli, N. Wittemeier, P. Ordejón, A. Fazzio, S. Roche, and J. H. Garcia, 2D Materials **9**, 015008 (2021).
[49] K. Zollner, S. a. M. João, B. K. Nikolić, and J. Fabian, Phys. Rev. B **108**, 235166 (2023).
[50] N. Ontoso, C. K. Safeer, F. Herling, J. Ingla-Aynés, H. Yang, Z. Chi, B. Martin-Garcia, I. n. Robredo, M. G. Vergniory, F. de Juan, M. Reyes Calvo, L. E. Hueso, and F. Casanova, Phys. Rev. Appl. **19**, 014053 (2023).
[51] I. Wojciechowska and A. Dyrdal, to be published (2025).
[52] H. Polshyn, J. Zhu, M. A. Kumar, Y. Zhang, F. Yang, C. L. Tschirhart, M. Serlin, K. Watanabe, T. Taniguchi, A. H. MacDonald, and A. F. Young, Nature **588**, 66 (2020).
[53] L. Peng, C. D. Beule, D. Li, L. Yang, E. J. Mele, and S. Adam, arXiv: 2503.09689 (2025).
[54] R. He, D. Wang, N. Luo, J. Zeng, K.-Q. Chen, and L.-M. Tang,

Phys. Rev. Lett. **130**, 046401 (2023).
[55] Y. Liu, J. Yu, and C.-C. Liu, Phys. Rev. Lett. **133**, 206702 (2024).
[56] S. Yan, S. Qi, D. Wang, and W. Mi, Physica E: Low-dimensional Systems and Nanostructures **134**, 114854 (2021).
[57] X. Han, J.-Y. You, S. Wu, R. Li, Y. P. Feng, K. P. Loh, and X. Zhao, Journal of the American Chemical Society **145**, 3624 (2023).
[58] L. Webster and J.-A. Yan, Phys. Rev. B **98**, 144411 (2018).
[59] B. Huang, G. Clark, D. R. Klein, D. MacNeill, E. Navarro-Moratalla, K. L. Seyler, N. Wilson, M. A. McGuire, D. H. Cobden, D. Xiao, W. Yao, P. Jarillo-Herrero, and X. Xu, Nature Nanotechnology **13**, 544 (2018).
[60] A. M. León, J. W. González, J. Mejía-López, F. Crasto de Lima, and E. Suárez Morell, 2D Materials **7**, 035008 (2020).
[61] A. Ebrahimian, A. Dyrdał, and A. Qaiumzadeh, Scientific Reports **13**, 5336 (2023).
[62] C.-C. Tseng, T. Song, Q. Jiang, Z. Lin, C. Wang, J. Suh, K. Watanabe, T. Taniguchi, M. A. McGuire, D. Xiao, J.-H. Chu, D. H. Cobden, X. Xu, and M. Yankowitz, Nano Letters **22**, 8495 (2022).
[63] G. Tenasini, D. Soler-Delgado, Z. Wang, F. Yao, D. Dumcenco, E. Giannini, K. Watanabe, T. Taniguchi, C. Moulsdale, A. Garcia-Ruiz, V. I. Fal'ko, I. Gutiérrez-Lezama, and A. F. Morpurgo, Nano Letters **22**, 6760 (2022).
[64] M. Farooq and J. Hong, npj 2D Mater Appl **13**, 3 (2019).
[65] J. Zhang, B. Zhao, T. Zhou, Y. Xue, C. Ma, and Z. Yang, Phys. Rev. B **97**, 085401 (2018).
[66] J.-T. Ren, Y. Feng, S.-S. Ke, and H.-F. Lü, Advanced Physics Research , 2300026 (2023).
[67] Z. Wang, Q. Chen, and J. Wang, The Journal of Physical Chemistry C **119**, 4752 (2015).
[68] D. S. Koda, F. Bechstedt, M. Marques, and L. K. Teles, The Journal of Physical Chemistry C **120**, 10895 (2016).
[69] S. Carr, S. Fang, and E. Kaxiras, Nature Reviews Materials **5**, 748 (2020).
[70] K. Zollner, M. Kurpas, M. Gmitra, and J. Fabian, Nature Reviews Physics 10.1038/s42254-025-00818-4 (2025).
[71] P. Hohenberg and W. Kohn, Physical review **136**, B864 (1964).
[72] J. P. Perdew, K. Burke, and M. Ernzerhof, Physical review letters **77**, 3865 (1996).
[73] G. Kresse and D. Joubert, Physical review b **59**, 1758 (1999).
[74] P. Giannozzi, S. Baroni, N. Bonini, M. Calandra, R. Car, C. Cavazzoni, D. Ceresoli, G. L. Chiarotti, M. Cococcioni, I. Dabo, *et al.*, Journal of physics: Condensed matter **21**, 395502 (2009).
[75] S. Grimme, Journal of computational chemistry **27**, 1787 (2006).
[76] N. Marzari, D. Vanderbilt, A. De Vita, and M. C. Payne, Physical review letters **82**, 3296 (1999).
[77] M. Cococcioni and S. De Gironcoli, Physical Review B—Condensed Matter and Materials Physics **71**, 035105 (2005).
[78] D. Kochan, S. Irmer, and J. Fabian, Phys. Rev. B **95**, 165415 (2017).
[79] C. L. Kane and E. J. Mele, Phys. Rev. Lett. **95**, 226801 (2005).
[80] V. T. Phong, N. R. Walet, and F. Guinea, 2D Materials **5**, 014004 (2017).
[81] K. Zollner, M. Gmitra, T. Frank, and J. Fabian, Phys. Rev. B **94**, 155441 (2016).
[82] P. Högl, T. Frank, K. Zollner, D. Kochan, M. Gmitra, and J. Fabian, Phys. Rev. Lett. **124**, 136403 (2020).
[83] M. V. Berry, Proceedings of the Royal Society of London. A. Mathematical and Physical Sciences **392**, 45 (1984).
[84] D. J. Thouless, M. Kohmoto, M. P. Nightingale, and M. den Nijs, Phys. Rev. Lett. **49**, 405 (1982).
[85] Q. Niu, D. J. Thouless, and Y.-S. Wu, Phys. Rev. B **31**, 3372 (1985).
[86] M.-C. Chang and Q. Niu, Phys. Rev. B **53**, 7010 (1996).
[87] D. Xiao, M.-C. Chang, and Q. Niu, Rev. Mod. Phys. **82**, 1959 (2010).
[88] N. Nagaosa, J. Sinova, S. Onoda, A. H. MacDonald, and N. P. Ong, Rev. Mod. Phys. **82**, 1539 (2010).
[89] N. Marzari and D. Vanderbilt, Physical review B **56**, 12847 (1997).
[90] A. A. Mostofi, J. R. Yates, Y.-S. Lee, I. Souza, D. Vanderbilt, and N. Marzari, Computer physics communications **178**, 685 (2008).
[91] Q. Wu, S. Zhang, H.-F. Song, M. Troyer, and A. A. Soluyanov, Computer Physics Communications **224**, 405 (2018).
[92] Z. Qiao, S. A. Yang, W. Feng, W.-K. Tse, J. Ding, Y. Yao, J. Wang, and Q. Niu, Phys. Rev. B **82**, 161414 (2010).
[93] Z. Qiao, H. Jiang, X. Li, Y. Yao, and Q. Niu, Phys. Rev. B **85**, 115439 (2012).
[94] A. Dyrdał and J. Barnaś, 2D Materials **4**, 034003 (2017).
[95] M. Inglot, V. K. Dugaev, A. Dyrdał, and J. Barnaś, Phys. Rev. B **104**, 214408 (2021).
[96] D. Xiao, W. Yao, and Q. Niu, Phys. Rev. Lett. **99**, 236809 (2007).
[97] T. Ando, Journal of the Physical Society of Japan **84**, 114705 (2015), https://doi.org/10.7566/JPSJ.84.114705.
[98] J. Yin, C. Tan, D. Barcons-Ruiz, I. Torre, K. Watanabe, T. Taniguchi, J. C. W. Song, J. Hone, and F. H. L. Koppens, Science **375**, 1398 (2022), https://www.science.org/doi/pdf/10.1126/science.abl4266.
[99] A. Johansson, Journal of Physics: Condensed Matter **36**, 423002 (2024).
[100] S. Bhowal and G. Vignale, Phys. Rev. B **103**, 195309 (2021).
[101] O. Busch, I. Mertig, and B. Göbel, Phys. Rev. Res. **5**, 043052 (2023).
[102] A. Pezo, D. García Ovalle, and A. Manchon, Phys. Rev. B **108**, 075427 (2023).
[103] J. Salvador-Sánchez, L. M. Canonico, A. Pérez-Rodríguez, T. P. Cysne, Y. Baba, V. Clericò, M. Vila, D. Vaquero, J. A. Delgado-Notario, J. M. Caridad, K. Watanabe, T. Taniguchi, R. A. Molina, F. Domínguez-Adame, S. Roche, E. Diez, T. G. Rappoport, and M. Amado, Phys. Rev. Res. **6**, 023212 (2024).
[104] M. Kögl, P. Soubelet, M. Brotons-Gisbert, A. V. Stier, B. D. Gerardot, and J. J. Finley, npj 2D Materials and Applications **7**, 32 (2023).
[105] Y. Liu, Y. Feng, T. Zhang, Z. He, Y. Dai, B. Huang, and Y. Ma, Advanced Functional Materials **33**, 2305130 (2023).
[106] D. L. Esteras, A. Rybakov, A. M. Ruiz, and J. J. Baldoví, Nano Letters **22**, 8771 (2022).
[107] S. Yang, H. Long, W. Chen, B. Sa, Z. Guo, J. Zheng, J. Pei, H. Zhan, and Y. Lu, Advanced Optical Materials **12**, 2302900 (2024).
[108] H. Yang, B. Martín-García, J. Kimák, E. Schmoranzerová, E. Dolan, Z. Chi, M. Gobbi, P. Němec, L. E. Hueso, and F. Casanova, Nature Materials **23**, 1502 (2024).
[109] A. Dyrdał and J. Barnaś, Phys. Rev. B **92**, 165404 (2015).
[110] A. Dyrdał, J. Barnaś, and V. K. Dugaev, Phys. Rev. B **95**, 245302 (2017).
[111] A. Krzyżewska and A. Dyrdał, Physica E: Low-dimensional Systems and Nanostructures **135**, 114961 (2022).
[112] R. González-Hernández, P. Ritzinger, K. Výborný, J. Železný, and A. Manchon, Nature Communications **15**, 7663 (2024).
[113] I. Wojciechowska and A. Dyrdal, to be published (2025).

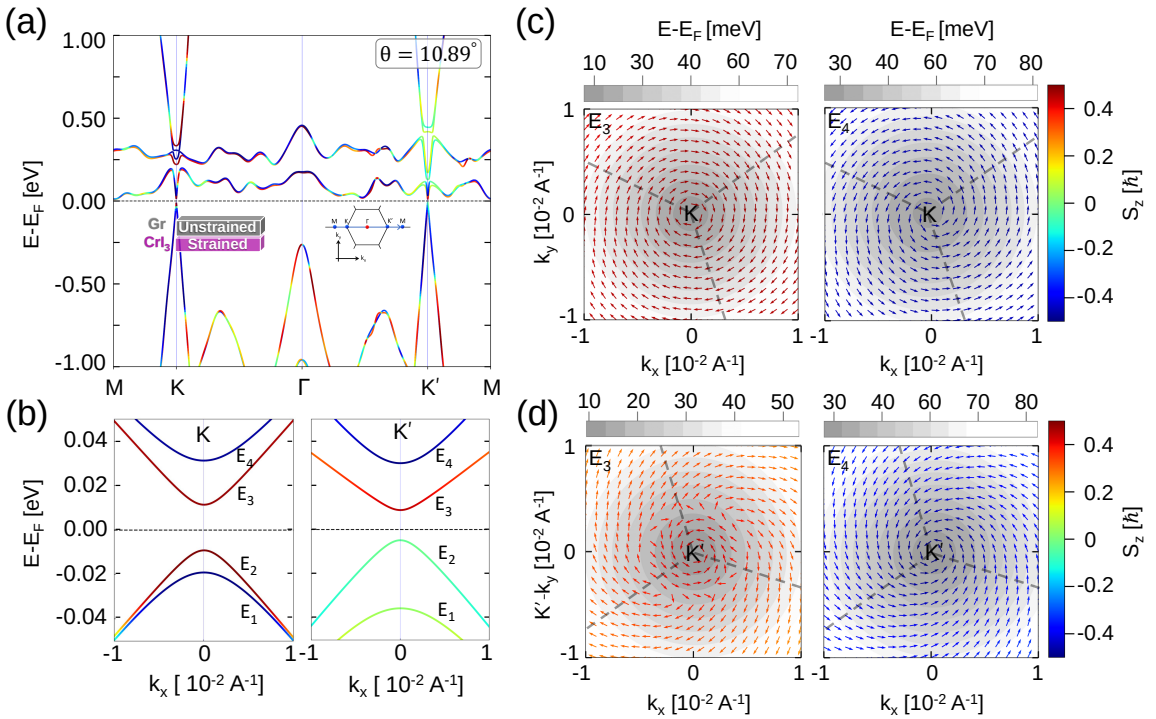

Figure 7.2. (a) Band structure of twisted Gr/CrI_3 from DFT calculations along the M–K–Γ–K′–M path $\Theta = 10.89°$ (b) Band structures of t-Gr/CrI_3 zoomed on graphene electronic states around the K and K′ points of the Brillouin zone. The colour scale represents the corresponding spin S_z expectation value. (c),(d) In-plane spin expectation values in the wavevector space, plotted in the vicinity of the K and K′ points (the point $(k_x, k_y) = (0, 0)$ defines K/K′ point, respectively).

7.1.3 Conclusion

In this chapter, we have provided a comprehensive analysis of the proximity-induced effects in twisted graphene/CrI_3 van der Waals (vdW) heterostructure. By combining the first-principles Density Functional Theory (DFT) calculations and an effective $k{\cdot}p$ model, we investigated the interplay between proximity-induced spin-orbit coupling (SOC), exchange interactions and the influence of the twist angle on the electronic and magnetic properties of the heterostructure. Our findings show that the placement of graphene on CrI_3 monolayer leads to significant modifications of the electronic band structure. In untwisted heterostructure the graphene's Dirac cones are strongly hybridized with electronic orbitals of CrI_3. However, by introducing a small twist angle ($\sim$10.89°), we successfully positioned the Dirac states of graphene within the energy gap of CrI_3. This observation highlights the important role of twist engineering in vdW heterostructures that allows for high tuneability of electronic and magnetic properties of the structure.

Our results confirm that CrI_3 monolayers keep their intrinsic ferromagnetic ground state, irrespective of the presence of graphene. However, proximity effects lead to valley-dependent spin splitting in graphene bands and nontrivial topological characteristics. Notably, our calculations of the Berry curvature and anomalous Hall conductivity (AHC) show that twisted graphene/CrI_3 reveals the quantum anomalous Hall (QAH) phase, with a computed Chern number of $C = -2$. This result confirms the emergence of topologically protected chiral edge states, a key signature of

the QAH effect.

In this work, we primarily applied bi-axial strain to graphene while keeping the CrI_3 monolayer lattice constant fixed. For completeness, we also considered the configuration for which the graphene lattice is fixed and CrI_3 monolayer is uniformly compressed, i.e. the biaxial strain of -5.90% is applied (negative sign denoting compression) to eliminate lattice mismatch. As known from pristine CrI_3 [431], this compressive strain drives a magnetic phase transition from ferromagnetic (FM) to antiferromagnetic (AFM) ground state. We found that this AFM ground state remains robust in the presence of graphene monolayer and under twisting. This is also consistent with the band-structure and spin-texture analysis, as presented in Fig. 7.2. In this configuration one can see a strong spin-splittig of graphene π bands and opening a large band gap. However, the anomalous Hall conductivity changes qualitatively: the computed AHC vanishes in the vicinity of the Fermi level, i.e., in the band gap (FIG. 6. in 7.1.2). This is in stark contrast to the finite AHC for the Fermi energy inside the band gap when strain is applied to graphene. This shows that the compressiv strain applied the magnetic substrate converts the graphene/CrI_3 stack from a topologically non-trivial (Chern insulator) regime to a trivial insulating state. Taken together, these results establish mechanical strain as an external force controlling the topological character and energy band gap in the heterostructure. This finding suggests a new approach to mechanically reconfigurable, low-power-consuming spintronics devices and phase-switchable topological circuitry.

Summary

Low-dimensional materials have always been of interest due to their unique electronic, magnetic, optical, and mechanical properties, originating from quantum confinement and reduced dimensionality. Among them, two-dimensional (2D) van der Waals materials such as graphene or transition metal dichalcogenides have shown fascinating behaviors with the ability to control their properties by external forces. This thesis presents comprehensive theoretical studies of 2D crystals and their stacks by employing different strategies to overcome its limitations, such as the lack of energy band gap. Chapter 1 concerns the brief history of low-dimensional materials and then the motivation and aims of the work by responding to questions like how we can overcome the limitations of a prominent material like graphene to preserve its extraordinary electronic properties and make it suitable for application in electronic and spintronics devices. Chapter 2 provides an extensive review of various 2D materials used in this thesis, with all details of their structure, properties, and synthesis methods. It includes graphene and graphene-like materials (such as silicene and hexagonal Boron Nitride), transition metal dichalcogenides (TMDCs), and magnetic materials like chromium trihalides (CrX3). Additionally, this chapter presents the concept of vdW heterostructures and twistronics, alongside experimental perspectives and applications.

As the primary theoretical approach used in this thesis is based on first-principles calculations and Density Functional Theory (DFT), Chapter 3 provides a brief overview of the theory behind these techniques, ranging from fundamental to advanced approximations, such as DFT-D corrections and the inclusion of Coulomb interactions and spin-orbit coupling corrections. The work contains modelling some magnetic devices. For describing their electrical/thermal properties, the non-equilibrium Green's function (NEGF) approach has been applied. To achieve more insight into the electronic and transport properties of proximitized graphene, the low-energy $\boldsymbol{k} \cdot \boldsymbol{p}$ model has been used.

In Chapter 4 the electronic and magnetic properties of silicene under Chromium doping and biaxial mechanical strain are studied. From the results, it is evident that Cr-doping significantly alters the pristine electronic structure of silicene and introduces magnetism, allowing for the tuning of the system's behaviour between metallic, semiconductor, and semimetallic phases. It has been shown that the different configurations (monomer, vertical, and horizontal dimers) alongside the bi-axial strain show new magnetic and electronic behavior. Interestingly, Chromium vertical dimer doping opens the energy band gap by approximately 0.13 eV in silicene without applying the strain. These findings give significant potential for strain-engineered silicene in spintronics devices.

In Chapter 5 the intrinsic magnetic behavior and electronic properties of Vanadium-based

monolayer and bilayer TMDCs (VS_2, VSe_2, and VTe_2) are considered. All the monolayer cases show ferromagnetic behavior. Importantly, VS_2 has a Curie temperature (T_C) above the room temperature, making it a promising material for applications in spintronics. On the other hand, VTe_2 has relatively weak magnetism and a lower T_C. The bilayers of TMDCs have an interesting interlayer coupling, i.e., the coupling between layers is antiferromagnetic, whereas the intralayer coupling preserves ferromagnetic order. In addition to the consideration in the first part of this chapter, the second part concerns the effect of strain on the electronic and magnetic properties of bilayer T-phase VS_2. The obtained results show that the magnetic moment generally increases in the presence of the compressive strain, while it decreases in the case of the tensile strain, demonstrating the tunability of this material. Magnetic anisotropy energy is intrinsically in-plane, which can become more assertive with the tensile strain, while compressive strain eliminates the anisotropy at higher percentage values. General results show the magnetic sensitivity of the T-phase of VS_2 to the strain and the potential of this group of materials in the new generation of electronic devices and technologies.

Chapter 6 of the thesis presents results regarding a proposed 2D spin-valve device using the bilayer of VSe_2 structure. Computational modeling of magnetoresistance and magneto-thermoelectric effects showed that the bilayer of VSe_2 can exhibit giant magnetoresistance (GMR)-like behavior controlled by the external magnetic field. This effect enables significant modulation of electrical resistance by altering the magnetic alignment between layers from antiparallel to parallel. Additionally, the chapter discusses thermoelectric responses to show how spin-dependent phenomena could contribute to thermoelectric applications.

Chapter 7 concerns the proximity-induced magnetic and spin-dependent electronic transport in a graphene-based vdW heterostructure with Chromium trihalides (CrI_3). The main finding of this work is a 10.89° twist angle for which the graphene Dirac cones are positioned inside the energy band gap of CrI_3 monolayer. Notably, the investigated graphene-based twisted structure reveals a quantum anomalous Hall (QAH) state and valley contrasting behaviour.

In conclusion, this thesis focuses on the theoretical studies of the electronic, magnetic, and transport properties in low-dimensional materials, particularly in two-dimensional vdW materials and their heterostructures. The results demonstrate how the control of doping, mechanical strain, layer stacking, and twist angles enables the efficient control of spin and topological properties of 2D crystals and their heterostructures. The thesis presents detailed studies of the electronic, magnetic and transport properties of selected vdW structures and provides practical guidance for designing vdW materials for advanced nanodevices and spintronics applications.

References

Bibliography

[1] Lev Davidovich Landau and LP Lifshitz. *Statistical physics: theory of the condensed state*, volume 9. Butterworth-Heinemann, 1980.

[2] Andrea C Ferrari. Raman spectroscopy of graphene and graphite: Disorder, electron–phonon coupling, doping and nonadiabatic effects. *Solid state communications*, 143(1-2):47–57, 2007.

[3] Andrea Damascelli, Zahid Hussain, and Zhi-Xun Shen. Angle-resolved photoemission studies of the cuprate superconductors. *Reviews of modern physics*, 75(2):473, 2003.

[4] Pere Miró, Martha Audiffred, and Thomas Heine. An atlas of two-dimensional materials. *Chemical Society Reviews*, 43(18):6537–6554, 2014.

[5] N David Mermin. Crystalline order in two dimensions. *Physical review*, 176(1):250, 1968.

[6] Kostya S Novoselov, Andre K Geim, Sergei V Morozov, De-eng Jiang, Yanshui Zhang, Sergey V Dubonos, Irina V Grigorieva, and Alexandr A Firsov. Electric field effect in atomically thin carbon films. *science*, 306(5696):666–669, 2004.

[7] S Novoselov. The nobel prize in physics 2010 honours two scientists, who have made the decisive contributions to this development. they are andre k. geim and konstantin s. novoselov, both at the university of manchester, uk. they have succeeded in producing, isolating, identifying and characterizing graphene. 2010.

[8] Frank Schwierz. Graphene transistors. *Nature nanotechnology*, 5(7):487–496, 2010.

[9] Andre K Geim and Konstantin S Novoselov. The rise of graphene. *Nature materials*, 6(3):183–191, 2007.

[10] C emsp14N emsp14R Rao, A emsp14K Sood, K emsp14S Subrahmanyam, and Achutharao Govindaraj. Graphene: the new two-dimensional nanomaterial. *Angewandte Chemie International Edition*, 48(42):7752–7777, 2009.

[11] Feng Wang, Zhenxing Wang, Qisheng Wang, Fengmei Wang, Lei Yin, Kai Xu, Yun Huang, and Jun He. Synthesis, properties and applications of 2d non-graphene materials. *Nanotechnology*, 26(29):292001, 2015.

[12] Jl A Wilson and AD Yoffe. The transition metal dichalcogenides discussion and interpretation of the observed optical, electrical and structural properties. *Advances in Physics*, 18(73):193–335, 1969.

[13] Haijun Zhang, Chao-Xing Liu, Xiao-Liang Qi, Xi Dai, Zhong Fang, and Shou-Cheng Zhang. Topological insulators in bi2se3, bi2te3 and sb2te3 with a single dirac cone on the surface. *Nature physics*, 5(6):438–442, 2009.

[14] Hao Tang, Dong Liang, Richard LJ Qiu, and Xuan PA Gao. Two-dimensional transport-induced linear magneto-resistance in topological insulator bi2se3 nanoribbons. *ACS nano*, 5(9):7510–7516, 2011.

[15] Dmitri Golberg, Yoshio Bando, Yang Huang, Takeshi Terao, Masanori Mitome, Chengchun Tang, and Chunyi Zhi. Boron nitride nanotubes and nanosheets. *ACS nano*, 4(6):2979–2993, 2010.

[16] Susumu Kitagawa et al. Metal–organic frameworks (mofs). *Chemical Society Reviews*, 43(16):5415–5418, 2014.

[17] Jacob Amontree, Xingzhou Yan, Christopher S DiMarco, Pierre L Levesque, Tehseen Adel, Jordan Pack, Madisen Holbrook, Christian Cupo, Zhiying Wang, Dihao Sun, et al. Reproducible graphene synthesis by oxygen-free chemical vapour deposition. *Nature*, pages 1–7, 2024.

[18] M Zahid Hasan and Charles L Kane. Colloquium: topological insulators. *Reviews of modern physics*, 82(4):3045–3067, 2010.

[19] Lihong Bao, Liang He, Nicholas Meyer, Xufeng Kou, Peng Zhang, Zhi-gang Chen, Alexei V Fedorov, Jin Zou, Trevor M Riedemann, Thomas A Lograsso, et al. Weak anti-localization and quantum oscillations of surface states in topological insulator bi2se2te. *Scientific reports*, 2(1):726, 2012.

[20] Kin Fai Mak, Changgu Lee, James Hone, Jie Shan, and Tony F Heinz. Atomically thin mos 2: a new direct-gap semiconductor. *Physical review letters*, 105(13):136805, 2010.

[21] Hualing Zeng, Junfeng Dai, Wang Yao, Di Xiao, and Xiaodong Cui. Valley polarization in mos2 monolayers by optical pumping. *Nature nanotechnology*, 7(8):490–493, 2012.

[22] Weijie Zhao, Zohreh Ghorannevis, Leiqiang Chu, Minglin Toh, Christian Kloc, Ping-Heng Tan, and Goki Eda. Evolution of electronic structure in atomically thin sheets of ws2 and wse2. *ACS nano*, 7(1):791–797, 2013.

[23] Xiaodong Xu, Wang Yao, Di Xiao, and Tony F Heinz. Spin and pseudospins in layered transition metal dichalcogenides. *Nature Physics*, 10(5):343–350, 2014.

[24] Harold W Kroto, James R Heath, Sean C O'Brien, Robert F Curl, and Richard E Smalley. C60: Buckminsterfullerene. *nature*, 318(6042):162–163, 1985.

[25] Sumio Iijima. Helical microtubules of graphitic carbon. *nature*, 354(6348):56–58, 1991.

[26] Manish Chhowalla, Hyeon Suk Shin, Goki Eda, Lain-Jong Li, Kian Ping Loh, and Hua Zhang. The chemistry of two-dimensional layered transition metal dichalcogenide nanosheets. *Nature chemistry*, 5(4):263–275, 2013.

[27] Kostya S Novoselov, Andre K Geim, Sergei Vladimirovich Morozov, Dingde Jiang, Michail I Katsnelson, Irina V Grigorieva, Sergey V Dubonos, and Alexandr A Firsov. Two-dimensional gas of massless dirac fermions in graphene. *nature*, 438(7065):197–200, 2005.

[28] Philip Richard Wallace. The band theory of graphite. *Physical review*, 71(9):622, 1947.

[29] DSL Abergel, Alan Russell, and Vladimir I Fal'ko. Visibility of graphene flakes on a dielectric substrate. *Applied Physics Letters*, 91(6), 2007.

[30] P Blake, EW Hill, AH Castro Neto, KS Novoselov, D Jiang, R Yang, TJ Booth, and AK Geim. Making graphene visible. *Applied physics letters*, 91(6), 2007.

[31] Cinzia Casiraghi, Achim Hartschuh, Elefterios Lidorikis, Huihong Qian, Hayk Harutyunyan, Tobias Gokus, Kostya Sergeevich Novoselov, and AC Ferrari. Rayleigh imaging of graphene and graphene layers. *Nano letters*, 7(9):2711–2717, 2007.

[32] K Novoselov. Konstantin novoselov—biographical. *Nobel Prize Outreach AB. Retrieved September*, 18:2021, 2010.

[33] Konstantin S Novoselov. Nobel lecture: Graphene: Materials in the flatland. *Reviews of modern physics*, 83(3):837–849, 2011.

[34] Andre Konstantin Geim. Graphene: status and prospects. *science*, 324(5934):1530–1534, 2009.

[35] Francesco Bonaccorso, Zhipei Sun, Tawfique Hasan, and Andrea C Ferrari. Graphene photonics and optoelectronics. *Nature photonics*, 4(9):611–622, 2010.

[36] Alexander A Balandin, Suchismita Ghosh, Wenzhong Bao, Irene Calizo, Desalegne Teweldebrhan, Feng Miao, and Chun Ning Lau. Superior thermal conductivity of single-layer graphene. *Nano letters*, 8(3):902–907, 2008.

[37] Nuno MR Peres. Colloquium: The transport properties of graphene: An introduction. *Reviews of modern physics*, 82(3):2673–2700, 2010.

[38] A Avsar, H Ochoa, Francisco Guinea, B Özyilmaz, BJ Van Wees, and Ivan J Vera-Marun. Colloquium: Spintronics in graphene and other two-dimensional materials. *Reviews of Modern Physics*, 92(2):021003, 2020.

[39] Antonio H Castro Neto, Francisco Guinea, Nuno MR Peres, Kostya S Novoselov, and Andre K Geim. The electronic properties of graphene. *Reviews of modern physics*, 81(1):109–162, 2009.

[40] Mikhail Iosifovich Katsnelson, Konstantin Sergejevic Novoselov, and Andre Konstantin Geim. Chiral tunnelling and the klein paradox in graphene. *Nature physics*, 2(9):620–625, 2006.

[41] Nabil A Abdel Ghany, Safaa A Elsherif, and Hala T Handal. Revolution of graphene for different applications: State-of-the-art. *Surfaces and Interfaces*, 9:93–106, 2017.

[42] Xuesong Li, Weiwei Cai, Jinho An, Seyoung Kim, Junghyo Nah, Dongxing Yang, Richard Piner, Aruna Velamakanni, Inhwa Jung, Emanuel Tutuc, et al. Large-area synthesis of high-quality and uniform graphene films on copper foils. *science*, 324(5932):1312–1314, 2009.

[43] Xianbao Wang, Haijun You, Fangming Liu, Mingjian Li, Li Wan, Shaoqing Li, Qin Li, Yang Xu, Rong Tian, Ziyong Yu, et al. Large-scale synthesis of few-layered graphene using cvd. *Chemical Vapor Deposition*, 15(1-3):53–56, 2009.

[44] Hailong Zhou, Woo Jong Yu, Lixin Liu, Rui Cheng, Yu Chen, Xiaoqing Huang, Yuan Liu, Yang Wang, Yu Huang, and Xiangfeng Duan. Chemical vapour deposition growth of large single crystals of monolayer and bilayer graphene. *Nature communications*, 4(1):2096, 2013.

[45] Konstantin V Emtsev, Aaron Bostwick, Karsten Horn, Johannes Jobst, Gary L Kellogg, Lothar Ley, Jessica L McChesney, Taisuke Ohta, Sergey A Reshanov, Jonas Röhrl, et al. Towards wafer-size graphene layers by atmospheric pressure graphitization of silicon carbide. *Nature materials*, 8(3):203–207, 2009.

[46] Claire Berger, Zhimin Song, Tianbo Li, Xuebin Li, Asmerom Y Ogbazghi, Rui Feng, Zhenting Dai, Alexei N Marchenkov, Edward H Conrad, Phillip N First, et al. Ultrathin epitaxial graphite: 2d electron gas properties and a route toward graphene-based nanoelectronics. *The Journal of Physical Chemistry B*, 108(52):19912–19916, 2004.

[47] Daniel R Dreyer, Sungjin Park, Christopher W Bielawski, and Rodney S Ruoff. The chemistry of graphene oxide. *Chemical society reviews*, 39(1):228–240, 2010.

[48] Sasha Stankovich, Dmitriy A Dikin, Richard D Piner, Kevin A Kohlhaas, Alfred Kleinhammes, Yuanyuan Jia, Yue Wu, SonBinh T Nguyen, and Rodney S Ruoff. Synthesis of graphene-based nanosheets via chemical reduction of exfoliated graphite oxide. *carbon*, 45(7):1558–1565, 2007.

[49] Changgu Lee, Xiaoding Wei, Jeffrey W Kysar, and James Hone. Measurement of the elastic properties and intrinsic strength of monolayer graphene. *science*, 321(5887):385–388, 2008.

[50] Rahul Raveendran Nair, Peter Blake, Alexander N Grigorenko, Konstantin S Novoselov, Tim J Booth, Tobias Stauber, Nuno MR Peres, and Andre K Geim. Fine structure constant defines visual transparency of graphene. *science*, 320(5881):1308–1308, 2008.

[51] Na Li, Zongping Chen, Wencai Ren, Feng Li, and Hui-Ming Cheng. Flexible graphene-based lithium ion batteries with ultrafast charge and discharge rates. *Proceedings of the National Academy of Sciences*, 109(43):17360–17365, 2012.

[52] Yanwu Zhu, Shanthi Murali, Meryl D Stoller, Kameswaran J Ganesh, Weiwei Cai, Paulo J Ferreira, Adam Pirkle, Robert M Wallace, Katie A Cychosz, Matthias Thommes, et al. Carbon-based supercapacitors produced by activation of graphene. *science*, 332(6037):1537–1541, 2011.

[53] Ahmet Avsar, Jun You Tan, T Taychatanapat, J Balakrishnan, GKW Koon, Y Yeo, J Lahiri, A Carvalho, AS Rodin, ECT O'farrell, et al. Spin-orbit proximity effect in graphene. *Nature communications*, 5(1):4875, 2014.

[54] Wei Han, Roland K Kawakami, Martin Gmitra, and Jaroslav Fabian. Graphene spintronics. *Nature nanotechnology*, 9(10):794–807, 2014.

[55] Q. Yang et al. Exciton physics in hexagonal boron nitride. *Physical Review Materials*, 5(7):074001, 2021.

[56] Cory R Dean, Andrea F Young, Inanc Meric, Chris Lee, Lei Wang, Sebastian Sorgenfrei, Kenji Watanabe, Takashi Taniguchi, Phillip Kim, Kenneth L Shepard, et al. Boron nitride substrates for high-quality graphene electronics. *Nature nanotechnology*, 5(10):722–726, 2010.

[57] Fei Hui, Chengbin Pan, Yuanyuan Shi, Yanfeng Ji, Enric Grustan-Gutierrez, and Mario Lanza. On the use of two dimensional hexagonal boron nitride as dielectric. *Microelectronic Engineering*, 163:119–133, 2016.

[58] Yufei Yang, Yi Peng, Muhammad Farooq Saleem, Ziqian Chen, and Wenhong Sun. Hexagonal boron nitride on iii–v compounds: a review of the synthesis and applications. *Materials*, 15(13):4396, 2022.

[59] Jingang Wang, Fengcai Ma, and Mengtao Sun. Graphene, hexagonal boron nitride, and their heterostructures: properties and applications. *RSC advances*, 7(27):16801–16822, 2017.

[60] A. Pakdel, C. Zhi, Y. Bando, and D. Golberg. Low-dimensional boron nitride nanostructures: fabrication, properties and applications. *Materials Today*, 15(6):256–265, 2012.

[61] Osamu Tsuda, Kenji Watanabe, and Takashi Taniguchi. Crystallization of hexagonal boron nitride exhibiting excitonic luminescence in the deep ultraviolet region at room temperature via thermal chemical vapor phase deposition. *Diamond and related materials*, 19(1):83–90, 2010.

[62] SD Nehate, AK Saikumar, A Prakash, and KB Sundaram. A review of boron carbon nitride thin films and progress in nanomaterials. *Materials Today Advances*, 8:100106, 2020.

[63] R. Geick, C.H. Perry, and G. Rupprecht. Normal modes in hexagonal boron nitride. *Physical Review*, 146(2):543–547, 1966.

[64] C. Zhi, Y. Bando, C. Tang, and D. Golberg. Large-scale fabrication of boron nitride nanosheets and their utilization in polymeric composites with improved thermal and mechanical properties. *Advanced Materials*, 22(5):553–556, 2010.

[65] K.S. Novoselov, A. Mishchenko, A. Carvalho, and A.H.C. Neto. 2d materials and van der waals heterostructures. *Science*, 353(6298):aac9439, 2016.

[66] Katherine A Su, Songying Li, Wei-Chen Wen, Yuji Yamamoto, and Michael S Arnold. Chemical vapor deposition of hexagonal boron nitride on germanium from borazine. *RSC advances*, 14(35):25378–25384, 2024.

[67] T.T. Tran, K. Bray, M.J. Ford, M. Toth, and I. Aharonovich. Quantum emission from hexagonal boron nitride monolayers. *Nature Nanotechnology*, 11(1):37–41, 2016.

[68] Viswanathan S Saji. 2d hexagonal boron nitride (h-bn) nanosheets in protective coatings: A literature review. *Heliyon*, 9(9), 2023.

[69] Kyozaburo Takeda and Kenji Shiraishi. Theoretical possibility of stage corrugation in si and ge analogs of graphite. *Physical Review B*, 50(20):14916, 1994.

[70] Patrick Vogt, Paola De Padova, Claudio Quaresima, Jose Avila, Emmanouil Frantzeskakis, Maria Carmen Asensio, Andrea Resta, Bénédicte Ealet, and Guy Le Lay. Silicene: compelling experimental evidence for graphenelike two-dimensional silicon. *Physical review letters*, 108(15):155501, 2012.

[71] ND Drummond, Viktor Zolyomi, and VI Fal'Ko. Electrically tunable band gap in silicene. *Physical Review B—Condensed Matter and Materials Physics*, 85(7):075423, 2012.

[72] Cheng-Cheng Liu, Wanxiang Feng, and Yugui Yao. Quantum spin hall effect in silicene and two-dimensional germanium. *Physical review letters*, 107(7):076802, 2011.

[73] Ruge Quhe, Ruixiang Fei, Qihang Liu, Jiaxin Zheng, Hong Li, Chengyong Xu, Zeyuan Ni, Yangyang Wang, Dapeng Yu, Zhengxiang Gao, et al. Tunable and sizable band gap in silicene by surface adsorption. *Scientific reports*, 2(1):853, 2012.

[74] Seymur Cahangirov, Mehmet Topsakal, Ethem Aktürk, Hasan Şahin, and Salim Ciraci. Two- and one-dimensional honeycomb structures of silicon and germanium. *Physical review letters*, 102(23):236804, 2009.

[75] Boubekeur Lalmi, Hamid Oughaddou, Hanna Enriquez, Abdelkader Kara, Sébastien Vizzini, Bénidicte Ealet, and Bernard Aufray. Epitaxial growth of a silicene sheet. *Applied Physics Letters*, 97(22), 2010.

[76] L. Tao and et al. Silicene field-effect transistors operating at room temperature. *Nature Nanotechnology*, 10:227, 2015.

[77] Mubashir A Kharadi, Gul Faroz A Malik, Farooq A Khanday, Khurshed A Shah, Sparsh Mittal, and Brajesh Kumar Kaushik. Silicene: From material to device applications. *ECS Journal of Solid State Science and Technology*, 9(11):115031, 2020.

[78] Quanyan Man, Yongling An, Hengtao Shen, Chuanliang Wei, Shenglin Xiong, and Jinkui Feng. Two-dimensional silicene/silicon and its derivatives: Properties, synthesis and frontier applications. *Materials Today*, 2023.

[79] M. Houssa, A. Dimoulas, and A. Molle. Silicene: A review of recent experimental and theoretical investigations. *Journal of Physics: Condensed Matter*, 27:253002, 2015.

[80] S. Cahangirov, M. Topsakal, E. Aktürk, H. Şahin, and S. Ciraci. Two- and one-dimensional honeycomb structures of silicon and germanium. *Physical Review Letters*, 102:236804, 2009.

[81] C. C. Liu, W. Feng, and Y. Yao. Quantum spin hall effect in silicene and two-dimensional germanium. *Physical Review Letters*, 107:076802, 2011.

[82] Z. Ni, Q. Liu, K. Tang, J. Zheng, J. Zhou, R. Qin, Z. Gao, D. Yu, and J. Lu. Tunable bandgap in silicene and germanene. *Nano Letters*, 12:113, 2012.

[83] Thaneshwor P Kaloni, Georg Schreckenbach, and Michael S Freund. Large enhancement and tunable band gap in silicene by small organic molecule adsorption. *The Journal of Physical Chemistry C*, 118(40):23361–23367, 2014.

[84] A. Fleurence, R. Friedlein, T. Ozaki, H. Kawai, Y. Wang, and Y. Yamada-Takamura. Experimental evidence for epitaxial silicene on diboride thin films. *Physical Review Letters*, 108:245501, 2012.

[85] L. Meng and et al. Buckled silicene formation on ir(111). *Nano Letters*, 13:685, 2013.

[86] C.-L. Lin, R. Arafune, K. Kawahara, N. Tsukahara, E. Minamitani, Y. Kim, N. Takagi, and M. Kawai. Structure of silicene grown on ag(111). *Applied Physics Express*, 5:045802, 2012.

[87] Carlo Grazianetti and Alessandro Molle. Engineering epitaxial silicene on functional substrates for nanotechnology. *Research*, 2019.

[88] N. D. Drummond, V. Zolyomi, and V. I. Fal'ko. Electrically tunable band gap in silicene. *Physical Review B*, 85:075423, 2012.

[89] R. Quhe, Q. Shu, H. Yang, and et al. Spin–orbit coupling and quantum spin hall effect in silicene from first principles. *Physical Review B*, 96:085424, 2017.

[90] H. Lu, X. Lin, Y.L. Wang, and S. Du. Epitaxial growth and physical properties of 2d materials beyond graphene: from monatomic materials to binary compounds. *Chemical Society Reviews*, 47(16):5824–5860, 2018.

[91] M. Galbiati, N. Motta, and M. De Crescenzi. Group-iv 2d materials beyond graphene on nonmetal substrates: challenges, recent progress, and future perspectives. *Applied Physics Reviews*, 6(4):041310, 2019.

[92] G. Shan, H. Tan, R. Ma, H. Zhao, and W. Huang. Recent progress in emergent two-dimensional silicene. *Nanoscale*, 15(1):50–75, 2023.

[93] C. Grazianetti and C. Martella. The rise of the xenes: From synthesis to integration processes for electronics and photonics. *Materials*, 14(15):4170, 2021.

[94] Abdul Kaium Mia, M Meyyappan, and PK Giri. Two-dimensional transition metal dichalcogenide based biosensors: from fundamentals to healthcare applications. *Biosensors*, 13(2):169, 2023.

[95] Sajedeh Manzeli, Dmitry Ovchinnikov, Diego Pasquier, Oleg V Yazyev, and Andras Kis. 2d transition metal dichalcogenides. *Nature Reviews Materials*, 2(8):1–15, 2017.

[96] Xiaorong Gan, Lawrence Yoon Suk Lee, Kwok-yin Wong, Tsz Wing Lo, Kwun Hei Ho, Dang Yuan Lei, and Huimin Zhao. 2h/1t phase transition of multilayer mos2 by electrochemical incorporation of s vacancies. *ACS Applied Energy Materials*, 1(9):4754–4765, 2018.

[97] Qing Hua Wang, Kourosh Kalantar-Zadeh, Andras Kis, Jonathan N Coleman, and Michael S Strano. Electronics and optoelectronics of two-dimensional transition metal dichalcogenides. *Nature nanotechnology*, 7(11):699–712, 2012.

[98] Q. H. Wang, A. Bedoya-Pinto, M. Blei, A. H. Dismukes, et al. The magnetic genome of two-dimensional van der waals materials. *ACS Nano*, 16(5):6960–6992, 2022.

[99] Paula Mariel Coelho. Magnetic doping in transition metal dichalcogenides. *Journal of Physics: Condensed Matter*, 36(20):203001, 2024.

[100] Yunliang Yue, Chao Jiang, Yilin Han, Min Wang, Jie Ren, and Yankai Wu. Magnetic anisotropies of mn-, fe-, and co-doped monolayer mos2. *Journal of Magnetism and Magnetic Materials*, 496:165929, 2020.

[101] Mayuri Bora and Pritam Deb. Magnetic proximity effect in two-dimensional van der waals heterostructure. *Journal of Physics: Materials*, 4(3):034014, 2021.

[102] C. Gong, L. Li, Z. Li, H. Li, et al. Discovery of intrinsic ferromagnetism in two-dimensional van der waals crystals. *Nature*, 546(7657):265–269, 2017.

[103] B. Huang, G. Clark, E. Navarro-Moratalla, D. R. Klein, et al. Layer-dependent ferromagnetism in a van der waals crystal down to the monolayer limit. *Nature*, 546(7657):270–273, 2017.

[104] Z. Fei, B. Huang, P. Guo, and X. Xu. Two-dimensional itinerant ferromagnetism in fe3gete2. *Nature Materials*, 17(9):778–782, 2018.

[105] Y. Deng, Y. Yu, Y. Song, J. Zhang, et al. Gate-tunable room-temperature ferromagnetism in two-dimensional fe3gete2. *Nature*, 563(7729):94–99, 2018.

[106] X. Jiang, Q. Liu, J. Xing, N. Liu, Y. Guo, Z. Liu, and J. Zhao. Recent progress on 2d magnets: Fundamental mechanism, structural design and modification. *Applied Physics Reviews*, 8(3):031305, 2021.

[107] Jozef Strecka and Michal Jascur. A brief account of the ising and ising-like models: Mean-field, effective-field and exact results. *arXiv preprint arXiv:1511.03031*, 2015.

[108] W. Heisenberg. Zur theorie des ferromagnetismus. *Zeitschrift für Physik*, 49(9–10):619–636, 1928.

[109] ST Bramwell, J-Y Fortin, PCW Holdsworth, S Peysson, J-F Pinton, B Portelli, and Mauro Sellitto. Magnetic fluctuations in the classical xy model: The origin of an exponential tail in a complex system. *Physical Review E*, 63(4):041106, 2001.

[110] N. D. Mermin and H. Wagner. Absence of ferromagnetism or antiferromagnetism in one- or two-dimensional isotropic heisenberg models. *Physical Review Letters*, 17(22):1133, 1966.

[111] K. S. Burch, D. Mandrus, and J.-G. Park. Magnetism in two-dimensional van der waals materials. *Nature*, 563(7729):47–52, 2018.

[112] M. Gibertini, M. Koperski, A. F. Morpurgo, and K. S. Novoselov. Magnetic 2d materials and heterostructures. *Nature Nanotechnology*, 14(5):408–419, 2019.

[113] H. Kurebayashi, J. H. Garcia, S. Khan, J. Sinova, and S. Roche. Magnetism, symmetry and spin transport in van der waals layered systems. arXiv preprint arXiv:2107.03763v2, 2021.

[114] Z. Zhang, Z. Lin, B. Shen, et al. Emergence of kondo lattice behavior in a van der waals itinerant ferromagnet, fe3gete2. *Journal of the American Chemical Society*, 141(15):6082–6088, 2019.

[115] Yongbing Xu, David D Awschalom, and Junsaku Nitta. *Handbook of spintronics*. Springer Publishing Company, Incorporated, 2016.

[116] X. Zhang, Q. Sun, Y. Zhang, and M. S. Dresselhaus. Raman spectroscopy of graphene and related materials. *Journal of Physics: Condensed Matter*, 28(35):353002, 2016.

[117] Yu-Jia Sun, Si-Min Pang, and Jun Zhang. Review of raman spectroscopy of two-dimensional magnetic van der waals materials. *Chinese Physics B*, 30(11):117104, 2021.

[118] Nicolas Ubrig, Zhe Wang, Jérémie Teyssier, Takashi Taniguchi, Kenji Watanabe, Enrico Giannini, Alberto F Morpurgo, and Marco Gibertini. Low-temperature monoclinic layer stacking in atomically thin cri3 crystals. *2D Materials*, 7(1):015007, 2020.

[119] AR Wildes, V Simonet, E Ressouche, R Ballou, and GJ McIntyre. The magnetic properties and structure of the quasi-two-dimensional antiferromagnet cops3. *Journal of Physics: Condensed Matter*, 29(45):455801, 2017.

[120] Anna Dyrdał. Spinowy efekt halla. 2013.

[121] J. Lee, S. Sohn, S. Cheon, and Y.-W. Son. Ising-type magnetic ordering in atomically thin feps3. *Nano Letters*, 16(12):7433–7438, 2016.

[122] C. Gong and X. Zhang. Two-dimensional magnetic crystals and emergent heterostructure devices. *Science*, 363(6428):eaav4450, 2019.

[123] S. Nadj-Perge, I. K. Drozdov, B. A. Bernevig, and A. Yazdani. Proposal for realizing majorana fermions in chains of magnetic atoms on a superconductor. *Physical Review B*, 88(2):020407(R), 2013.

[124] Q. L. He, L. Pan, A. L. Stern, et al. Chiral majorana fermion modes in a quantum anomalous hall insulator–superconductor structure. *Science*, 357(6348):294–299, 2017.

[125] Mongur Hossain, Biao Qin, Bo Li, and Xidong Duan. Synthesis, characterization, properties and applications of two-dimensional magnetic materials. *Nano Today*, 42:101338, 2022.

[126] David L Cortie, Grace L Causer, Kirrily C Rule, Helmut Fritzsche, Wolfgang Kreuzpaintner, and Frank Klose. Two-dimensional magnets: forgotten history and recent progress towards spintronic applications. *Advanced Functional Materials*, 30(18):1901414, 2020.

[127] Jl A Wilson, FJ Di Salvo, and S Mahajan. Charge-density waves and superlattices in the metallic layered transition metal dichalcogenides. *Advances in Physics*, 24(2):117–201, 1975.

[128] Lothar H Brixner. Preparation and properties of the single crystalline ab2-type selenides and tellurides of niobium, tantalum, molybdenum and tungsten. *Journal of Inorganic and Nuclear Chemistry*, 24(3):257–263, 1962.

[129] Bruce E Brown. The crystal structures of nbt2 and tate2. *Acta Crystallographica*, 20(2):264–267, 1966.

[130] R Nitsche, HU Blsterli, and M Lichtensteiger. Crystal growth by chemical transport reactions—i: Binary, ternary, and mixed-crystal chalcogenides. *Journal of Physics and Chemistry of Solids*, 21(3-4):199–205, 1961.

[131] Hongxiang Chen, Zhilin Li, Xiao Fan, Liwei Guo, and Xiaolong Chen. Quantum linear magnetoresistance in nbte2. *Solid State Communications*, 275:16–20, 2018.

[132] F Clerc, Corsin Battaglia, H Cercellier, Claude Monney, H Berger, Laurent Despont, MG Garnier, and Philipp Aebi. Fermi surface of layered compounds and bulk charge density wave systems. *Journal of Physics: Condensed Matter*, 19(35):355002, 2007.

[133] Klaas Derk Bronsema, GW Bus, and GA Wiegers. The crystal structure of vanadium ditelluride, v1+ xte2. *Journal of Solid State Chemistry*, 53(3):415–421, 1984.

[134] Yu Liu, Ding-Fu Shao, LJ Li, WJ Lu, XD Zhu, Peng Tong, RC Xiao, LS Ling, CY Xi, L Pi, et al. Nature of charge density waves and superconductivity in 1 t- tase 2- x te x. *Physical Review B*, 94(4):045131, 2016.

[135] T Sörgel, J Nuss, U Wedig, RK Kremer, and M Jansen. A new low temperature modification of tate2—comparison to the room temperature and the hypothetical 1t-tate2 modification. *Materials research bulletin*, 41(5):987–1000, 2006.

[136] Kari Selte, Arne Kjekshus, H Listou, Hertta Kyyhkynen, Ragnar A Hoffman, and Anders Westerdahl. On the magnetic properties of niobium selenides and tellurides. *Acta Chem. Scand*, 19(1), 1965.

[137] Tomohisa Kumakura, Hiroki Tan, Tetsuya Handa, Masashi Morishita, and Hiroshi Fukuyama. Charge density waves and superconductivity in 2h-tase 2. *Czechoslovak Journal of Physics*, 46:2611–2612, 1996.

[138] Maxime Leroux, Laurent Cario, Alexei Bosak, and Pierre Rodiere. Traces of charge density waves in nbs 2. *Physical Review B*, 97(19):195140, 2018.

[139] Gyeongcheol Gye, Eunseok Oh, and Han Woong Yeom. Topological landscape of competing charge density waves in 2 h-nbse 2. *Physical review letters*, 122(1):016403, 2019.

[140] Kensei Terashima, T Sato, H Komatsu, T Takahashi, N Maeda, and K Hayashi. Charge-density wave transition of 1 t- v s e 2 studied by angle-resolved photoemission spectroscopy. *Physical Review B*, 68(15):155108, 2003.

[141] T Ohtani, K Hayashi, M Nakahira, and H Nozaki. Phase transition in v1+ xte2. *Solid State Communications*, 40(5):629–631, 1981.

[142] T Ohtani, S Onoue, and M Nakahira. Phase relationships and properties in the vte system. *Materials research bulletin*, 19(10):1367–1375, 1984.

[143] AH Thompson and BG Silbernagel. Magnetic properties of vse2: Inferences from the study of metal-rich v1+ δse2 compounds. *Journal of Applied Physics*, 49(3):1477–1479, 1978.

[144] LF Schneemeyer and Michell J Sienko. The effect of niobium substitution on charge density wave anomalies in vanadium diselenide. *Journal of the Less Common Metals*, 62:343–348, 1978.

[145] AHM Abdul Wasey and GP Das. Electronic and magnetic properties of vanadium dichalcogenides: A brief overview on theory and experiment. *Journal of Applied Physics*, 131(19), 2022.

[146] Jinwoong Hwang, Wei Ruan, Yi Chen, Shujie Tang, Michael F Crommie, Zhi-Xun Shen, and Sung-Kwan Mo. Charge density waves in two-dimensional transition metal dichalcogenides. *Reports on Progress in Physics*, 2024.

[147] Yao Xiao, Mengyue Zhou, Jinglu Liu, Jing Xu, and Lei Fu. Phase engineering of two-dimensional transition metal dichalcogenides. *Science China Materials*, 6(62):759–775, 2019.

[148] Ulysse Chazarin. *Engineering the electronic properties of 2D transition metal dichalcogenides by defects and charge doping*. PhD thesis, Université Paris Cité; National Taiwan University (Taipei), 2022.

[149] Min Kan, Bo Wang, Young Hee Lee, and Qiang Sun. A density functional theory study of the tunable structure, magnetism and metal-insulator phase transition in vs 2 monolayers induced by in-plane biaxial strain. *Nano Research*, 8:1348–1356, 2015.

[150] Hui Zhang, Li-Min Liu, and Woon-Ming Lau. Dimension-dependent phase transition and magnetic properties of vs 2. *Journal of Materials Chemistry A*, 1(36):10821–10828, 2013.

[151] Mongur Hossain, Muhammad Ahsan Iqbal, Juanxia Wu, and Liming Xie. Chemical vapor deposition and temperature-dependent raman characterization of two-dimensional vanadium ditelluride. *RSC advances*, 11(5):2624–2629, 2021.

[152] Paula Mariel Coelho, Kinga Lasek, Kien Nguyen Cong, Jingfeng Li, Wei Niu, Wenqing Liu, Ivan I Oleynik, and Matthias Batzill. Monolayer modification of vte2 and its charge density wave. *The journal of physical chemistry letters*, 10(17):4987–4993, 2019.

[153] Manuel Bonilla, Sadhu Kolekar, Yujing Ma, Horacio Coy Diaz, Vijaysankar Kalappattil, Raja Das, Tatiana Eggers, Humberto R Gutierrez, Manh-Huong Phan, and Matthias Batzill. Strong room-temperature ferromagnetism in vse2 monolayers on van der waals substrates. *Nature nanotechnology*, 13(4):289–293, 2018.

[154] Rutuparna Samal and Chandra Sekhar Rout. Recent developments on emerging properties, growth approaches, and advanced applications of metallic 2d layered vanadium dichalcogenides. *Advanced Materials Interfaces*, 7(8):1901682, 2020.

[155] Angus Huang, Chin-Hsuan Chen, Ching-Hao Chang, and Horng-Tay Jeng. Topological phase and quantum anomalous hall effect in ferromagnetic transition-metal dichalcogenides monolayer 1 t- v se 2. *Nanomaterials*, 11(8):1998, 2021.

[156] Manuel Tuniz, Davide Soranzio, Davide Bidoggia, Denny Puntel, Wibke Bronsch, Steven L Johnson, Maria Peressi, Fulvio Parmigiani, and Federico Cilento. Ultrafast all-optical manipulation of the charge-density wave in vte 2. *Physical Review Research*, 5(4):043276, 2023.

[157] Xiaoyin Li, Shunhong Zhang, and Qian Wang. Topological insulating states in 2d transition metal dichalcogenides induced by defects and strain. *Nanoscale*, 9(2):562–569, 2017.

[158] Changsheng Zhu, Bin Lei, Fanbao Meng, Jianhua Cui, Weizhuang Zhuo, Wenxiang Wang, Ziji Xiang, and Xianhui Chen. Realizing ferromagnetism in a field-effect transistor based on VSe_2 thin flakes. *Advanced Electronic Materials*, 8(7):2101383, 2022.

[159] N Mitsuishi, Y Sugita, MS Bahramy, M Kamitani, T Sonobe, M Sakano, T Shimojima, H Takahashi, H Sakai, K Horiba, et al. Switching of band inversion and topological surface states by charge density wave. *Nature communications*, 11(1):2466, 2020.

[160] Guodong Xue, Biao Qin, Chaojie Ma, Peng Yin, Can Liu, and Kaihui Liu. Large-area epitaxial growth of transition metal dichalcogenides. *Chemical Reviews*, 124(17):9785–9865, 2024.

[161] Biao Zhang, Yi Zeng, Zi-Jing Zhao, Da-Ping Qiu, Teng Zhang, and Yang-Long Hou. Magnetic two-dimensional chromium trihalides: structure, properties and modulation. *Rare Metals*, 41(9):2921–2942, 2022.

[162] M Blei, JL Lado, Q Song, D Dey, O Erten, Victor Pardo, R Comin, S Tongay, and AS Botana. Synthesis, engineering, and theory of 2d van der waals magnets. *Applied Physics Reviews*, 8(2), 2021.

[163] Ping Liu, Ying Zhang, Kehan Li, Yongde Li, and Yong Pu. Recent advances in 2d van der waals magnets: Detection, modulation, and applications. *Iscience*, 26(9), 2023.

[164] Daniele Torelli and Thomas Olsen. Calculating critical temperatures for ferromagnetic order in two-dimensional materials. *2D Materials*, 6(1):015028, 2018.

[165] Shengwei Jiang, Jie Shan, and Kin Fai Mak. Electric-field switching of two-dimensional van der waals magnets. *Nature materials*, 17(5):406–410, 2018.

[166] Nikhil Sivadas, Satoshi Okamoto, Xiaodong Xu, Craig J Fennie, and Di Xiao. Stacking-dependent magnetism in bilayer cri3. *Nano letters*, 18(12):7658–7664, 2018.

[167] Jose L Lado and Joaquín Fernández-Rossier. On the origin of magnetic anisotropy in two dimensional cri3. *2D Materials*, 4(3):035002, 2017.

[168] Xiaobo Lu, Ruixiang Fei, Linghan Zhu, and Li Yang. Meron-like topological spin defects in monolayer crcl3. *Nature communications*, 11(1):4724, 2020.

[169] Yong Zhong, Cheng Peng, Haili Huang, Dandan Guan, Jinwoong Hwang, Kuan H Hsu, Yi Hu, Chunjing Jia, Brian Moritz, Donghui Lu, et al. From stoner to local moment magnetism in atomically thin cr2te3. *Nature Communications*, 14(1):5340, 2023.

[170] Wei He, Lingling Kong, Weina Zhao, and Peng Yu. Atomically thin 2d van der waals magnetic materials: fabrications, structure, magnetic properties and applications. *Coatings*, 12(2):122, 2022.

[171] Yusheng Hou and Ruqian Wu. Magnetic anisotropy in 2d van der waals magnetic materials and their heterostructures: Importance, mechanisms, and opportunities. *Advanced Functional Materials*, page e09453, 2025.

[172] A.I. Liechtenstein, M.I. Katsnelson, V.P. Antropov, and V.A. Gubanov. Local spin density functional approach to the theory of exchange interactions in ferromagnetic metals and alloys. *Journal of Magnetism and Magnetic Materials*, 67:65–74, 1987.

[173] V.P. Antropov, M.I. Katsnelson, B.N. Harmon, M. van Schilfgaarde, and D. Kusnezov. Spin dynamics in magnets: Equation of motion and finite temperature effects. *Physical Review B*, 54:1019–1035, 1996.

[174] N.D. Mermin and H. Wagner. Absence of ferromagnetism or antiferromagnetism in one- or two-dimensional isotropic heisenberg models. *Physical Review Letters*, 17:1133–1136, 1966.

[175] P. Gambardella, A. Dallmeyer, K. Maiti, M. Malagoli, W. Eberhardt, C. Carbone, and S.S. Dhesi. Giant magnetic anisotropy of single cobalt atoms and nanoparticles. *Science*, 300(5622):1130–1133, 2003.

[176] M. Bonilla, S. Kolekar, Y. Ma, H.C. Diaz, V. Kalappattil, R. Das, U. Eggert, and M. Batzill. Strong room-temperature ferromagnetism in vse_2 monolayers on van der waals substrates. *Nature Nanotechnology*, 13:289–293, 2018.

[177] I. Dzyaloshinsky. A thermodynamic theory of "weak" ferromagnetism of antiferromagnetics. *Journal of Physics and Chemistry of Solids*, 4:241–255, 1958.

[178] T. Moriya. Anisotropic superexchange interaction and weak ferromagnetism. *Physical Review*, 120(1):91–98, 1960.

[179] S. Heinze, K. von Bergmann, M. Menzel, J. Brede, A. Kubetzka, R. Wiesendanger, G. Bihlmayer, and S. Blügel. Spontaneous atomic-scale magnetic skyrmion lattice in two dimensions. *Nature Physics*, 7:713–718, 2011.

[180] M. Gibertini, M. Koperski, A.F. Morpurgo, and K.S. Novoselov. Magnetism in two-dimensional van der waals materials. *Nature Nanotechnology*, 14(5):408–419, 2019.

[181] K.S. Burch, D. Mandrus, and J.-G. Park. Magnetism in two-dimensional van der waals materials. *Nature Reviews Materials*, 3(1):17095, 2018.

[182] B.L. Gyorffy, A.J. Pindor, J. Staunton, G.M. Stocks, and H. Winter. A first-principles theory of ferromagnetic phase transitions in metals. *Journal of Physics F: Metal Physics*, 15:1337–1347, 1985.

[183] AA Katanin. Exchange interactions in itinerant magnets: Effects of local particle-hole irreducible vertex corrections and su (2) symmetry of hund interaction. *Physical Review B*, 112(8):085141, 2025.

[184] BL Gyorffy, AJ Pindor, J Staunton, GM Stocks, and H Winter. A first-principles theory of ferromagnetic phase transitions in metals. *Journal of Physics F: Metal Physics*, 15(6):1337, 1985.

[185] M.A. Ruderman and C. Kittel. Indirect exchange coupling of nuclear magnetic moments by conduction electrons. *Physical Review*, 96:99–102, 1954.

[186] T. Kasuya. A theory of metallic ferro- and antiferromagnetism on zener's model. *Progress of Theoretical Physics*, 16:45–57, 1956.

[187] K. Yosida. Magnetic properties of cu-mn alloys. *Physical Review*, 106:893–898, 1957.

[188] Sergeĭ Vladimirovich Tiablikov. *Methods in the quantum theory of magnetism*. Springer, 2013.

[189] Herbert B Callen. Green function theory of ferromagnetism. *Physical Review*, 130(3):890, 1963.

[190] A Lyberatos. Monte carlo models of the magnetization reversal in thin films withstrong perpendicular anisotropy. *Journal of Physics D: Applied Physics*, 33(13):R117, 2000.

[191] A Il Liechtenstein, MI Katsnelson, VP Antropov, and VA Gubanov. Local spin density functional approach to the theory of exchange interactions in ferromagnetic metals and alloys. *Journal of Magnetism and Magnetic Materials*, 67(1):65–74, 1987.

[192] Marek Pajda, J Kudrnovskỳ, Ilja Turek, Vaclav Drchal, and Patrick Bruno. Ab initio calculations of exchange interactions, spin-wave stiffness constants, and curie temperatures of fe, co, and ni. *Physical Review B*, 64(17):174402, 2001.

[193] John MD Coey. *Magnetism and magnetic materials*. Cambridge university press, 2010.

[194] Alexander S Mayorov, Roman V Gorbachev, Sergey V Morozov, Liam Britnell, Rashid Jalil, Leonid A Ponomarenko, Peter Blake, Kostya S Novoselov, Kenji Watanabe, Takashi Taniguchi, et al. Micrometer-scale ballistic transport in encapsulated graphene at room temperature. *Nano letters*, 11(6):2396–2399, 2011.

[195] Alexander S Mayorov, Daniel C Elias, Ivan S Mukhin, Sergey V Morozov, Leonid A Ponomarenko, Kostya S Novoselov, AK Geim, and Roman V Gorbachev. How close can one approach the dirac point in graphene experimentally? *Nano letters*, 12(9):4629–4634, 2012.

[196] Wenzhong Bao, Jairo Velasco Jr, Fan Zhang, Lei Jing, Brian Standley, Dmitry Smirnov, Marc Bockrath, Allan H MacDonald, and Chun Ning Lau. Evidence for a spontaneous gapped state in ultraclean bilayer graphene. *Proceedings of the National Academy of Sciences*, 109(27):10802–10805, 2012.

[197] Ruben Mas-Balleste, Cristina Gomez-Navarro, Julio Gomez-Herrero, and Felix Zamora. 2d materials: to graphene and beyond. *Nanoscale*, 3(1):20–30, 2011.

[198] Minoru Osada and Takayoshi Sasaki. Two-dimensional dielectric nanosheets: novel nanoelectronics from nanocrystal building blocks. *Advanced Materials*, 24(2):210–228, 2012.

[199] Mingsheng Xu, Tao Liang, Minmin Shi, and Hongzheng Chen. Graphene-like two-dimensional materials. *Chemical reviews*, 113(5):3766–3798, 2013.

[200] Sheneve Z Butler, Shawna M Hollen, Linyou Cao, Yi Cui, Jay A Gupta, Humberto R Gutiérrez, Tony F Heinz, Seung Sae Hong, Jiaxing Huang, Ariel F Ismach, et al. Progress, challenges, and opportunities in two-dimensional materials beyond graphene. *ACS nano*, 7(4):2898–2926, 2013.

[201] Branimir Radisavljevic, Aleksandra Radenovic, Jacopo Brivio, Valentina Giacometti, and Andras Kis. Single-layer mos2 transistors. *Nature nanotechnology*, 6(3):147–150, 2011.

[202] Michael S Fuhrer and James Hone. Measurement of mobility in dual-gated mos2 transistors. *Nature nanotechnology*, 8(3):146–147, 2013.

[203] Songrui Wei, Xian Tang, Xiaoqi Liao, Yanqi Ge, Hao Jin, Weicheng Chen, Han Zhang, and Yadong Wei. Recent progress of spintronics based on emerging 2d materials: Cri3 and xenes. *Materials Research Express*, 6(12):122004, 2019.

[204] LA Ponomarenko, AK Geim, AA Zhukov, Rashid Jalil, SV Morozov, KS Novoselov, IV Grigorieva, EH Hill, VV Cheianov, VI Fal'Ko, et al. Tunable metal–insulator transition in double-layer graphene heterostructures. *Nature Physics*, 7(12):958–961, 2011.

[205] Liam Britnell, RV Gorbachev, Rashid Jalil, BD Belle, Fredrik Schedin, Artem Mishchenko, Thanasis Georgiou, MI Katsnelson, Laurence Eaves, SV Morozov, et al. Field-effect tunneling transistor based on vertical graphene heterostructures. *Science*, 335(6071):947–950, 2012.

[206] Sarah J Haigh, Ali Gholinia, Rashid Jalil, Simon Romani, Liam Britnell, Daniel C Elias, Konstantin S Novoselov, Leonid A Ponomarenko, Andre K Geim, and Roman Gorbachev. Cross-sectional imaging of individual layers and buried interfaces of graphene-based heterostructures and superlattices. *Nature materials*, 11(9):764–767, 2012.

[207] C Dean, AF Young, L Wang, I Meric, G-H Lee, K Watanabe, T Taniguchi, K Shepard, P Kim, and J Hone. Graphene based heterostructures. *Solid State Communications*, 152(15):1275–1282, 2012.

[208] RV Gorbachev, Al K Geim, MI Katsnelson, KS Novoselov, T Tudorovskiy, IV Grigorieva, AH MacDonald, SV Morozov, K Watanabe, T Taniguchi, et al. Strong coulomb drag and broken symmetry in double-layer graphene. *Nature Physics*, 8(12):896–901, 2012.

[209] Thanasis Georgiou, Rashid Jalil, Branson D Belle, Liam Britnell, Roman V Gorbachev, Sergey V Morozov, Yong-Jin Kim, Ali Gholinia, Sarah J Haigh, Oleg Makarovsky, et al. Vertical field-effect transistor based on graphene–ws2 heterostructures for flexible and transparent electronics. *Nature nanotechnology*, 8(2):100–103, 2013.

[210] Andre K Geim and Irina V Grigorieva. Van der waals heterostructures. *Nature*, 499(7459):419–425, 2013.

[211] Wing Kin Chan and Tong-Yi Zhang. Mechanics analysis and atomistic simulations of nanobridge tests. *Journal of Applied Physics*, 107(2), 2010.

[212] Andre K Geim. Random walk to graphene. *International Journal of Modern Physics B*, 25(30):4055–4080, 2011.

[213] Li Liu, Sunmin Ryu, Michelle R Tomasik, Elena Stolyarova, Naeyoung Jung, Mark S Hybertsen, Michael L Steigerwald, Louis E Brus, and George W Flynn. Graphene oxidation: thickness-dependent etching and strong chemical doping. *Nano letters*, 8(7):1965–1970, 2008.

[214] Daniel C Elias, Rahul Raveendran Nair, TMG Mohiuddin, SV Morozov, P Blake, MP Halsall, Andrea Carlo Ferrari, DW Boukhvalov, MI Katsnelson, AK Geim, et al. Control of graphene's properties by reversible hydrogenation: evidence for graphane. *Science*, 323(5914):610–613, 2009.

[215] Sydney Ross and Alan Sussman. Surface oxidation of molybdenum disulfide. *The Journal of Physical Chemistry*, 59(9):889–892, 1955.

[216] Antoine Fleurence, Rainer Friedlein, Taisuke Ozaki, Hiroyuki Kawai, Ying Wang, and Yukiko Yamada-Takamura. Experimental evidence for epitaxial silicene on diboride thin films. *Physical review letters*, 108(24):245501, 2012.

[217] Chun Hung Lui, Li Liu, Kin Fai Mak, George W Flynn, and Tony F Heinz. Ultraflat graphene. *Nature*, 462(7271):339–341, 2009.

[218] Francesco Reale, Kanudha Sharda, and Cecilia Mattevi. From bulk crystals to atomically thin layers of group vi-transition metal dichalcogenides vapour phase synthesis. *Applied Materials Today*, 3:11–22, 2016.

[219] Likai Li, Yijun Yu, Guo Jun Ye, Qingqin Ge, Xuedong Ou, Hua Wu, Donglai Feng, Xian Hui Chen, and Yuanbo Zhang. Black phosphorus field-effect transistors. *Nature nanotechnology*, 9(5):372–377, 2014.

[220] Valeria Nicolosi, Manish Chhowalla, Mercouri G Kanatzidis, Michael S Strano, and Jonathan N Coleman. Liquid exfoliation of layered materials. *Science*, 340(6139):1226419, 2013.

[221] Udayabagya Halim, Chu Ran Zheng, Yu Chen, Zhaoyang Lin, Shan Jiang, Rui Cheng, Yu Huang, and Xiangfeng Duan. A rational design of cosolvent exfoliation of layered materials by directly probing liquid–solid interaction. *Nature communications*, 4(1):2213, 2013.

[222] Qipeng Lu, Yifu Yu, Qinglang Ma, Bo Chen, and Hua Zhang. 2d transition-metal-dichalcogenide-nanosheet-based composites for photocatalytic and electrocatalytic hydrogen evolution reactions. *Advanced Materials*, 28(10):1917–1933, 2016.

[223] Yi-Hsien Lee, Xin-Quan Zhang, Wenjing Zhang, Mu-Tung Chang, Cheng-Te Lin, Kai-Di Chang, Ya-Chu Yu, Jacob Tse-Wei Wang, Chia-Seng Chang, Lain-Jong Li, et al. Synthesis of large-area mos2 atomic layers with chemical vapor deposition. *arXiv preprint arXiv:1202.5458*, 2012.

[224] Jonathan C Shaw, Hailong Zhou, Yu Chen, Nathan O Weiss, Yuan Liu, Yu Huang, and Xiangfeng Duan. Chemical vapor deposition growth of monolayer mose 2 nanosheets. *Nano Research*, 7:511–517, 2014.

[225] Hailong Zhou, Chen Wang, Jonathan C Shaw, Rui Cheng, Yu Chen, Xiaoqing Huang, Yuan Liu, Nathan O Weiss, Zhaoyang Lin, Yu Huang, et al. Large area growth and electrical properties of p-type wse2 atomic layers. *Nano letters*, 15(1):709–713, 2015.

[226] Kibum Kang, Saien Xie, Lujie Huang, Yimo Han, Pinshane Y Huang, Kin Fai Mak, Cheol-Joo Kim, David Muller, and Jiwoong Park. High-mobility three-atom-thick semiconducting films with wafer-scale homogeneity. *Nature*, 520(7549):656–660, 2015.

[227] Xidong Duan, Chen Wang, Jonathan C Shaw, Rui Cheng, Yu Chen, Honglai Li, Xueping Wu, Ying Tang, Qinling Zhang, Anlian Pan, et al. Lateral epitaxial growth of two-dimensional layered semiconductor heterojunctions. *Nature nanotechnology*, 9(12):1024–1030, 2014.

[228] Xidong Duan, Chen Wang, Zheng Fan, Guolin Hao, Liangzhi Kou, Udayabagya Halim, Honglai Li, Xueping Wu, Yicheng Wang, Jianhui Jiang, et al. Synthesis of ws2 x se2–2 x alloy nanosheets with composition-tunable electronic properties. *Nano letters*, 16(1):264–269, 2016.

[229] Li Song, Lijie Ci, Hao Lu, Pavel B Sorokin, Chuanhong Jin, Jie Ni, Alexander G Kvashnin, Dmitry G Kvashnin, Jun Lou, Boris I Yakobson, et al. Large scale growth and characterization of atomic hexagonal boron nitride layers. *Nano letters*, 10(8):3209–3215, 2010.

[230] Lei Liu, Jewook Park, David A Siegel, Kevin F McCarty, Kendal W Clark, Wan Deng, Leonardo Basile, Juan Carlos Idrobo, An-Ping Li, and Gong Gu. Heteroepitaxial growth of two-dimensional hexagonal boron nitride templated by graphene edges. *Science*, 343(6167):163–167, 2014.

[231] Jingxue Yu, Jie Li, Wenfeng Zhang, and Haixin Chang. Synthesis of high quality two-dimensional materials via chemical vapor deposition. *Chemical science*, 6(12):6705–6716, 2015.

[232] Guangyuan Lu, Tianru Wu, Qinghong Yuan, Huishan Wang, Haomin Wang, Feng Ding, Xiaoming Xie, and Mianheng Jiang. Synthesis of large single-crystal hexagonal boron nitride grains on cu–ni alloy. *Nature communications*, 6(1):6160, 2015.

[233] Tianru Wu, Xuefu Zhang, Qinghong Yuan, Jiachen Xue, Guangyuan Lu, Zhihong Liu, Huishan Wang, Haomin Wang, Feng Ding, Qingkai Yu, et al. Fast growth of inch-sized single-crystalline graphene from a controlled single nucleus on cu–ni alloys. *Nature materials*, 15(1):43–47, 2016.

[234] Rui Cheng, Shan Jiang, Yu Chen, Yuan Liu, Nathan Weiss, Hung-Chieh Cheng, Hao Wu, Yu Huang, and Xiangfeng Duan. Few-layer molybdenum disulfide transistors and circuits for high-speed flexible electronics. *Nature communications*, 5(1):5143, 2014.

[235] Adrien Allain, Jiahao Kang, Kaustav Banerjee, and Andras Kis. Electrical contacts to two-dimensional semiconductors. *Nature materials*, 14(12):1195–1205, 2015.

[236] Saptarshi Das, Hong-Yan Chen, Ashish Verma Penumatcha, and Joerg Appenzeller. High performance multilayer mos2 transistors with scandium contacts. *Nano letters*, 13(1):100–105, 2013.

[237] Yuan Liu, Hao Wu, Hung-Chieh Cheng, Sen Yang, Enbo Zhu, Qiyuan He, Mengning Ding, Dehui Li, Jian Guo, Nathan O Weiss, et al. Toward barrier free contact to molybdenum disulfide using graphene electrodes. *Nano letters*, 15(5):3030–3034, 2015.

[238] Xu Cui, Gwan-Hyoung Lee, Young Duck Kim, Ghidewon Arefe, Pinshane Y Huang, Chul-Ho Lee, Daniel A Chenet, Xian Zhang, Lei Wang, Fan Ye, et al. Multi-terminal transport measurements of mos2 using a van der waals heterostructure device platform. *Nature nanotechnology*, 10(6):534–540, 2015.

[239] Yuan Liu, Nathan O Weiss, Xidong Duan, Hung-Chieh Cheng, Yu Huang, and Xiangfeng Duan. Van der waals heterostructures and devices. *Nature Reviews Materials*, 1(9):1–17, 2016.

[240] Deshun Qu, Xiaochi Liu, Faisal Ahmed, Daeyeong Lee, and Won Jong Yoo. Self-screened high performance multi-layer mos 2 transistor formed by using a bottom graphene electrode. *Nanoscale*, 7(45):19273–19281, 2015.

[241] Tania Roy, Mahmut Tosun, Jeong Seuk Kang, Angada B Sachid, Sujay B Desai, Mark Hettick, Chenming C Hu, and Ali Javey. Field-effect transistors built from all two-dimensional material components. *ACS nano*, 8(6):6259–6264, 2014.

[242] Hsun-Jen Chuang, Xuebin Tan, Nirmal Jeevi Ghimire, Meeghage Madusanka Perera, Bhim Chamlagain, Mark Ming-Cheng Cheng, Jiaqiang Yan, David Mandrus, David Tomanek, and Zhixian Zhou. High mobility wse2 p-and n-type field-effect transistors contacted by highly doped graphene for low-resistance contacts. *Nano letters*, 14(6):3594–3601, 2014.

[243] Ahmet Avsar, Ivan J Vera-Marun, Jun You Tan, Kenji Watanabe, Takashi Taniguchi, Antonio H Castro Neto, and Barbaros Ozyilmaz. Air-stable transport in graphene-contacted, fully encapsulated ultrathin black phosphorus-based field-effect transistors. *ACS nano*, 9(4):4138–4145, 2015.

[244] Saptarshi Das, Richard Gulotty, Anirudha V Sumant, and Andreas Roelofs. All two-dimensional, flexible, transparent, and thinnest thin film transistor. *Nano letters*, 14(5):2861–2866, 2014.

[245] Jongwon Yoon, Woojin Park, Ga-Yeong Bae, Yonghun Kim, Hun Soo Jang, Yujun Hyun, Sung Kwan Lim, Yung Ho Kahng, Woong-Ki Hong, Byoung Hun Lee, et al. Highly flexible and transparent multilayer mos2 transistors with graphene electrodes. *Small*, 9(19):3295–3300, 2013.

[246] Lili Yu, Yi-Hsien Lee, Xi Ling, Elton JG Santos, Yong Cheol Shin, Yuxuan Lin, Madan Dubey, Efthimios Kaxiras, Jing Kong, Han Wang, et al. Graphene/mos2 hybrid technology for large-scale two-dimensional electronics. *Nano letters*, 14(6):3055–3063, 2014.

[247] Gwan-Hyoung Lee, Xu Cui, Young Duck Kim, Ghidewon Arefe, Xian Zhang, Chul-Ho Lee, Fan Ye, Kenji Watanabe, Takashi Taniguchi, Philip Kim, et al. Highly stable, dual-gated mos2 transistors encapsulated by hexagonal boron nitride with gate-controllable contact, resistance, and threshold voltage. *ACS nano*, 9(7):7019–7026, 2015.

[248] Saptarshi Das and Joerg Appenzeller. Where does the current flow in two-dimensional layered systems? *Nano letters*, 13(7):3396–3402, 2013.

[249] Saptarshi Das and Joerg Appenzeller. Screening and interlayer coupling in multilayer mos2. *physica status solidi (RRL)–Rapid Research Letters*, 7(4):268–273, 2013.

[250] Yuchen Du, Lingming Yang, Jingyun Zhang, Han Liu, Kausik Majumdar, Paul D Kirsch, and D Ye Peide. Field-effect transistors with graphene/metal heterocontacts. *IEEE electron device letters*, 35(5):599–601, 2014.

[251] Wei Sun Leong, Xin Luo, Yida Li, Khoong Hong Khoo, Su Ying Quek, and John TL Thong. Low resistance metal contacts to mos2 devices with nickel-etched-graphene electrodes. *ACS nano*, 9(1):869–877, 2015.

[252] Lingming Yang, Kausik Majumdar, Han Liu, Yuchen Du, Heng Wu, Michael Hatzistergos, PY Hung, Robert Tieckelmann, Wilman Tsai, Chris Hobbs, et al. Chloride molecular doping technique on 2d materials: Ws2 and mos2. *Nano letters*, 14(11):6275–6280, 2014.

[253] Rajesh Kappera, Damien Voiry, Sibel Ebru Yalcin, Brittany Branch, Gautam Gupta, Aditya D Mohite, and Manish Chhowalla. Phase-engineered low-resistance contacts for ultrathin mos2 transistors. *Nature materials*, 13(12):1128–1134, 2014.

[254] Daisuke Kiriya, Mahmut Tosun, Peida Zhao, Jeong Seuk Kang, and Ali Javey. Air-stable surface charge transfer doping of mos2 by benzyl viologen. *Journal of the American Chemical Society*, 136(22):7853–7856, 2014.

[255] Suyeon Cho, Sera Kim, Jung Ho Kim, Jiong Zhao, Jinbong Seok, Dong Hoon Keum, Jaeyoon Baik, Duk-Hyun Choe, Kee Joo Chang, Kazu Suenaga, et al. Phase patterning for ohmic homojunction contact in mote2. *Science*, 349(6248):625–628, 2015.

[256] Xuefei Li, Lingming Yang, Mengwei Si, Sichao Li, Mingqiang Huang, Peide Ye, and Yanqing Wu. Performance potential and limit of mos2 transistors. *Advanced Materials*, 27(9):1547–1552, 2015.

[257] Johannes Christian Leutenantsmeyer, Josep Ingla-Aynés, Mallikarjuna Gurram, and Bart J van Wees. Efficient spin injection into graphene through trilayer hbn tunnel barriers. *Journal of Applied Physics*, 124(19), 2018.

[258] CK Safeer, Josep Ingla-Aynés, Franz Herling, José H Garcia, Marc Vila, Nerea Ontoso, M Reyes Calvo, Stephan Roche, Luis E Hueso, and Fèlix Casanova. Room-temperature spin hall effect in graphene/mos2 van der waals heterostructures. *Nano letters*, 19(2):1074–1082, 2019.

[259] Ahmet Avsar, Dmitrii Unuchek, Jiawei Liu, Oriol Lopez Sanchez, Kenji Watanabe, Takashi Taniguchi, Barbaros Ozyilmaz, and Andras Kis. Optospintronics in graphene via proximity coupling. *ACS nano*, 11(11):11678–11686, 2017.

[260] Marc Drogeler, Christopher Franzen, Frank Volmer, Tobias Pohlmann, Luca Banszerus, Maik Wolter, Kenji Watanabe, Takashi Taniguchi, Christoph Stampfer, and Bernd Beschoten. Spin lifetimes exceeding 12 ns in graphene nonlocal spin valve devices. *Nano letters*, 16(6):3533–3539, 2016.

[261] Marc Drogeler, Frank Volmer, Maik Wolter, Bernat Terres, Kenji Watanabe, Takashi Taniguchi, Gernot Guntherodt, Christoph Stampfer, and Bernd Beschoten. Nanosecond spin lifetimes in single-and few-layer graphene–hbn heterostructures at room temperature. *Nano letters*, 14(11):6050–6055, 2014.

[262] Juan F Sierra, Jaroslav Fabian, Roland K Kawakami, Stephan Roche, and Sergio O Valenzuela. Van der waals heterostructures for spintronics and opto-spintronics. *Nature Nanotechnology*, 16(8):856–868, 2021.

[263] Yunqiu Kelly Luo, Jinsong Xu, Tiancong Zhu, Guanzhong Wu, Elizabeth J McCormick, Wenbo Zhan, Mahesh R Neupane, and Roland K Kawakami. Opto-valleytronic spin injection in monolayer mos2/few-layer graphene hybrid spin valves. *Nano letters*, 17(6):3877–3883, 2017.

[264] Josep Ingla-Aynés, Rick J Meijerink, and Bart J van Wees. Eighty-eight percent directional guiding of spin currents with 90 μm relaxation length in bilayer graphene using carrier drift. *Nano Letters*, 16(8):4825–4830, 2016.

[265] Juan F Sierra, Ingmar Neumann, Jo Cuppens, Bart Raes, Marius V Costache, and Sergio O Valenzuela. Thermoelectric spin voltage in graphene. *Nature nanotechnology*, 13(2):107–111, 2018.

[266] Martin Gmitra and Jaroslav Fabian. Graphene on transition-metal dichalcogenides: A platform for proximity spin-orbit physics and optospintronics. *Physical Review B*, 92(15):155403, 2015.

[267] Klaus Zollner, Simão M João, Branislav K Nikolić, and Jaroslav Fabian. Twist-and gate-tunable proximity spin-orbit coupling, spin relaxation anisotropy, and charge-to-spin conversion in heterostructures of graphene and transition metal dichalcogenides. *Physical Review B*, 108(23):235166, 2023.

[268] Martin Gmitra, Sergej Konschuh, Christian Ertler, Claudia Ambrosch-Draxl, and Jaroslav Fabian. Band-structure topologies of graphene: Spin-orbit coupling effects from first principles. *Physical Review B—Condensed Matter and Materials Physics*, 80(23):235431, 2009.

[269] Martin Gmitra, Denis Kochan, Petra Högl, and Jaroslav Fabian. Trivial and inverted dirac bands and the emergence of quantum spin hall states in graphene on transition-metal dichalcogenides. *Physical Review B*, 93(15):155104, 2016.

[270] Klaus Zollner and Jaroslav Fabian. Heterostructures of graphene and topological insulators bi2se3, bi2te3, and sb2te3. *physica status solidi (b)*, 258(1):2000081, 2021.

[271] Klaus Zollner, Marko D Petrović, Kapildeb Dolui, Petr Plecháč, Branislav K Nikolić, and Jaroslav Fabian. Scattering-induced and highly tunable by gate damping-like spin-orbit torque in graphene doubly proximitized by two-dimensional magnet cr 2 ge 2 te 6 and monolayer ws 2. *Physical Review Research*, 2(4):043057, 2020.

[272] Petra Högl, Tobias Frank, Klaus Zollner, Denis Kochan, Martin Gmitra, and Jaroslav Fabian. Quantum anomalous hall effects in graphene from proximity-induced uniform and staggered spin-orbit and exchange coupling. *Physical Review Letters*, 124(13):136403, 2020.

[273] L Antonio Benítez, Juan F Sierra, Williams Savero Torres, Aloïs Arrighi, Frédéric Bonell, Marius V Costache, and Sergio O Valenzuela. Strongly anisotropic spin relaxation in graphene–transition metal dichalcogenide heterostructures at room temperature. *Nature Physics*, 14(3):303–308, 2018.

[274] JO Island, X Cui, C Lewandowski, Jun Yong Khoo, EM Spanton, H Zhou, D Rhodes, JC Hone, T Taniguchi, K Watanabe, et al. Spin–orbit-driven band inversion in bilayer graphene by the van der waals proximity effect. *Nature*, 571(7763):85–89, 2019.

[275] L Antonio Benitez, Williams Savero Torres, Juan F Sierra, Matias Timmermans, Jose H Garcia, Stephan Roche, Marius V Costache, and Sergio O Valenzuela. Tunable room-temperature spin galvanic and spin hall effects in van der waals heterostructures. *Nature materials*, 19(2):170–175, 2020.

[276] Talieh S Ghiasi, Alexey A Kaverzin, Patrick J Blah, and Bart J Van Wees. Charge-to-spin conversion by the rashba–edelstein effect in two-dimensional van der waals heterostructures up to room temperature. *Nano letters*, 19(9):5959–5966, 2019.

[277] HL Ning, X Zhang, JS Huang, B Liu, MQ Dong, and Zhi-Xin Guo. Efficient spin transfer in wte2/fe3gete2 van der waals heterostructure enabled by direct interlayer p-orbital hybridization. *arXiv preprint arXiv:2412.02966*, 2024.

[278] Talieh Ghiasi, Alexey A Kaverzin, Avalon H Dismukes, Dennis K de Wal, Xavier Roy, and Bart J van Wees. Electrical and thermal generation of spin currents by magnetic graphene.

[279] Yingying Wu, Gen Yin, Lei Pan, Alexander J Grutter, Quanjun Pan, Albert Lee, Dustin A Gilbert, Julie A Borchers, William Ratcliff, Ang Li, et al. Large exchange splitting in monolayer graphene magnetized by an antiferromagnet. *Nature Electronics*, 3(10):604–611, 2020.

[280] Ding Zhong, Kyle L Seyler, Xiayu Linpeng, Ran Cheng, Nikhil Sivadas, Bevin Huang, Emma Schmidgall, Takashi Taniguchi, Kenji Watanabe, Michael A McGuire, et al. Van der waals engineering of ferromagnetic semiconductor heterostructures for spin and valleytronics. *Science advances*, 3(5):e1603113, 2017.

[281] Wenjing Yan, Oihana Txoperena, Roger Llopis, Hanan Dery, Luis E Hueso, and Felix Casanova. A two-dimensional spin field-effect switch. *Nature communications*, 7(1):13372, 2016.

[282] Talieh S Ghiasi, Josep Ingla-Aynés, Alexey A Kaverzin, and Bart J Van Wees. Large proximity-induced spin lifetime anisotropy in transition-metal dichalcogenide/graphene heterostructures. *Nano letters*, 17(12):7528–7532, 2017.

[283] K. F. Mak, J. Shan, and D. C. Ralph. Probing and controlling magnetic states in 2d layered magnetic materials. *Nature Reviews Physics*, 1(11):646–661, 2019.

[284] Yuan Cao, Valla Fatemi, Shiang Fang, Kenji Watanabe, Takashi Taniguchi, Efthimios Kaxiras, and Pablo Jarillo-Herrero. Unconventional superconductivity in magic-angle graphene superlattices. *Nature*, 556(7699):43–50, 2018.

[285] Yuan Cao, Valla Fatemi, Ahmet Demir, Shiang Fang, Spencer L Tomarken, Jason Y Luo, Javier D Sanchez-Yamagishi, Kenji Watanabe, Takashi Taniguchi, Efthimios Kaxiras, et al. Correlated insulator behaviour at half-filling in magic-angle graphene superlattices. *Nature*, 556(7699):80–84, 2018.

[286] Eva Y Andrei and Allan H MacDonald. Graphene bilayers with a twist. *Nature materials*, 19(12):1265–1275, 2020.

[287] Jong Yeon Lee, Eslam Khalaf, Shang Liu, Xiaomeng Liu, Zeyu Hao, Philip Kim, and Ashvin Vishwanath. Theory of correlated insulating behaviour and spin-triplet superconductivity in twisted double bilayer graphene. *Nature communications*, 10(1):5333, 2019.

[288] Zachariah Hennighausen and Swastik Kar. Twistronics: a turning point in 2d quantum materials. *Electronic Structure*, 3(1):014004, 2021.

[289] Rafi Bistritzer and Allan H MacDonald. Moiré bands in twisted double-layer graphene. *Proceedings of the National Academy of Sciences*, 108(30):12233–12237, 2011.

[290] Tawfiqur Rakib, Pascal Pochet, Elif Ertekin, and Harley T Johnson. Corrugation-driven symmetry breaking in magic-angle twisted bilayer graphene. *Communications Physics*, 5(1):242, 2022.

[291] Stephen Carr, Shiang Fang, and Efthimios Kaxiras. Electronic-structure methods for twisted moire layers. *Nature Reviews Materials*, 5(10):748–763, 2020.

[292] Jianwei Sun, Adrienn Ruzsinszky, and John P Perdew. Strongly constrained and appropriately normed semilocal density functional. *Physical review letters*, 115(3):036402, 2015.

[293] Ioana-Gianina Buda, Christopher Lane, Bernardo Barbiellini, Adrienn Ruzsinszky, Jianwei Sun, and A Bansil. Characterization of thin film materials using scan meta-gga, an accurate nonempirical density functional. *Scientific reports*, 7(1):44766, 2017.

[294] Jianwei Sun, Richard C Remsing, Yubo Zhang, Zhaoru Sun, Adrienn Ruzsinszky, Haowei Peng, Zenghui Yang, Arpita Paul, Umesh Waghmare, Xifan Wu, et al. Scan: An efficient density functional yielding accurate structures and energies of diversely-bonded materials. *arXiv preprint arXiv:1511.01089*, 2015.

[295] Stephen Carr, Daniel Massatt, Shiang Fang, Paul Cazeaux, Mitchell Luskin, and Efthimios Kaxiras. Twistronics: Manipulating the electronic properties of two-dimensional layered structures through their twist angle. *Physical Review B*, 95(7):075420, 2017.

[296] Kuan Zhang and Ellad B Tadmor. Structural and electron diffraction scaling of twisted graphene bilayers. *Journal of the Mechanics and Physics of Solids*, 112:225–238, 2018.

[297] Aleksey N Kolmogorov and Vincent H Crespi. Registry-dependent interlayer potential for graphitic systems. *Physical Review B—Condensed Matter and Materials Physics*, 71(23):235415, 2005.

[298] Mit H Naik, Indrajit Maity, Prabal K Maiti, and Manish Jain. Kolmogorov–crespi potential for multilayer transition-metal dichalcogenides: capturing structural transformations in moiré superlattices. *The Journal of Physical Chemistry C*, 123(15):9770–9778, 2019.

[299] F Rost, R Gupta, M Fleischmann, D Weckbecker, N Ray, J Olivares, M Vogl, S Sharma, O Pankratov, and S Shallcross. Nonperturbative theory of effective hamiltonians for deformations in two-dimensional materials: Moiré systems and dislocations. *Physical Review B*, 100(3):035101, 2019.

[300] Sandeep K Jain, Vladimir Juričić, and Gerard T Barkema. Structure of twisted and buckled bilayer graphene. *2D Materials*, 4(1):015018, 2016.

[301] Cameron J Shearer, Ashley D Slattery, Andrew J Stapleton, Joseph G Shapter, and Christopher T Gibson. Accurate thickness measurement of graphene. *Nanotechnology*, 27(12):125704, 2016.

[302] Yee Kan Koh, Myung-Ho Bae, David G Cahill, and Eric Pop. Reliably counting atomic planes of few-layer graphene (n> 4). *ACS nano*, 5(1):269–274, 2011.

[303] GE Bacon. The interlayer spacing of graphite. *Acta crystallographica*, 4(6):558–561, 1951.

[304] Julia Berashevich and Tapash Chakraborty. Interlayer repulsion and decoupling effects in stacked turbostratic graphene flakes. *Physical Review B—Condensed Matter and Materials Physics*, 84(3):033403, 2011.

[305] Julia Berashevich and Tapash Chakraborty. On the nature of interlayer interactions in a system of two graphene fragments. *The Journal of Physical Chemistry C*, 115(50):24666–24673, 2011.

[306] MAH Vozmediano, MP López-Sancho, and F Guinea. Interlayer hopping properties of electrons in layered metals. *Physical Review B*, 68(19):195122, 2003.

[307] Dmitry K Efimkin, G William Burg, Emanuel Tutuc, and Allan H MacDonald. Tunneling and fluctuating electron-hole cooper pairs in double bilayer graphene. *Physical Review B*, 101(3):035413, 2020.

[308] Riccardo Pisoni, Tim Davatz, Kenji Watanabe, Takashi Taniguchi, Thomas Ihn, and Klaus Ensslin. Absence of interlayer tunnel coupling of k-valley electrons in bilayer mos 2. *Physical review letters*, 123(11):117702, 2019.

[309] Zachariah Hennighausen, Christopher Lane, Ioana Gianina Buda, Vineet K Mathur, Arun Bansil, and Swastik Kar. Evidence of a purely electronic two-dimensional lattice at the interface of tmd/bi 2 se 3 heterostructures. *Nanoscale*, 11(34):15929–15938, 2019.

[310] Anthony Vargas, Fangze Liu, Christopher Lane, Daniel Rubin, Ismail Bilgin, Zachariah Hennighausen, Matthew DeCapua, Arun Bansil, and Swastik Kar. Tunable and laser-reconfigurable 2d heterocrystals obtained by epitaxial stacking of crystallographically incommensurate bi2se3 and mos2 atomic layers. *Science advances*, 3(7):e1601741, 2017.

[311] Isaac Amidror and Roger D Hersch. Mathematical moiré models and their limitations. *Journal of Modern Optics*, 57(1):23–36, 2010.

[312] Guy Lebanon and Alfred M Bruckstein. Variational approach to moiré pattern synthesis. *JOSA A*, 18(6):1371–1382, 2001.

[313] Guy Lebanon and Alfred M Bruckstein. Designing moiré patterns. In *International Workshop on Energy Minimization Methods in Computer Vision and Pattern Recognition*, pages 185–200. Springer, 2001.

[314] Patrick Zeller and Sebastian Günther. What are the possible moiré patterns of graphene on hexagonally packed surfaces? universal solution for hexagonal coincidence lattices, derived by a geometric construction. *New Journal of Physics*, 16(8):083028, 2014.

[315] Patrick Zeller, Xinzhou Ma, and Sebastian Günther. Indexing moiré patterns of metal-supported graphene and related systems: strategies and pitfalls. *New Journal of Physics*, 19(1):013015, 2017.

[316] Matthew R Rosenberger, Hsun-Jen Chuang, Madeleine Phillips, Vladimir P Oleshko, Kathleen M McCreary, Saujan V Sivaram, C Stephen Hellberg, and Berend T Jonker. Atomic reconstruction and moiré patterns in transition metal dichalcogenide van der waals heterostructures. *arXiv e-prints*, pages arXiv–1911, 2019.

[317] Stephen Carr, Daniel Massatt, Steven B Torrisi, Paul Cazeaux, Mitchell Luskin, and Efthimios Kaxiras. Relaxation and domain formation in incommensurate two-dimensional heterostructures. *Physical Review B*, 98(22):224102, 2018.

[318] Shuyang Dai, Yang Xiang, and David J Srolovitz. Twisted bilayer graphene: Moiré with a twist. *Nano letters*, 16(9):5923–5927, 2016.

[319] Leonid A Bendersky and Frank W Gayle. Electron diffraction using transmission electron microscopy. *Journal of research of the National Institute of Standards and Technology*, 106(6):997, 2001.

[320] C Barry Carter and David B Williams. *Transmission electron microscopy: Diffraction, imaging, and spectrometry*. Springer, 2016.

[321] Hyobin Yoo, Rebecca Engelke, Stephen Carr, Shiang Fang, Kuan Zhang, Paul Cazeaux, Suk Hyun Sung, Robert Hovden, Adam W Tsen, Takashi Taniguchi, et al. Atomic and electronic reconstruction at the van der waals interface in twisted bilayer graphene. *Nature materials*, 18(5):448–453, 2019.

[322] Kyounghwan Kim, Ashley DaSilva, Shengqiang Huang, Babak Fallahazad, Stefano Larentis, Takashi Taniguchi, Kenji Watanabe, Brian J LeRoy, Allan H MacDonald, and Emanuel Tutuc. Tunable moiré bands and strong correlations in small-twist-angle bilayer graphene. *Proceedings of the National Academy of Sciences*, 114(13):3364–3369, 2017.

[323] Cory R Dean, Lei Wang, P Maher, Carlos Forsythe, Fereshte Ghahari, Y Gao, Jyoti Katoch, Masa Ishigami, Pilkyung Moon, Mikito Koshino, et al. Hofstadter's butterfly and the fractal quantum hall effect in moiré superlattices. *Nature*, 497(7451):598–602, 2013.

[324] Peter Rickhaus, John Wallbank, Sergey Slizovskiy, Riccardo Pisoni, Hiske Overweg, Yongjin Lee, Marius Eich, Ming-Hao Liu, Kenji Watanabe, Takashi Taniguchi, et al. Transport through a network of topological channels in twisted bilayer graphene. *Nano letters*, 18(11):6725–6730, 2018.

[325] Aaron L Sharpe, Eli J Fox, Arthur W Barnard, Joe Finney, Kenji Watanabe, Takashi Taniguchi, MA Kastner, and David Goldhaber-Gordon. Emergent ferromagnetism near three-quarters filling in twisted bilayer graphene. *Science*, 365(6453):605–608, 2019.

[326] Matthew R Rosenberger, Hsun-Jen Chuang, Kathleen M McCreary, Aubrey T Hanbicki, Saujan V Sivaram, and Berend T Jonker. Nano-"squeegee" for the creation of clean 2d material interfaces. *ACS applied materials & interfaces*, 10(12):10379–10387, 2018.

[327] Evgeny M Alexeev, David A Ruiz-Tijerina, Mark Danovich, Matthew J Hamer, Daniel J Terry, Pramoda K Nayak, Seongjoon Ahn, Sangyeon Pak, Juwon Lee, Jung Inn Sohn, et al. Resonantly hybridized excitons in moiré superlattices in van der waals heterostructures. *Nature*, 567(7746):81–86, 2019.

[328] Kha Tran, Galan Moody, Fengcheng Wu, Xiaobo Lu, Junho Choi, Kyounghwan Kim, Amritesh Rai, Daniel A Sanchez, Jiamin Quan, Akshay Singh, et al. Evidence for moiré excitons in van der waals heterostructures. *Nature*, 567(7746):71–75, 2019.

[329] Kyle L Seyler, Pasqual Rivera, Hongyi Yu, Nathan P Wilson, Essance L Ray, David G Mandrus, Jiaqiang Yan, Wang Yao, and Xiaodong Xu. Signatures of moiré-trapped valley excitons in mose2/wse2 heterobilayers. *Nature*, 567(7746):66–70, 2019.

[330] Chenhao Jin, Emma C Regan, Aiming Yan, M Iqbal Bakti Utama, Danqing Wang, Sihan Zhao, Ying Qin, Sijie Yang, Zhiren Zheng, Shenyang Shi, et al. Observation of moiré excitons in wse2/ws2 heterostructure superlattices. *Nature*, 567(7746):76–80, 2019.

[331] Xiaobo Lu, Xiaoqin Li, and Li Yang. Modulated interlayer exciton properties in a two-dimensional moiré crystal. *Physical Review B*, 100(15):155416, 2019.

[332] Ya-Hui Zhang, Dan Mao, and Th Senthil. Twisted bilayer graphene aligned with hexagonal boron nitride: Anomalous hall effect and a lattice model. *Physical Review Research*, 1(3):033126, 2019.

[333] M Serlin, CL Tschirhart, H Polshyn, Y Zhang, J Zhu, K Watanabe, T Taniguchi, L Balents, and AF Young. Intrinsic quantized anomalous hall effect in a moiré heterostructure. *Science*, 367(6480):900–903, 2020.

[334] Zachariah Hennighausen, Christopher Lane, Abdelkrim Benabbas, Kevin Mendez, Monika Eggenberger, Paul M Champion, Jeremy T Robinson, Arun Bansil, and Swastik Kar. Oxygen-induced in situ manipulation of the interlayer coupling and exciton recombination in bi2se3/mos2 2d heterostructures. *ACS applied materials & interfaces*, 11(17):15913–15921, 2019.

[335] Zachariah Hennighausen, Ismail Bilgin, Colin Casey, and Swastik Kar. Widely tunable bi2se3/transition metal dichalcogenide 2d heterostructures for write-read-erase-reuse applications. *2D Materials*, 6(4):041003, 2019.

[336] Feliciano Giustino. *Materials modelling using density functional theory: properties and predictions*. Oxford University Press, 2014.

[337] Jean-Yves Raty, Giulia Galli, C Bostedt, Tony W Van Buuren, and Louis J Terminello. Quantum confinement and fullerenelike surface reconstructions in nanodiamonds. *Physical review letters*, 90(3):037401, 2003.

[338] John Bardeen, Leon N Cooper, and John Robert Schrieffer. Theory of superconductivity. *Physical review*, 108(5):1175, 1957.

[339] Jun Nagamatsu, Norimasa Nakagawa, Takahiro Muranaka, Yuji Zenitani, and Jun Akimitsu. Superconductivity at 39 k in magnesium diboride. *nature*, 410(6824):63–64, 2001.

[340] Hyoung Joon Choi, David Roundy, Hong Sun, Marvin L Cohen, and Steven G Louie. The origin of the anomalous superconducting properties of mgb2. *Nature*, 418(6899):758–760, 2002.

[341] Kisuk Kang, Ying Shirley Meng, Julien Breger, Clare P Grey, and Gerbrand Ceder. Electrodes with high power and high capacity for rechargeable lithium batteries. *Science*, 311(5763):977–980, 2006.

[342] Jeff Greeley, Thomas F Jaramillo, Jacob Bonde, IB Chorkendorff, and Jens K Nørskov. Computational high-throughput screening of electrocatalytic materials for hydrogen evolution. *Nature materials*, 5(11):909–913, 2006.

[343] Kimball Milton and Julian Schwinger. *Classical electrodynamics*. CRC Press, 1998.

[344] Erwin Schrödinger. Quantisierung als eigenwertproblem. *Annalen der physik*, 385(13):437–490, 1926.

[345] Charles Kittel. Introduction to solid state physics eighth edition. 2021.

[346] Frank Jackson. *From metaphysics to ethics: A defence of conceptual analysis*. Clarendon Press, 1998.

[347] Vladimir Fock. Näherungsmethode zur lösung des quantenmechanischen mehrkörperproblems. *Zeitschrift für Physik*, 61:126–148, 1930.

[348] John C Slater. A simplification of the hartree-fock method. *Physical review*, 81(3):385, 1951.

[349] Paul AM Dirac. Note on exchange phenomena in the thomas atom. In *Mathematical proceedings of the Cambridge philosophical society*, volume 26, pages 376–385. Cambridge University Press, 1930.

[350] David M Ceperley and Berni J Alder. Ground state of the electron gas by a stochastic method. *Physical review letters*, 45(7):566, 1980.

[351] John P Perdew and Yue Wang. Accurate and simple analytic representation of the electron-gas correlation energy. *Physical review B*, 45(23):13244, 1992.

[352] Enrico Fermi. Eine statistische methode zur bestimmung einiger eigenschaften des atoms und ihre anwendung auf die theorie des periodischen systems der elemente. *Zeitschrift für Physik*, 48(1):73–79, 1928.

[353] Llewellyn H Thomas. The calculation of atomic fields. In *Mathematical proceedings of the Cambridge philosophical society*, volume 23, pages 542–548. Cambridge University Press, 1927.

[354] Axel D Becke. Density-functional exchange-energy approximation with correct asymptotic behavior. *Physical review A*, 38(6):3098, 1988.

[355] Chengteh Lee, Weitao Yang, and Robert G Parr. Development of the colle-salvetti correlation-energy formula into a functional of the electron density. *Physical review B*, 37(2):785, 1988.

[356] John P Perdew, Kieron Burke, and Matthias Ernzerhof. Generalized gradient approximation made simple. *Physical review letters*, 77(18):3865, 1996.

[357] Kurt Lejaeghere, Gustav Bihlmayer, Torbjörn Björkman, Peter Blaha, Stefan Blügel, Volker Blum, Damien Caliste, Ivano E Castelli, Stewart J Clark, Andrea Dal Corso, et al. Reproducibility in density functional theory calculations of solids. *Science*, 351(6280):aad3000, 2016.

[358] Richard M Martin. *Electronic structure: basic theory and practical methods*. Cambridge university press, 2020.

[359] Thomas L Beck. Real-space mesh techniques in density-functional theory. *Reviews of Modern Physics*, 72(4):1041, 2000.

[360] Hans Hellmann. A new approximation method in the problem of many electrons. *The Journal of Chemical Physics*, 3(1):61–61, 1935.

[361] H Hellmann and W Kassatotschkin. Metallic binding according to the combined approximation procedure. *The Journal of Chemical Physics*, 4(5):324–325, 1936.

[362] John C Slater. Wave functions in a periodic potential. *Physical Review*, 51(10):846, 1937.

[363] VL Moruzzi, AR Williams, and JF Janak. Local density theory of metallic cohesion. *Physical Review B*, 15(6):2854, 1977.

[364] Victor L Moruzzi, James F Janak, and Arthur R Williams. *Calculated electronic properties of metals*. Elsevier, 2013.

[365] David J Singh and Lars Nordstrom. *Planewaves, Pseudopotentials, and the LAPW method*. Springer Science & Business Media, 2006.

[366] H Krakauer, M Posternak, and AJ Freeman. Linearized augmented plane-wave method for the electronic band structure of thin films. *Physical Review B*, 19(4):1706, 1979.

[367] HL Skriver. The lmto method, springer series in solid state sciences vol. 41. 1984.

[368] O Krogh Andersen. Linear methods in band theory. *Physical Review B*, 12(8):3060, 1975.

[369] David Vanderbilt. Soft self-consistent pseudopotentials in a generalized eigenvalue formalism. *Physical review B*, 41(11):7892, 1990.

[370] Ian Morrison, DM Bylander, and Leonard Kleinman. Nonlocal hermitian norm-conserving vanderbilt pseudopotential. *Physical Review B*, 47(11):6728, 1993.

[371] Stefan Grimme. Semiempirical gga-type density functional constructed with a long-range dispersion correction. *Journal of computational chemistry*, 27(15):1787–1799, 2006.

[372] Stefan Grimme, Jens Antony, Stephan Ehrlich, and Helge Krieg. A consistent and accurate ab initio parametrization of density functional dispersion correction (dft-d) for the 94 elements h-pu. *The Journal of chemical physics*, 132(15), 2010.

[373] Sergei L Dudarev, Gianluigi A Botton, Sergey Y Savrasov, CJ Humphreys, and Adrian P Sutton. Electron-energy-loss spectra and the structural stability of nickel oxide: An lsda+ u study. *Physical Review B*, 57(3):1505, 1998.

[374] Matteo Cococcioni and Stefano De Gironcoli. Linear response approach to the calculation of the effective interaction parameters in the lda+ u method. *Physical Review B—Condensed Matter and Materials Physics*, 71(3):035105, 2005.

[375] Yue-Chao Wang and Hong Jiang. Local screened coulomb correction approach to strongly correlated d-electron systems. *The Journal of chemical physics*, 150(15), 2019.

[376] Denis Kochan, Susanne Irmer, and Jaroslav Fabian. Model spin-orbit coupling Hamiltonians for graphene systems. *Phys. Rev. B*, 95:165415, Apr 2017.

[377] Vo Tien Phong, Niels R Walet, and Francisco Guinea. Effective interactions in a graphene layer induced by the proximity to a ferromagnet. *2D Materials*, 5(1):014004, dec 2017.

[378] C. L. Kane and E. J. Mele. Quantum Spin Hall Effect in Graphene. *Phys. Rev. Lett.*, 95:226801, Nov 2005.

[379] Yang Li and Mikito Koshino. Twist-angle dependence of the proximity spin-orbit coupling in graphene on transition-metal dichalcogenides. *Phys. Rev. B*, 99:075438, Feb 2019.

[380] Alessandro David, Péter Rakyta, Andor Kormányos, and Guido Burkard. Induced spin-orbit coupling in twisted graphene–transition metal dichalcogenide heterobilayers: Twistronics meets spintronics. *Phys. Rev. B*, 100:085412, Aug 2019.

[381] Csaba G. Péterfalvi, Alessandro David, Péter Rakyta, Guido Burkard, and Andor Kormányos. Quantum interference tuning of spin-orbit coupling in twisted van der Waals trilayers. *Phys. Rev. Res.*, 4:L022049, May 2022.

[382] Petra Högl, Tobias Frank, Klaus Zollner, Denis Kochan, Martin Gmitra, and Jaroslav Fabian. Quantum Anomalous Hall Effects in Graphene from Proximity-Induced Uniform and Staggered Spin-Orbit and Exchange Coupling. *Phys. Rev. Lett.*, 124:136403, Mar 2020.

[383] Klaus Zollner, Martin Gmitra, Tobias Frank, and Jaroslav Fabian. Theory of proximity-induced exchange coupling in graphene on hBN/(Co, Ni). *Phys. Rev. B*, 94:155441, Oct 2016.

[384] Supriyo Datta. *Quantum transport: atom to transistor*. Cambridge university press, 2005.

[385] Eckehard Schöll. *Theory of transport properties of semiconductor nanostructures*, volume 4. Springer Science & Business Media, 2013.

[386] Supriyo Datta. *Electronic transport in mesoscopic systems*. Cambridge university press, 1997.

[387] Paul Ellinghaus. *Two-dimensional Wigner Monte Carlo simulation for time-resolved quantum transport with scattering*. PhD thesis, Technische Universität Wien, 2016.

[388] Rolf Landauer. Electrical resistance of disordered one-dimensional lattices. *Philosophical magazine*, 21(172):863–867, 1970.

[389] David Ferry and Stephen Marshall Goodnick. *Transport in nanostructures*. Number 6. Cambridge university press, 1999.

[390] M Büttiker, Y Imry, R Landauer, and S Pinhas. Generalized many-channel conductance formula with application to small rings. *Physical Review B*, 31(10):6207, 1985.

[391] Paul C Martin and Julian Schwinger. Theory of many-particle systems. i. *Physical Review*, 115(6):1342, 1959.

[392] Yigal Meir and Ned S Wingreen. Landauer formula for the current through an interacting electron region. *Physical review letters*, 68(16):2512, 1992.

[393] Roger Lake and Supriyo Datta. Nonequilibrium green's-function method applied to double-barrier resonant-tunneling diodes. *Physical Review B*, 45(12):6670, 1992.

[394] Mads Brandbyge, José-Luis Mozos, Pablo Ordejón, Jeremy Taylor, and Kurt Stokbro. Density-functional method for nonequilibrium electron transport. *Physical Review B*, 65(16):165401, 2002.

[395] Kurt Stokbro, Jeremy Taylor, Mads Brandbyge, and HONG Guo. Ab-initio non-equilibrium green's function formalism for calculating electron transport in molecular devices. *Introducing Molecular Electronics*, pages 117–151, 2005.

[396] Hartmut Haug, Antti-Pekka Jauho, et al. *Quantum kinetics in transport and optics of semiconductors*, volume 2. Springer, 2008.

[397] Dan Erik Petersen, Hans Henrik B Sørensen, Per Christian Hansen, Stig Skelboe, and Kurt Stokbro. Block tridiagonal matrix inversion and fast transmission calculations. *Journal of Computational Physics*, 227(6):3174–3190, 2008.

[398] S Sanvito, CJ Lambert, JH Jefferson, and AM Bratkovsky. General green's-function formalism for transport calculations with spd hamiltonians and giant magnetoresistance in co-and ni-based magnetic multilayers. *Physical Review B*, 59(18):11936, 1999.

[399] MP Lopez Sancho, JM Lopez Sancho, JM Lopez Sancho, and J Rubio. Highly convergent schemes for the calculation of bulk and surface green functions. *Journal of Physics F: Metal Physics*, 15(4):851, 1985.

[400] Hans Henrik B Sørensen, Per Christian Hansen, Dan Erik Petersen, Stig Skelboe, and Kurt Stokbro. Efficient wave-function matching approach for quantum transport calculations. *Physical Review B—Condensed Matter and Materials Physics*, 79(20):205322, 2009.

[401] Hans Henrik B Sørensen, Per Christian Hansen, Dan Erik Petersen, Stig Skelboe, and Kurt Stokbro. Krylov subspace method for evaluating the self-energy matrices in electron transport calculations. *Physical Review B—Condensed Matter and Materials Physics*, 77(15):155301, 2008.

[402] Conor S Boland, Yiwei Sun, and Dimitrios G Papageorgiou. Bandgap engineering of 2d materials toward high-performing straintronics. *Nano Letters*, 24(41):12722–12732, 2024.

[403] Sivabrata Sahu and GC Rout. Band gap opening in graphene: a short theoretical study. *International Nano Letters*, 7:81–89, 2017.

[404] Duy Khanh Nguyen, Ngoc Thanh Thuy Tran, Yu-Huang Chiu, and Ming-Fa Lin. Concentration-diversified magnetic and electronic properties of halogen-adsorbed silicene. *Scientific reports*, 9(1):13746, 2019.

[405] Deepthi Jose and Ayan Datta. Structures and chemical properties of silicene: unlike graphene. *Accounts of chemical research*, 47(2):593–602, 2014.

[406] Lucca Moraes Gomes and Andreia Luisa da Rosa. Magnetic interactions in chromium adsorption on silicene. *Journal of Magnetism and Magnetic Materials*, 610:172496, 2024.

[407] Rui Qin, Chun-Hai Wang, Wenjun Zhu, and Yalin Zhang. First-principles calculations of mechanical and electronic properties of silicene under strain. *Aip Advances*, 2(2), 2012.

[408] Ngoc Thanh Thuy Tran, Godfrey Gumbs, Duy Khanh Nguyen, and Ming-Fa Lin. Fundamental properties of metal-adsorbed silicene: a dft study. *ACS omega*, 5(23):13760–13769, 2020.

[409] Xu He, Nicole Helbig, Matthieu J Verstraete, and Eric Bousquet. Tb2j: A python package for computing magnetic interaction parameters. *Computer Physics Communications*, 264:107938, 2021.

[410] Richard FL Evans, Weijia J Fan, Phanwadee Chureemart, Thomas A Ostler, Matthew OA Ellis, and Roy W Chantrell. Atomistic spin model simulations of magnetic nanomaterials. *Journal of Physics: Condensed Matter*, 26(10):103202, 2014.

[411] Mario Norberto Baibich, Jean Marc Broto, Albert Fert, F Nguyen Van Dau, Frédéric Petroff, P Etienne, G Creuzet, A Friederich, and J Chazelas. Giant magnetoresistance of (001) fe/(001) cr magnetic superlattices. *Physical review letters*, 61(21):2472, 1988.

[412] Grünberg Binasch, Peter Grünberg, F Saurenbach, and W Zinn. Enhanced magnetoresistance in layered magnetic structures with antiferromagnetic interlayer exchange. *Physical review B*, 39(7):4828, 1989.

[413] J Barnaś, A Fuss, RE Camley, P Grünberg, and W Zinn. Novel magnetoresistance effect in layered magnetic structures: Theory and experiment. *Physical Review B*, 42(13):8110, 1990.

[414] J Barnaś. Coupling between two ferromagnetic films through a non-magnetic metallic layer. *Journal of magnetism and magnetic materials*, 111(3):L215–L219, 1992.

[415] Robert E Camley and J Barnaś. Theory of giant magnetoresistance effects in magnetic layered structures with antiferromagnetic coupling. *Physical review letters*, 63(6):664, 1989.

[416] Bernard Dieny, Virgil S Speriosu, Stuart SP Parkin, Bruce A Gurney, Dennis R Wilhoit, and Daniele Mauri. Giant magnetoresistive in soft ferromagnetic multilayers. *Physical Review B*, 43(1):1297, 1991.

[417] Stuart Parkin, Xin Jiang, Christian Kaiser, Alex Panchula, Kevin Roche, and Mahesh Samant. Magnetically engineered spintronic sensors and memory. *Proceedings of the IEEE*, 91(5):661–680, 2003.

[418] SA Wolf, DD Awschalom, RA Buhrman, JM Daughton, von S von Molnár, ML Roukes, A Yu Chtchelkanova, and DM Treger. Spintronics: a spin-based electronics vision for the future. *science*, 294(5546):1488–1495, 2001.

[419] Claude Chappert, Albert Fert, and Frédéric Nguyen Van Dau. The emergence of spin electronics in data storage. *Nature materials*, 6(11):813–823, 2007.

[420] Xiangyu Zeng, Ge Ye, Shuyi Huang, Qikai Ye, Wei Li, Chufan Chen, Haoze Kuang, Menglu Li, Yulu Liu, Zhijin Pan, et al. Thickness modulations enable multi-functional spin valves based on van der waals hetero-structure. *Nano Today*, 42:101373, 2022.

[421] Wen Jin, Gaojie Zhang, Hao Wu, Li Yang, Bichen Xiao, Jie Yu, Wenfeng Zhang, and Haixin Chang. Nonvolatile multistate magnetoresistance in all-van der waals antiferromagnet-based spin valves. *Applied Physics Letters*, 126(15), 2025.

[422] Ma Luo. Antiferromagnetic spin valve based on a heterostructure of two-dimensional hexagonal crystals. *Physical Review B*, 99(16):165407, 2019.

[423] Ali Hallal, Fatima Ibrahim, Hongxin Yang, Stephan Roche, and Mairbek Chshiev. Tailoring magnetic insulator proximity effects in graphene: first-principles calculations. *2D Materials*, 4(2):025074, 2017.

[424] Hong-Xin Yang, Ali Hallal, D Terrade, Xavier Waintal, Stephan Roche, and Mairbek Chshiev. Proximity effects induced in graphene by magnetic insulators: First-principles calculations<? format?> on spin filtering and exchange-splitting gaps. *Physical review letters*, 110(4):046603, 2013.

[425] Zhenhua Qiao, Wei Ren, Hua Chen, L Bellaiche, Zhenyu Zhang, AH MacDonald, and Qian Niu. Quantum anomalous hall effect in graphene proximity coupled to an antiferromagnetic insulator. *Physical review letters*, 112(11):116404, 2014.

[426] Zhiyong Wang, Chi Tang, Raymond Sachs, Yafis Barlas, and Jing Shi. Proximity-induced ferromagnetism in graphene revealed by the anomalous hall effect. *Physical review letters*, 114(1):016603, 2015.

[427] Johannes Christian Leutenantsmeyer, Alexey A Kaverzin, Magdalena Wojtaszek, and Bart J Van Wees. Proximity induced room temperature ferromagnetism in graphene probed with spin currents. *2D Materials*, 4(1):014001, 2016.

[428] Jiayong Zhang, Bao Zhao, Tong Zhou, Yang Xue, Chunlan Ma, and Zhongqin Yang. Strong magnetization and chern insulators in compressed graphene/cri 3 van der waals heterostructures. *Physical Review B*, 97(8):085401, 2018.

[429] M Umar Farooq and Jisang Hong. Switchable valley splitting by external electric field effect in graphene/cri3 heterostructures. *npj 2D Materials and Applications*, 3(1):3, 2019.

[430] Thomas Naimer, Klaus Zollner, Martin Gmitra, and Jaroslav Fabian. Twist-angle dependent proximity induced spin-orbit coupling in graphene/transition metal dichalcogenide heterostructures. *Physical Review B*, 104(19):195156, 2021.

[431] Lucas Webster and Jia-An Yan. Strain-tunable magnetic anisotropy in monolayer crcl 3, crbr 3, and cri 3. *Physical Review B*, 98(14):144411, 2018.

[432] MA Jafari, Małgorzata Wawrzyniak-Adamczewska, S Stagraczyński, A Dyrdal, and J Barnaś. Spin valve effect in two-dimensional vse2 system. *Journal of Magnetism and Magnetic Materials*, 548:168921, 2022.

[433] Mirali Jafari and Anna Dyrdał. First principle study on electronic and transport properties of finite-length nanoribbons and nanodiscs for selected two-dimensional materials. *Molecules*, 27(7):2228, 2022.

[434] MA Jafari, AA Kordbacheh, and A Dyrdal. Electronic and magnetic properties of silicene monolayer under bi-axial mechanical strain: First principles study. *Journal of Magnetism and Magnetic Materials*, 554:169260, 2022.

[435] Mirali Jafari, Wojciech Rudziński, Józef Barnaś, and Anna Dyrdał. Electronic and magnetic properties of 2d vanadium-based transition metal dichalcogenides. *Scientific Reports*, 13(1):20947, 2023.

[436] Mirali Jafari and Anna Dyrdał. Effect of strain on the electronic and magnetic properties of bilayer t-phase vs2: A first-principles study. *Journal of Magnetism and Magnetic Materials*, 589:171618, 2024.

[437] S Stagraczyński, P Baláž, Mirali Jafari, Józef Barnaś, and Anna Dyrdał. Magnetic ordering and dynamics in monolayers and bilayers of chromium trihalides: atomistic simulations approach. *Scientific Reports*, 14(1):25552, 2024.

[438] Mir Ali Jafari, Amirhossein Ahmadkhan Kordbacheh, Soheil Mahdian, and Narges Ghasemi. Electronic and transport properties of (6, 2) carbon and silicon nanotubes: A first-principles calculation. *Physica E: Low-dimensional Systems and Nanostructures*, 117:113855, 2020.

[439] Mirali Jafari, Nasim Rahmani-Ivriq, and Anna Dyrdal. Effect of fe-doping on vs2 monolayer: A first-principles study. *arXiv preprint arXiv:2411.12001*, 2024.

[440] Wojciech Rudziński, Mirali Jafari, Józef Barnaś, and Anna Dyrdał. Magnon-plasmon hybridization mediated by dzyaloshinskii-moriya interaction in two-dimensional crystals: tuning with electric field. *arXiv preprint arXiv:2506.11834*, 2025.

[441] M Jafari, M Gmitra, and A Dyrdał. Exchange and spin-orbit proximity driven topological and transport phenomena in twisted graphene/cri _3 heterostructures. *arXiv preprint arXiv:2509.11670*, 2025.

Appendices

Appendix A: Introduction To the Used Code Packages

This thesis includes a range of electronic, magnetic, and transport properties. Obtaining all results with self-developed code is both challenging and time-consuming. Therefore, in addition to our code to obtain most of the results, we used the DFT code packages developed by others as the basis of calculations and solved the self-consistent parts. Furthermore, some post-processing tools also helped us obtain additional results in more efficient ways. This appendix briefly introduces the utilized code packages in this thesis.

Quantum Espresso

General Description

One of the popular open-source software packages in Density functional theory is Quantum Espresso (QE). It performs first-principle simulations and can predict a wide range of properties, such as mechanical, electronic, magnetic, optical, and transport properties. This code's core is based on the plane-wave pseudopotential methods with the highest possible accuracy and efficiency at the atomic scale. QE is flexible and can perform single-atom simulations of complex molecular dynamics or materials optimization and minimizations. Moreover, this code can calculate periodic structures, such as crystals and, in this thesis, 2D materials and finite systems, like molecules like 0D nanodiscs. Quantum Espresso has many features, but the main one is its modularity. It uses different programs to compute each part. For instance, it uses the **pw.x** program to solve the main DFT problem; the **ph.x** program is used for phonon calculations; **bands.x** is used for electronic bandstructure plotting, and many other ***.x** excavators are used for specific tasks. The QE uses the input file to start the calculations, and it is user-defined for novel materials and advanced functionalities. This code can be run in a single node, or its efficiency is enhanced by parallelization. It is crucial in DFT calculations since we deal with a massive number of atoms. Fortunately, many sources exist for various functional exchange correlations and pseudopotentials, which can be chosen according to the investigating materials and the level of accuracy.

Role in this thesis

In this thesis, the QE was used to perform most of the DFT calculations directly, such as calculations of the electronic and magnetic properties, or we used its KS states/magnetization information to be used in other linked codes like Wannier90/Vampire tools. Moreover, we used this code to cross-check some other codes like Quantum ATK. The major use of the QE in this thesis refers to calculations of the electronic and magnetic proximity effect of the twisted graphene on the CrI_3 monolayer. In this work, we use QE for the DFT part and then use Kohn-Sham states, and then using Wannier90 code, we calculated our desired properties (for more details about the methodology,

please see our paper in 7.1.3).

Resources and References

Quantum Espresso is distributed under the GNU General Public License (GPL) and is free and only for academic and non-commercial use. Users can contribute to developing new features for this code in addition to reporting bugs and solving them in the forums. For more details about this code and all features it can compute, and also access to the source code, users can visit the official Quantum Espresso website at www.quantum-espresso.org. This website provides all the information concerning the code, different pseudopotentials, and many other handy information. In a nutshell, Quantum Espresso is one of the most well-known and widespread tools. At the same time, it is a powerful and versatile tool for researchers in materials sciences, condensed matter physics, and chemistry.

Quantum ATK

General Description

Quantum ATK (Atomistix ToolKit) is one of the well-known code packages designed for performing first-principle calculations and analyzing the properties of nanoscale materials and devices. ATK is a totally commercial software package and has been designed for computing several methods, such as Density Functional Theory [DFT], tight-binding, and classical simulations, which allows users to have access to a wide range of simulations in one code package. This versatile code is popular for studying the electronic, magnetic, optical, and transport properties. One of the unique features of this code is that QATK is mainly combined with the non-equilibrium Green's function (NEGF) method to calculate the quantum transport properties. With this extra feature, one can model the nanoscale devices and study them under applied bias. This code is excellent for those who do not have enough knowledge concerning Unix as it is entirely user-friendly and has a NanoLab graphical interface. The key feature of this code, as mentioned similarly for the QE, is the parallelization of the nodes to compute the large structures efficiently. However, as commercial software, it usually requires a license, which can be supposed to have weaknesses.

Role in This Thesis

Most of this thesis's primary and main results were obtained using the Quantum ATK (QATK) code package. We have obtained the electronic, magnetic, and transport properties of the structures and published our results, or we have calculated the preliminary results to gain insight into the material and generate a novel idea. For transport properties, using QATK and combined with the NEGF method, we designed unique devices and then calculated the I-V curve characteristics.

Resources and References

The official Quantum ATK website is www.synopsys.com provides an excellent tutorial with all the background physics of all features used in the code, which is suitable even for those who want to learn condensed matter physics without simulation.

Wannier90 code package

General Description

Wannier90 is an open-source code package for calculating maximally localized Wannier functions (MLWFs). It powerfully analyzes the electronic and magnetic structure of materials. Wannier functions mainly interpret the electronic properties of materials in terms of localized orbitals and can be applied to both metallic and insulating systems. To perform the calculations in Wannier90, one needs to use one of the DFT code packages, like Quantum Espresso, to generate and manipulate the Wannier functions from their results. As already mentioned in the QE's section, one of the key features of Wannier90 is projections of the KS states onto a chosen set of local functions and subsequently constructing the maximally localized Wannier functions. This is much more useful for several properties, such as electronic polarization, optical response, and conductivity. The accuracy of the Wannier function highly depends on the DFT calculations.

Role in This Thesis

In this thesis, we first used Wannier90 to extract maximally localized Wannier functions from the DFT calculations [QE code package]. Then, we used these functions to provide the electronics and magnetic properties of twisted graphene on the CrI_3 monolayer, such as the nature of bouning, hybridization of orbital, and the electronic density distribution. Then, we used these functions to compute the topological properties and explore the effective tight-binding Hamiltonians. One unique feature also conducted using Wannier90 in this thesis to obtain the post-processing calculations like Quantum Anamoulas Hall Conductivity [QAHC], Spin Hall Conductivity [SHC], Berry Curvature [BC], Berry Curvature Dipole [BCD], and many other properties.

Resources and References

The official website of the Wannier90 code package is www.wannier.org. On the website, one can get the source code plus all the examples in the repository, and also there is one helpful forum to discuss and ask questions. Moreover, the Wannier90 developers conduct workshops every year, and videos of them can be found on the website.

WannierTools

General Description

WannierTools is another open-source code package that uses the maximally localized Wannier functions (MLWFs) generated by Wannier90 code. The primary idea of developing this code is to study the topological properties of materials and their electronic structure in real and reciprocal space. This code uses the tight-binding Hamiltonian extracted from the Wannier90 code to compute a wide range of physical properties such as electronics and spin-resolved band structures, Fermi surfaces, Berry curvature, orbital magnetization, spin texture, and surface states. One of the prominent features of the WannierTools is its ability to visualize and analyze the surface electronic states and Fermi arcs using the iterative Green's function method. It makes this post-processing code an excellent tool for studying topological materials like topological insulators, Weyl semimetal, and Chern insulators. This code can also be parallelized with many cores, and its accuracy directly depends on Wannier functions extracted from DFT code like Quantum Espresso.

Role in This Thesis

In this work, we used WannierTools to investigate the topological properties of our materials, such as MnBi2Te4 and twisted Graphene on CrI_3, by analyzing the surface states and Fermi arcs. WannierTools gives us topological invariants such as Chern numbers, Berry Curvature, Fermi surfaces, Spin texture, unfolding bands from the supercell to the primitive cell, and many other features.

Resources and References

The official website for the WannierTools is www.wanniertools.org and you can find the repository access to the source of code, user manual, examples, and a perfect tutorial step-by-step.

Vampire

General Description

Vampire is another open-source code package explicitly designed for atomistic simulations of magnetic materials. This code is mainly appropriate for studying magnetic dynamics at the atomic scale, such as the ultra-fast magnetization process, spin waves, domain wall motion, and thermal effects on magnetic materials. Vampire uses an atomistic spin model, which provides a detailed and, most of the time, accurate definition of magnetic interactions. This software has a broad framework for simulating different magnetic behaviors like equilibrium and non-equilibrium processes, hysteresis loops, and temperature-dependent magnetic properties. The significant feature of this code is that it supports realistic materials modeling and makes it a powerful tool for understanding and predicting the magnetic behavior in new technologies such as spintronics, data storage, and magnetic sensors. However, Vampire requires some input parameters like exchange coupling constant for different neighbors and magnetic anisotropy energy in other planes, which needs extra computations.

Role in This Thesis

In this thesis, we have used the VAMPIRE code package in several projects to simulate the magnetic properties and dynamics of the considered systems. For instance, we have used this code to investigate important properties like spin wave dispersion, domain wall motion, or the changes of the magnetization as a function of the temperature to estimate the Curie/ Neel temperature, calculate the changes of magnetization as a function of the magnetic field and plot the hysteresis loops, and several other properties.

Resources and References

The official website of the VAMPIRE code is www.vampire.york.ac.uk . This website has an excellent landing page with manuals, tutorials, and examples of input files for different structures, from monolayer systems to multilayer. The website also lists all the publications published using VAMPIRE, which is handy for users to find related works.

TB2J code package

General Description

Using DFT code packages such as QE or VASP, we are able to calculate the electronic structure calculations, and the TB2J (Tight-binding to J) is an open-source tool that gives the Heisenberg exchange coupling constant between atoms (J parameters). It constructures the Heisenberg Hamiltonian using isotropic exchange calculations, Dzyaloshinskii–Moriya interaction (DMI), and anisotropic exchange from tight-binding or Wannier Hamiltonians. This code is essential as we use the J parameters in different properties like Magnon spectrum calculations.

Role in This Thesis

In this thesis, we have used TB2J to calculate the Nearest neighbor, next-nearest neighbor, and interlayer neighbor coupling constants and then constructed the Heisenberg spin model. We used this to plot the magnon dispersion, VAMPIRE calculations, and other properties.

Resources and References

The official website of the TB2J is www.tb2j.readthedocs.io and it is an open source code with a lot of examples and documents for introducing and analyzing.

Custom Python Tools

In addition to the main codes described above, I built several small, focused Python tools to close practical gaps in the thesis. These scripts add features missing in existing packages or replace

heavy computations with faster routines. Most tools target twisted 2D magnets and proximity systems, and they interoperate with Quantum ESPRESSO (QE), Wannier90, and TB2J. I also wrote an automated script to fit DFT results to a $k \cdot p$ model with the optimization methods which make the procedure of fitting easy and fast. Using Wannier tight-binding and the $k \cdot p$ model, few codes developed to compute anomalous Hall conductivity (AHC) and anomalous Nernst effect (ANE) versus temperature and chemical potential, and compare the two frameworks side-by-side. For Berry-phase physics, the scripts evaluate Berry curvature (and related geometry) and, alongside with DFT outputs, extract and analyze spin textures $(S_x, S_y, S_z)(\mathbf{k})$. Finally, using Heisenberg exchange constants J_{ij} from TB2J, I implemented a separate module that assembles magnon spectra along chosen high-symmetry paths, with flexible control over neighbor shells. Overall, these tools improve efficiency, reduce computational cost, and make the analysis reproducible and easy to extend. Once a user-friendly version of the codes is finalized, they will be released as open-source on GitHub.

Appendix B: Statements about the contributions to the publications

Attached below are the signed statements of both the author of this thesis and the co-authors of the publications included herein, confirming their respective contributions to the works constituting the dissertation.

ADAM MICKIEWICZ UNIVERSITY, POZNAŃ
Faculty of Physics and Astronomy
Institute of Spintronics and Quantum Information

Poznań, 1st October 2025

Mirali Jafari
Mesoscopic Physics Department
Institute of Spintronics and Quantum Information
Faculty of Physics and Astronomy
Adam Mickiewicz University in Poznań

Statement about the contribution to the publications

I hereby declare, as the author of this doctoral dissertation written based on the series of the following articles:

1. **M. Jafari**, A. Kordbacheh, A. Dyrdal, *Electronic and magnetic properties of silicene monolayer under bi-axial mechanical strain: First principles study*, Journal of Magnetism and Magnetic Materials 554, 169260 (2022)

2. **M. Jafari**, W. Rudziński, J. Barnaś, A. Dyrdał, *Electronic and magnetic properties of 2D vanadium-based transition metal dichalcogenides*, Scientific Reports 13, 20947 (2023)

3. **M. Jafari**, A. Dyrdał, *Effect of strain on the electronic and magnetic properties of bilayer T-phase VS2: A first-principles study*, Journal of Magnetism and Magnetic Materials 589, 171618 (2024).

4. **M. Jafari**, M. Wawrzyniak–Adamczewska, S. Stagraczyński, A. Dyrdał, J. Barnaś, *Spin valve effect in two-dimensional VSe2 system*, Journal of Magnetism and Magnetic Materials 548, 168921 (2022)

5. **M. Jafari**, M. Gmitra, A. Dyrdał, *Exchange and spin-orbit proximity driven topological and transport phenomena in twisted graphene/CrI_3 heterostructures*, preprint: arXiv:2509.11670 (2025)

that I was responsible for all DFT calculations, data analysis, preparing the figures, discussion of results and preparing the first draft of the articles. Additionally, in [3] I was the corresponding author, and in papers [1] and [3], I took part in the formulation and conceptualisation of the work.

Supervisor's signature

Author of the dissertation's signature

ADAM MICKIEWICZ UNIVERSITY, POZNAŃ
Faculty of Physics and Astronomy
Institute of Spintronics and Quantum Information

Poznań, 2nd October 2025

prof. UAM dr hab. Anna Dyrdał
Mesoscopic Physics Department
Institute of Spintronics and Quantum Information
Faculty of Physics and Astronomy
Adam Mickiewicz University in Poznań

Statement about the contribution to the publications

I hereby declare that I am aware that the following publications:

[1] M. A. Jafari, A. A. Kordbacheh, and A. Dyrdał,
Electronic and magnetic properties of silicene monolayer under bi-axial mechanical strain: a first-principles study,
Journal of Magnetism and Magnetic Materials, 554, 169260 (2022)

[2] M. A. Jafari and A. Dyrdał,
Effect of strain on the electronic and magnetic properties of bilayer T-phase VS_2: A first-principles study,
Journal of Magnetism and Magnetic Materials 589, 171618 (2024)

[3] M. A. Jafari, W. Rudzinski, J. Barnaś, and A. Dyrdał,
Electronic and magnetic properties of 2D vanadium-based transition metal dichalcogenides,
Scientific Reports 13, 20947 (2023)

[4] M. A. Jafari, M. Wawrzyniak-Adamczewska, S. Stagraczyński, A. Dyrdał, and J. Barnaś,
Spin valve effect in two-dimensional VSe_2 system,
Journal of Magnetism and Magnetic Materials 548, 168921 (2022)

[5] M. A. Jafari, M. Gmitra, and A. Dyrdał,
Exchange and spin-orbit proximity driven topological and transport phenomena in twisted graphene/CrI_3 heterostructures,
arXiv:2509.11670 (2025)

of which I am a co-author, have been included in the doctoral thesis of Mirali Jafari.

I also declare that my contributions to these papers include: formulating the problems, discussing and interpreting the obtained numerical results, supervising Mirali Jafari, and writing and editing the final versions of the manuscripts.

A. Dyrdał

ul. Uniwersytetu Poznańskiego 2, 61-614 Poznań, Poland
tel. +48 61 829 52 88 e-mail: adyrdal@amu.edu.pl
fizyka.amu.edu.pl

ADAM MICKIEWICZ UNIVERSITY, POZNAŃ
Faculty of Physics and Astronomy

Poznań, 25th September 2025

Prof. dr hab. Józef Barnaś
Mesoscopic Physics Department
Institute of Spintronics and Quantum Information
Faculty of Physics and Astronomy,
Adam Mickiewicz University in Poznań

Statement about the contribution to the publications

I hereby declare that I am aware that the following publications:

1. M. A. Jafari, W. Rudzinski, J. Barnaś, and A. Dyrdał, *Electronic and magnetic properties of 2D vanadium-based transition metal dichalcogenvides,* Scientific Reports, vol. 13, no. 1, p. 20947, 2023.
2. M. A. Jafari, M. Wawrzyniak-Adamczewska, S. Stagraczyński, A. Dyrdał, and J. Barnaś, *Spin valve effect in two-dimensional VSe_2 system*, Journal of Magnetism and Magnetic Materials, p. 168921, 2022.

of which I am a co-author, have been included in the doctoral thesis of M. A. Jafari. I also declare that my contribution to these papers includes discussions of the problem at the initial stage, help in the interpretation of numerical results, and help in the editing of the final versions of the manuscripts.

Józef Barnaś

Košice, 3rd October 2025

Dr. Martin Gmitra
Centre of Low Temperature Physics
Slovak Academy of Sciences, Slovakia

Department of Theoretical Physics and Astrophysics
Pavol Jozef Šafárik University in Košice, Slovakia

Statement about the contribution to the publications

I hereby declare that I am aware that the following publication:

M. A. Jafari, M. Gmitra, and A. Dyrdał,
Exchange and spin-orbit proximity driven topological and transport phenomena in twisted graphene/CrI_3 heterostructures,
arXiv:2509.11670 (2025)

of which I am a co-author, has been included in the doctoral thesis of Mirali Jafari.

I also declare that my contribution to this paper includes participation in the supervision of numerical work by Mirali Jafari, and reading and correcting the final version of the manuscript.

ADAM MICKIEWICZ UNIVERSITY, POZNAŃ
Faculty of Physics and Astronomy
Institute of Spintronics and Quantum Information

Poznań, 2nd October 2025

prof. UAM dr hab. Wojciech Rudziński
Mesoscopic Physics Department
Institute of Spintronics and Quantum Information
Faculty of Physics and Astronomy
Adam Mickiewicz University in Poznań

Statement about the contribution to the publications

I hereby declare that I am aware that the following publication:

M. A. Jafari, W. Rudzinski, J. Barnaś, and A. Dyrdał,
Electronic and magnetic properties of 2D vanadium-based transition metal dichalcogenides,
Scientific Reports 13, 20947 (2023)

of which I am a co-author, has been included in the doctoral thesis of Mirali Jafari.

I also declare that my contribution to this paper includes the calculation of spinwave dispersion relations from the analytical formalism of spin-waves and in discussions of the results.

Wojciech Rudziński

ul. Uniwersytetu Poznańskiego 2, 61-614 Poznań, Poland
tel. +48 61 829 52 88 e-mail: adyrdal@amu.edu.pl
fizyka.amu.edu.pl

جمهوری اسلامی ایران

IRAN UNIVERSITY OF SCIENCE & TECHNOLOGY

To:

Tehran, 2nd October 2025

Subject: Statement of contribution to publication

I hereby declare that I am fully aware that the following publication:

Jafari, M. A., A. A. Kordbacheh, and A. Dyrdal. "Electronic and magnetic properties of silicene monolayer under bi-axial mechanical strain: First principles study." Journal of Magnetism and Magnetic Materials 554 (2022): 169260,

of which I am a co-author, has been incorporated in the doctoral thesis of Mr. Mirali Jafari.

Furthermore, I confirm that my contribution to this paper involved participation in the data analysis and manuscript preparation undertaken by Mr. Mirali Jafari.

Yours truly,

Amirhosssein Ahmadkhan Kordbacheh

Department of Physics, Iran University of Science and Technology

Narmak, Tehran, Iran, 13114-16846

Tel:0098-21-77240540 , Fax:0098-21-77240497
Email: akordbacheh@iust.ac.ir

Poznań, 2nd October 2025

dr Stefan Stagraczyński
Faculty of Mathematics and Applied Physics
Rzeszów University of Technology

Statement about the contribution to the publications

I hereby declare that I am aware that the following publications:

M. A. Jafari, M. Wawrzyniak-Adamczewska, S. Stagraczyński, A. Dyrdał, and J. Barnaś,
Spin valve effect in two-dimensional VSe_2 system,
Journal of Magnetism and Magnetic Materials 548, 168921 (2022)

of which I am a co-author, have been included in the doctoral thesis of Mirali Jafari.

I also declare that my contribution to this paper includes cross-checking of DOS calculations, and discussion of the results.

Stefan Stagraczyński

Poznań, 2nd October 2025

dr Małgorzata Wawrzyniak – Adamczewska
Faculty of Physics and Astronomy
Adam Mickiewicz University in Poznań

Statement about the contribution to the publications

I hereby declare that I am aware that the following publication:

M. A. Jafari, M. Wawrzyniak-Adamczewska, S. Stagraczyński, A. Dyrdał, and J. Barnaś,
Spin valve effect in two-dimensional VSe_2 system,
Journal of Magnetism and Magnetic Materials 548, 168921 (2022)

of which I am a co-author, have been included in the doctoral thesis of Mirali Jafari.

I also declare that my contribution to this paper includes preliminary calculations of electronic band structures.

M. Wawrzyniak Adamczewska

Appendix C: Copy-Right Statements

Figure (1.1): The photographs of Nobel Prize laureates Andre Geim and Konstantin Novoselov are reproduced from the Nobel Prize website under their editorial use policy. These images are credited as: Source: https://www.nobelprize.org/organization/copyright-information/ © The Nobel Foundation, **Photographer: U. Montan**

Figure (2.2): is reproduced from: https://doi.org/10.1038/ncomms3096/ © Nature Communications, 2013. This figure is used with permission from Springer Nature (**License Number: 5990150903280**). Further reproduction or distribution is not permitted without written permission from Springer Nature.

Figure (2.4): is reproduced from https://doi.org/10.1039/D4RA03704A/ © RSC Advances, 2024, 14, 25378–25384 under the **Creative Commons Attribution-NonCommercial 3.0 (CC BY-NC 3.0) license**. No additional permission is required for non-commercial reuse.

Figure (2.6): is reproduced from https://doi.org/10.1103/PhysRevLett.108.155501, under **license RNP/25/MAR/089112 from the American Physical Society (APS)**. This material is used with permission, and further reproduction or distribution is not allowed without explicit approval from APS.

Figure (2.10) is reproduced from https://doi.org/10.1063/5.0039979/ © under the Creative Commons Attribution 4.0 International **(CC BY 4.0) license**. This allows reuse, distribution, and modification as long as proper credit is given to the original authors.

Figure (2.11) is reproduced from https://doi.org/10.1088/2053-1583/ab4c64, © under the Creative Commons Attribution **3.0 (CC BY 3.0) license**. Any further distribution of this work must maintain attribution to the author(s) and the title of the work, journal citation, and DOI.

Figures 2.14 and 2.15 is reproduced from: https://doi.org/10.1038/nature12385/ © Nature, 2013. This figure is used with permission from Springer Nature (**License Number: 5990180248156**). Further reproduction or distribution is not permitted without written permission from Springer Nature.

Figure (2.16) is reproduced from: https://doi.org/10.1038/natrevmats.2016.42/ © Nature Reviews Materials, 2016. This figure is used with permission from Springer Nature (**License Number: 5990180773380**). Further reproduction or distribution is not permitted without written permission from Springer Nature.

Figures 2.17, and 2.18 is reproduced from: https://doi.org/10.1038/s41565-021-00936-x/ © Nature Technology, 2016. This figure is used with permission from Springer Nature (**License Number: 5990181398741**). Further reproduction or distribution is not permitted without written permission from Springer Nature.

Figures 2.19 is reproduced from: https://doi.org/10.1038/s41563-020-00840-0/ © Nature Materials , 2020. This figure is used with permission from Springer Nature (**License Number: 5990191463735**).

Short about the author

I began my Ph.D. journey in February 2021 at Adam Mickiewicz University under the supervision of Professor Anna Dyrdał after completing my master's degree in solid-state physics at the Iran University of Science and Technology. My main area of research focuses on solid-state physics, with theoretical works on Density Functional Theory (DFT) methods and their subsequent analytical aspects. My research aims to study and explore the wide range of electronics and spintronics aspects, focusing on van der Waals (vdW) materials with specific work on the magnetic and transport properties of low-dimensionally van der Waals structures.

My primary motivation for studying solid-state physics is its vast potential for real-world applications. From semiconductors to quantum materials and even interdisciplinary collaborations with biology and medical science, it allows the discovery of new physical phenomena in these areas and new methods to improve the currently used methods.

Academic Contributions

- **Seven published papers**
- **Three under-review article**
- **One to be published articles**
- Participated in **three workshops** on the methods I am working on
- **One talk as an invited speaker**
- **Nine talk as a contributed speaker** at conferences and seminars
- **Thirteen poster presentations**
- Contributed as **a reviewer for three journals**
- Member of a **2DQMS workshop organizing committee**
- Completed a **four-month internship** / and **Two visits**
- Recognized with **three awards and one research grant**
- Worked as **a part-time assistant for one year** during the final year of my Ph.D.

My journey doesn't end with my Ph.D. but is the beginning of a lifelong dream of knowledge and discovery. I aim to contribute to a deeper understanding of low-dimensional materials and their potential applications. I also aim to engage in new areas, such as machine learning in physics and collaborations with experimental and medical science groups.

List of Publications

[1] M. A. Jafari, M. Wawrzyniak-Adamczewska, S. Stagraczyński, A. Dyrdał, and J. Barnaś, *"Spin valve effect in two-dimensional VSe_2 system,"* *Journal of Magnetism and Magnetic Materials*, p. 168921, 2022. [432]

[2] M. A. Jafari and A. Dyrdał, *"First Principle Study on Electronic and Transport Properties of Finite-Length Nanoribbons and Nanodiscs for Selected Two-Dimensional Materials,"* *Molecules*, vol. 27, no. 2228, 2022. [433]

[3] M. A. Jafari, A. A. Kordbacheh, and A. Dyrdał, *"Electronic and magnetic properties of silicene monolayer under bi-axial mechanical strain: a first-principles study,"* *Journal of Magnetism and Magnetic Materials*, p. 169260, 2022. [434]

[4] M. A. Jafari, W. Rudzinski, J. Barnaś, and A. Dyrdał, *"Electronic and magnetic properties of 2D vanadium-based transition metal dichalcogenides,"* *Scientific Reports*, vol. 13, no. 1, p. 20947, 2023. [435]

[5] M. A. Jafari and A. Dyrdał, *"Effect of strain on the electronic and magnetic properties of bilayer T-phase VS_2: A first-principles study,"* *Journal of Magnetism and Magnetic Materials*, vol. 589, p. 171618, 2024. [436]

[6] S. Stagraczyński, P. Baláž, M. A. Jafari, J. Barnaś, and A. Dyrdał, *"Magnetic ordering and dynamics in monolayers and bilayers of chromium trihalides: atomistic simulations approach,"* *Scientific Reports*, vol. 14, no. 1, p. 25552, 2024. [437]

[7] M. A. Jafari, at al., *"Electronic and transport properties of (6, 2) carbon and silicon nanotubes: A first-principles calculation,"* *Physica E: Low-dimensional Systems and Nanostructures*, vol. 117, no. 1, p. 113855, 2020. [438]

[8] M. Jafari, N. Rahmani-Ivriq, and A. Dyrdał, *"Effect of Fe-doping on VS_2 monolayer: A first-principles study,"* arXiv preprint arXiv:2411.12001 (2024). [439]

[9] Wójciech Rudziński, M. Jafari, Józef Barnaś and A. Dyrdał, *"Magnon-plasmon hybridization mediated by Dzyaloshinskii-Moriya interaction in two-dimensional crystals: tuning with electric field,"* arXiv preprint arXiv:2506.11834 (2025). [440]

[10] M. Jafari, M. Gmitra, and A. Dyrdał, *"Exchange and spin-orbit proximity driven topological and transport phenomena in twisted graphene/CrI_3 heterostructures,"* arXiv preprint arXiv:2509.11670v1 (2025). [441]

[11] M. Jafari, M. Gmitra, and A. Dyrdał, *"First-Principles Investigation of the Electronic, Magnetic, and*

Transport Properties of $MnBi_2Te_4$," **(To be published)**.

List of Participated technical Workshops

[1] GPAW 2021: Users and Developers Meeting, *June 1, 2021 - June 4, 2021*, Online.

[2] First steps with SIESTA: from zero to hero, *2nd - 6th October 2023*, Online.

[3] Density Functional Theory and Artificial Intelligence learning from each other, *March 3, 2025 - March 6, 2025*, Switzerland - online (hybrid format).

Reviews and Memberships

- Reviewer for *Journal of Physics: Condensed Matter* (IOP Publishing, UK) — a leading journal in condensed matter and materials physics.
- Reviewer for *AIP Advances* (AIP Publishing LLC, Melville, New York, USA; Source Work ID: IL5oHmMw3fmG52CbGBOkg)
- Reviewer for *Journal of Superconductivity and Novel Magnetism*

Internships and visits

[1] Four-month Internship from 01.02.2023 to 31.05.2023 at Pavol Jozef Šafárik University in Košice, in collaboration with Dr.Martin Gmitra.

[2] One week visit from 30 June to 5 July at Pavol Jozef Šafárik University in Košice, in collaboration with Dr.Martin Gmitra.

Awards, grants, and scholarships

- Preludium 23 Grant, NCN Poland – Project: "Electronic and magnetic properties of two-dimensional crystals of transition metal iodides encapsulated by graphene" (Reg. No: 2024/53/N/ST3/02621).
- Rector's Award for achievement in scientific research (Adam Mickiewicz University, Poznań - 2025)
- Rector's Award for achievement in scientific research (Adam Mickiewicz University, Poznań - 2024)

- Third Prize for the best oral presentation at the European Conference Physics of Magnetism 2023.
- Scholarship for Ph.D. from Grieg Project (2020-2024) under the Norwegian Financial Mechanism (Project No. 2019/34/H/ST3/00515).
- Received four plus two years scholarships for bachelor's and master's degrees from the Iran Ministry of Science, Research and Technology.

Conferences / Seminars presentations

Oral Presentation: (Invited Speaker)

1. Mirali Jafari, "Electronic and magnetic properties of van der Waals materials: first-principles studies", van der Waals Materials for Nanoelectronics, 1–2 September 2025, Poznan, Poland.

Oral Presentations: (Contributed Speaker)

1. Mirali Jafari, Nasim Rahmani, Anna Dyrdał, "Effect of Fe-doping on VS2 monolayer: A first-principles study" (Talk), Graphene and other 2D materials, 08th-10th of September 2024, Poznan, Poland.
2. Mirali Jafari, Wojciech Rudziński, Józef Barnaś, Anna Dyrdał, "Magnetic properties of Vanadium-based Transition metal dichalcogenides" (Talk), 2DQMS 2024, 29th-31st of January 2024, Poznan, Poland.
3. Mirali Jafari, Wojciech Rudziński, Józef Barnaś, Anna Dyrdał, "Static and Dynamic Magnetic Properties of Two-Dimensional Van Der Waals Materials: Vanadium-Based Transition-Metal Dichalcogenides, VX2 for X= S, Se, and Te." (Talk), MagIC+ 2023, 24-28 July 2023, Będlewo, Poland.
4. Mirali Jafari, and Anna Dyrdał, "Effect of Strain on Bilayer of T-VS2" (Talk), PHYSICS OF MAGNETISM 2023 (PM'23), June 26-30, 2023, Poznan, Poland.
5. Mirali Jafari, "Magnetic and Transport Properties of Low-Dimensional van der Waals Structures" (Talk), KTFA Seminars of Pavol Jozef Šafárik University, 9 February 2023, Košice, Slovakia.
6. Mirali Jafari, Anna Dyrdał, "Magnetic Properties of Monolayer and Bilayer of Vanadium-based Transition Metal Dichalcogenides VX2 (X=S, Se, and Te)" (Talk), Symposium on Spintronics and Quantum Information 2022, 9 December 2022, Poznan, Poland.
7. M.A. Jafari, Magnetic and transport properties of low-dimensional van-der-Waals structures, (Doctoral forum talk), Doctoral School of Adam Mickiewicz University, 23.09.2021, Poznań (Poland).

8. M.A. Jafari, M. Wawrzyniak-Adamczewska, A. Dyrdał, and J.Barnaś, "Spin valve effect in two-dimensional VSe2 system" (Talk), The European Conference Physics of Magnetism, PM21, 02.07.2021, Poznań (Poland).
9. M.A. Jafari, "Electronic and magnetic properties of nanostructures based on novel 2D materials: DFT Approach" (Talk), 2Dtronics Kickoff Meeting, 11-12.03.2021, Poland.

Poster Presentations:

1. Mirali Jafari, Anna Dyrdał, "First-principal Analysis of Electronic and Transport Properties in Finite Nanoribbons and Nanodiscs of selected 2D Materials" (Poster), 2DQMS 2024, 29th-31st of January 2024, Poznan, Poland.
2. Mirali Jafari, Martin Gmitra, and Anna Dyrdał, “Electronic, Magnetic, and Transport Properties of the Topological Insulator MnBi2Te4 through First-Principles Calculations” (Poster), JEMS 2023, 27 August – 1st September 2023, Madrid, Spain.
3. Mirali Jafari, Wojciech Rudziński, Józef Barnaś, Anna Dyrdał, "Static and Dynamic Magnetic Properties of Vanadium-Based Transition-Metal Dichalcogenides, VX2 for X= S, Se, and Te." (Poster), Magnonics 2023, 30 July - 3 August 2023, Le Touquet – Paris – Plage, France.
4. Mirali Jafari, "Magnetic and transport properties of van der Waals heterostructure materials" (poster), Doctoral Forum, 3 July 2023, Faculty of Physics, AMU, Poznan, Poland.
5. Mirali Jafari, Martin Gmitra, and Anna Dyrdał, "First-Principles Investigation of the Electronic, Magnetic, and Transport properties of MnBi2Te4" (Poster), PHYSICS OF MAGNETISM 2023 (PM’23), June 26-30, 2023, Poznan, Poland.
6. Mirali Jafari, Magnetic and transport properties of van der Waals heterostructure materials (poster), Doctoral Forum, 28 September 2022, Faculty of Physics, AMU, Poznan, Poland.
7. Mirali Jafari, Anna Dyrdał, Józef Barnaś, Electronic and Magnetic Properties of Monolayer and Bilayer Films of Vanadium-based Transition Metal Dichalcogenides VX2 (X=S, Se, and Te) (poster), IEEE NAP 2022 Conference, 11-16 September 2022, Krakow, Poland.
8. Mirali Jafari, Anna Dyrdał, DFT study of the electronic and magnetic properties of monolayer and bilayer of VS2 (poster), JEMS2022 conference, 24 - 29 July 2022, Warsaw, Poland.
9. Mirali Jafari, M. Wawrzyniak-Adamczewska, A. Dyrdał, and J.Barnaś, Spin-valve effect in graphene/2H-VSe2/graphene junctions (poster), Magic+ Workshop: Magnetism, Interactions and Complexity; 05-07.07.2021, Poznań (Poland).
10. M.A. Jafari, A. Ahmadkhan Kordbacheh, A. Dyrdał, First principal study on electronic properties of nanoribbons and nanodisks for the Molybdenite and Graphene (poster), Nanotech Poland, 09-11.06.2021, Poznań (Poland).
11. M.A. Jafari, A. Ahmadkhan Kordbacheh, A. Dyrdał, Tuning the electronic and magnetic structures of silicene monolayer by biaxial strain: A DFT study (poster), Nanotech Poland 2021, 09-11.06.2021, Poznań (Poland).

12. M.A. Jafari, A. Ahmadkhan Kordbacheh, A. Dyrdał, Electronic and magnetic properties of silicene monolayer under bi-axial mechanical strain: A first principle study (poster), The European Conference Physics of Magnetism, PM21, 02.07.2021 Poznań (Poland).
13. MA Jafari, N Ghasemi, A Kordbacheh, Tuning the Electronic, Optical, and Transport Properties of Zigzag WSe2 Nanoribbons by Edge Passivated and Width Variation (Poster), 7th International Conference on Nanostructures (ICNS7) at Sharif University of Technology, March 2018, Tehran, Iran.